

**INFRARED MICROSPECTROSCOPY OF PLANTS: USE OF SYNCHROTRON  
RADIATION INFRARED MICROSPECTROSCOPY TO STUDY PLANT ROOT  
ANATOMY AND TO MONITOR THE FATE OF ORGANIC CONTAMINANTS IN  
THOSE ROOTS**

by

**KENNETH M. DOKKEN**

B.S., University of Texas at El Paso, 1999

M.S., University of Texas at El Paso, 2001

**AN ABSTRACT OF A DISSERTATION**

submitted in partial fulfillment of the requirements for the degree

**DOCTOR OF PHILOSOPHY**

Graduate Biochemistry Group

**KANSAS STATE UNIVERSITY**

Manhattan, Kansas

2006

## ABSTRACT

The fate and bioavailability of organic contaminants in plants is a major ecological and human health concern. Current wet chemistry techniques that employ strong chemical treatments and extractions with volatile solvents, such as GC-MS, HPLC, and radiolabeling, although helpful, degrade plant tissue resulting in the loss of spatial distribution and the production of artifacts. Synchrotron radiation infrared microspectroscopy (SR-IMS) permits direct analysis of plant cell wall architecture at the cellular level *in situ*, combining spatially localized information and chemical information from the IR absorbances to produce a chemical map that can be linked to a particular morphology or functional group. This study demonstrated the use of SR-IMS to probe biopolymers such as cellulose, lignin, and proteins in the root tissue of hydroponically grown sunflower and maize plants as well as to determine the fate and effect of several organic contaminants in those root tissues. Principal components analysis (PCA), a data compression technique, was employed to reveal the major spectral variances between untreated and organic contaminant treated root tissues. Treatment with 1H-benzotriazole (BT) caused alterations to the lignin component in the root tissue of plants. The BT was found in xylem and epidermal tissue of sunflower plants but not associated with any particular tissue in maize roots. 2,4-dinitrotoluene (2,4-DNT) and 2,6-dinitrotoluene (2,6-DNT) altered the pectin and polysaccharide structure in both maize and sunflower. SR-IMS revealed the reduction of DNTs to their aromatic amine form in the vascular and epidermal tissues at low concentration. At high concentration, DNTs appeared to be associated with all the plant tissues in maize and sunflower. Exposure of sunflower and maize to 2,6-dichlorophenol (2,6-DCP) caused alterations to the polysaccharide and protein component of the root tissue. In some cases, phenolic compounds were observed in the epidermal tissue of maize and sunflower roots. The results of this research indicate that SR-IMS has the potential to become an important analytical tool for determining the fate and effect of organic contaminants in plants.

**INFRARED MICROSPECTROSCOPY OF PLANTS: USE OF SYNCHROTRON  
RADIATION INFRARED MICROSPECTROSCOPY TO STUDY PLANT ROOT  
ANATOMY AND TO MONITOR THE FATE OF ORGANIC CONTAMINANTS IN  
THOSE ROOTS**

by

**KENNETH M. DOKKEN**

B.S., University of Texas at El Paso, 1999

M.S., University of Texas at El Paso, 2001

**A DISSERTATION**

submitted in partial fulfillment of the requirements for the degree

**DOCTOR OF PHILOSOPHY**

Graduate Biochemistry Group

**KANSAS STATE UNIVERSITY**

Manhattan, Kansas

2006

Approved by:

Major Professor

Lawrence C. Davis

Department of Biochemistry

**COPYRIGHT**

Kenneth M. Dokken

2006

## ABSTRACT

The fate and bioavailability of organic contaminants in plants is a major ecological and human health concern. Current wet chemistry techniques that employ strong chemical treatments and extractions with volatile solvents, such as GC-MS, HPLC, and radiolabeling, although helpful, degrade plant tissue resulting in the loss of spatial distribution and the production of artifacts. Synchrotron radiation infrared microspectroscopy (SR-IMS) permits direct analysis of plant cell wall architecture at the cellular level *in situ*, combining spatially localized information and chemical information from the IR absorbances to produce a chemical map that can be linked to a particular morphology or functional group. This study demonstrated the use of SR-IMS to probe biopolymers such as cellulose, lignin, and proteins in the root tissue of hydroponically grown sunflower and maize plants as well as to determine the fate and effect of several organic contaminants in those root tissues. Principal components analysis (PCA), a data compression technique, was employed to reveal the major spectral variances between untreated and organic contaminant treated root tissues. Treatment with 1H-benzotriazole (BT) caused alterations to the lignin component in the root tissue of plants. The BT was found in xylem and epidermal tissue of sunflower plants but not associated with any particular tissue in maize roots. 2,4-dinitrotoluene (2,4-DNT) and 2,6-dinitrotoluene (2,6-DNT) altered the pectin and polysaccharide structure in both maize and sunflower. SR-IMS revealed the reduction of DNTs to their aromatic amine form in the vascular and epidermal tissues at low concentration. At high concentration, DNTs appeared to be associated with all the plant tissues in maize and sunflower. Exposure of sunflower and maize to 2,6-dichlorophenol (2,6-DCP) caused alterations to the polysaccharide and protein component of the root tissue. In some cases, phenolic compounds were observed in the epidermal tissue of maize and sunflower roots. The results of this research indicate that SR-IMS has the potential to become an important analytical tool for determining the fate and effect of organic contaminants in plants.

## TABLE OF CONTENTS

LIST OF FIGURES .....	viii
LIST OF TABLES .....	xiv
ACKNOWLEDGEMENTS .....	xv
DEDICATION .....	xvi
CHAPTER 1 - INTRODUCTION .....	1
Phytoremediation .....	2
Infrared (IR) Spectroscopy .....	5
Infrared Techniques .....	7
<i>Infrared Microspectroscopy (IMS)</i> .....	7
<i>Synchrotron Radiation Infrared Microspectroscopy (SR-IMS)</i> .....	7
<i>Attenuated Total Reflection (ATR) Spectroscopy</i> .....	9
Chemometric techniques for infrared spectral analysis .....	10
Using IMS to monitor the fate of organic contaminants in maize and sunflower plants.....	12
CHAPTER 2 - EXPERIMENTAL METHODS .....	22
Rationale .....	23
Reagents and Plant Culture Solutions .....	23
Growth of Plants .....	24
Preparation of Plant Tissue .....	26
<i>Potassium Bromide Pellets for Conventional IR Spectroscopy</i> .....	26
<i>Dry Tissue Sections for ATR Spectroscopy</i> .....	27
<i>Cryosectioning of Plant Roots for SR-IMS</i> .....	27
Analytical Methods .....	28
<i>HPLC Methods</i> .....	28
<i>IR Methods</i> .....	29
Principal Components Analysis (PCA) .....	32
CHAPTER 3 - INFRARED IMAGING OF SUNFLOWER AND MAIZE ROOT ANATOMY	42
Introduction .....	43
Results and Discussion .....	45

<i>Assignment of IR bands in maize and sunflower root tissue</i> .....	45
<i>Infrared dissection of sunflower root tissue</i> .....	46
<i>Infrared dissection of maize root tissue</i> .....	50
<i>Comparison of maize and sunflower root tissues</i> .....	53
CHAPTER 4 - MONITORING THE FATE AND EFFECT OF 1H-BENZOTRIAZOLE (BT) IN SUNFLOWER AND MAIZE PLANTS USING SR-IMS .....	83
Introduction.....	84
Results and Discussion .....	85
<i>Uptake of BT by maize and sunflower plants</i> .....	85
<i>Conventional FTIR and ATR spectroscopy of BT in Dried Sunflower Root Tissue</i> .....	86
<i>SR-IMS of sunflower root tissue exposed to BT</i> .....	88
<i>SR-IMS of maize root tissue exposed to BT</i> .....	93
CHAPTER 5 - MONITORING THE FATE AND EFFECT OF 2,4-DINITROTOLUENE (2,4- DNT) AND 2,6-DINITROTOLUENE (2,6-DNT) IN SUNFLOWER AND MAIZE PLANTS USING SR-IMS .....	116
Introduction.....	117
Results and Discussion .....	119
<i>Uptake of 2,4-DNT and 2,6-DNT by maize and sunflower plants</i> .....	119
<i>Interpretation of the FTIR spectra of 2,4-DNT and 2,6-DNT</i> .....	120
<i>SR-IMS of sunflower roots exposed to 2,4-DNT</i> .....	120
<i>SR-IMS of maize roots exposed to 2,4-DNT and 2,6-DNT</i> .....	123
CHAPTER 6 - MONITORING THE FATE AND EFFECT OF 2,6-DICHLOROPHENOL (2,6- DCP) IN SUNFLOWER AND MAIZE PLANTS USING SR-IMS .....	147
Introduction.....	148
Results and Discussion .....	149
<i>Loss of 2,6-DCP with maize and sunflower plants</i> .....	149
<i>Interpretation of the FTIR spectrum 2,6-DCP</i> .....	150
<i>SR-IMS of sunflower roots exposed to 2,6-DCP</i> .....	151
<i>SR-IMS of maize roots exposed to 2,6-DCP</i> .....	153
CHAPTER 7 - FUTURE RESEARCH.....	167
CHAPTER 8 - REFERENCES.....	169

## LIST OF FIGURES

Figure 1. The Electromagnetic Spectrum. ....	16
Figure 2. Some typical vibration modes found in organic molecules.....	17
Figure 3. Comparison of brightness in the infrared emission from a globar source and the synchrotron ring at the National Synchrotron Light Source at Brookhaven National Laboratory.....	18
Figure 4. Typical synchrotron radiation storage ring.....	19
Figure 5. Diamond ATR objective.....	20
Figure 6. Schematic representation of PCA analysis of infrared imaging data.....	21
Figure 7. Longitudinal section of dry sunflower root tissue for ATR spectroscopic analysis.....	36
Figure 8. NSLS experimental floor.....	37
Figure 9. Features of Beamline U2B at the NSLS.....	38
Figure 10. Example of a principal components score plot using maize and sunflower epidermis samples.....	39
Figure 11. The principal component loadings depicting the major variation between maize and sunflower epidermis.....	40
Figure 12. Example of a validation score plot used to test the robustness of the model set. The hollow symbols represent the (□) maize and (○) sunflower group centers. ....	41
Figure 13. Typical plant root anatomy.....	59
Figure 14. Line map and typical IR spectrum of sunflower root cap approximately 100 μm from the root tip. ....	60
Figure 15. Line map and typical IR spectrum of sunflower root approximately 250 μm from the root tip.....	61
Figure 16. Functional group area maps of sunflower root tissue approximately 500 μm from root tip. ....	62
Figure 17. Typical spectrum of sunflower root cortex (black), boundary between epidermis and cortex (blue), and epidermis (red) tissue approximately 500 μm from tip.....	63
Figure 18. Functional group area maps of sunflower root tissue approximately 1 mm from root tip. ....	64



Figure 19. Typical spectrum of sunflower root cortex (black), boundary tissue between epidermis and cortex (blue), epidermis (red), vascular tissue (green), and endodermis (purple) approximately 1 mm from the root tip.....	65
Figure 20. Functional group area maps of sunflower root tissue approximately 1 cm from the root tip.....	66
Figure 21. Typical spectrum of sunflower root cortex (black), epidermis (red), and phloem (blue), and xylem (green) tissue approximately 1 cm from the tip.....	67
Figure 22. Line map and typical IR spectrum of maize root cap approximately 150 $\mu\text{m}$ from the root tip.....	68
Figure 23. Line map and typical IR spectrum of maize root approximately 400 $\mu\text{m}$ from the root tip.....	69
Figure 24. Functional group area maps of maize root tissue approximately 800 $\mu\text{m}$ from root tip.....	70
Figure 25. Typical spectrum of maize root cortex (black), epidermis (red), and vascular tissue (green) approximately 800 $\mu\text{m}$ from the root tip.....	71
Figure 26. Functional group area maps of maize root tissue approximately 1 cm from the root tip.....	72
Figure 27. Typical spectrum of maize root cortex (black), epidermis (red), xylem tissue (green), and pith (blue), approximately 1 cm from the root tip.....	73
Figure 28. A PCA score plot shows that maize and sunflower epidermis can be separated by the first 2 PCs.....	74
Figure 29. The loadings for the first (A) and second (B) principal components depicting the major variation between maize and sunflower epidermis spectra.....	75
Figure 30. Validation plot used to test the robustness of the model set for maize and sunflower epidermis.....	76
Figure 31. PCA score plots of using the first and second principal component (A) and the third and fifth principal component (B).....	77
Figure 32. The loadings for the first (A), second (B), third (C), fourth (D), and fifth (E) principal components.....	78
Figure 33. The reassignment and assignment success rates based on the number of PC scores used in LDA.....	79

Figure 34. A PCA score plot shows that maize and sunflower xylem can be separated by the first 2 PCs. ....	80
Figure 35. The loadings for the first (A) and second (B) principal components depicting the major variation between maize and sunflower xylem spectra. ....	81
Figure 36. Validation plot used to test the robustness of the model set for maize and sunflower xylem. ....	82
Figure 37. FTIR spectrum of 1H-benzotriazole (BT) in KBr. ....	99
Figure 38. FTIR spectra of dried sunflower root samples that were untreated and treated with 30, 60, and 90 mg/L benzotriazole, respectively. ....	100
Figure 39. FTIR spectra of sunflower root samples that are untreated, untreated spiked with 5% benzotriazole, and treated with 60 mg/L benzotriazole respectively. ....	101
Figure 40. ATR spectra of secondary roots taken from sunflower plants untreated (••••) and treated (—) with 60 mg/L BT. ....	102
Figure 41. ATR spectra of primary root taken from sunflower plants untreated (••••) and treated (—) with 60 mg/L 1H-benzotriazole. ....	103
Figure 42. FTIR spectra of root cortex sectioned at 400 $\mu$ m from the roots of untreated control, 10 mg/L BT treated and 30 mg/L treated sunflower plants. ....	104
Figure 43. Functional group area maps showing the distribution of protein and BT in the root tissue of untreated and BT treated sunflowers sectioned at about 400 $\mu$ m from the root tip. ....	105
Figure 44. PCA shows separation between the vascular (cortex) tissue of untreated control (●) and the BT treated sunflower plants, 10 mg/L BT (▲) and 30 mg/L (■) using the first 2 PC scores. ....	106
Figure 45. LDA using the Mahalanobis distance metric was performed on 60 observations arbitrarily selected from independent sample sets to validate the model set. ....	107
Figure 46. The PC loadings derived from the exploratory PCA of vascular (cortex) tissue from untreated control, 10 mg/L BT treated and 30 mg/L treated sunflower plants. ....	108
Figure 47. Functional group area maps showing the spatial distribution and concentration of BT in the root tissue of untreated and 30 mg/L BT treated sunflowers sectioned at about 1cm from the root tip. ....	109
Figure 48. IR spectra of root xylem from untreated and 30 mg/L BT treated sunflower plants	110

Figure 49. Exploratory PCA shows separation between the root vascular (cortex) tissue of untreated control (■) and the 90 mg/L BT treated maize plants (▲) using the first 2 PC scores.....	111
Figure 50. The PC loadings derived from the exploratory PCA of vascular (cortex) tissue from untreated control and 90 mg/L BT treated maize plants.....	112
Figure 51. Exploratory PCA shows separation between the root epidermal tissue of untreated control (■) and the 90 mg/L BT treated maize plants (▲) using the first 2 PC scores. ....	113
Figure 52. The PC loadings derived from the exploratory PCA of epidermal tissue from untreated control and 90 mg/L BT maize plants.....	114
Figure 53. Functional group area maps showing the spatial distribution and concentration of lignin components in the root tissue of untreated, 30 mg/L BT, 60 mg/L BT, and 90 mg/L BT treated maize plants sectioned at about 400 μm from the root tip.....	115
Figure 54. FTIR spectrum of (A) 2,4-dinitrotoluene (2,4-DNT) and (B) 2,6-dinitrotoluene (2,6-DNT) in KBr. ....	131
Figure 55. An example of the SR-IMS spectra taken from a section of a dark brown sunflower root from 2,6-DNT treated plants. ....	132
Figure 56. Exploratory PCA shows separation between the root vascular (cortex) tissue of untreated control (■) and 5 mg/L 2,4-DNT treated sunflower plants (●) using the first 2 PC scores.....	133
Figure 57. The PC loadings derived from the exploratory PCA of vascular (cortex) tissue from untreated control and 5 mg/L 2,4-DNT treated sunflower plants. ....	134
Figure 58. Typical spectra of epidermis tissue from untreated and 5 mg/L 2,4-DNT treated sunflower plants.....	135
Figure 59. Functional group area maps showing the spatial distribution and concentration of 2,4-DNT and pectic polysaccharides in the root tissue of untreated and 5 mg/L 2,4-DNT treated sunflowers sectioned at about 400 μm from the root tip. ....	136
Figure 60. Exploratory PCA shows separation between the root epidermis of untreated control (■) and 5 mg/L 2,4-DNT treated maize plants (●) using the first 2 PC scores.....	137
Figure 61. The PC loadings derived from the exploratory PCA of epidermal tissue from untreated control and 5 mg/L 2,4-DNT treated maize plants. ....	138

Figure 62. Functional group area maps showing the distribution of aromatic amines and pectic polysaccharides in the root tissue of untreated and 5 mg/L 2,4-DNT treated maize plants sectioned between 700 and 800 $\mu\text{m}$ from the root tip.....	139
Figure 63. Typical spectra of xylem tissue from untreated and 10 mg/L 2,4-DNT treated maize plants.....	140
Figure 64. Functional group area maps showing the distribution of DNT and proteins in the root tissue of untreated and 10 mg/L 2,4-DNT treated maize plants sectioned about 1 cm from the root tip. ....	141
Figure 65. Exploratory PCA shows separation between the root vascular (cortex) tissue of untreated control (■) and 10 mg/L 2,6-DNT treated maize plants (●) using the second and third PC scores. ....	142
Figure 66. The PC loadings derived from the exploratory PCA of vascular (cortex) tissue from untreated control and 10 mg/L 2,6-DNT treated maize sunflower plants. ....	143
Figure 67. Exploratory PCA shows separation between the root epidermis of untreated control (■) and 10 mg/L 2,6-DNT treated maize plants (●) using the first 2 PC scores. ....	144
Figure 68. The PC loadings derived from the exploratory PCA of epidermal tissue from untreated control and 10 mg/L 2,6-DNT treated maize plants. ....	145
Figure 69. Functional group area maps showing the spatial distribution of DNT in the root tissue of untreated and 10 mg/L 2,6-DNT treated maize plants sectioned between 700 and 800 $\mu\text{m}$ from the root tip. ....	146
Figure 70. FTIR spectrum of 2,6-dichlorophenol (2,6-DCP) in KBr. ....	158
Figure 71. Exploratory PCA shows separation between the root vascular (cortex) tissue of untreated control (■) and 3 mg/L 2,6-DCP treated sunflower plants (●) using the first and third PC scores. ....	159
Figure 72. The PC loadings derived from the exploratory PCA of vascular (cortex) tissue from untreated control and 3 mg/L 2,6-DCP treated sunflower plants. ....	160
Figure 73. Functional group area maps showing the spatial distribution and concentration of 2,6-DCP or phenolics and proteins in the root tissue of untreated and 3, 6, and 10 mg/L 2,6-DCP treated sunflowers sectioned at about 400 $\mu\text{m}$ from the root tip.....	161

Figure 74. Exploratory PCA shows separation between the root vascular (cortex) tissue of untreated control (■) and 6 mg/L 2,6-DCP treated maize plants (●) using the first two PC scores.....	163
Figure 75. The PC loadings derived from the exploratory PCA of vascular (cortex) tissue from untreated control and 6 mg/L 2,6-DCP treated maize plants.....	164
Figure 76. Typical spectra of epidermis tissue from untreated and 10 mg/L 2,6-DCP treated maize plants. ....	165
Figure 77. Functional group area maps showing the spatial distribution and concentration of 2,6-DCP or phenolics and proteins in the root tissue of untreated and 6 and 10 mg/L 2,6-DCP treated maize sectioned at about 700 μm from the root tip. ....	166

## LIST OF TABLES

Table 1. Characteristic IR absorptions for common functional groups .....	14
Table 2. Physical properties of organic compounds selected for study .....	35
Table 3. Assignment of the main IR bands in IR spectra of sunflower and maize secondary roots. .....	58
Table 4. Uptake of BT by maize and sunflower plants exposed to various concentrations of BT for a 2 week growth period .....	97
Table 5. Assignment of important bands in the FTIR spectrum of pure 1H-benzotriazole.....	98
Table 6. Plant growth and uptake of 2,4-DNT and 2,6-DNT by maize and sunflower plants exposed to various concentrations of DNTs for a 1 week growth period.....	129
Table 7. Assignment of some important bands in the FTIR spectrum of pure 2,4-DNT and 2,6- DNT .....	130
Table 8. Plant growth and uptake of 2,6-DCP by maize and sunflower plants exposed to various concentrations of 2,6-DCP for a 1 week growth period .....	156
Table 9. Assignment of some important bands in the FTIR spectrum of pure 2,6-DCP .....	157

## ACKNOWLEDGEMENTS

First and foremost I must express my sincerest gratitude to my advisor Dr. Lawrence Davis for providing me the opportunity to be a part of his research group. I cannot thank him enough for all of his support, patience, and the knowledge he has given me. I not only consider him my advisor but a wonderful friend. I must also thank Dr. Larry Erickson for introducing me to Kansas State University and Dr. Davis and for the wealth of knowledge and support he has provided me as my co-advisor.

I want to thank Dr. Paul Smith and Dr. Carolyn Ferguson for serving on my dissertation committee and Dr. Krishnamoorthi for graciously becoming part of my committee just several months ago. I would also like to thank Dr. Xeumin Wang for serving on my committee until his departure to start a new position at the University of St. Louis. To the faculty and staff of the Department of Biochemistry, thank you so much for providing a wonderful environment that encourages learning and collaboration.

I would like to express my appreciation for all of the help and support from my dear friend Dr. Sigifredo Castro-Diaz. Also, I cannot express enough gratitude to my fellow lab members, Jwan Ibbini, Danielle Ngaba, and Tanner Callender, for all of their support and hours of time spent on this project. I would also like to thank Dave Hogenkamp and Navdeep Mutti for their friendship and support.

I would like to thank Dr. Klabunde from the Department of Chemistry for the use of his Fourier Transform Infrared spectrometer. To the members of his lab, Dr. Gavin Medine, Dr. Pethaiyan Jeevanandam, and Dr. Al Smetana, thanks for always being helpful and making me feel a part of the lab group. I would also like to thank all of my friends from the Department of Chemistry: Dr. Desper, Dr. Levin, Angelo, Jeff, Kris, Joe, Ben, Michelle, Dipesh, Azi, Kurt, and Scott. You are all wonderful people and I wish I could take you with me when I go.

My thanks to the Kansas State University Veterinary Diagnostic Laboratory, supervised by Cindy Chard-Bergstrom, for the use of their cryomicrotome. I would also like to thank Dr. Wetzel from the department of Grain Science and Industry for introducing me to Brookhaven National Laboratory. I am also grateful for the use of the ATR microspectrometer provided by Dr. John Reffner and SensIR Technologies.

I would like to thank the staff at Brookhaven National Laboratory, particularly Dr. Nebojsa Marinkovic and Dr. Alex Ignatov for all of their help during my research time at the National Synchrotron Light Source.

I cannot thank my family enough for their love, support, and their faith in me throughout my educational endeavors. I cannot express enough appreciation to my parents Katherine and William Tinklepaugh, grandparents Ron and Maria Dokken, my brother Raun, and Tim, Angela, and Cassie Dokken. To Irene, thank you so much for your unending love and devotion. I couldn't have done it without you!! To my daughters Kylie and Ariana, who have inspired me to be the best I can be. To all of my friends back home, thanks for believing in me. To my previous advisor, Dr. Gardea-Torresdey, thanks for urging me to pursue my PhD and your neverending support.

I would like to acknowledge financial support from the Kansas Agricultural Experiment Station and the Great Plains/Rocky Mountain Hazardous Substance Research Center funded by the U.S. Environmental protection Agency under assistance agreement R-825550. Funding for experimentation and travel to the NSLS at Brookhaven National Laboratories was provided by the U.S. Department of Energy.

## **DEDICATION**

To Irene, Kylie and Ariana for their love and inspiration and to the loving memory of my Oma  
Katharina Kramer and my Great Grandfather Russell Dokken



## **CHAPTER 1 - INTRODUCTION**

## **Phytoremediation**

The most powerful influence for remediating sites containing organic contaminants is the major health risks they pose to humans and their ability to bioconcentrate in the food chain. Organic contaminants can cause a variety of health problems such as cancer, seizures, anemia, or behavioral disorders, and can severely affect the development of children and unborn fetuses (Barile, 2004). Contamination of soil and water by these toxic agents also poses a risk to ecological systems due to their phytotoxicity. The U.S. Environmental Protection Agency (USEPA) lists 1481 superfund sites containing organic contaminants, most of which are on the National Priorities List (NPL) (USEPA, 2005). Economics has become the driving force behind developing new remediation technologies. Conventional remediation technologies such as excavation, landfilling, and incineration are costly, environmentally destructive, and labor intensive. Some have suggested that remediation of sites contaminated with organics could cost an estimated \$35 billion over 5 years (Brown, 1995). Phytoremediation, using plants to remove contaminants from water and soil, has demonstrated considerable potential for the clean-up of heavy metals and organics (Davis *et al.*, 2002; Prasad and Freitas, 2003; McCutcheon and Schnoor, 2003; Cunningham *et al.*, 1996). This lower cost, environmentally-friendly, and less labor intensive technology has gained public acceptance and is being used by government and commercial entities.

Phytoremediation consists of several categories based on type of contaminant and means of contaminant uptake. Phytoextraction is plant uptake of heavy metals from soil by roots, usually followed by translocation into the harvestable shoots, whereas rhizofiltration is uptake of heavy metals in water or aqueous environments with contaminants remaining on or in the roots (Ensley, 2000; Cunningham *et al.*, 1996; Prasad and Freitas, 2003; Gardea-Torresdey

*et al.*, 2005). Phytotransformation occurs when plants take up organic contaminants from soil or water and metabolize them into a less toxic or less bioavailable form (Davis *et al.*, 2002; McCutcheon and Schnoor, 2003; Cunningham *et al.*, 1996).

The uptake of heavy metals and organics may occur by different pathways. Plants naturally take up metals, as many are essential micronutrients. Movement across the cell membrane is mediated by transporter proteins that preferentially bind certain metal ions over others. The mediation of metal uptake by these transporters may be based on size or valency and may be very energy consuming. Some plants are capable of accumulating a particular metal up to concentrations of 100-fold greater than a non-accumulator plant. Such plants have been named hyperaccumulators and may possess mechanisms to detoxify high metal levels by oxidation, reduction, or sequestration (Prasad and Freitas, 2003; Gardea-Torresdey *et al.*, 2005; Lasat *et al.*, 1996; Brooks, 1998). The uptake of organics is generally a passive process that is based on the pH, solubility, and lipophilicity of the organic compound (Davis *et al.*, 2002; McCutcheon and Schnoor, 2003; Cunningham *et al.*, 1996; Korte *et al.*, 2000). After absorption through the roots, organics are often translocated into the xylem before transformation of the compound begins. The ability of the compound to translocate to the xylem is related to the transpiration stream concentration factor (TSCF) (Shone and Wood, 1974). The TSCF defines the compound concentration of the xylem stream fluid with respect to the concentration in the bulk solution in the root zone as a simple ratio. Briggs determined that the TSCF is related to the lipophilicity of a compound which may be defined based on the octanol-water partition coefficient,  $\log K_{ow}$  (Briggs, 1981). Compounds, such as TNT, that possess a  $\log K_{ow}$  between 1 and 3 are moderately lipophilic and are optimally translocated into the xylem (Sung *et al.*, 2001).

Plants do not rely on exogenous organic compounds as an energy source and have to use enzymatic mechanisms to prevent buildup and toxicity to sensitive plant structures, in a fashion similar to the mammalian liver system. The “green liver” model proposes metabolism of organics in three steps: transformation, conjugation, and elimination or storage (Burken, 2002). Transformation is characterized predominantly by oxidation of the organic compound conducted by enzymes such as cytochrome P-450, peroxidases, and carboxylesterases (Komossa *et al.*, 1995). Conjugation of the transformed products occurs with glutathione, amino acids, or sugars. In the final step, the conjugated product can be stored in vacuoles or irreversibly bound to plant tissues like hemicellulose or lignin.

Even though researchers are beginning to understand how plants metabolize and process foreign organic compounds, a few fundamental questions have yet to be fully answered. What is the ultimate fate of organic compounds within the plant? What effect do these contaminants ultimately have on plant structure and development? The answers to these questions vary depending on the type of plant and the organic compound that is taken up. The main hindrance for addressing these issues are the shortcomings in the current analytical methods used to study the fate of organic contaminants in plants. Most techniques rely on strong chemical treatments and extraction of native or radiolabeled compounds from intact plant tissue using volatile solvents which destroy the spatial distribution of the compound being studied as well as creating potential artifacts. Since there are a limited number of cell wall epitopes, antibody probes are inadequate in determining the composition of plant cell walls or changes caused by organic contaminants. This provides an immediate need for a nondestructive, direct method for monitoring the fate and effect of organic contaminants in plants. Infrared microspectroscopy (IMS) has shown potential as an attractive analytical

technique in plant science (Dokken *et al.*, 2005a; Wetzell and LeVine, 2001). This potential stems from the fact that most common biomolecules, such as proteins, lipids, and carbohydrates possess highly characterized vibrational IR fingerprints (Jackson and Mantsch, 1996). Further discussion of infrared spectroscopy and its applications to plant science will be covered in the following sections.

### **Infrared (IR) Spectroscopy**

Infrared (IR) spectroscopy measures the intensity of IR light absorbed at frequencies spanning from 14,300 to 20  $\text{cm}^{-1}$  on the electromagnetic spectrum (see Figure 1) due to the vibration of chemical bonds within a molecule. The wavelength shown in Figure 1 is the reciprocal of frequency. A molecule absorbs infrared radiation when a vibrational transition of its chemical bonds results in a change in the molecule's dipole moment. Molecules that experience a dipole moment are considered IR active while linear diatomics, such as nitrogen and hydrogen, do not absorb IR light and are infrared-inactive. The greater the change in dipole moment, the more intense the absorption of IR radiation by the chemical bond. Intensity also depends on the concentration of the vibrating molecule as defined by the Beer-Lambert law (Coates, 2000). The amount and intensity of IR absorbed by a molecule depends on the nature and type of bond which is also influenced by inter- and intra-molecular interactions. The number of vibrational modes for a given molecule is  $3N-6$  for nonlinear molecules and  $3N-5$  for linear molecules where  $N$  is the number of atoms in a molecule (Coates, 2000). Some typical vibration modes found in organic compounds are displayed in Figure 2.

The IR spectrum from a molecule is a unique physical property and is characteristic of the types of bonds within the molecule. Therefore, an IR spectrum is considered a molecular

fingerprint providing information related to the quantity, composition, structure, and environment of a particular sample. The mid-infrared region of  $3500\text{-}500\text{ cm}^{-1}$  is most commonly referred to as the fingerprint region because it contains the characteristic group vibrations. Functional groups of organic molecules, such as carbonyl or amide bonds, possess a distinct characteristic set of vibrational frequencies that can be used to identify a compound in a sample. Table 1 shows the characteristic IR absorption frequencies for common functional groups (Lin-Vien *et al.*, 1991).

IR spectroscopy provides a number of advantages for the analysis of biological materials. Samples can be examined in the liquid or solid states without destruction of the sample. Depending on the size and type of sample, data acquisition can be quite rapid and dilute species to the nanogram level can be detected (Marinkovic and Chance, 2005). IR spectroscopy of pure, homogeneous compounds is quite simple, but biological samples are commonly both spatially and chemically heterogeneous, complicating IR analysis. The IR beam size of common IR spectrometers is larger than the discrete microstructures in biological samples, thus producing an average spectrum of the area probed by the beam. A sufficiently small beam is needed to probe these microstructures in biological samples. Also, the bulk sampling nature of the KBr pellet technique eliminates any ability to visualize the spatial distribution of IR absorbing materials within a system. IR techniques like infrared microspectroscopy (IMS) and attenuated total reflection (ATR) spectroscopy have been developed to address these problems.

## **Infrared Techniques**

### *Infrared Microspectroscopy (IMS)*

The marriage of microscopy and infrared spectroscopy has allowed infrared light to be focused to a spot size small enough to probe heterogeneous biological samples such as plant tissues which contain microstructures like lignin and cellulose. IR microspectrometers can produce a two-dimensional array of spectra in which a chemical image is generated, commonly presented as a false color intensity map. A functional group map can then be derived from a false color intensity map by selecting a wavelength that corresponds to a particular functional group by using software commonly provided by the manufacturer of the instrument. This functional group map produces a spatially localized image revealing the type, distribution, and relative amount of a chemical component with respect to plant anatomy. The imaging ability of IMS can provide a more complete picture of the interactions and orientations of the intact polymers found in plant cell walls by focusing on a sample area at a resolution of tens of microns. This permits analysis of plant cell wall architecture at the cellular level *in situ*. A comprehensive review by Dokken *et al.* (2005a) covers applications of IMS to study cell wall architecture and the major cell wall components: lignin, cellulose, and polysaccharides; applications for agricultural and feed products; and changes to plant structure due to biotic and abiotic stressors.

### *Synchrotron Radiation Infrared Microspectroscopy (SR-IMS)*

The limited source intensity from conventional IR thermal (globar) sources only provides a spatial resolution of tens of microns in reasonable analysis times, thus restricting analysis to the tissue level (Carr, 1999). Ideally, plant researchers are interested in investigating

samples at the cellular level, requiring a spatial resolution of better than 10  $\mu\text{m}$ . Coupling a synchrotron IR source to IMS can overcome this difficulty due to the high brightness of the IR radiation emitted, which is 100 to 1000 times brighter than conventional sources (Duncan and Williams, 1983). Figure 3 shows the comparison of the brightness in the infrared emission from a global source and a synchrotron ring (Dumas and Miller, 2003). The small effective source size and the narrow range of angles in which the IR radiation is emitted provide high spatial resolution and a high signal-to-noise ratio (SNR). That is, one can have a highly collimated yet intense source. Diffraction limits resolution as a function of wavelength unless one uses near-field microscopy. Thus for spectral features absorbing at  $1000\text{ cm}^{-1}$ , the resolution limit is 10  $\mu\text{m}$ .

Synchrotron IR radiation is produced by electrons traveling at relativistic velocities inside a curved path through a constant magnetic field (Duncan and Williams, 1983). An example of a typical synchrotron ring is depicted in Figure 4. An electron gun emits electrons into the synchrotron ring containing several types of magnets. The focusing magnets are placed in the straight sections of the ring and are used to focus the electron beam, keeping it well-defined. A periodic array of magnets with alternating polarity of the magnetic field is called an undulator. When the synchrotron beams pass through the undulator they overlap and constructively interfere to generate an intense beam. Synchrotron radiation ranging from ultraviolet (UV) to hard X-rays is then emitted at the curves of the ring through bending magnets to the experimental stations. There are 10 synchrotron laboratories worldwide that have facilities to perform SR-IMS. A book chapter by Marinkovic and Chance covering SR-IMS provides a list of these facilities and various IR techniques and applications (Marinkovic



and Chance, 2005). There are also several reviews that discuss the application of SR-IMS on plant tissues (Dokken *et al.*, 2005a; Raab and Vogel, 2004; Wetzel *et al.*, 1998).

#### *Attenuated Total Reflection (ATR) Spectroscopy*

ATR objectives have become commonplace on infrared microspectrometers. Most ATR objectives are Schwarzschild IR objectives that contain an internal reflection element (IRE) usually made of ZnSe, Ge, or diamond (see Figure 5) (Smiths Detection, 2005). Ease of use and rapid sampling time has made ATR an attractive technique for studying plants and plant materials *in situ*. The ability to examine most samples types without preparation has largely replaced the KBr pellet technique. The physical phenomenon of the evanescent field formed by penetration from the IRE into the sample allows analysis in the aqueous phase. This makes ATR analysis less impeded by the high IR absorptivity of water commonly seen in conventional transmission IR spectroscopy because only the sample material probed by the evanescent field is being investigated, when the sample thickness is as large as the penetration depth of the radiation (Fringlei, 1992). Samples can be analyzed in their natural environment or solutes can be added to mimic these environments, so changes in surface chemistry due to the chemical or physical changes, can be observed over time (Heberle and Zscherp, 1996). ATR is commonly used to study thin films, biofilms, and membranes. More recently, it has been applied in the determination of sugars in cell culture media (Hashimoto *et al.*, 2001; Hashimoto and Kameoka, 2000; Cadet *et al.*, 1997), secondary structure of proteins in cell membranes (Marsh, 1999) changes of leaf carbohydrates due to enzymatic degradation (Mascarenhas *et al.*, 2000), lignin in flax fibers (Morrison *et al.*, 2003), and the interaction of polysaccharides with different surfaces (Reiter *et al.*, 2002).

## **Chemometric techniques for infrared spectral analysis**

The IR spectra of plant tissue are very complex, containing features from chemical bonds from cellulose, carbohydrates, proteins, lignin and other biopolymers that overlap because of the many interactions between these molecules. Natural variations in biological samples and varying sample thickness present additional complications. This presents a major challenge in determining spectral differences in large sample sets. Chemometric techniques such as principal components analysis (PCA), canonical variate analysis (CVA), discriminant analysis (DA), and partial least squares (PLS) have gained in popularity over the last 15 years, especially since technological advancements in instrumentation and sampling techniques have made it easier to collect spectra rapidly. Typical mapping experiments that utilize small apertures often require the coaddition of many scans to improve S/N ratio while maintaining high spatial resolution, and may result in the production of 100 or more spectra, depending on the size of the mapping area. Analyzing this amount of data in a two dimensional plot is not always practical especially when looking for underlying differences. Most often researchers use the univariate approach of functional group imaging, which represents the peak height or integrated absorbance under the peak of interest. Although useful as a qualitative measure, only general conclusions can be drawn from this approach. Thus, the next logical step is to apply a multivariate statistical approach. For this project, the primary focus will be on PCA as it is the most often used chemometric method for IR spectroscopic data. Additional information on this technique and many applications is provided in Dokken *et al.* (2005a).

Figure 6 shows a schematic representation of PCA analysis of infrared imaging data. A mapping experiment produces a data set that is comprised of observations of  $d$  variates on  $n$  specimens and can be arranged in a matrix  $[n \times d]$ . For data sets where  $d > n$ , as in the case of

spectroscopic data, PCA is the most often used technique (Deferenez and Kemsley, 1997; Kemsley, 1998). PCA can convert a large data matrix into a set of principal components (PCs) that represent the variability of each spectrum relative to mean of the population. This concentrates the sources of spectral variability in the data into the first several PCs. The PCs matrix represents the independent orthogonal variations in the spectral data while the matrix of scores represents the contribution of each PC to the original spectrum. Plots of the PC scores against one another can reveal clustering or patterns in the data set. A spectrum is then mathematically derived from the PC score, called a loading, which represents an independent source of spectral variability in the spectral data set. Budevskaja and co-workers have shown the application of PCA to infrared imaging of plant tissue (Budevskaja *et al.*, 2003). In order to carry out some sort of prediction or assignment, the data has to be fit to a model. This is accomplished by applying linear discriminant analysis (LDA) to a set of PC scores.

Observations can be assigned to pre-defined groups by calculating the mean observation of each group and the distance, commonly the Mahalanobis distance, of each observation to the nearest group. The Mahalanobis distance is defined as a weighted Euclidian distance where the weighting is determined by the sample variance-covariance matrix. This results in zero mean and unit variance, essentially rescaling the data so that the absolute magnitude of PCs is replaced by relative magnitude. This allows convenient visualization of data points, but caution is needed when using PCs that contribute little of the overall variance of the data set. Each observation is reassigned to a certain group based on its nearest group mean. This will then inform the analyst how successful they were at assigning each observation to the proper group. The better the classification rate, the more robust the model set. Validation of the model set can then be performed using independent test specimens. Each test observation is assigned to the

nearest group based on the group centers established in the training phase. Since the group membership of the test observations is already known, the reliability of the model set can be assessed based on the assignments. This will provide an idea of how well the model set will perform with unknown observations.

### **Using IMS to monitor the fate of organic contaminants in maize and sunflower plants**

For this study, sunflower (*Helianthus annuus*) was used as a representative organism for dicots and maize (*Zea mays*) was used as a representative organism for monocots. Both plants are fast growing in hydroponic culture, produce a large amount of biomass, and have been used for phytoremediation. Sunflowers have been used in treatment wetlands for the removal of 2,4,6-trinitrotoluene (TNT), dinitrotoluene (DNT), nitrobenzene, nitrotoluene, and hexahydro-1,3,5-trinitro-1,3,5-triazine (RDX) from runoff and contaminated groundwater (McCutcheon *et al.*, 2003) and have been found growing in soils contaminated with polyaromatic hydrocarbons (PAHs) (Olson and Fletcher, 2000; Olson *et al.*, 2001). Sunflowers have also demonstrated the ability to grow in hydroponic solutions containing trichloroethylene (Davis *et al.*, 1999) and benzotriazole (Castro *et al.*, 2004; 2003; 2001). Maize has also shown the ability to remove explosive compounds such as TNT and RDX from soil (Larson, 1997; Larson *et al.*, 1999; Burken *et al.*, 2000) and hydroponic solution (Chen, 1993). However, not much is known about the fate and effect of these contaminants in sunflower and maize plants. Typical analytical methods have provided some evidence on how some contaminants are taken up and possibly transformed or bound within the plant. As previously mentioned, these methods are harsh and damage plant tissue yielding results which may contain artifacts. IMS is a direct, non-destructive technique that has shown the potential to determine the fate and effect of organic

contaminants in plants (Dokken *et al.*, 2004; 2005b; 2005c). This dissertation will focus on the use of IMS to determine the fate and effect of several organic compounds in maize and sunflower plants. The plants were grown in hydroponic solution containing various types of organic compounds. Hydroponic culture was used to ensure direct contact of the organic compound with the root system without the interference of soil. The organic compounds chosen for this study represent specific classes of compounds commonly found at many sites containing organic contamination: 1H-benzotriazole (BT), a heterocyclic aromatic, 2,4- and 2,6-dinitrotoluene (2,4-DNT, 2,6-DNT), which are explosive (nitroaromatic) compounds that are byproducts of TNT production, and 2,6-dichlorophenol (2,6-DCP), a chlorinated phenol.

**Table 1.** Characteristic IR absorptions for common functional groups (Lin-Vien et al., 1991)

<b>Frequency, cm<sup>-1</sup></b>	<b>Bond</b>	<b>Functional Group</b>
3500-3200 (s, b)	O-H stretch, H-bonded	alcohols, phenols
3400-3250 (m)	N-H stretch	1°, 2° amines, amides
3300-2500 (m)	O-H stretch	carboxylic acids
3330-3270 (n, s)	-C≡C-H: C-H stretch	alkynes (terminal)
3100-3000 (s)	C-H stretch	aromatics
3100-3000 (m)	=C-H stretch	alkenes
3000-2850 (m)	C-H stretch	alkanes
2830-2695 (m)	H-C=O: C-H stretch	aldehydes
2260-2210 (v)	C≡N stretch	nitriles
2260-2100 (w)	-C≡C- stretch	alkynes
1760-1665 (s)	C=O stretch	carbonyls
1760-1690 (s)	C=O stretch	carboxylic acids
1750-1735 (s)	C=O stretch	esters, saturated aliphatic
1740-1720 (s)	C=O stretch	aldehydes, saturated aliphatic
1730-1715 (s)	C=O stretch	α, β-unsaturated esters
1715 (s)	C=O stretch	ketones, saturated aliphatic
1710-1665 (s)	C=O stretch	α, β-unsaturated aldehydes, ketones
1680-1640 (m)	-C=C- stretch	alkenes
1650-1580 (m)	N-H bend	1° amines
1600-1585 (m)	C-C stretch (in-ring)	aromatics

**Table 1. continued**

<b>Frequency, cm<sup>-1</sup></b>	<b>Bond</b>	<b>Functional Group</b>
1550-1475 (s)	N-O asymmetric stretch	nitro compounds
1500-1400 (m)	C-C stretch (in-ring)	aromatics
1470-1450 (m)	C-H bend	alkanes
1370-1350 (m)	C-H rock	alkanes
1360-1290 (m)	N-O symmetric stretch	nitro compounds
1335-1250 (s)	C-N stretch	aromatic amines
1320-1000 (s)	C-O stretch	alcohols, carboxylic acids, esters
1300-1150 (m)	C-H wag	alkyl halides
1250-1020 (m)	C-N stretch	aliphatic amines
1000-650 (s)	=C-H bend	alkenes
950-910 (m)	O-H bend	carboxylic acids
910-665 (s, b)	N-H wag	1°, 2° amines
900-675 (s)	C-H “oop”	aromatics
850-550 (m)	C-Cl stretch	alkyl halides
725-720 (m)	C-H rock	alkanes
700-610 (s, b)	-C=C-H: C-H bend	alkynes
690-515 (m)	C-Br stretch	alkyl halides

m = medium, w = weak, s = strong, n = narrow, b = broad, s = sharp

**Figure 1.** The Electromagnetic Spectrum (Zumdahl, 1997).

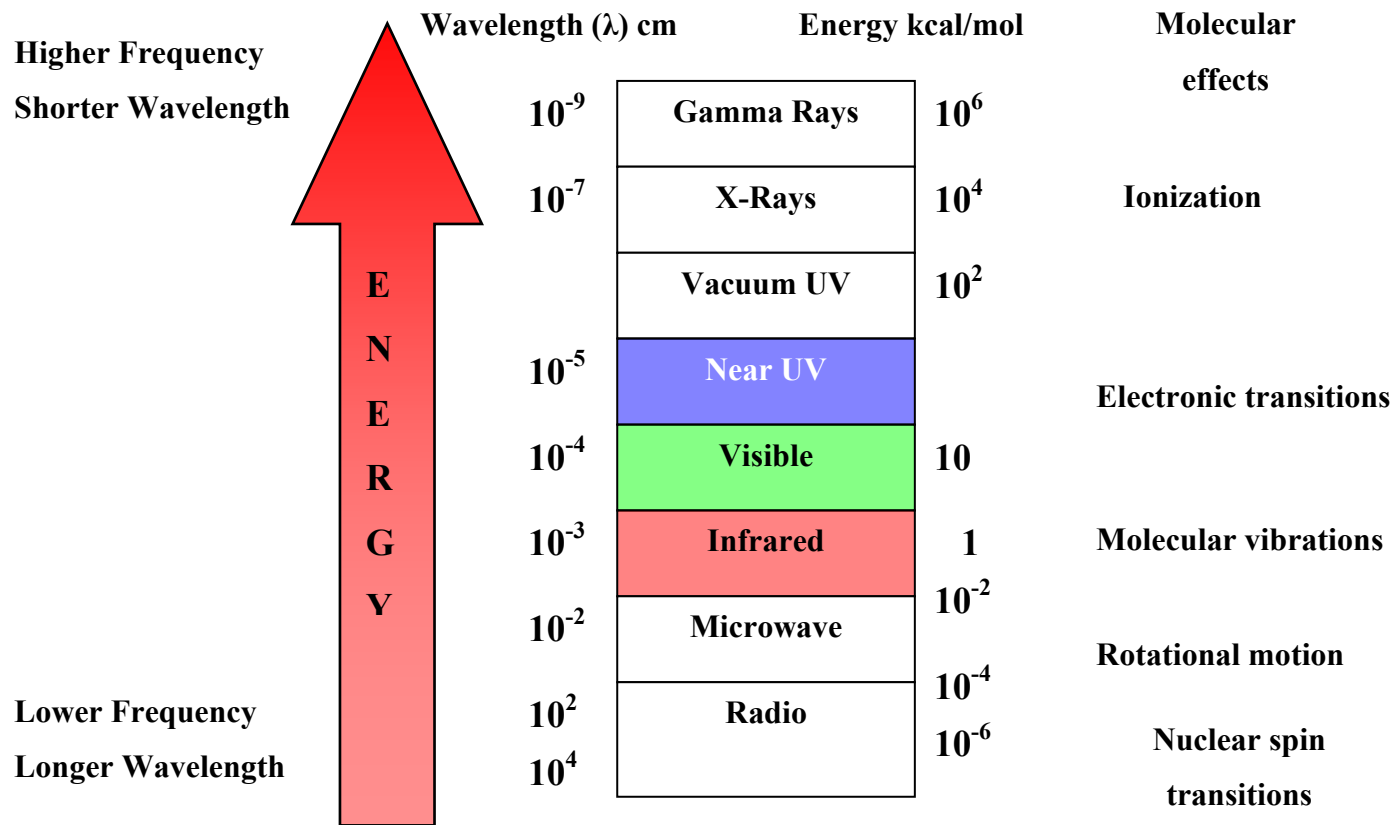




**Figure 2.** Some typical vibration modes found in organic molecules (Coates, 2000).

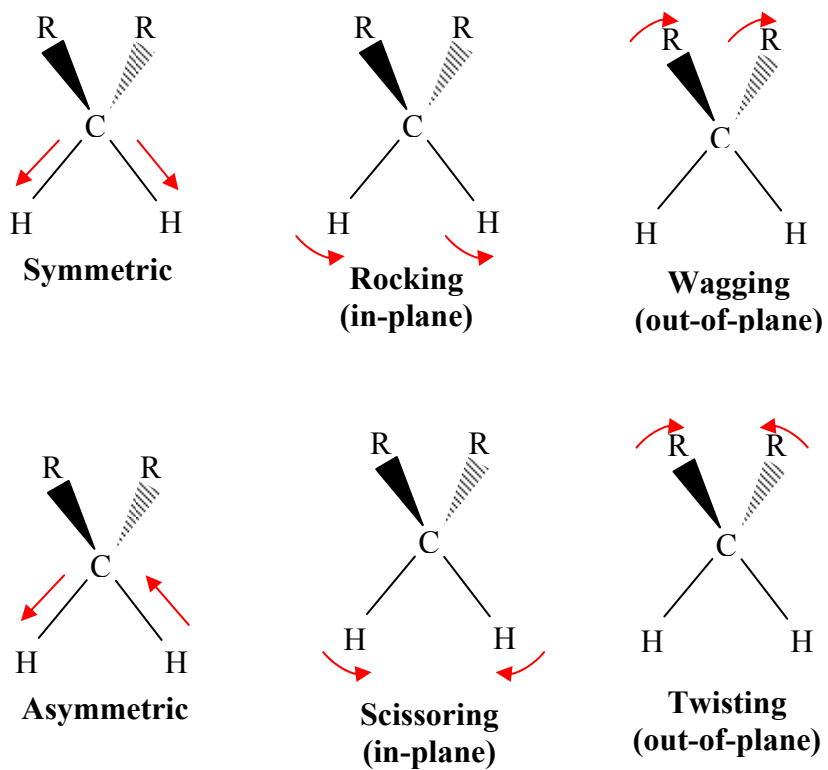


**Figure 3.** Comparison of brightness in the infrared emission from a globar source and the synchrotron ring at the National Synchrotron Light Source at Brookhaven National Laboratory (Dumas and Miller, 2003).

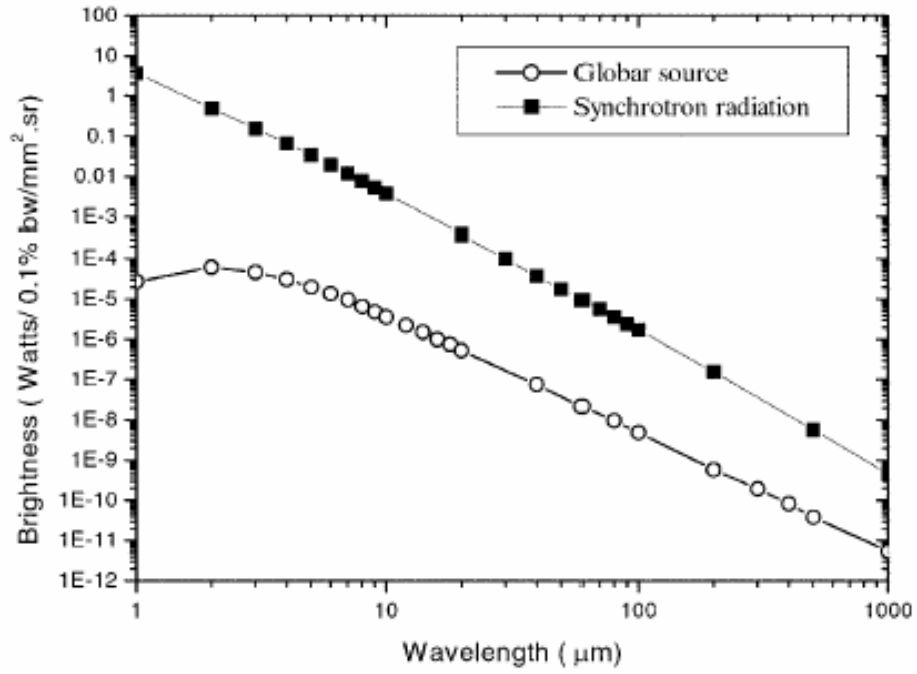


**Figure 4.** Typical synchrotron radiation storage ring.

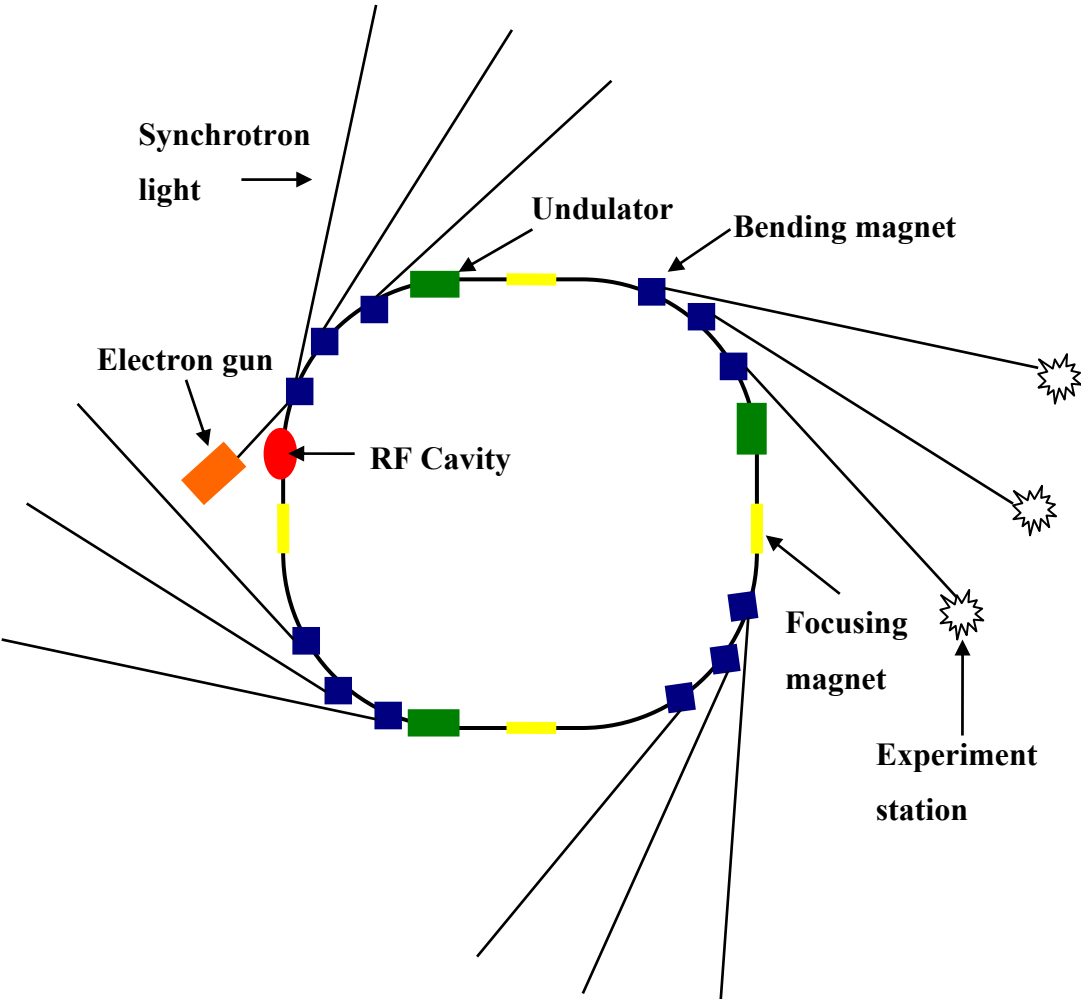


**Figure 5.** Diamond ATR objective (modified from Smiths Detection, 2004).

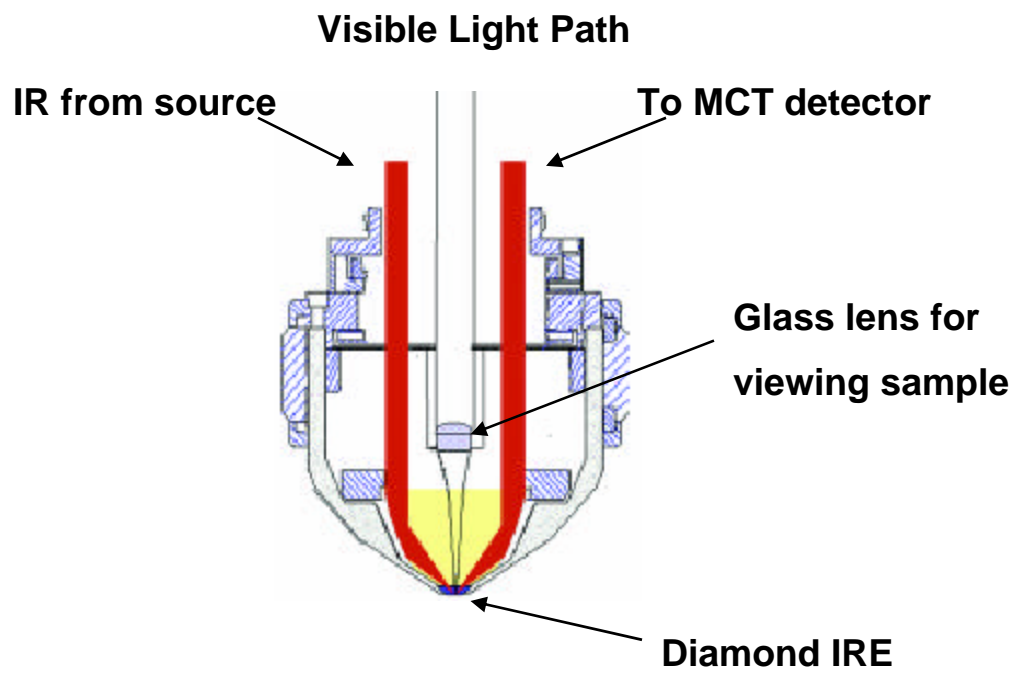
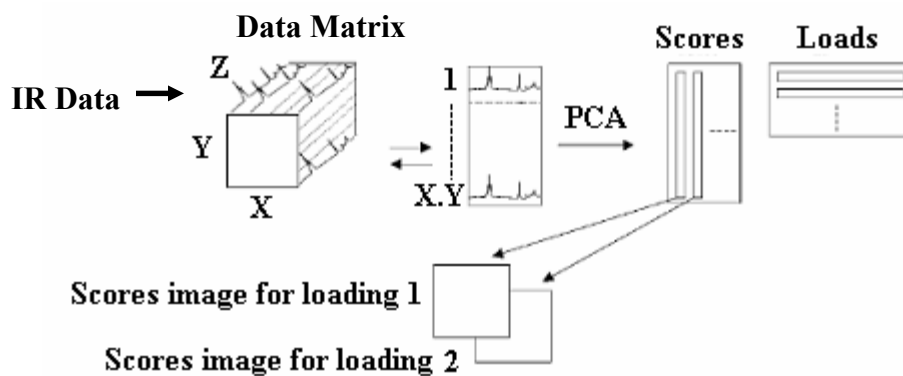


**Figure 6.** Schematic representation of PCA analysis of infrared imaging data (modified from Budevskaa et al., 2003).



## **CHAPTER 2 - EXPERIMENTAL METHODS**

## **Rationale**

Infrared spectroscopy has become an important tool in the study of plant structure. This provides the potential for the use of IR to monitor the fate and effect of organic contaminants in plants. In this study, sunflower and maize plants were grown in hydroponic solutions spiked with various concentrations of contaminants from three different classes of organic compounds. The root tissue of these plants were then analyzed by conventional IR, ATR, and SR-IMS in order to determine changes to plant structure due to exposure to the contaminants. The spatial distribution of the organic compound within the root tissue as well as the final form the organic compound was also studied. The results of this work could lead to an understanding of how plant development is affected by organic compounds and the route of metabolism for certain types of organic compounds. This research will also lead to a better comprehension of the metabolism of organic compounds in plants and factors such as bioavailability and bioconcentration.

## **Reagents and Plant Culture Solutions**

Pure benzotriazole (BT), 2,4-dinitrotoluene (2,4-DNT), 2,6-dinitrotoluene (2,6-DNT), 2,4-dichlorophenol (2,4-DCP), and 2,6-dichlorophenol (2,6-DCP) were purchased from Sigma/Aldrich Chemical Company (See Table 2 to see physical properties of these compounds). Stock solutions for all compounds were prepared in sealed glass bottles and used for dilution into hydroponic plant culture solutions and calibration standards for high performance liquid chromatography (HPLC). BT was stored as a 2 g/L stock solution. Due to lower solubilities, 1 g/L stock solutions for 2,6-DCP were prepared while 0.5 g/L was the concentration used for stock solutions of 2,4- and 2,6-DNT. When sealed, all stock solutions

remain stable for at least six months due to the low vapor pressure of these compounds (less than  $1.5 \times 10^{-4}$  atm) which ensures negligible volatilization of these compounds over a relatively short period of time. Hydroponic plant culture solutions were prepared by diluting the stock solutions into standard Hoagland's nutrient solution as previously described by Castro *et al.* (2004b).

### **Growth of Plants**

Commercial oilseed type sunflower seeds and Pioneer Maize seeds (hybrid 32M38) were germinated by either the vermiculite method, as previously reported by Castro *et al.* (2004b), or the Petri dish method. All seeds were soaked for 10 minutes in a 10% ethanol/water solution, washed with sterilized deionized water, surface sterilized for 20 minutes using a 20% bleach/water solution and then washed several times with sterilized deionized water. The maize seeds were also surface sterilized using the same method. Initially, all seeds were germinated in vermiculite moistened with sterilized tap water for five days. Plastic wrap was placed over the seeds to maintain a humid environment. However, due to poor germination, about 30% or less (particularly for the sunflower seeds), and problems with fungal pathogens, a germination method using Petri dishes was performed. Surface sterilized seeds were germinated upon 2.4 g of sterilized filter paper moistened with 8 mL of sterilized tap water inside sterilized Petri dishes. Five seeds were placed in each Petri dish and each dish was sealed with parafilm. The placement of the seeds into Petri dishes was conducted on a sterilized benchtop in a small room adjacent to the lab that had no air circulation and no prior history of fungal growth. The germination time for both procedures was five to seven days. After the germination period, only the healthy seedlings were transferred to amber stock jars containing 1X Hoagland's



hydroponic nutrient solution. Amber stock jars were used to deter algal growth. The seedlings were suspended in the amber stock jars using polyurethane foam plugs so only the roots were in contact with the hydroponic growth solution. The seedlings were then placed under 40-watt cool white fluorescent tubes (about 1 tube/ft<sup>2</sup>) with continuous lighting for two or three days to allow the seedlings to adapt to the hydroponic growth solution. During the adaptation period, the water level was maintained nearly constant by adding fresh 1X Hoagland's solution every day. After the adaptation period, the fresh weights of the seedlings were recorded. Typical germinations yielded two leaf seedlings ranging in weight from 1.4 – 2.5 g and shoot heights of 2.5 to 4.5 cm after adaptation. In most cases, seedlings under 1.8 g were discarded. This is because seedlings weighing under 1.8 g did not typically develop well once exposed to solutions containing the organic compounds. After adaptation, the seedlings were then placed into stratified groups. The amount of seedlings used for each growth study varied. However, in most cases, three or four seedlings (never less than three) were used for each experimental treatment group.

The concentration and volume of the hydroponic solutions containing the organic compounds varied for each growth study. These parameters are further discussed in their respective chapters. The plants were placed in sterilized amber stock jars containing their respective hydroponic growth solution prepared from the aforementioned stock solutions of BT, 2,4- and 2,6-DNT, and 2,6-DCP. Plant growth took place under constant (24 hour) lighting at room temperature (25 °C) for a 7 to 14 day period. The amount of hydroponic growth solution was maintained throughout the experiment by adding fresh solution as needed. After the designated growth period, fresh weights (in some instances shoot height) were recorded for each plant. The volume of the remaining growth solution was also noted. A 1 mL aliquot was

taken from the remaining growth solutions and stock solutions and stored in the refrigerator at 4 °C until HPLC analysis. HPLC was used to measure loss of organic compounds from the growth solutions.

The roots of the plants were washed with deionized water to remove any unadsorbed solution on the root surface. Root tips were dissected for crysectioning as explained below. The plants were then harvested and the roots, shoots, and leaves were separated and placed into appropriately labeled containers for drying. After the drying period (typically a one to two week depending the humidity), the dry weights were recorded. The dried tissues were then stored in labeled Ziploc bags. The dried root tissue from BT treated sunflowers were used for further analysis by conventional IR and ATR spectroscopy.

### **Preparation of Plant Tissue**

#### *Potassium Bromide Pellets for Conventional IR Spectroscopy*

The roots of untreated and benzotriazole treated sunflower plants were ground with a Wiley mill, and sieved to 100 mesh. Potassium bromide pellets were made consisting of 5% plant matter by weight or 0.5% for pure benzotriazole. In order to determine if the sunflower plant actually biotransforms benzotriazole, a simple spiking experiment was performed. Dried root samples (about 1g) untreated and treated with benzotriazole were spiked by mixing with 0.1 mL of a 5% benzotriazole solution in methanol. The spiked samples were allowed to dry in open air for 24 hours. KBr pellets were then prepared consisting of 5% by weight of the spiked samples. KBr pellets for all samples were all mixed and prepared using a mortar and pestle. After all samples were mixed with KBr, they were stored in clean, dry glass vials with screw

caps inside a dessicator. Pellets for each sample were prepared using a 13 mm KBr die (International Crystal Laboratories, Garfield, NJ) and a 5 ton hydraulic press.

#### *Dry Tissue Sections for ATR Spectroscopy*

Specimens for ATR spectroscopy were prepared by longitudinal dissection of a primary root in the center with a razor blade. To prepare a parallel backside to this exposed face, a miniature plane was constructed from two single edged razor blades and small strips of glass cut from an ordinary microscope slide were placed in between as spacers. Spring-loaded clips held the ends of the parallel blades together. An offset of 2 mm in the edges of the two blades allowed the freshly cut face of the stem to be placed against the protruding blade to allow the miniature plane cut to produce a lateral section with parallel faces in which all three tissue layers are exposed as shown in Figure 7. These sections were mounted onto ordinary glass microscope slides using transparent double stick tape for analysis by the diamond ATR techniques. Smaller secondary roots had their outer surface analyzed first and subsequently had successive layers below the surface analyzed after scraping away the outer portions using a razor blade.

#### *Cryosectioning of Plant Roots for SR-IMS*

Cryosectioning of the root tissue was conducted on an IEC minotome with cryostat (Triangle Biomedical Sciences, Durham, NC) at the Diagnostic Laboratory at the College of Veterinary Medicine located on the campus of Kansas State University. The representative roots from each treatment were pooled (~ 5 roots/treatment) and samples were dissected in 1 cm sections from the tip. The root tissues were frozen onto specimen blocks surrounded by

Tissue Tek (Sakura Finetek USA, Inc., Torrance, CA) at -40°C, in preparation for sectioning at -20°C. The 4 µm thick frozen sections were thaw mounted onto infrared-reflecting “E” glass microscope slides (Smiths Detection, Danbury, CT). The slides were then stored at room temperature until analysis.

## **Analytical Methods**

### *HPLC Methods*

High performance liquid chromatography (HPLC) was conducted on an Altex liquid chromatograph Model 330 attached to a spectrophotometer flow cell (Altex / Hitachi Model 100-40). Analysis of BT, 2,4-DNT, and 2,6-DNT was performed at 275 nm and detection of 2,6-DCP was conducted at 285 nm . The separation was carried out through a Hamilton PRP-1 Column (150 x 4.1 mm) with an eluant flow rate of 1.0 mL/min. All samples were centrifuged before injection to prevent solid contaminants from entering the analytical column. As detailed by Castro *et al.* (2001), the quantification of benzotriazole uptake by the sunflower and maize plants was performed using an eluant consisting of 1 mg/L of CIBT and 1mM K<sub>2</sub>HPO<sub>4</sub> in methanol (50-70 vol.%) and water was used for BT analysis. A methanol:water(9:1) mixture was used as the eluant for DNT analysis. The eluant for 2,4- and 2,6-DCP analysis consisted of 425 mL of methanol and 90 mL of deionized water. The injection loop volume was 20 µL for BT and DNT analysis and 100 µL for DCP analysis.

## *IR Methods*

### Conventional IR Spectroscopy

All KBr pellet samples were analyzed in triplicate on a Nicolet Nexus 670 Fourier Transform Infrared (FTIR) Spectrometer located in the laboratory of Dr. Klabunde in the Department of Chemistry at Kansas State University. To reduce the signal-to-noise ratio, 64 scans co-added at  $2\text{ cm}^{-1}$  resolution were collected for each sample. As reference, a pure KBr pellet was analyzed using the same parameters. Spectral analysis was performed using OMNIC E.S.P. 5.2 software (Nicolet Instrument Corp., Madison, WI). The final spectra were baseline corrected and expressed as absorbance. All spectra shown here reflect the average of three spectra taken for each sample.

### ATR Spectroscopy

The instrument used to obtain the ATR spectral data was an IlluminatIR<sup>®</sup> (SensIR<sup>®</sup> Technologies, Danbury, CT). The IlluminatIR<sup>®</sup> is a miniaturized FT-IR spectrometer attachment that mounts between the eyepiece and the body of an infinity corrected microscope. In addition to conventional refractive lenses the nosepiece of the microscope has been outfitted with a 15X diamond internal reflection objective for micro-ATR spectral data collection. It also has a modified Shwartzschild all-reflecting objective. The design of the internal reflection objective (see Figure 5) includes a refractive lens that can be lowered to enable visible focus on the sample surface either during sample survey or data collection.

For analysis of root sections, the sample area is sighted through the visible optics, and the internal reflection optic is rotated into position. The sample area can then be viewed through the IR internal reflection objective at which point the microscope stage is raised until

the diamond internal reflection element makes contact with the sample. The diamond internal reflection element has a curved surface to facilitate optical contact with surfaces that are pitted, rough, or not flat. With this microspectrometer, projected image plane masks provided apertures of 100  $\mu\text{m}$  or less to allow selection of specific targets within the root section to the exclusion of other parts of the tissue.

ATR spectra were collected in the reflection absorption mode at  $8\text{ cm}^{-1}$  resolution with 256 scans co-added to reduce the signal-to-noise ratio. Spectra were recorded using the SynchronizIR software and saved using the .spc file extension so they can be further analyzed using Omnic 6.1a software. A reference spectrum was collected from an empty IR reflective slide. The final spectra are generated by the ratio of the relative intensity of the reference baseline from the relative intensity of the sample baseline. The IR spectra were expressed as  $\log(1/R)$ , where R is reflectance. The infrared light passes through the sample twice since it is mounted on reflective slide. Therefore, R is transmission of light through two passes of the specimen, so the  $\log(1/R)$  is equivalent to absorbance.

## SR-IMS

FTIR microspectroscopy was conducted at the National Synchrotron Light Source (NSLS) at Brookhaven National Laboratory (BNL) in Upton, NY using a Nicolet NicPlan IR microscope and Thermo-Nicolet Magna 860 spectrometer equipped with a KBr beamsplitter on beamline U2B. A floorplan of the NSLS is depicted in Figure 8 and a schematic of the beamline U2B can be seen in Figures 9. The narrow-range, internal mercury cadmium telluride (MCT/A) detector was used, covering a range of  $4000\text{-}650\text{ cm}^{-1}$ . Collimated synchrotron light with a beam energy of 800 MeV is passed through an external beam pipe into the IR

microspectrometer (see Figure 9B) to perform reflection spectroscopy. The IR spectra were collected in absorption mode at a resolution of  $4\text{ cm}^{-1}$  with 64 scans co-added to reduce signal to noise ratio. Each spectrum is ratioed to a reference, taken at an empty part of the low “E” slide, which was recorded with the same parameters and conditions (128 scans used for reference). A  $30\text{ }\mu\text{m}$  square aperture was used for scouting potential specimens for mapping and taking individual spectra. A  $12\text{ }\mu\text{m}$  square aperture with  $10\text{ }\mu\text{m}$  steps was used for generating an IR map of root sections using the Atl $\mu\text{s}$ , a component of the Omnic 6.0 software package (Thermo-Electron, Madison, WI) used to control the microscope stage. The optics were purged using dry  $\text{N}_2$  to minimize absorption of  $\text{CO}_2$  and water vapor in the ambient air. SR-IMS spectra were expressed as  $\log(1/R)$  (equal to absorbance) and a baseline correction was used to generate the final spectra.

Specific regions of root tissue were selected for line and area mapping using Atl $\mu\text{s}$ . The motorized computer controlled microscope stage traced the designated tissue area for sampling into an  $XY$  grid for the synchrotron beam to follow. IR spectra were taken by a point-by-point sequence across the designated area to form an  $XY$  surface that corresponded to the morphology of the sample and a  $z$  direction containing the spectral information. The resulting data can be displayed as a series of spectroscopic images collected at individual wavelengths or as a series of IR spectra obtained at each pixel position of the image mapped. The spectra from the data set were area-normalized in order to compensate for changes in thickness across the section. Functional group images were produced by plotting the intensity of the IR spectral bands as a function of the  $XY$  position. False color intensity maps were derived from the area under particular spectral features. The number of samples and areas examined varied due to limited

synchrotron beam time as well as the status of the synchrotron beam. The details of how each sample was studied are discussed further in their respective chapters.

### **Principal Components Analysis (PCA)**

Principal Components Analysis of the FTIR spectra was performed using the WINDAS software package (Kemsley, 1998). FTIR spectra must be saved under the jcamp-dx (.jdx) file extension. This can be accomplished by choosing the .jdx file extension under the SAVE AS option in the FILE menu of the Omnic 6.0 software package. However, WINDAS only supports the .dx jcamp-dx file extension. To rectify this issue, the .jdx file extension can be changed to the .dx file extension in the MS-DOS prompt. The data are then ready to be analyzed by WINDAS. In order to better explain the PCA process, an example will be used which compares SR-IMS spectra from maize and sunflower epidermis samples.

The first step involves building a “Construct Matrix”. The “Construct Matrix” consists of the raw preprocessed spectra used to construct the model and test the model. In this case, 36 spectra of maize epidermis and 37 spectra of sunflower were arbitrarily selected from spot, line, and area maps. Two-thirds of the spectra were used as the training set to develop the model (24 for maize and 25 for sunflower) and one-third of the spectra were used to test the model set. It is crucial that all the spectra have the same wavelength range because PCA can only process data with the same number of variates. In this case, all spectra were taken in the range of 4000-680  $\text{cm}^{-1}$ . For all PCA experiments the IR fingerprint region, 1800-700  $\text{cm}^{-1}$ , was used in order to reduce the number of variates to be calculated. Also, this region possesses all the major peaks of interest pertaining to biopolymers like protein and lignin. All the spectra were processed in the following manner: (1) All spectra were truncated to the region of 1800-700



cm<sup>-1</sup>; (2) A single point baseline correction was performed at 1800 cm<sup>-1</sup> followed by area normalization of the region of 1800-700 cm<sup>-1</sup>. The spectra are now ready for PCA.

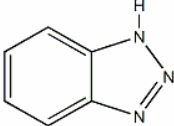
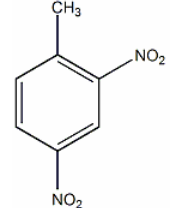
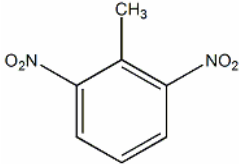
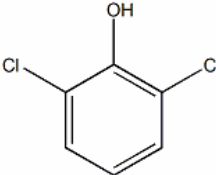
The next step is to define the groups for the model set. In this case, the two sets are maize epidermis and sunflower epidermis. Once the spectra or observations are selected to their respective group, a data matrix is formed. The data matrix is compressed using the covariance method yielding principal components or PCs which represent the major variation between maize and sunflower epidermis. A PC score plot (Figure 10) is then created to show the distribution of the samples. The first 2 PCs were the only PCs needed to show distinct separation between the maize and sunflower samples in the PC score plot since, combined, they represent 83% of the total variance. Figure 11 displays the first two PC loadings derived from the PC scores that contributed 64% and 19% to the variance between the maize and sunflower epidermis spectra.

In order to further insure that there are two distinct groups representing maize and sunflower epidermis, Linear Discriminant Analysis (LDA) was carried out using the Squared Mahalanobis distance metric (Kemsley, 1998). A group center is calculated based on the two sample sets. Next, the distance of each observation (sample) from the group center is determined. The observations are then assigned based on their location to the nearest group center. In this case, all of the samples were assigned appropriately to their respective group. Thus, a model set is constructed with two distinct groups. However, it is important to test the set with independent samples in order to determine if is reliable to use for future experiments.

In order to test the robustness of the model set, a test set comprised of 12 spectra (observations) from maize and sunflower epidermis extracted from various SR-IMS mapping experiments was used. The observations were reassigned to their nearest group based on the

squared Mahalanobis distance. For this example, all of the observations were correctly assigned to their respective group. The validation plot is shown in Figure 12 depicting both groups clearly separated by 2 PC scores. The ovals represent the 95% tolerance region for each sample set. Samples that fall outside the region are considered unclassified or not classified to a particular group. In this case, 2 samples from sunflower epidermis fell outside of the region and consequently are not classified, while all of the maize samples fell within the 95% tolerance region. A total of 25 out of 27 observations were correctly assigned which is a statistically reasonable outcome. It is important to note that the sunflower samples that were not classified to a group were closest to the sunflower group center. The model set can be interpreted as fairly robust. To increase the robustness of the model set more independent observations should be added.

**Table 2.** Physical properties of organic compounds selected for study (TOXNET, 2004)

Compound	Vapor pressure (atm)	Water solubility (mg/l, 25°C)	Henry's constant (atm-m <sup>3</sup> /mole)	log K <sub>OW</sub> <sup>†</sup> , Exp	Chemical structure
1-H- Benzotriazole (BT)	5.26x10 <sup>-5</sup>	1.98x10 <sup>4</sup>	2.66x10 <sup>-9*</sup>	1.23 <sup>‡</sup>	
2,4-Dinitrotoluene (2,4-DNT)	1.93x10 <sup>-7</sup>	2.70x10 <sup>2</sup>	5.40x10 <sup>-8</sup>	1.98	
2,6-Dinitrotoluene (2,6-DNT)	7.46x10 <sup>-7</sup>	1.82x10 <sup>2</sup>	7.47x10 <sup>-7</sup>	2.10	
2,6-Dichlorophenol (2,6-DCP)	4.74x10 <sup>-5</sup>	2.65x10 <sup>3</sup>	2.67x10 <sup>-6</sup>	2.75	

\*Henry's constant derived from the ratio of vapor pressure to water solubility. <sup>†</sup>Log octanol/water partition coefficient. <sup>‡</sup>Value from Hart *et al.* (2004).

**Figure 7.** Longitudinal section of dry sunflower root tissue for ATR spectroscopic analysis. X. xylem, C. cortex, E. epidermis.

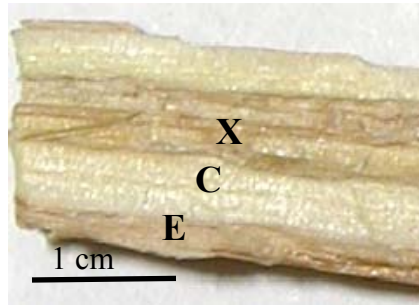
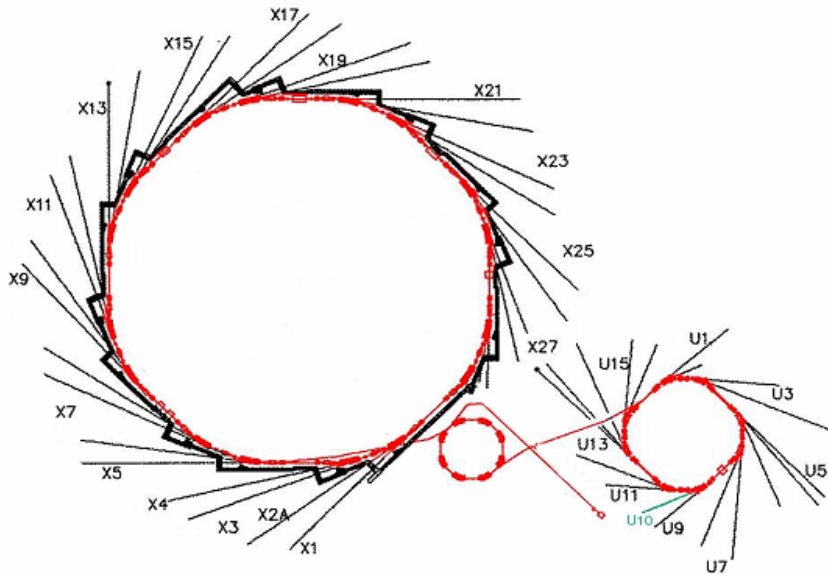
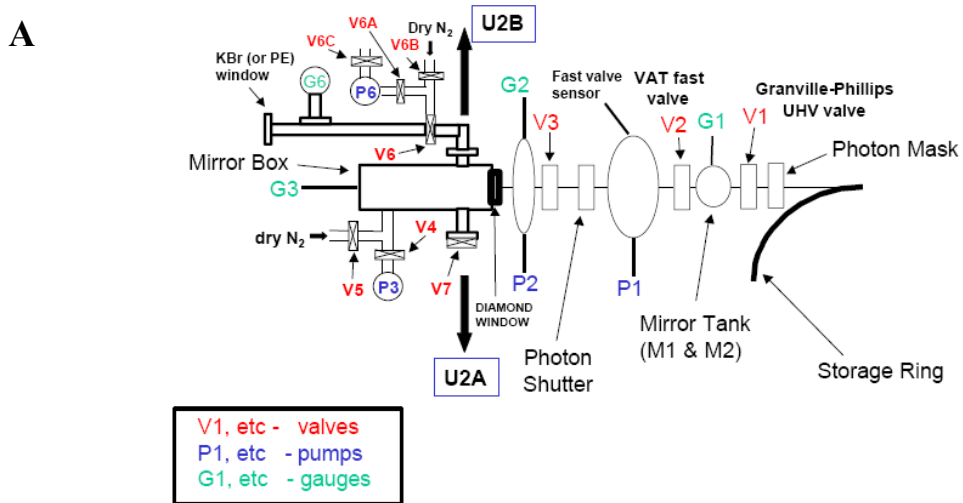


Figure 8. NSLS experimental floor (www.bnl.nsls.gov, 2004).



**Figure 9.** Features of Beamline U2B at the NSLS. A. Schematic of Beamline U2B. B. Instrument setup at Beamline U2B. ([www.bnl.nsls.gov](http://www.bnl.nsls.gov), 2004).



**B** Synchrotron infrared beam

Nicolet Nic Plan IR  
Microscope

Nicolet Magna  
860 FTIR

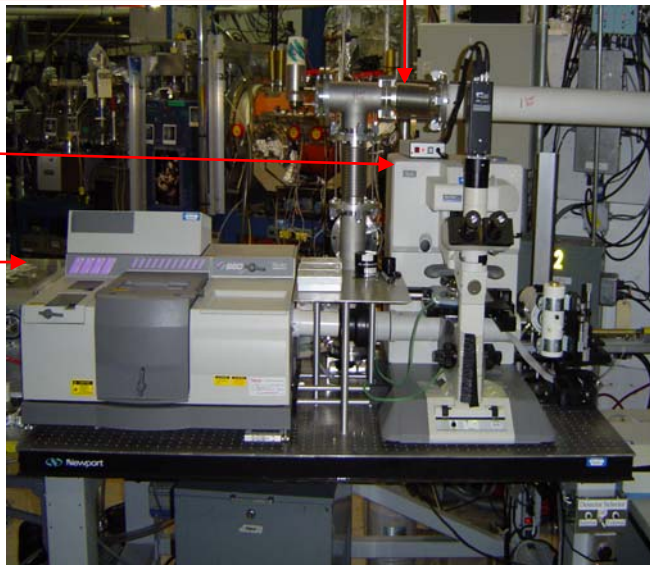


**Figure 10.** Example of a principal components score plot using maize and sunflower epidermis samples.

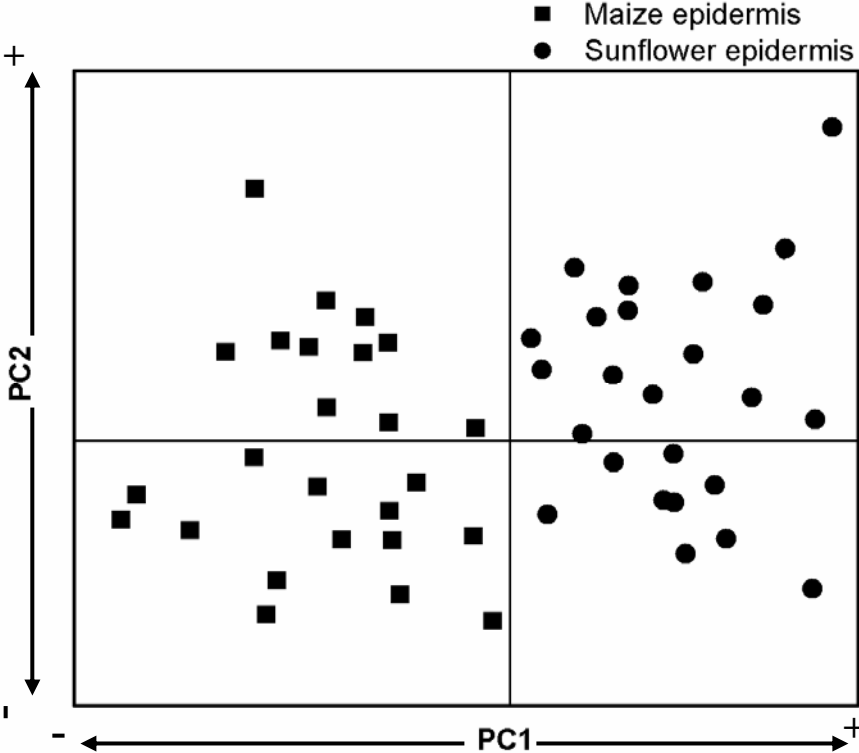


**Figure 11.** The principal component loadings depicting the major variation between maize and sunflower epidermis. A. First principal component (PC1). B. Second principal component (PC2).

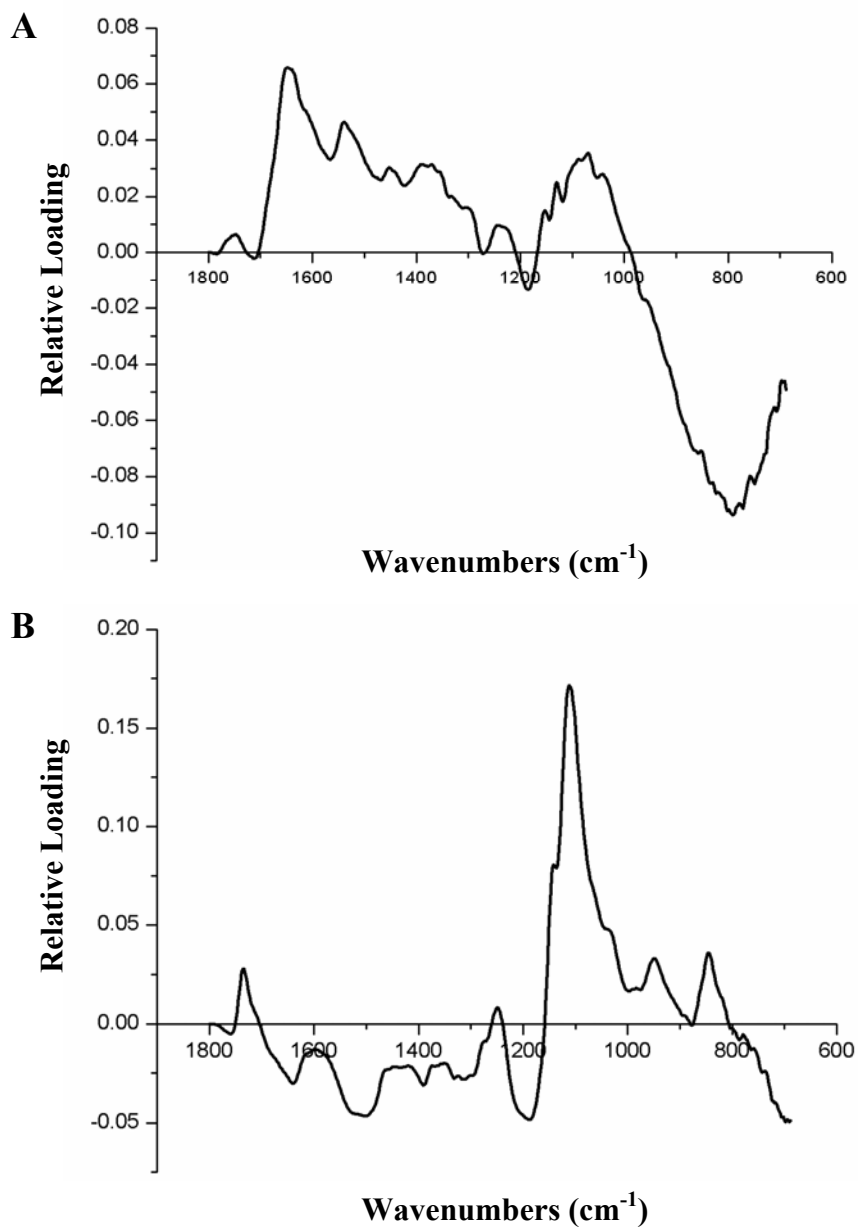
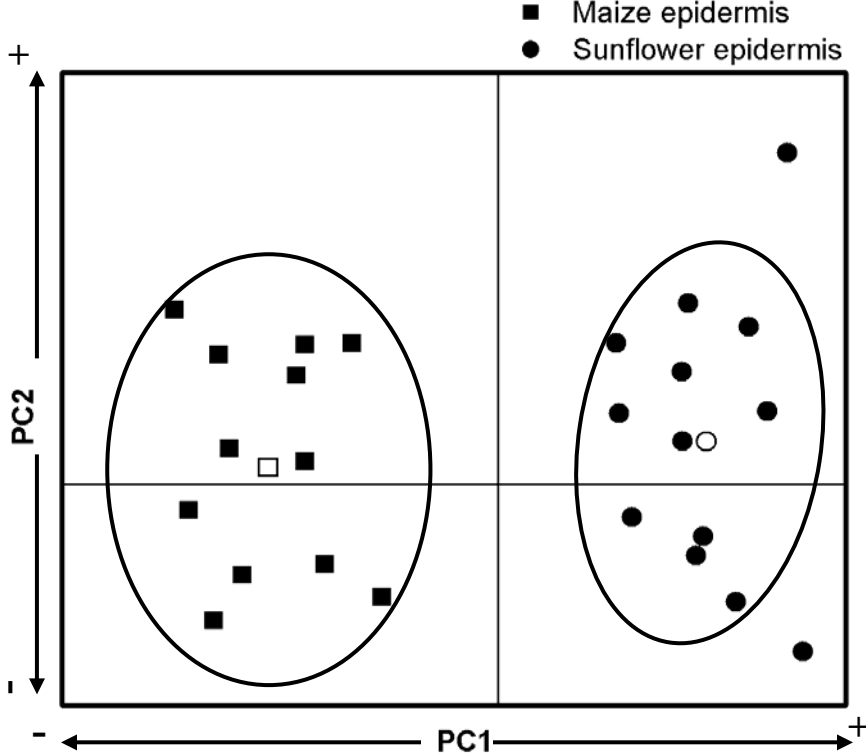




**Figure 12.** Example of a validation score plot used to test the robustness of the model set. The hollow symbols represent the (□) maize and (○) sunflower group centers.



**CHAPTER 3 - INFRARED IMAGING OF SUNFLOWER AND MAIZE ROOT  
ANATOMY**

## Introduction

Over the past decade infrared microspectroscopy (IMS) has emerged as a tool to study plant growth and development at the molecular level. Researchers at the Department of Botany and Plant Physiology at Purdue University have published many papers using IMS to study plant cell wall architecture (Carpita and McCann, 2002; Carpita *et al.*, 2001; McCann *et al.*, 2001; 1997; 1995; 1994; 1992; Jarvis and McCann, 2000; Chen *et al.*, 1998, 1997; Sene *et al.*, 1994). However, their work has focused primarily on cell wall extracts and very little on whole plant tissue. One major disadvantage for studying extracted cell wall material is the loss of the spatial distribution of microstructures in the plant tissue. The low source brightness of global sources from conventional benchtop instruments does not provide adequate resolution to study plant tissue at the molecular level. It was not until the last five years that study of whole plant tissue using IMS became more feasible due to the coupling of IMS to a synchrotron source. Synchrotron radiation (SR) as high energy a source for IMS provided improvements to studying plant samples with limited light throughput. The small effective source size and high brightness of the synchrotron beam also allows study of samples with small areas with spatial resolution to the diffraction limit of 5 – 15  $\mu\text{m}$ . However, the use of SR-IMS to study plant structures is still in its infancy. There are a limited number of research groups that use SR-IMS to study plant microstructures. Most of these studies have focused on feed (seed) tissues such as wheat (Wetzel *et al.*, 2003; Wetzel and LeVine, 2001;1998; Yu, 2004; Yu *et al.*, 2004b), corn (Yu, 2005; 2004; Yu *et al.*, 2004c), oat (Yu, 2004; Yu *et al.*, 2004b; Wetzel *et al.*, 1998), barley (Yu, 2004; Yu *et al.*, 2004a; 2004b; 2004d; 2003), and canola seeds (Yu, 2004; Yu *et al.*, 2005). Fewer than ten reports have focused on whole plant tissue (Carpita *et al.*, 2001; Dokken *et al.*, 2005b; 2005c; 2004; Raab and Martin, 2001; Raab and Vogel, 2004; Wetzel *et al.*, 1998). The

lack of research on whole plant tissue may stem from the complexity of the biopolymers in plant tissues, such as cellulose and lignin, compared to seed tissue composed primarily of a starchy matrix containing lipids and proteins. The less complex structure of seed tissues makes it easier to resolve the spatial distribution of infrared functional groups with respect to seed microstructures.

This chapter will focus on the ability of SR-IMS to probe complex microstructures and biopolymers in the root tissue of sunflower and maize plants. The intention will be to perform an “infrared dissection,” from the root cap to 1cm up the root, to observe the spectral differences between different tissues types, such as xylem and epidermis. Figure 13 shows the typical structural components in root tissue and their organization in the monocot and dicot root. Immunocytochemistry methods in conjunction with electron microscopy have provided a wealth of data on the compositional differences between monocots and dicots. However, there is a lack of immunological (antibody) probes for many types of biopolymers. Thus, the potential of SR-IMS to differentiate between two different plant species, using maize and sunflower as the representative organisms, will also be assessed. Very few works have looked at the spectral differences between monocots and dicots. Sene *et al.* (1994) and McCann *et al.* (1997) used IMS to study cell wall material of several different monocots and dicots and noted some broad differences in the spectral regions associated with pectins and proteins. However, the high complexity of plant cell walls and natural variation between plants of the same group has made this task difficult. PCA was employed to further uncover spectral differences between the two plant types.

## Results and Discussion

### *Assignment of IR bands in maize and sunflower root tissue*

The assignment of the main IR bands found in sunflower and maize secondary roots grown hydroponically in Hoagland's solution are displayed in Table 3. IR bands mainly associated with lipids are located between 3000 – 2800  $\text{cm}^{-1}$  (bands A – D) and correspond to asymmetric and symmetric stretches of  $\text{CH}_3$  and  $\text{CH}_2$  (Yu *et al.*, 2005). Carbonyl stretches of carboxyl and phenolic esters at 1740  $\text{cm}^{-1}$  (band E) and 1720  $\text{cm}^{-1}$  (band F), respectively, also signify the presence of lipids (Yu *et al.*, 2005; Sene *et al.*, 1994). Proteins are represented by IR bands near 1650  $\text{cm}^{-1}$  (amide I, band G) and 1550  $\text{cm}^{-1}$  (amide II, band J) due to the amide linkage (Sutherland, 1952). The aromatic rings of lignin give rise to IR bands from C=C stretching at 1635  $\text{cm}^{-1}$  (band H) (Sene *et al.*, 1994) and 1515  $\text{cm}^{-1}$  (band K) (Sene *et al.*, 1994; Williams and Fleming, 1980) and a sharp band at 845  $\text{cm}^{-1}$  (band Q) (Hergert, 1971). IR bands from polysaccharides, cellulose, and carbohydrates overlap in the carbohydrate fingerprint region of 1200 – 900  $\text{cm}^{-1}$  (band P) (Williams and Fleming, 1980). There are also some regions of overlap with components of polysaccharides, cellulose, and lipids in the region of 1447 – 1459  $\text{cm}^{-1}$  (band M) and 1395 – 1364  $\text{cm}^{-1}$  (band N) representing C-H bends of symmetric and asymmetric  $\text{CH}_3$  (Sene *et al.*, 1994). However, there are several diagnostic peaks for cellulose which are located at 1240  $\text{cm}^{-1}$  (band O) (Sene *et al.*, 1994) and 1420  $\text{cm}^{-1}$  (band L) (Zeier and Schreiber, 1999). The presence of many types of polysaccharides in plants makes it difficult to make an exact qualitative assessment of which polysaccharides are present in the root tissue. However, Kacurakova *et al.* (2000) have studied the cell wall compounds, like cellulose and pectic polysaccharides, and have determined some major peaks which can aid in identifying some key polysaccharides in root tissue.

### *Infrared dissection of sunflower root tissue*

Figures 14 – 21 depict spectra and line or area maps of functional groups of sunflower secondary root tissue at different distances from the root cap. They show the distribution and relative concentration of specific biopolymers associated with particular root structural components. All area and line maps were sampled with a 12 x 12  $\mu\text{m}$  aperture with every pixel corresponding to a spectrum taken at the sample location. The groups of spectra are then collectively represented as a false color intensity map. The line maps depict overall peak intensities throughout the spectrum while area maps represent the magnitude of the area under a particular peak that corresponds to a particular functional group. Red color represents high intensity and blue color stands for little or no intensity. The blue lines or rectangles on the visible image of each root section represent the area studied. Representative spectra show the different spectral characteristics associated with a particular structural component of secondary root tissue.

Figure 14 shows a line map of the sunflower root cap approximately 100  $\mu\text{m}$  from the root tip. The intensities of the peaks under each spectrum are constant throughout the line studied meaning the root cap is fairly homogeneous in structure. A representative spectrum of root cap tissue (Figure 14D) shows that root cap is dominated by the carbohydrate fingerprint region (band P). This is to be expected since root caps of dicots excrete pectic polysaccharides and arabinogalactan-proteins (AGPs) (Vigre *et al.*, 2005) and often contain starch grains. Since there are many overlaps in the carbohydrate fingerprint region, some peaks represent more than one type of polysaccharide. The strong peak at  $1080\text{ cm}^{-1}$  is commonly found in spectra of arabinogalactan (Kacurakova *et al.*, 2000) and in pectins. Further confirmation of pectin or pectic polysaccharides is denoted by peaks at  $1418\text{ cm}^{-1}$  (band L),  $953\text{ cm}^{-1}$ ,  $890\text{ cm}^{-1}$  and  $833$

$\text{cm}^{-1}$ . The strong peak at  $1025 \text{ cm}^{-1}$  is indicative of starch (Kacurakova *et al.*, 2000) and peaks at  $1240 \text{ cm}^{-1}$  and  $1373 \text{ cm}^{-1}$  ( bands O and N) are diagnostic for cellulose. Bands G (amide I) and J (amide II) reflect the obvious presence of protein while the presence of lipids is represented by bands A, B, and E.

Figure 15 presents the line map of the root cap approximately  $250 \mu\text{m}$  from the root tip, near the apical meristem. Two distinct regions representing epidermis and cortex can be observed. The cortex is more proteinaceous (bands G and J) and, overall, contains less lipid than the epidermis. The spectrum of epidermis (Figure 15D) has sharp peaks at  $1740 \text{ cm}^{-1}$  (band E, C=O ester) and  $845 \text{ cm}^{-1}$  (band Q), a peak diagnostic for some types of lignin (mainly ferulic acid). The epidermis also has a higher relative concentration of cellulose (bands L, N, and O) and pectin (band L). However, both still maintain pectic polysaccharide and starch components similar to those seen in the root cap because the root tissue at  $250 \mu\text{m}$  is still predominantly made up of root cap tissue with cells beginning to differentiate into vascular tissue.

Figure 16 shows the functional group area maps of sunflower root tissue about  $500 \mu\text{m}$  from the root tip. The spatial protein distribution and concentration is depicted in the functional group map of the area under peaks centered at  $1650 \text{ cm}^{-1}$  (Figure 16C). The protein is mostly concentrated in the center of the cortex region where it appears the organization of the vascular tissue is beginning to take place. The spatial distribution of lipids is concentrated in the epidermis as seen in the functional group map of the area under the peak centered at  $1740 \text{ cm}^{-1}$  (C=O ester) in Figure 16D. A similar pattern of distribution can also be seen for cellulose (Figure 3.4E), carbohydrates (Figure 16F) and lignin (Figure 16G). These observations can be confirmed by examining the spectra of cortex, epidermis, and boundary tissue between cortex

and epidermis in Figure 17. The spectrum of boundary tissue resembles a mixture of cortex and epidermis, containing protein, lipid, and lignin functionalities. Both epidermis and boundary tissues possess arabinogalactan type polysaccharides (band P) and starch. The carbohydrate fingerprint region (band P) of the cortex spectrum resembles a similar pattern to xyloglucan (Kacurakova *et al.*, 2000), a noncellulosic polysaccharide found in most angiosperms that is a major component in cell walls of suspension cultured dicots (Aspinall, 1980).

Figure 18 presents the functional group area maps of sunflower root tissue about 1 mm from the root tip. At this distance, the endodermis has begun to form. A similar distribution of proteins (Figure 18C), lipids (Figure 18D), cellulose (Figure 18E), carbohydrates (Figure 18F), and lignin (Figure 18G) is concentrated in the boundary tissue and endodermis. There is a circular area of protein concentrated in the vascular tissue (inside endodermis) that overlaps with the lignin distribution which may signify the development of a xylem vessel. The spectra of the different structural components in the root at 1 mm are displayed in Figure 19. The spectrum of vascular tissue is similar to the cortex but has a relative higher concentration of lipids due to the higher intensities of bands A, B, C, E, and N. Also, the lignin peak at  $845\text{ cm}^{-1}$  (band Q) is twice as intense in the spectrum of vascular tissue when compared to the spectrum of cortex. The endodermis has features similar to the boundary tissue but is more proteinaceous. The epidermis and cortex are relatively unchanged when compared to the root at about  $500\text{ }\mu\text{m}$ .

Figure 20 shows the functional group area maps of sunflower root tissue about 1 cm from the root tip where the vascular region has fully developed xylem and phloem. The spatial distribution of lipids (Figure 20D), cellulose (Figure 20E), carbohydrates (Figure 20F), and lignin (Figure 20G) are most concentrated in the xylem, followed by the epidermis, and, to a



lesser degree, in the phloem. This is expected since the xylem is very thick and highly lignified, thus providing structure for the root and the passage for water and minerals to the aerial parts of the plants. There is also a high concentration of protein (Figure 20C) in the xylem coinciding with lignin (Figure 20G) deposition. This same overlapping pattern of protein and lignin was also observed at 1 mm. Figure 21 shows the spectra of the different structural components observed at 1 cm. Due to the lignification of the xylem, there is an intense peak representing phenolic or aromatic compounds  $845\text{ cm}^{-1}$  (band Q). Also, the xylem IR spectrum has peaks for lipids (bands A, B, C, D, E, M, and N) and cellulose (bands L, M, N, and O). The peaks in the carbohydrate fingerprint region (band P) are similar to those indicative of arabinogalactan and pectic polysaccharides. Intense peaks at  $1282\text{ cm}^{-1}$  and  $953\text{ cm}^{-1}$  are related to pectic and xyloglucan type polysaccharides, respectively (Kacurakova *et al.*, 2000). The IR spectrum of the phloem contains the same IR bands observed in the xylem but with less intensity. However, the phloem IR spectrum has a different band pattern in the carbohydrate fingerprint region (band P) suggesting the presence of different polysaccharides. The epidermis spectrum also has the same IR peaks seen in the xylem and phloem. There is the appearance of protein bands not previously observed in the epidermis closer to the root tip. It is possible that the IR spectrum representing the epidermis may be a mixture of epidermis and exodermis (boundary tissue between epidermis and cortex that contains proteins). The cortex spectrum contains lignin and lipid bands and lacks the intense amide I (band G) and amide II (band J) bands typically observed in cortex closer to the tip. As it often occurs, older developed tissue may contain less protein and become more rigid and lignified.

### *Infrared dissection of maize root tissue*

Figures 22 – 27 depict spectra and line or area maps of functional groups of maize secondary root tissue at different distances from the root cap. The sampling of the maize tissue and generation of line and functional group area maps were conducted under the same conditions and parameters as previously discussed for sunflower secondary root tissue.

Figure 22 represents a line map of the maize root cap approximately 150  $\mu\text{m}$  from the root tip. As in the case of the sunflower root cap, the intensities of the peaks under each spectrum are fairly constant throughout the line studied meaning the root cap is fairly homogeneous in structure. A representative spectrum of root cap tissue (Figure 22D) shows that root cap is dominated by lipid indicated by the presence of IR bands A, B, E, M, and N. IR bands L, M, N, and O denote the presence of cellulose. Maize root caps possess proteins signified by IR peaks at  $1650\text{ cm}^{-1}$  (band G) and  $1550\text{ cm}^{-1}$  (band J). A unique feature of maize plants is the presence of aromatic substances in nonlignified cell walls (Carpita, 1996) indicated by the presence of a peak at  $845\text{ cm}^{-1}$  (band Q). These aromatic substances predominantly consist of esters of lignin monomers, such as ferulate and *p*-coumarate, which are cross-linked to pectic polysaccharides. The pattern of IR bands in the carbohydrate fingerprint region (band P) is similar to that of rhamnogalacturonan (Kacurakova *et al.*, 2000), a pectic polysaccharide found in cell walls of somatic cells in maize and rice (Carpita, 1996). Also, intense peaks at  $1282\text{ cm}^{-1}$  and  $953\text{ cm}^{-1}$  indicate the presence of pectic and xyloglucan type polysaccharides, respectively. Xyloglucans are known to be present in cell walls in the root tips and meristematic cells of grasses (Carpita, 1996).

Figure 23 presents the line map of the maize root approximately 400  $\mu\text{m}$  from the root tip. Two distinct regions in the line map can be observed representing the epidermis and cortex.

The most intense IR peaks can be found in the epidermis. There is a strong presence of protein, lipids, polysaccharides, cellulose, and aromatic compounds (due to lignin monomers cross-linked to pectic polysaccharides) in the epidermis (Figure 23D). IR bands associated with pectin and rhamnogalacturonan can be observed in the carbohydrate fingerprint region (band P). The cortex IR spectrum contains less intense peaks for lipids, proteins, and cellulose and the lack of the band Q ( $845\text{ cm}^{-1}$ ) denotes the absence of lignin or lignin monomers. The IR bands in the carbohydrate fingerprint region:  $1155\text{ cm}^{-1}$ ,  $1080\text{ cm}^{-1}$ , and  $1040\text{ cm}^{-1}$ , are indicative of arabinogalactan and xyloglucan (Kacurakova *et al.*, 2000). Arabinogalactans are found in numerous cellular locations and usually associated with plasma membrane and cell wall compartments in grasses (Gibeaut and Carpita, 1991).

Figure 24 shows the functional group area maps of maize root tissue about  $800\text{ }\mu\text{m}$  from the root tip. The spatial distribution of protein (Figure 24C) shows that it is concentrated most heavily in the epidermis and slightly less throughout the cortex. There is a circular distribution of protein in the center of the root section signifying the formation of xylem in the vascular tissue. The functional group maps for lipids (Figure 24D), cellulose (Figure 24E), carbohydrates (Figure 24F), and lignin (Figure 24G) show a concentrated distribution of these biopolymers in the epidermis. Cellulose is uniformly distributed throughout the cortex and vascular tissue. A circular distribution of lipids, carbohydrates, and lignin in the vascular tissue coincides with distribution pattern of protein previously described. The spectra of the different structural components in the root at  $800\text{ }\mu\text{m}$  are displayed in Figure 25. The representative spectrum of cortex possesses the same IR peaks as the cortex spectrum at  $400\text{ }\mu\text{m}$ . The carbohydrate fingerprint region dominates the epidermis IR spectrum with peaks corresponding to pectin or pectic polysaccharides ( $1144\text{ cm}^{-1}$ ,  $1080\text{ cm}^{-1}$ ,  $1052\text{ cm}^{-1}$ ,  $1021\text{ cm}^{-1}$ , and  $953\text{ cm}^{-1}$ ),

arabinogalactan ( $1144\text{ cm}^{-1}$  and  $1080\text{ cm}^{-1}$ ) and xyloglucan ( $1282\text{ cm}^{-1}$ ). The presence of pectin or pectic polysaccharides is also evidenced by band L ( $1458\text{ cm}^{-1}$ ). The lipid peak in the region  $3000 - 2800\text{ cm}^{-1}$  is very intense particularly for band B (asymmetric  $\text{CH}_3$  stretch).

Lignification of the epidermis is marked by band Q.

Figure 26 shows the functional group area maps of maize root tissue about 1 cm from the root tip where the vascular region has formed the typical xylem ring surrounding pith tissue. The spatial distribution of all the biopolymers is concentrated in the epidermis and xylem regions with higher intensity in the xylem. The spectra of the different structural components in the root at 1 cm from the root tip are displayed in Figure 27. All the structural components possess the same spectral features with the exception of the IR bands attributed to protein. Only the spectra of epidermis and xylem contain bands G and J. The cortex has the least amount of overall intensity for all of the IR bands. The cortex at 1 cm contains little or no protein and contains IR bands not previously observed in the cortex at distances closer to the root tip. The degree of lignification has increased in all of the structural components as shown by the sharp intense band at  $845\text{ cm}^{-1}$  (band Q). As the root develops, forming the xylem components, more and more lignin becomes deposited in the cell wall of tissues, especially in the xylem. The presence of band H in the xylem spectrum and higher peak intensity for band Q confirms that the xylem is more lignified than the other structural components. All of the structural components in the root at 1 cm also possess similar types of pectic polysaccharides, xyloglucan, and arabinogalactan as corroborated by the IR peaks diagnostic for these biopolymers.

### *Comparison of maize and sunflower root tissues*

Since all plant tissues are made up of protein, cellulose, polysaccharides, lipids, and lignin and have similar IR spectral features, it can be difficult to visually distinguish between spectra of a particular structural component from two different plants. This issue may be resolved by using principal components analysis (PCA) to uncover the most minor of differences between root tissues of hydroponically grown maize and sunflower plants. This section will discuss the ability of PCA to differentiate between the biopolymer makeup of the structural components of maize and sunflower root tissue using spectra from the epidermis, cortex, and xylem.

To compare the epidermis of the root tissue of maize and sunflower plants, spectra were randomly selected from spot, line, and area maps collected under the same experimental conditions. Thirty-seven epidermal spectra were extracted from twelve different maize samples and 37 epidermal spectra were obtained from thirteen different sunflower samples that ranged in position from 400  $\mu\text{m}$  to 1 mm from the root tip (this was the region with the most samples from both plants). Two-thirds of the spectra or observations were used for the training set yielding 25 observations for each plant. A plot of the first two principal components (PCs) (Figure 28) shows a distinct separation between maize and sunflower epidermal tissue. The first two PC loadings seen in Figures 29A and B account for 64 % and 19 % of the variability between maize and sunflower epidermal spectra. Through inspection of the peaks present in PC1 (Figure 29A), maize appears to possess a higher concentration of proteins, lipids, lignin, and polysaccharides in its epidermis. Monocots, particularly grasses, contain more lignin than dicots, overall (Hose et al., 2001). It also important to note that the lignin in dicots is typically composed of guaiacyl (G type) and syringyl (S type) rings while the lignin in monocots,

especially grasses, possesses G, S, and H (hydrocinnamic acid) type rings (Zeier and Schreiber, 1997). The positive presence of peaks due to aromatic C=C stretch at  $1635\text{ cm}^{-1}$  (band H) and  $1515\text{ cm}^{-1}$  (band K), which appear as shoulders on the amide I and amide II peaks, and the positive peak at  $845\text{ cm}^{-1}$  (band Q) in the loading of PC2 (Figure 29B) provide evidence of this. The  $1515\text{ cm}^{-1}$  band corresponds to G and S type lignin and the  $1635\text{ cm}^{-1}$  represents C=C stretching in the hydrocinnamic acid ring (Sene *et al.*, 1994). The  $1635\text{ cm}^{-1}$  may be the most useful peak in distinguishing between maize and sunflower epidermis. The carbohydrate fingerprint region (band P) in the first PC loading does not represent one particular polysaccharide; however, it does signify that maize root contains different types of polysaccharides than sunflower root tissue. This same region in the second PC loading has significantly positive peaks that correspond to arabinogalactans. This is very plausible as the cell wall of maize seedlings are rich in arabinogalactans some of which are in the form of arabinogalactan proteins (AGPs) (Carpita, 1996). Using the first two PCs, linear discriminant analysis (LDA) resulted in a 100% correct assignment of the observations to their appropriate group. Twenty-five spectra from independent samples of maize and sunflower root tissue were used as the test set. Based on the Mahalanobis distance metric, the group centers were calculated from the model set. A validation plot was generated (Figure 30) displaying the distance of each sample from its particular group center. Two of the samples from the sunflower test set were considered unclassified as they lie outside the 95% tolerance region. All of the samples from the maize test set were correctly assigned to the maize group. This shows that it is feasible to use PCA to distinguish between maize and sunflower epidermal tissue.

The data set used to for the PCA of maize and sunflower cortex tissue consisted of 96 spectra, 48 observations from each plant. The spectra were obtained and placed into the training

and test sets using the same protocol described for the epidermal samples. Thirty-two cortex spectra from each plant were used to construct the model set. Figures 31A and B depict the PCA score plots generated using PCs 1 and 2 and PCs 3 and 5. The PCA plot using PC1 and PC2 shows that the samples were fairly dispersed with no separation between the two groups. However, a plot of PC5 versus PC3 reveals some separation between the maize and sunflower samples. Even though the first and second PC loadings accounted for almost 85% of the overall variability, they were not able to separate the data into two distinct groups. The five PC loadings generated from PCA of maize and sunflower cortex can be seen in Figure 32. The first PC loading (Figure 32A) shows positive peaks related to protein with a shoulder on the amide II peak (band G) representing C=O stretching of the carboxyl ester (band E). The second PC loading contains the amide I peak (band G) and peaks for polysaccharides and cellulose (Band P). The third (Figure 32C) and fifth (Figure 32E) PC loadings account for 2.88% and 1.59% of the variability, respectively. The constituents of the fifth PC loading are not noise, but, in fact, are spectral bands associated polysaccharides, protein, and cellulose. This loading, even though it contributes very little to the overall variability, represents some systematic variation between the maize and sunflower cortex. Twenty-four (12 for each plant) cortex spectra were taken from samples independent from the model set and used as the training set. Seven PC scores were used in the LDA, resulting in the correct assignment of 21 observations out of a total of 24 observations. The assignment and reassignment success rates based on the number of PC scores used in LDA are shown in Figure 33. In the training set, 6 PC scores were needed for a 100% success rate. The maximum success rate for the test set was 84% meaning the success rate did improve when increasing the PC scores as witnessed in the training set. This means that sunflower and maize cortex tissues are very similar and infrared spectroscopy may

not be sensitive enough to distinguish between them. Adding more independent samples to the model set may improve the ability to distinguish between maize and sunflower cortex tissue.

Thirty-six xylem spectra were extracted from twelve different maize samples and 37 xylem spectra were obtained from thirteen different sunflower samples using the same parameters mentioned for the comparison of sunflower and maize epidermal tissue. However, xylem spectra were sampled from maps of root tissue taken between 1mm and 1cm from the root tip. PCA was performed using 24 maize xylem spectra and 25 sunflower xylem spectra. The PCA score plot shown in Figure 34 shows clear separation of the maize and sunflower xylem samples using the first 2 PC scores. The first PC score accounted for 71% of the variability while the second PC score accounted for 16.5% of the variability, with an overall variability of 87.5%. The first PC loading (Figure 35A) indicates that maize xylem contains more protein (bands G and J) and sunflower xylem has more lipids (band E) and cellulose (band O). The second PC loading (Figure 35B) is somewhat similar to the second PC loading seen for the PCA of maize and sunflower epidermal tissue (Figure 29B). The positive peaks in the carbohydrate fingerprint region (band P) are representative of arabinogalactan as seen in maize epidermal tissue. The appearance of the IR peak at  $1635\text{ cm}^{-1}$  (band H) representing the presence of H type lignin is very significant as it also appeared in the PCA of epidermal tissue. In this study, the H type lignin is unique to maize, thus providing a means of distinguishing maize from sunflower. 24 xylem spectra taken from independent samples (12 for each plant) were used as the test set. Using the first two PC scores, 20 out of 24 observations were correctly assigned to their appropriate group as seen in the validation score plot in Figure 36. Two observations from each plant fell outside of the 95% tolerance region. This is probably just due to natural variation within the plants themselves.



Since the IR bands for the common plant biopolymers were present in all the IR spectra, it was clearly not possible to distinguish between maize and sunflower root tissue based merely on visual inspection of the IR spectra. This was especially true for samples from cortex or vascular tissue. The use of PCA allowed for the distinct separation of maize and sunflower samples using IR spectra from the epidermis and xylem. Even though it appeared that maize contained more protein and polysaccharides, like arabinogalactan, these components were not sufficient to provide distinction between maize and sunflower samples. The  $1635\text{ cm}^{-1}$  peak for hydrocinnamic acid in (H type) lignin uncovered by PCA provided a conclusive means of distinguishing between maize and sunflower due to its uniqueness to maize, in this case. One could probably not distinguish between maize and another grass based on this parameter as H type lignin is found in most monocots and all grasses. It is important to also note that this type of analysis is only semi-quantitative. More independent samples are required for the training set in order to provide a more reliable means to quantify the biopolymers present in the maize and sunflower samples.

**Table 3.** Assignment of the main IR bands in IR spectra of sunflower and maize secondary roots.

Band	Assignment	Frequency range (cm <sup>-1</sup> )	Comments
A <sup>*</sup>	Asymmetric CH <sub>3</sub> stretch	2940 – 2960	Lipids; exact frequency varies on attached groups
B <sup>*</sup>	Asymmetric CH <sub>2</sub> stretch	2910 – 2930	Lipids; exact frequency varies on attached groups
C <sup>*</sup>	Symmetric CH <sub>3</sub> stretch	2860 – 2885	Lipids; exact frequency varies on attached groups
D <sup>*</sup>	Symmetric CH <sub>2</sub> stretch	2840 – 2860	Lipids; exact frequency varies on attached groups
E <sup>*†</sup>	C=O stretching of carboxyl ester (alkyl)	≈1740	Lipids; exact frequency varies on attached groups, esterified pectins
F <sup>†</sup>	C=O stretching of phenolic ester	≈1720	Phenolics; due to lipids or uronic acids
G <sup>‡</sup>	Amide I: C=O stretch + C-N stretch	≈1650	Protein; exact frequency based on secondary structure
H <sup>†</sup>	Aromatic C=C stretch	≈1635	Hydrocinnamic acid in lignin
I <sup>†§</sup>	COO <sup>-</sup> asymmetric stretch	≈1600	Acidic groups of pectic polysaccharides
J <sup>‡</sup>	Amide II: N-H deformation + C-N stretch	≈1550	Protein; exact frequency based on secondary structure
K <sup>†§</sup>	C=C phenolic stretch	≈1515	Guaiacyl ring of lignin
L <sup>£</sup>	C-H bend of OCH <sub>3</sub>	1445 – 1460	Cellulose and/or pectin
M <sup>†</sup>	C-H bends from asymmetric CH <sub>3</sub>	1410 – 1420	Lipids, polysaccharides, cellulose
N <sup>†</sup>	C-H bends from symmetric CH <sub>3</sub>	1395 – 1364	Lipids, polysaccharides, cellulose
O <sup>†</sup>	C-O-H deformation + asymmetric C-C-O stretch of ester	1240 – 1250	Diagnostic peak for hemicellulose or cellulose
P <sup>§</sup>		1200 – 900	Carbohydrate fingerprint region; Very complex and depends on contributions from polysaccharides, cellulose, hemicellulose, and pectins
Q <sup>¶</sup>	Aromatic C-H wag of para-substituted benzene ring	≈845	Aromatic ring associated with lignin or lignin monomers

\*Yu *et al.*, 2005b; †Sene *et al.*, 1994; ‡Sutherland, 1952, § Williams and Fleming, 1980; £ Zeier and Schreiber, 1999; ¶Hergert, 1971.

**Figure 13.** Typical plant root anatomy. A. Drawing depicting the different structures and tissues commonly found in plant roots B. Comparison of the root anatomy of monocots and dicots. The main difference between monocot and dicot root structure is the organization of their vascular tissues. Monocotyledonous plants, like maize, have their xylem arranged in ring surrounding the pith. In dicotyledonous plants, like sunflowers, the xylem is a 3 or 4 pronged star structure with phloem in between each prong. (<http://www.ualr.edu/botany/rootanatomy.html>).

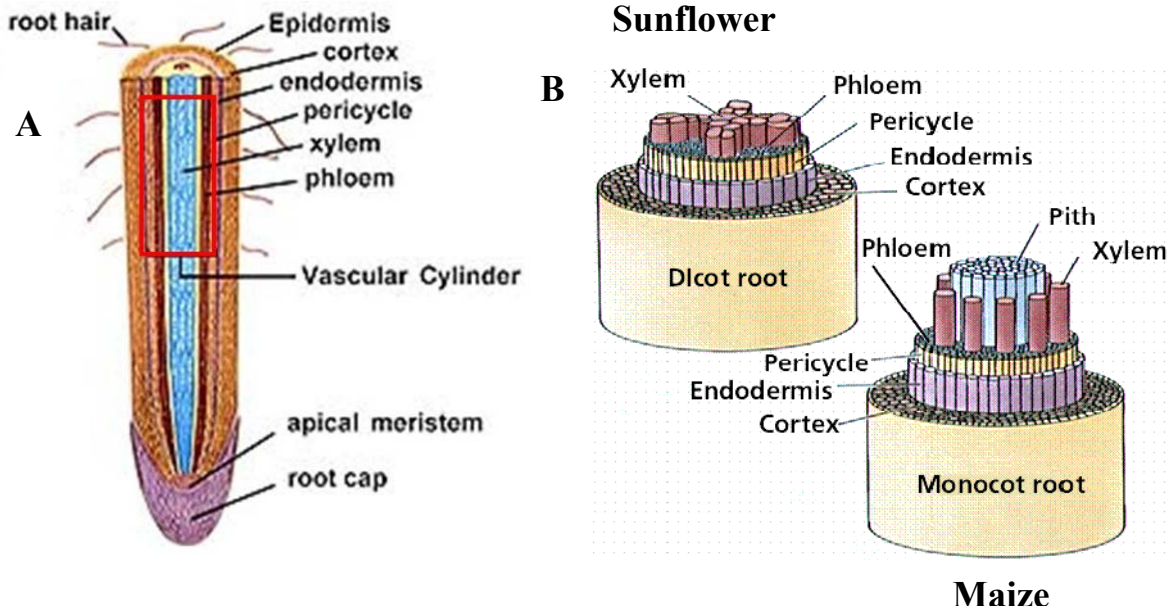


**Figure 14.** Line map and typical IR spectrum of sunflower root cap approximately 100  $\mu\text{m}$  from the root tip. (A) Visible image of root cap. (B) False color intensity line map of root cap. Line length: 120  $\mu\text{m}$ . The blue line indicates the line mapped starting from the right and ending on the left. (C) Intensity ruler. (D) Typical spectrum of sunflower root cap tissue. The spectrum is an average of 10 root cap spectra. The spectra were normalized to the carbohydrate region between 1150 and 1000  $\text{cm}^{-1}$ . Refer to Table 3 for description of band assignments.

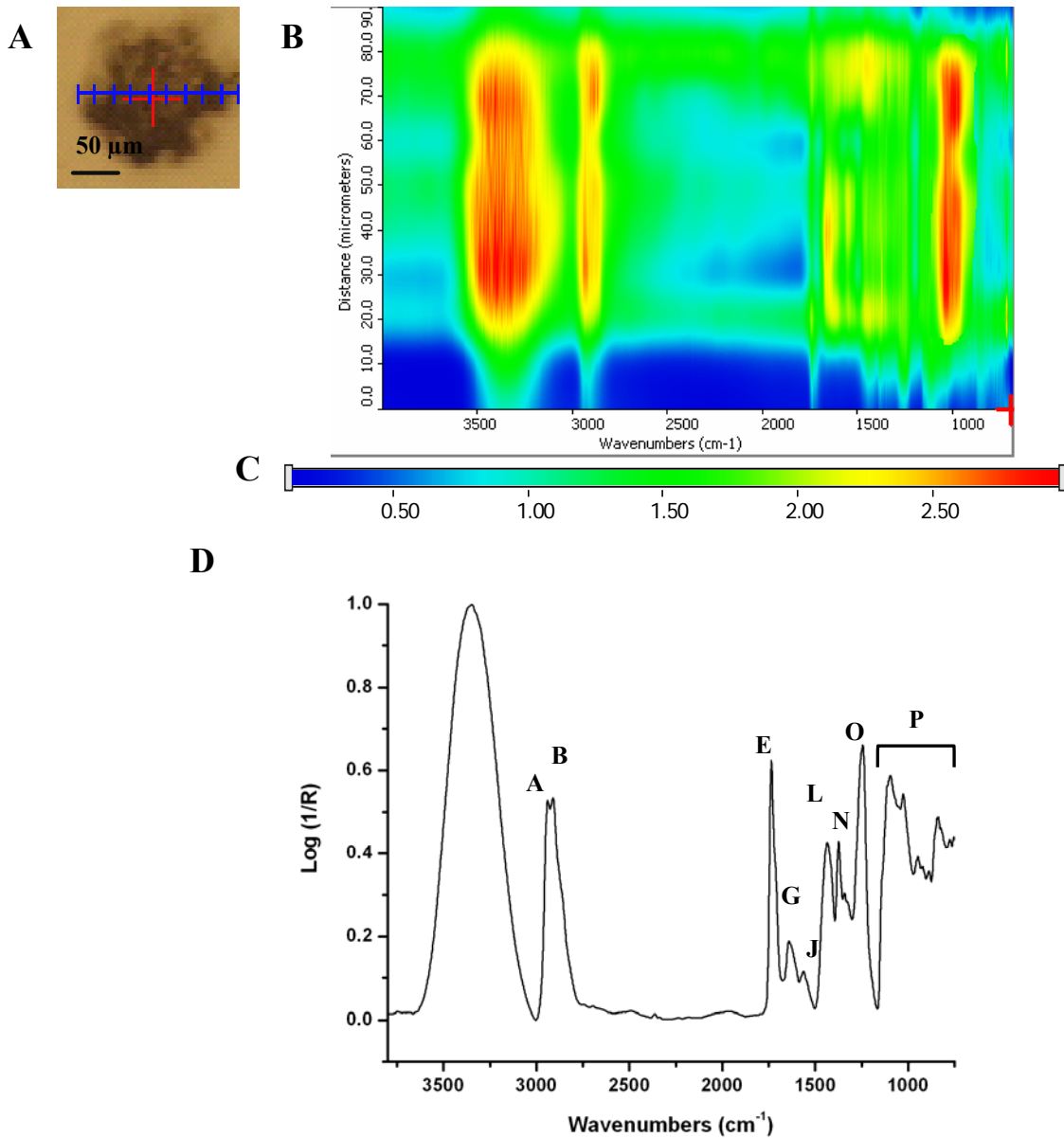


**Figure 15.** Line map and typical IR spectrum of sunflower root approximately 250  $\mu\text{m}$  from the root tip. (A) Visible image of root section. (B) False color intensity line map of root section. Line length: 150  $\mu\text{m}$ . The blue line indicates the line mapped starting from the right and ending on the left. (C) Intensity ruler. (D) Typical spectrum of sunflower root cortex (black) and epidermis (red) tissue (listed bottom to top). Each spectrum is an average of 10 spectra. The epidermis spectra were normalized to the OH peak at  $3350\text{ cm}^{-1}$  and the cortex spectra were normalized to the amide II band at  $1650\text{ cm}^{-1}$ . Refer to Table 3 for description of band assignments. Spectra are arbitrarily offset for ease of presentation.

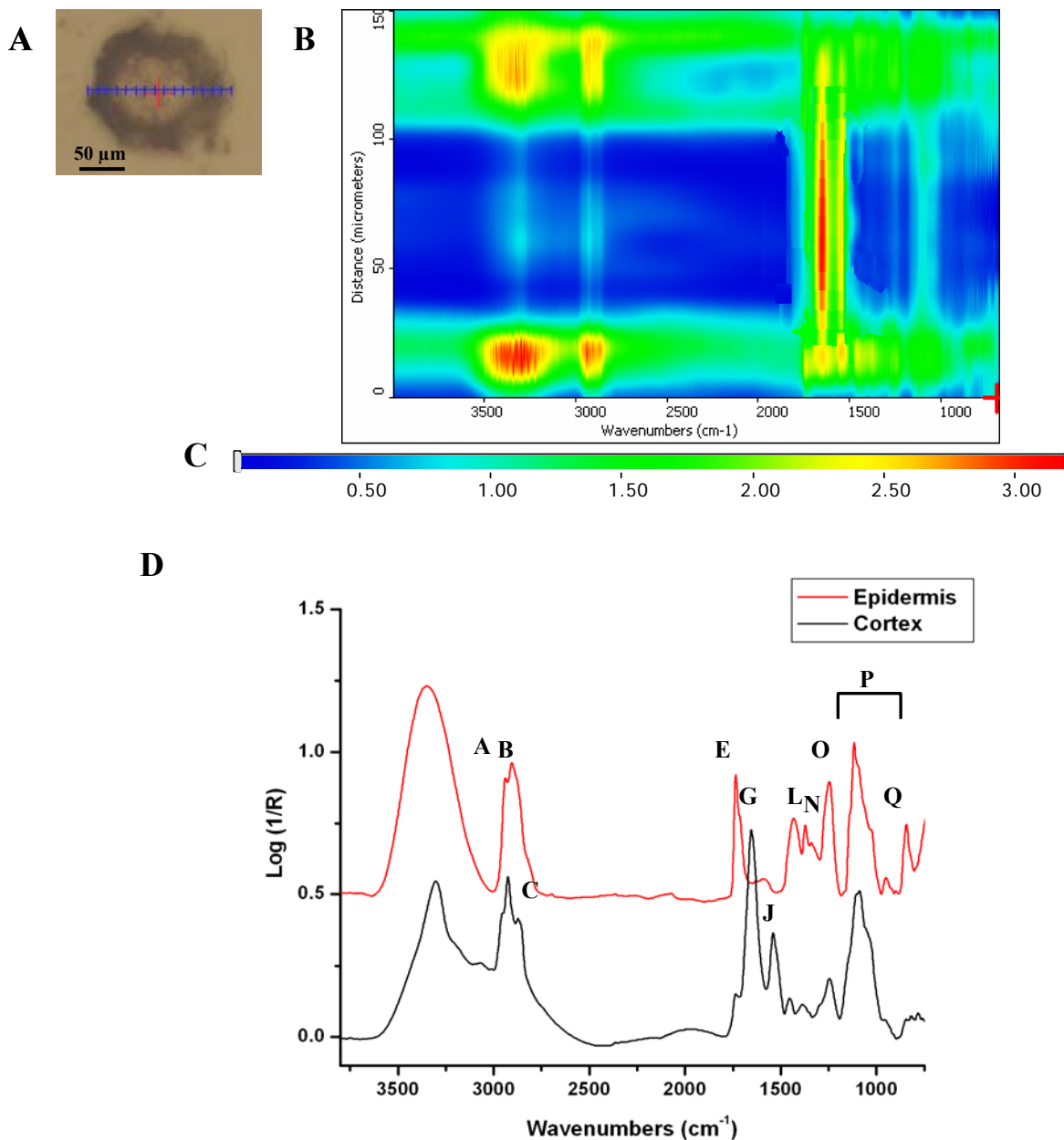


**Figure 16.** Functional group area maps of sunflower root tissue approximately 500  $\mu\text{m}$  from root tip. Dimensions of the area studied: 200  $\mu\text{m}$  x 30  $\mu\text{m}$ . Functional group images were produced by plotting the area under the IR spectral band as a function of the XY position. The intensity ruler is displayed under each functional group map. (A) Visible image of root section. The blue rectangle denotes the area studied (B). (C) Area under the peak centered at 1650  $\text{cm}^{-1}$  representing the protein concentration and distribution. (D) Area under the peak at 1735  $\text{cm}^{-1}$  (C=O esters) showing the concentration and distribution of lipids. (E) Area under peaks at 1240  $\text{cm}^{-1}$  indicating the concentration and distribution of cellulosic material. (F) Area under peaks between 1200 – 1000  $\text{cm}^{-1}$  indicating the concentration and distribution of carbohydrates. (G) Area under the peak at 845  $\text{cm}^{-1}$  signifying the distribution and concentration of lignin.

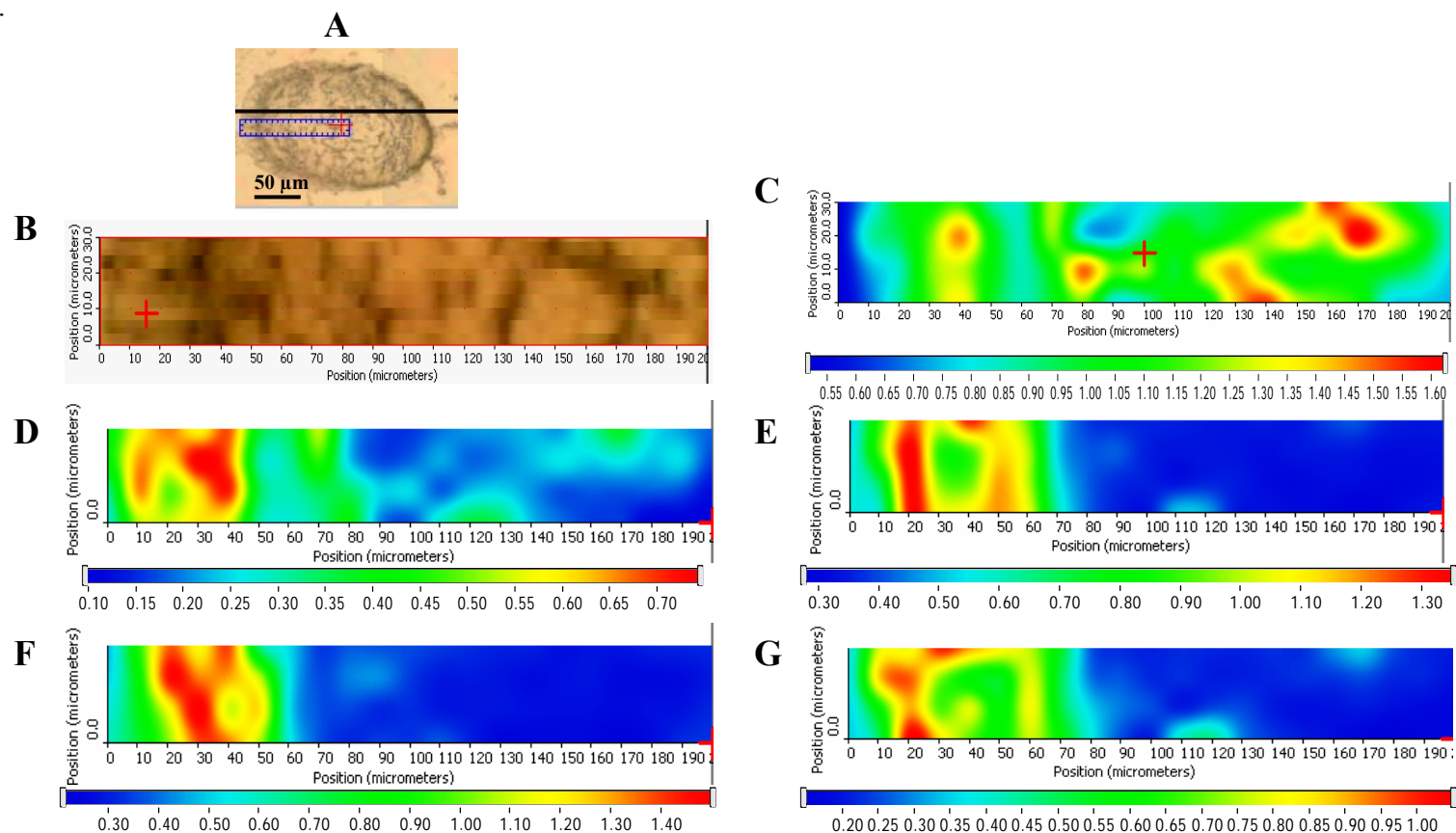


**Figure 17.** Typical spectrum of sunflower root cortex (black), boundary between epidermis and cortex (blue), and epidermis (red) tissue approximately 500  $\mu\text{m}$  from tip (listed bottom to top). Each spectrum is an average of 10 spectra. The epidermis and boundary tissue spectra were normalized to the OH peak at  $3350\text{ cm}^{-1}$  and the cortex spectra were normalized to the amide II band at  $1650\text{ cm}^{-1}$ . Refer to Table 3 for description of band assignments. Spectra are arbitrarily offset for ease of presentation.

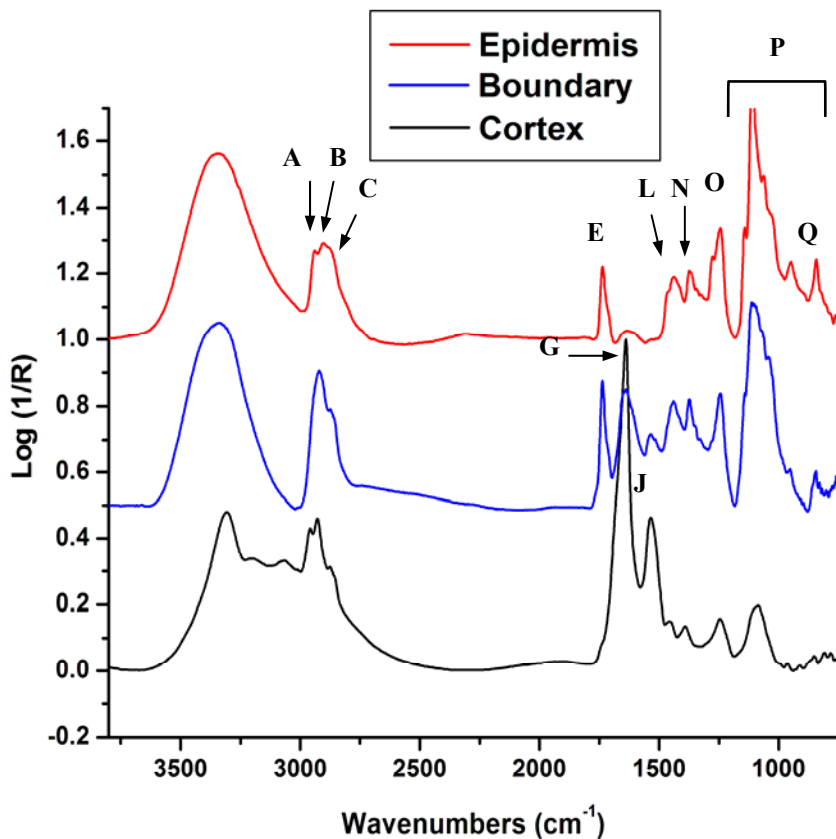


**Figure 18.** Functional group area maps of sunflower root tissue approximately 1 mm from root tip. Dimensions of the area studied: 350  $\mu\text{m}$  x 100  $\mu\text{m}$ . Functional group images were produced by plotting the area under the IR spectral band as a function of the  $XY$  position. The intensity ruler is displayed under each functional group map. (A) Visible image of root section. The blue rectangle denotes the area studied (B). (C) Area under the peak centered at 1650  $\text{cm}^{-1}$  representing the protein concentration and distribution. (D) Area under the peak at 1735  $\text{cm}^{-1}$  (C=O esters) showing the concentration and distribution of lipids. (E) Area under peaks at 1240  $\text{cm}^{-1}$  indicating the concentration and distribution of cellulosic material. (F) Area under peaks between 1200 – 1000  $\text{cm}^{-1}$  indicating the concentration and distribution of carbohydrates. (G) Area under the peak at 845  $\text{cm}^{-1}$  signifying the distribution and concentration of lignin.

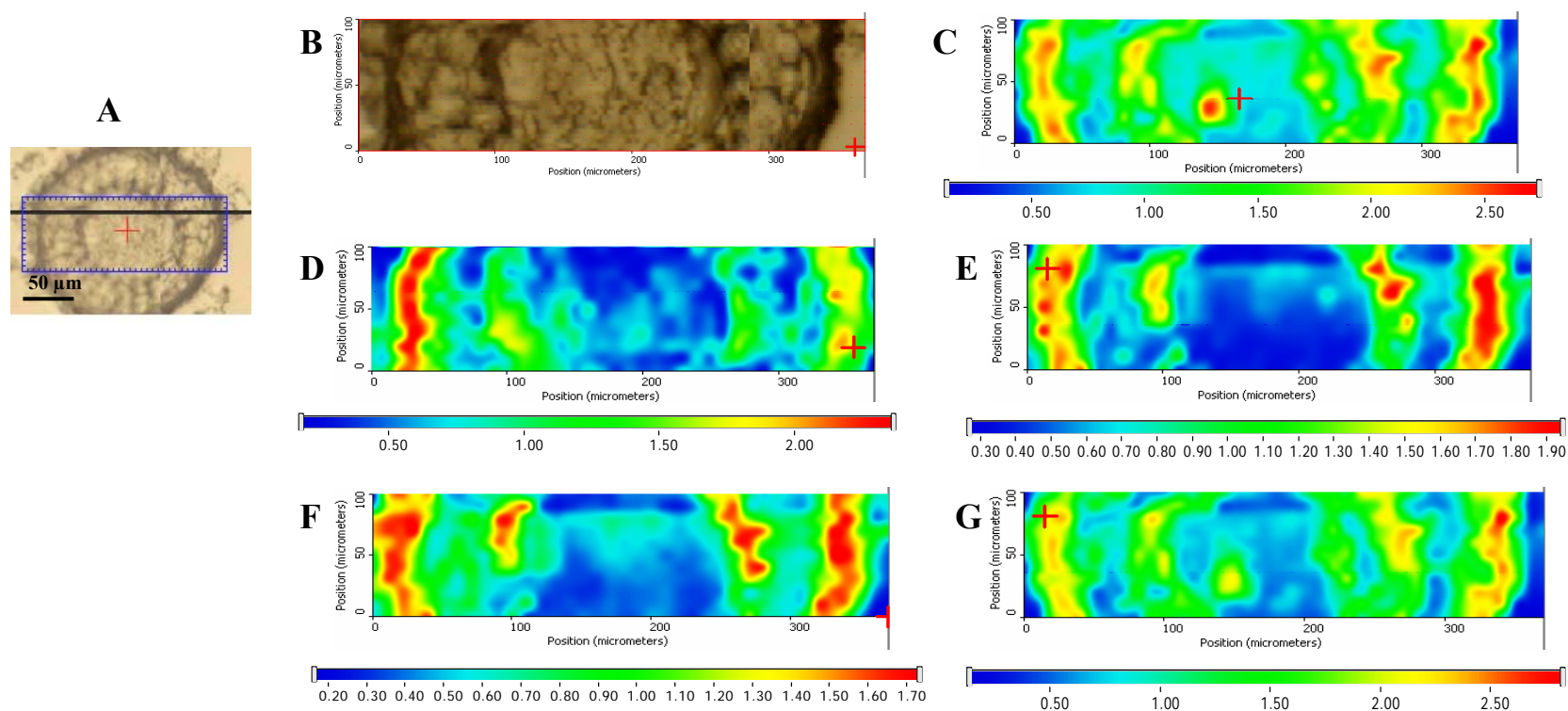




**Figure 19.** Typical spectrum of sunflower root cortex (black), boundary tissue between epidermis and cortex (blue), epidermis (red), vascular tissue (green), and endodermis (purple) approximately 1 mm from the root tip (listed bottom to top). Each spectrum is an average of 10 spectra. The epidermis, endodermis, boundary, and vascular tissue spectra were normalized to the OH peak at  $3350\text{ cm}^{-1}$  and the cortex spectra were normalized to the amide II band at  $1650\text{ cm}^{-1}$ . Refer to Table 3 for description of band assignments. Spectra are arbitrarily offset for ease of presentation.

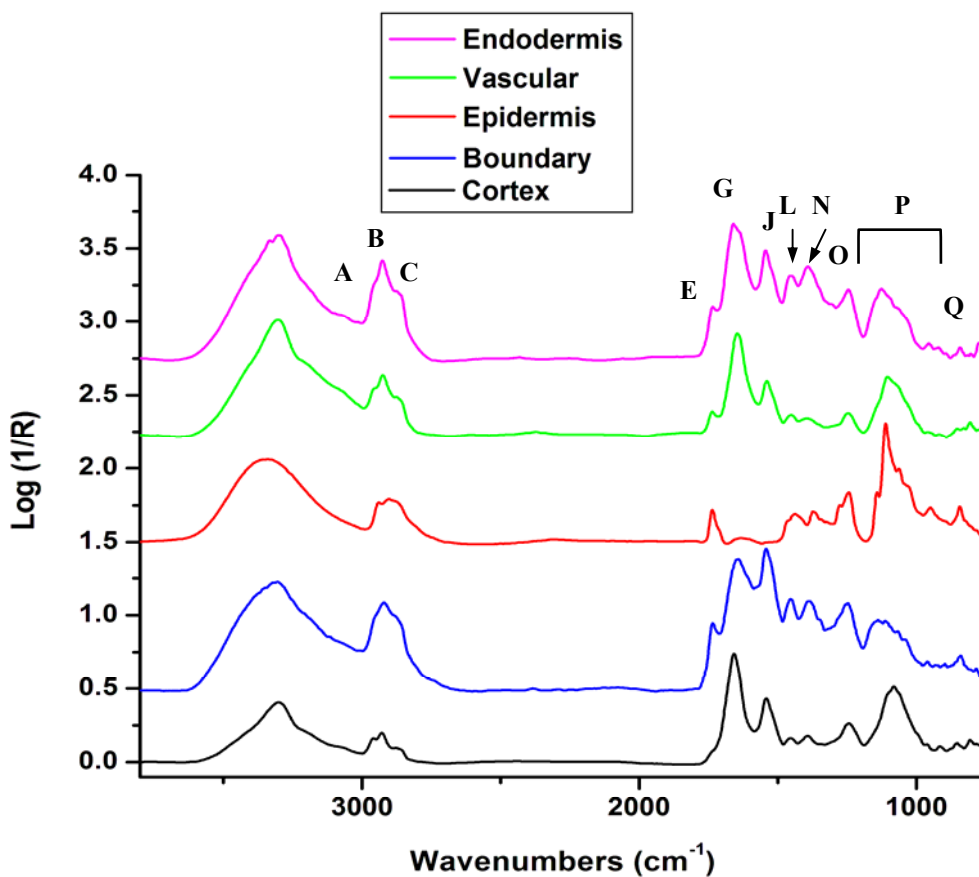


**Figure 20.** Functional group area maps of sunflower root tissue approximately 1 cm from the root tip. Dimensions of the area studied: 320  $\mu\text{m}$  x 90  $\mu\text{m}$ . Functional group images were produced by plotting the area under the IR spectral band as a function of the XY position. The intensity ruler is displayed under each functional group map. (A) Visible image of root section. The blue rectangle denotes the area studied (B). (C) Area under the peak centered at 1650  $\text{cm}^{-1}$  representing the protein concentration and distribution. (D) Area under the peak at 1735  $\text{cm}^{-1}$  (C=O esters) showing the concentration and distribution of lipids. (E) Area under peaks at 1240  $\text{cm}^{-1}$  indicating the concentration and distribution of cellulosic material. (F) Area under peaks between 1200 – 1000  $\text{cm}^{-1}$  indicating the concentration and distribution of carbohydrates. (G) Area under the peak at 845  $\text{cm}^{-1}$  signifying the distribution and concentration of lignin.

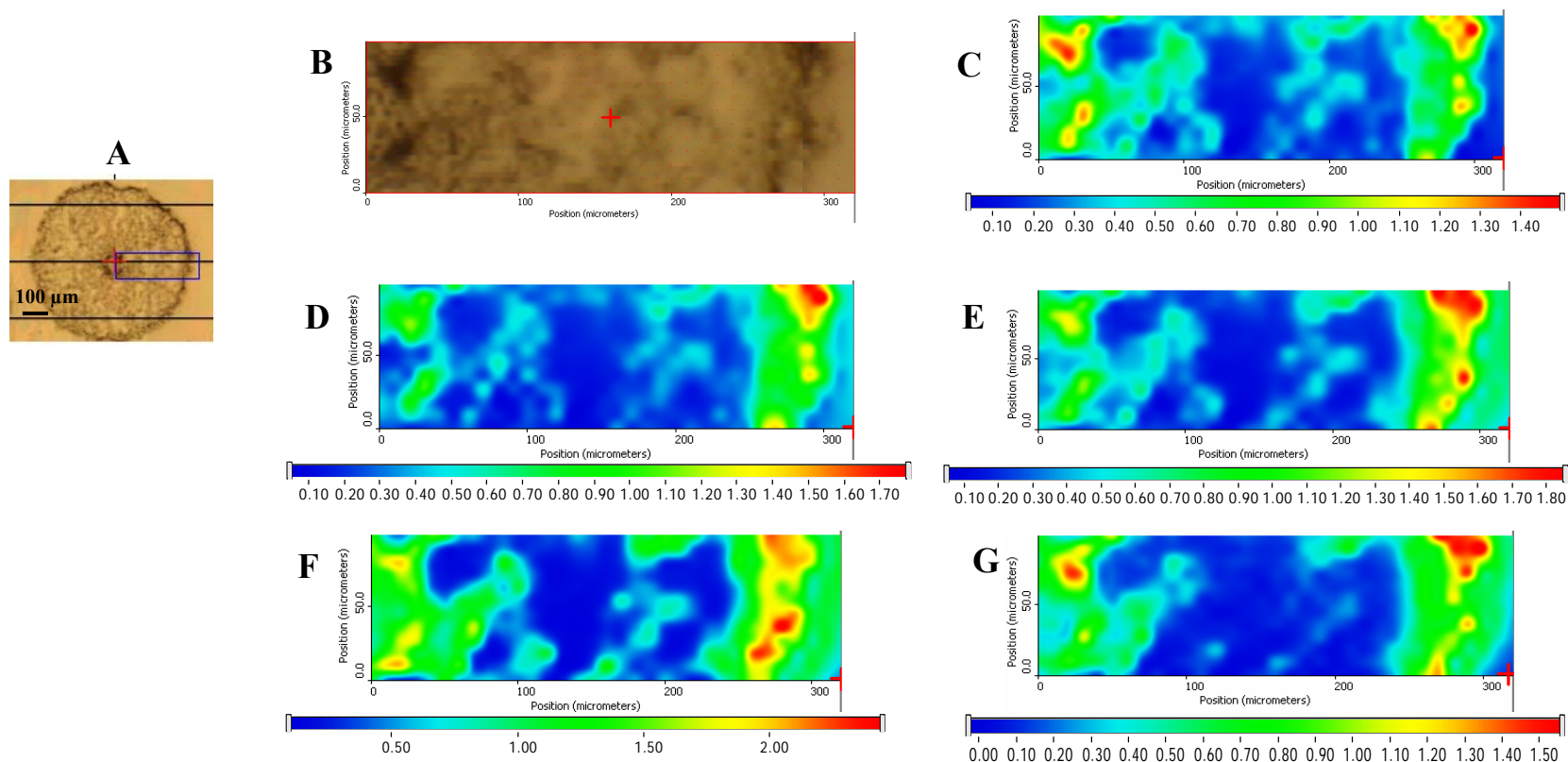


**Figure 21.** Typical spectrum of sunflower root cortex (black), epidermis (red), and phloem (blue), and xylem (green) tissue approximately 1 cm from the tip (listed bottom to top). Each spectrum is an average of 10 spectra. All spectra were normalized to the carbohydrate region between 1150 and 1000  $\text{cm}^{-1}$ . Refer to Table 3 for description of band assignments. Spectra are arbitrarily offset for ease of presentation.

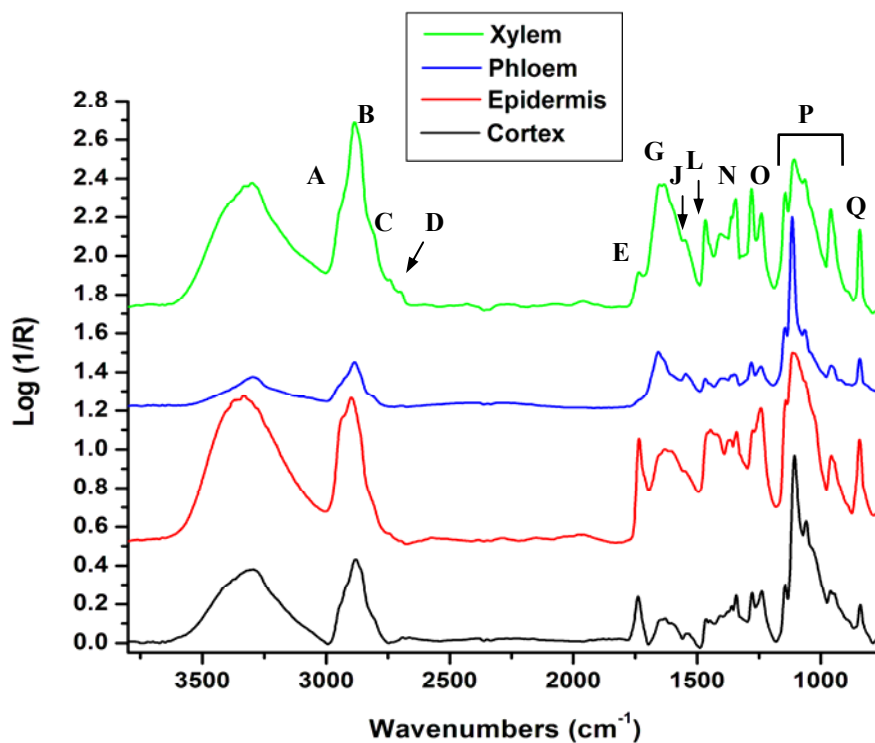


**Figure 22.** Line map and typical IR spectrum of maize root cap approximately 150  $\mu\text{m}$  from the root tip. (A) Visible image of root cap. (B) False color intensity line map of root cap. Line length: 70  $\mu\text{m}$ . The blue line indicates the line mapped starting from the right and ending on the left. (C) Intensity ruler. (D) Typical spectrum of maize root cap tissue. The spectrum is an average of 10 root cap spectra. The spectra were normalized to the OH peak at 3350  $\text{cm}^{-1}$ . Refer to Table 3 for description of band assignments.

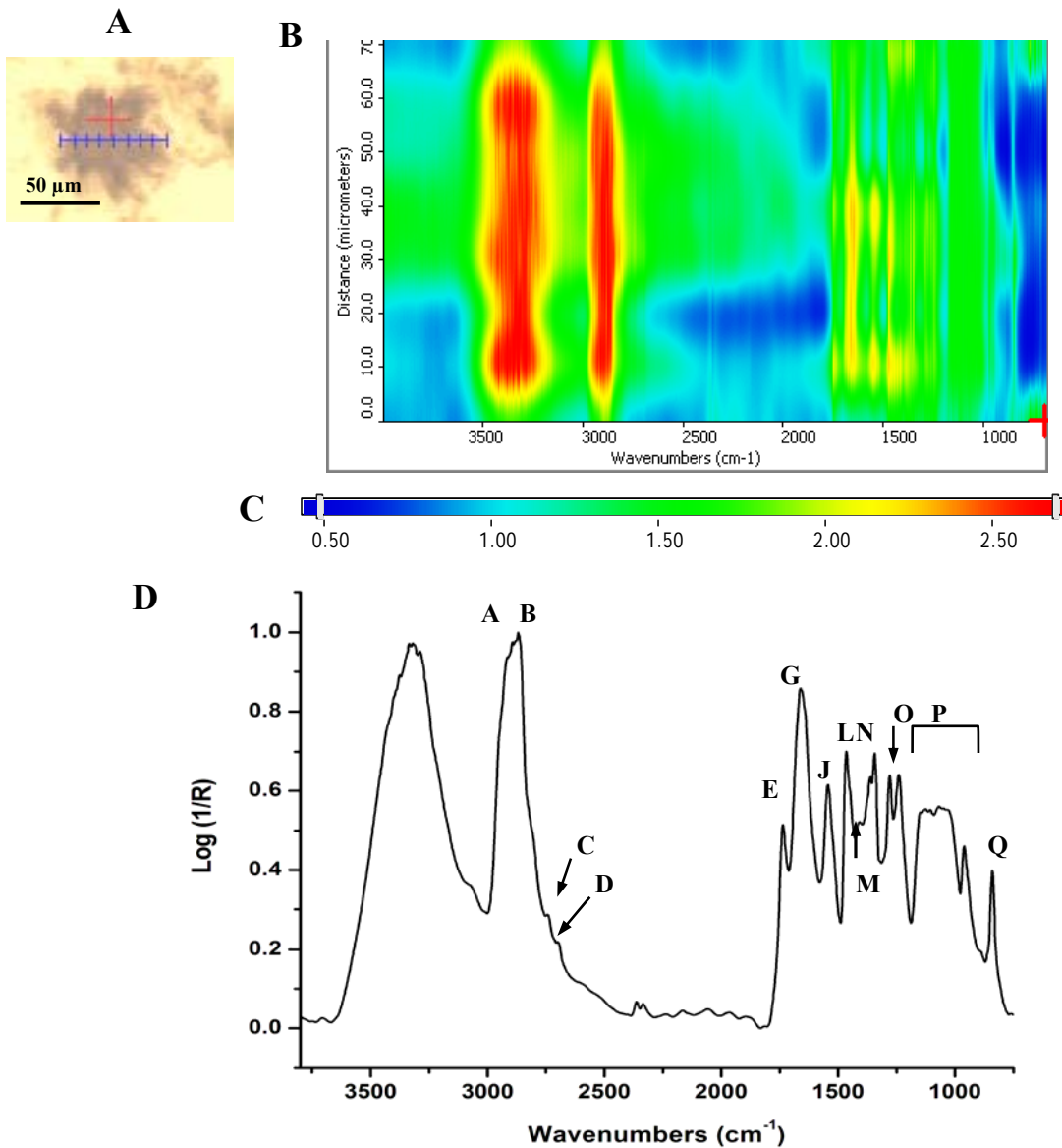


**Figure 23.** Line map and typical IR spectrum of maize root approximately 400  $\mu\text{m}$  from the root tip. (A) Visible image of root section. (B) False color intensity line map of root section. Line length: 220  $\mu\text{m}$ . The blue line indicates the line mapped starting from the right and ending on the left. (C) Intensity ruler. (D) Typical spectrum of maize root cortex (black) and epidermis (red) tissue (listed bottom to top). Each spectrum is an average of 10 spectra. The epidermis spectra were normalized to the OH peak at  $3350\text{ cm}^{-1}$  and the cortex spectra were normalized to the amide II band at  $1650\text{ cm}^{-1}$ . Refer to Table 3 for description of band assignments. Spectra are arbitrarily offset for ease of presentation.

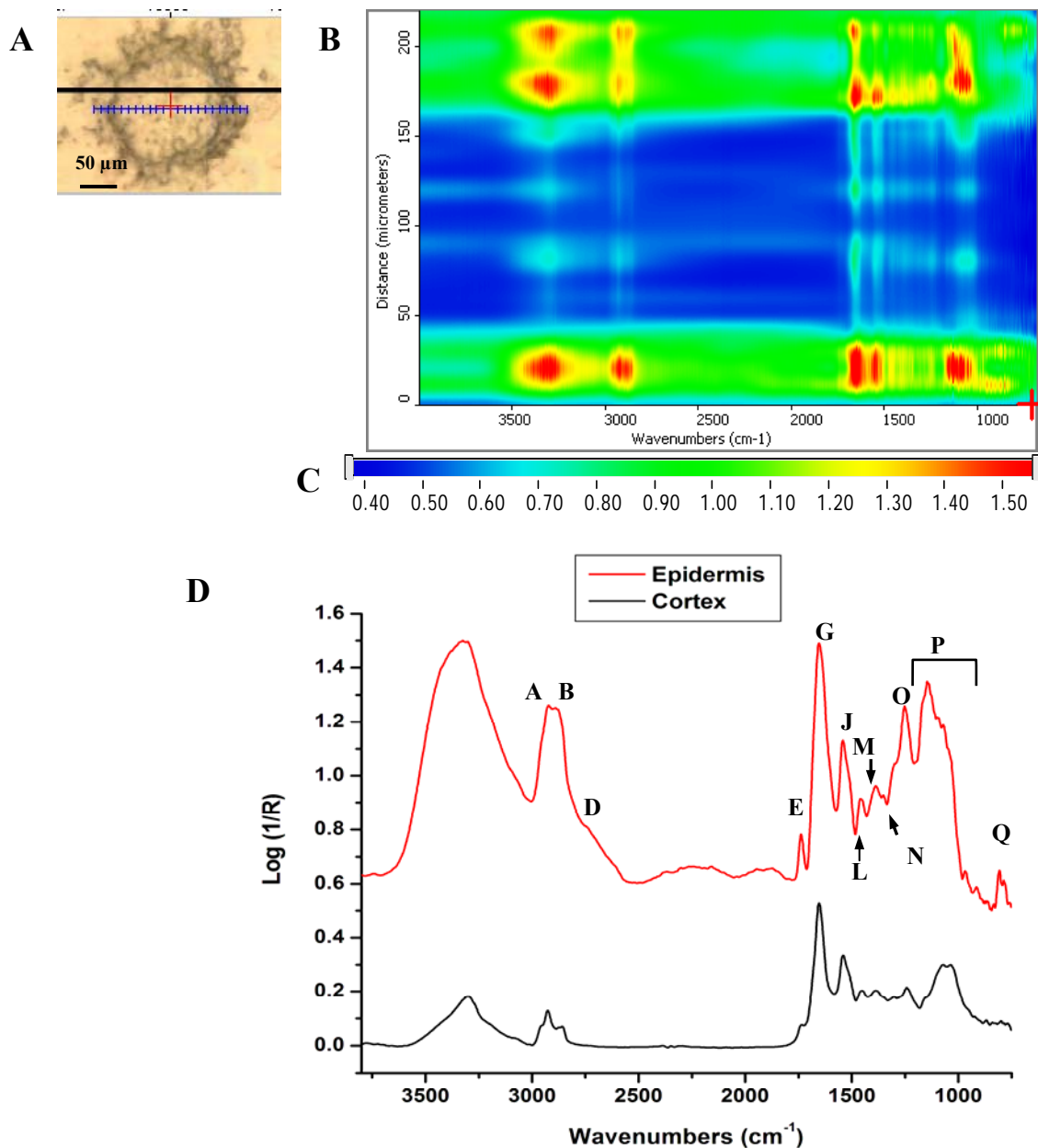


**Figure 24.** Functional group area maps of maize root tissue approximately 800  $\mu\text{m}$  from root tip. Dimensions of the area studied: 380  $\mu\text{m}$  x 45  $\mu\text{m}$ . Functional group images were produced by plotting the area under the IR spectral band as a function of the XY position. The intensity ruler is displayed under each functional group map. (A) Visible image of root section. The blue rectangle denotes the area studied (B). (C) Area under the peak centered at 1650  $\text{cm}^{-1}$  representing the protein concentration and distribution. (D) Area under the peak at 1735  $\text{cm}^{-1}$  (C=O esters) showing the concentration and distribution of lipids. (E) Area under peaks at 1240  $\text{cm}^{-1}$  indicating the concentration and distribution of cellulosic material. (F) Area under peaks between 1200 – 1000  $\text{cm}^{-1}$  indicating the concentration and distribution of carbohydrates. (G) Area under the peak at 845  $\text{cm}^{-1}$  signifying the distribution and concentration of lignin.

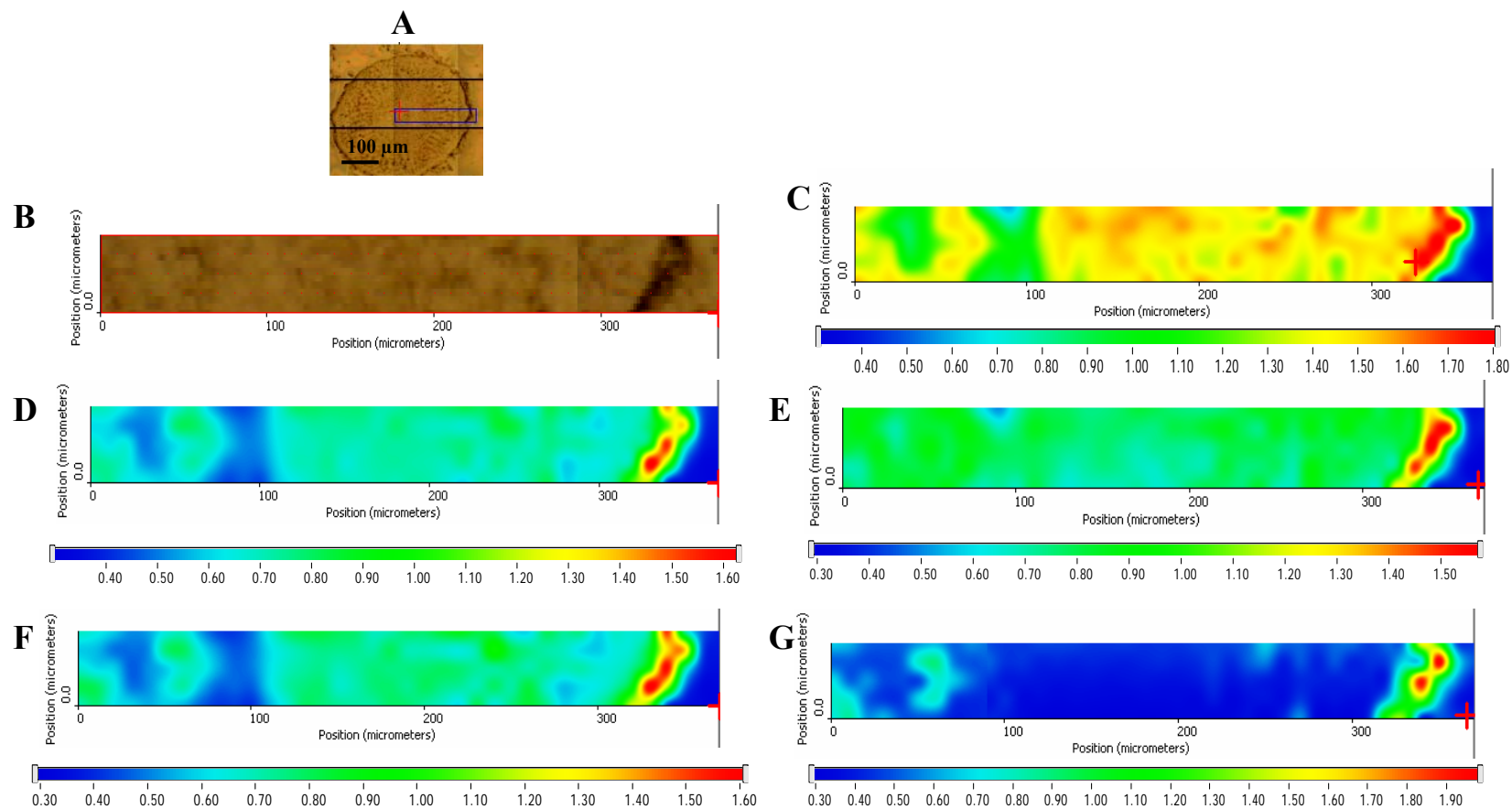


**Figure 25.** Typical spectrum of maize root cortex (black), epidermis (red), and vascular tissue (green) approximately 800  $\mu\text{m}$  from the root tip (listed bottom to top). Each spectrum is an average of 10 spectra. The epidermis spectrum was normalized to the carbohydrate region between 1150 and 1000  $\text{cm}^{-1}$ . The cortex and vascular tissue spectra were normalized to the amide II band at 1650  $\text{cm}^{-1}$ . Refer to Table 3 for description of band assignments. Spectra are arbitrarily offset for ease of presentation.

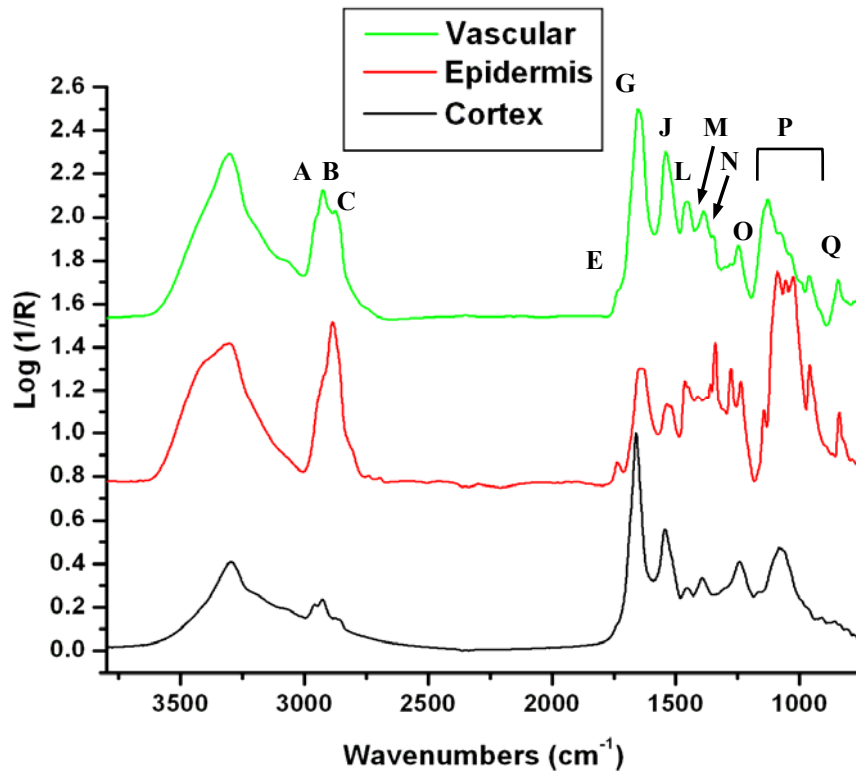


**Figure 26.** Functional group area maps of maize root tissue approximately 1 cm from the root tip. Dimensions of the area studied: 480  $\mu\text{m}$  x 50  $\mu\text{m}$ . Functional group images were produced by plotting the area under the IR spectral band as a function of the XY position. The intensity ruler is displayed under each functional group map. (A) Visible image of root section. The blue rectangle denotes the area studied (B). (C) Area under the peak centered at 1650  $\text{cm}^{-1}$  representing the protein concentration and distribution. (D) Area under the peak at 1735  $\text{cm}^{-1}$  (C=O esters) showing the concentration and distribution of lipids. (E) Area under peaks at 1240  $\text{cm}^{-1}$  indicating the concentration and distribution of cellulosic material. (F) Area under peaks between 1200 – 1000  $\text{cm}^{-1}$  indicating the concentration and distribution of carbohydrates. (G) Area under the peak at 845  $\text{cm}^{-1}$  signifying the distribution and concentration of lignin.

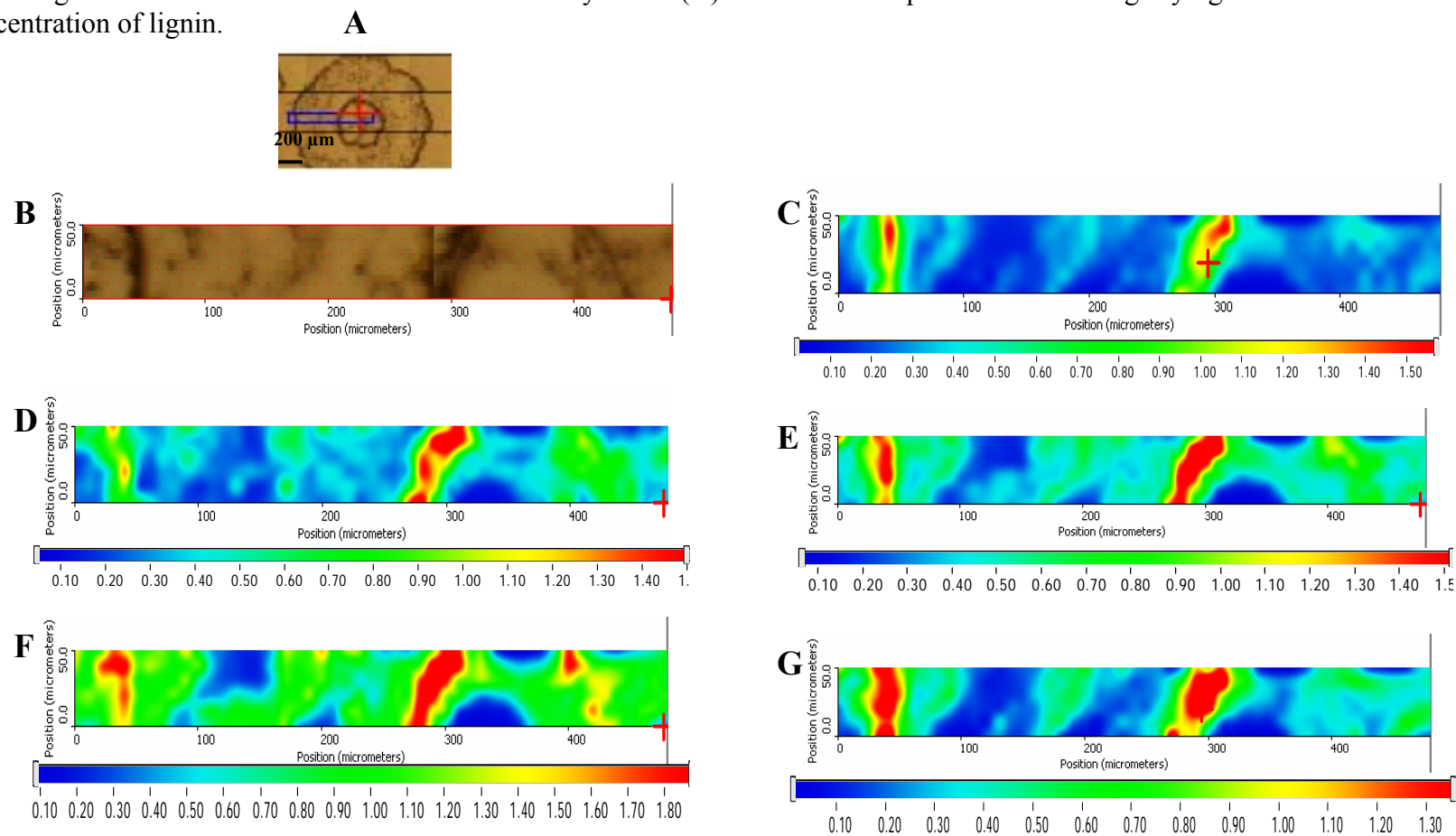




**Figure 27.** Typical spectrum of maize root cortex (black), epidermis (red), xylem tissue (green), and pith (blue), approximately 1 cm from the root tip (listed bottom to top). Each spectrum is an average of 10 spectra. All spectra were normalized to the carbohydrate region between 1150 and 1000  $\text{cm}^{-1}$ . Refer to Table 3 for description of band assignments. Spectra are arbitrarily offset for ease of presentation.

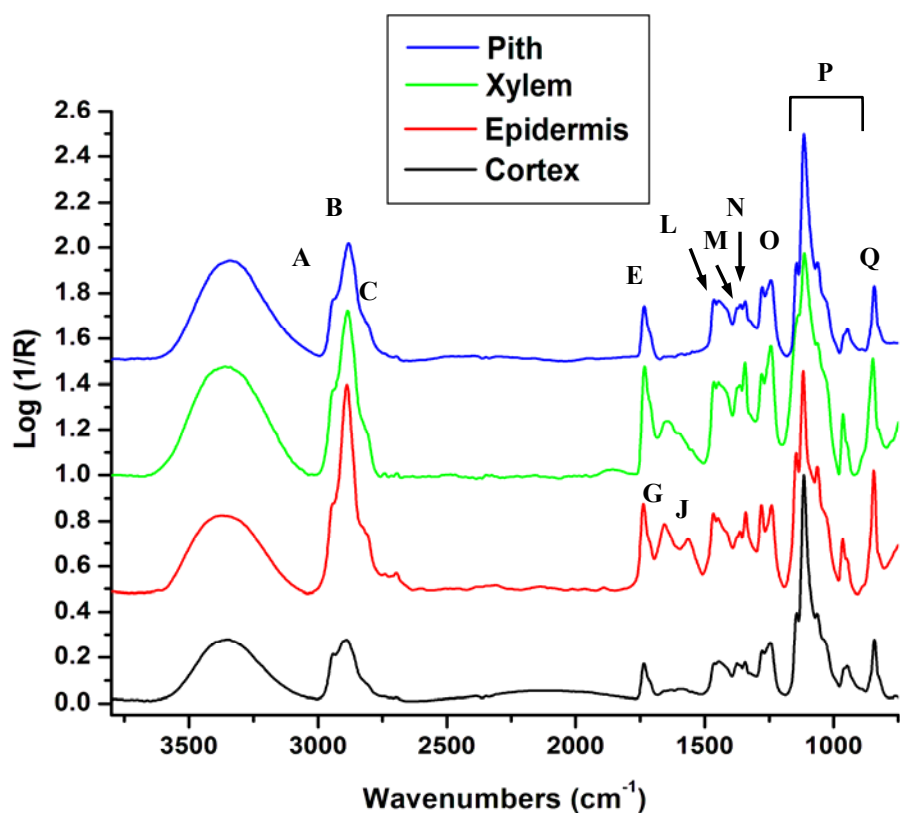


**Figure 28.** A PCA score plot shows that maize and sunflower epidermis can be separated by the first 2 PCs.

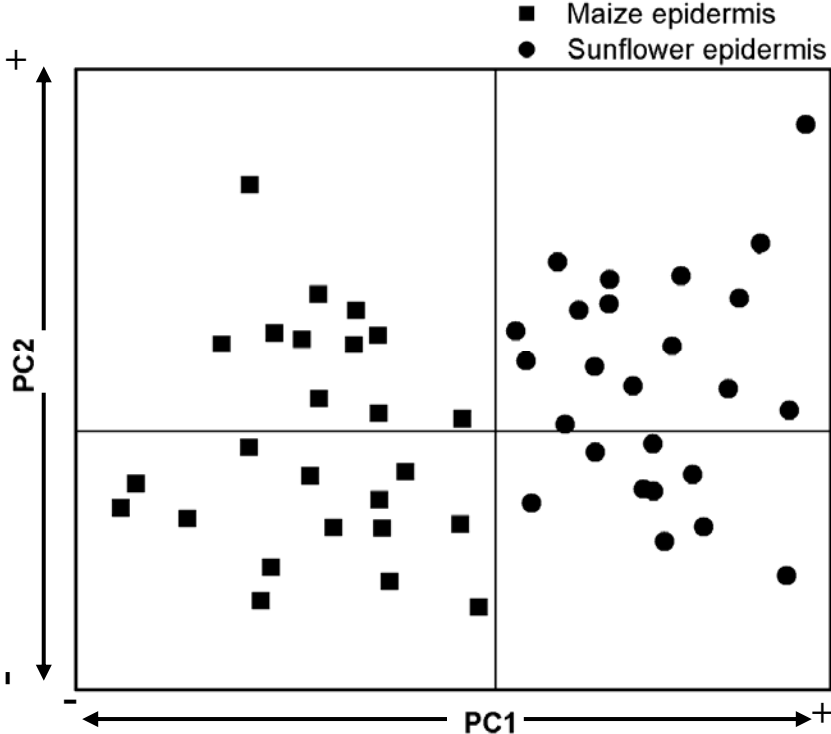


**Figure 29.** The loadings for the first (A) and second (B) principal components depicting the major variation between maize and sunflower epidermis spectra. The first principal component loading contains IR bands from all the biopolymers. The second principal component loading mostly contains peaks from the carbohydrate fingerprint, 1200 – 900  $\text{cm}^{-1}$  (band P). Refer to Table 3 for description of band assignments.

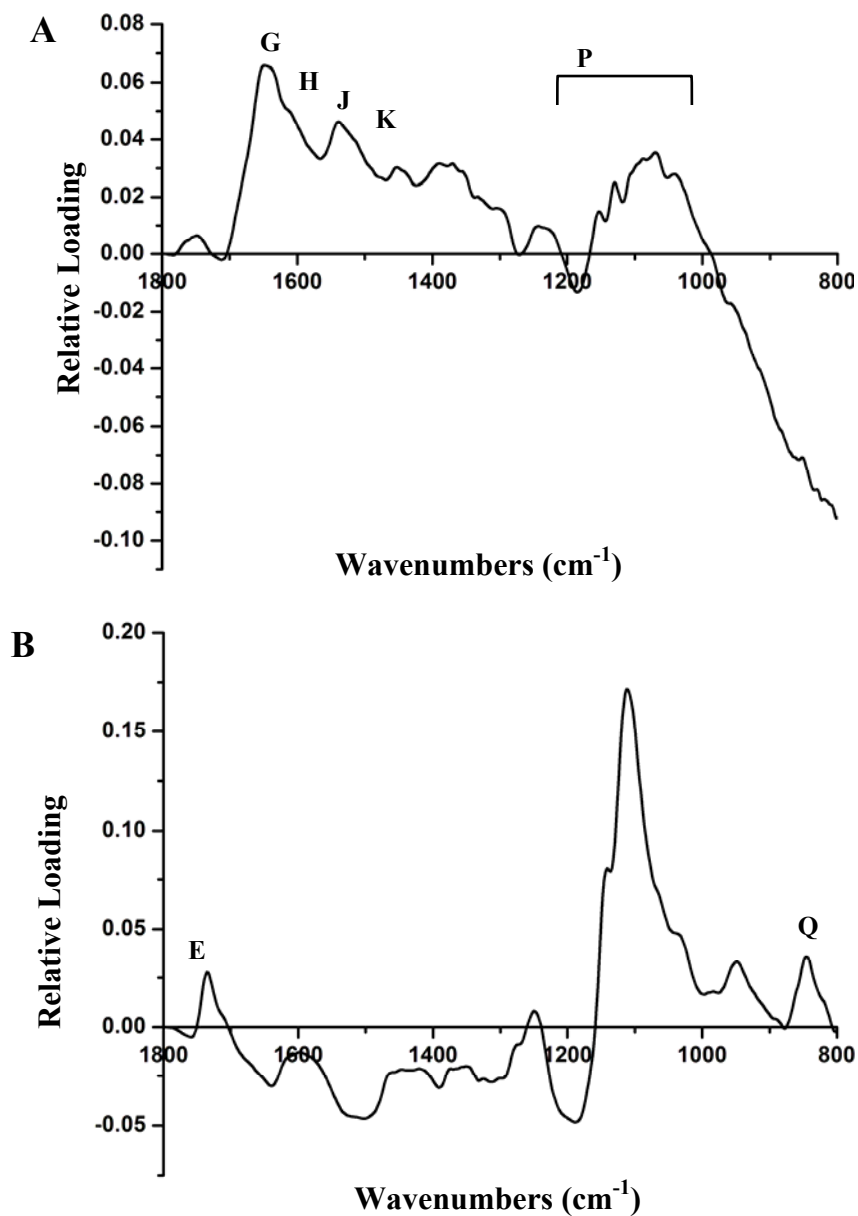


**Figure 30.** Validation plot used to test the robustness of the model set for maize and sunflower epidermis. The hollow symbols represent the (□) maize and (○) sunflower group centers. The ovals represent the 95% tolerance region. 2 observations from the sunflower test set fell outside the 95% tolerance region and were not assigned to a group.

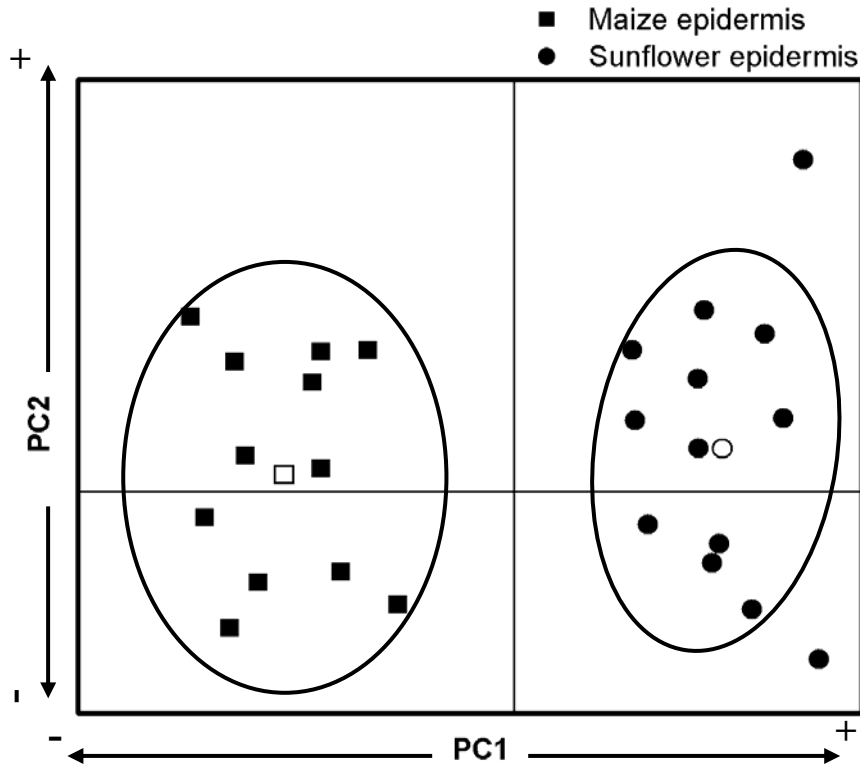


**Figure 31.** PCA score plots of using the first and second principal component (A) and the third and fifth principal component (B). There no clear separation of maize and sunflower cortex using PC1 and PC2. A good separation is achieved using the first and fifth principal component.

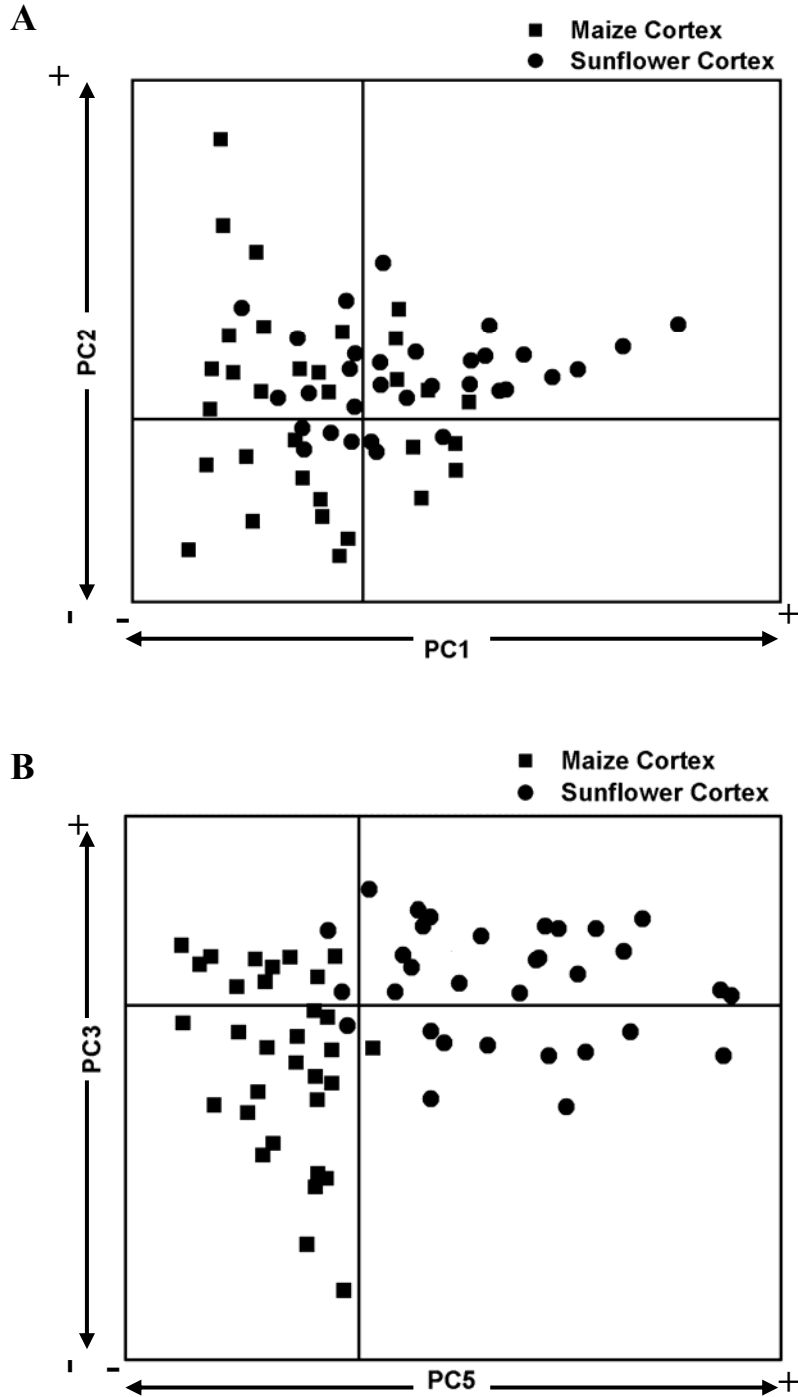


**Figure 32.** The loadings for the first (A), second (B), third (C), fourth (D), and fifth (E) principal components. The first and second principal component loadings represent a combined 85% of the spectral variability. The third, fourth, and fifth principal component loadings represent 2.88%, 1.92%, and 1.59% of the overall spectral variability. Refer to Table 3.1 for description of band assignments. The X-axis represents frequency as wavenumbers ( $\text{cm}^{-1}$ ) and the Y-axis represents relative loading.

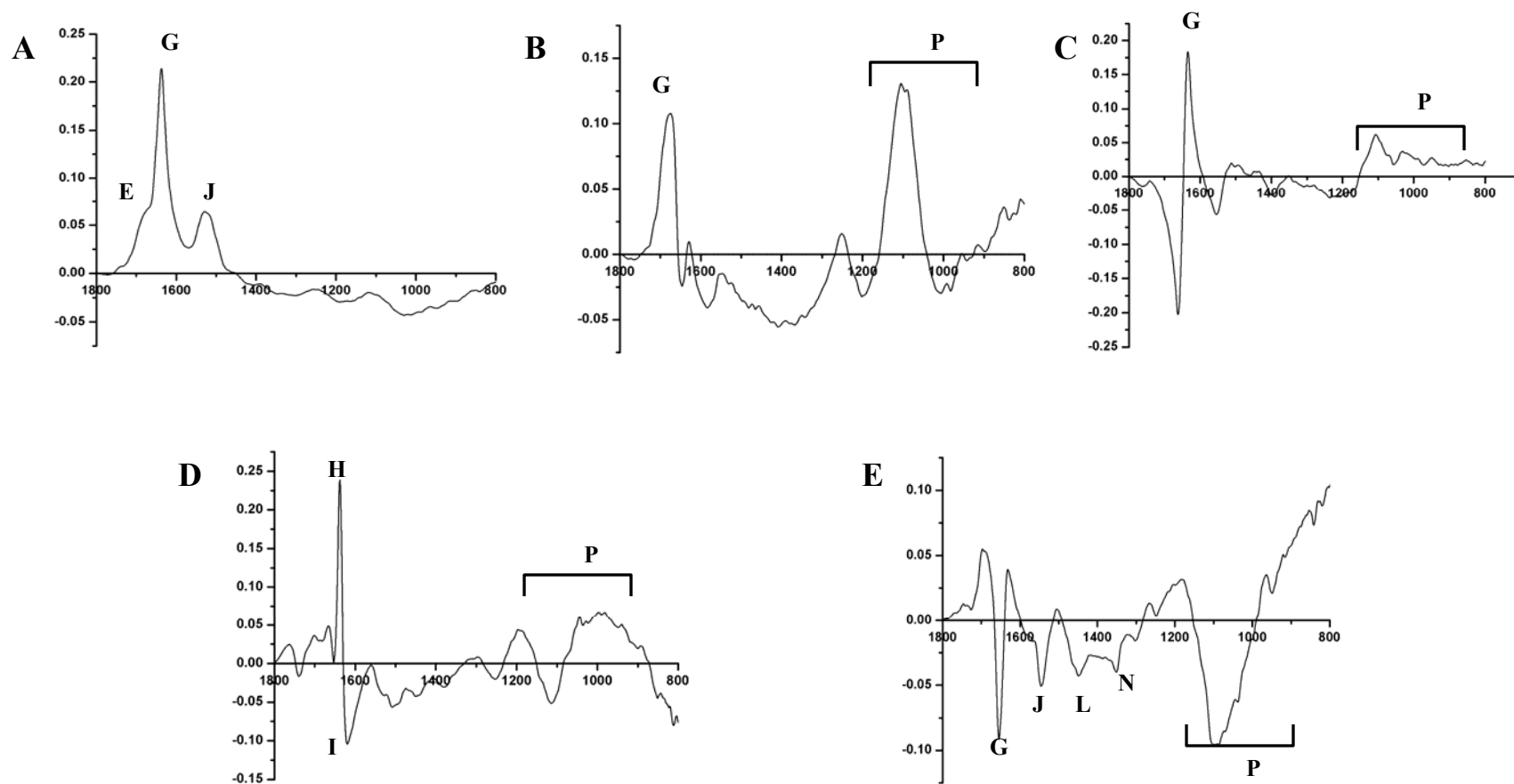


**Figure 33.** The reassignment and assignment success rates based on the number of PC scores used in LDA. Six PC scores were needed to assign 100% of the observations in the training set. 83% was the best achievable assignment rate for the test set.

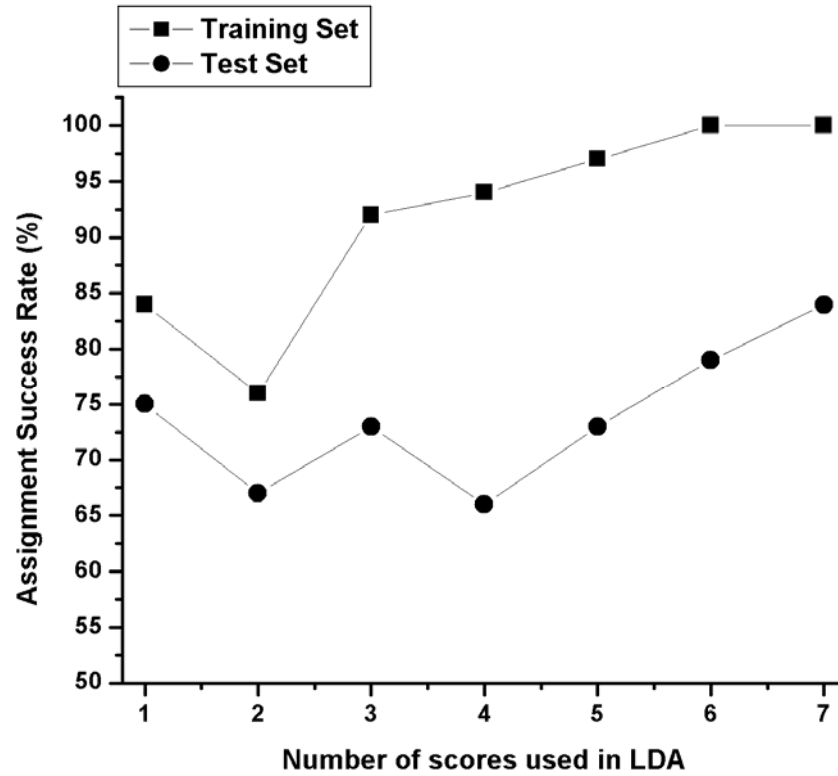


**Figure 34.** A PCA score plot shows that maize and sunflower xylem can be separated by the first 2 PCs.

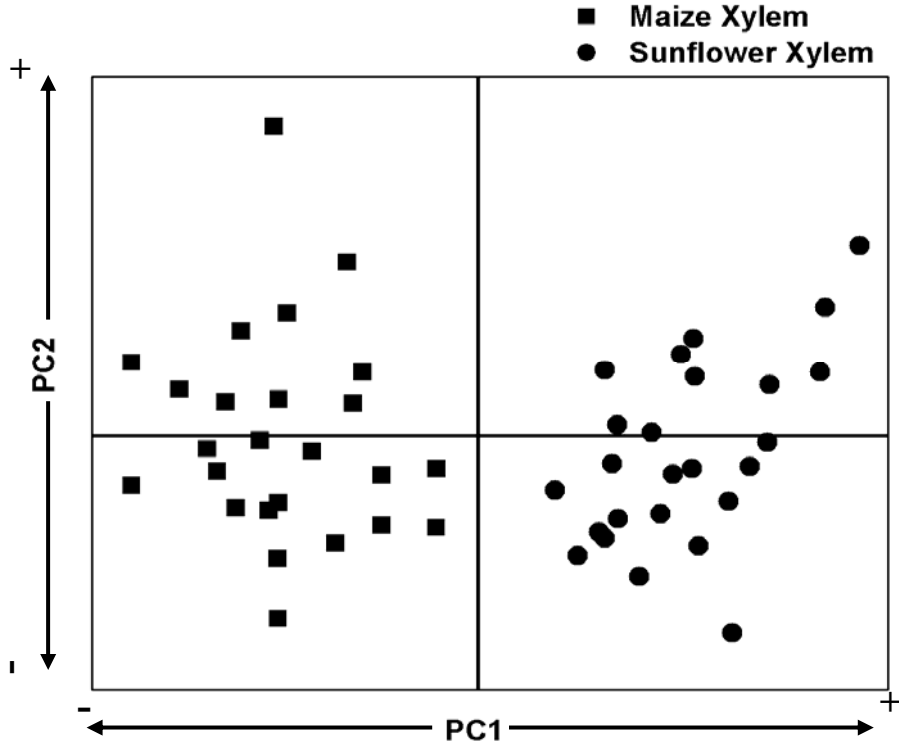




**Figure 35.** The loadings for the first (A) and second (B) principal components depicting the major variation between maize and sunflower xylem spectra. The first principal component loading contains IR bands from all the biopolymers. The second principal component loading mostly contains peaks from the carbohydrate fingerprint region (band P). Refer to Table 3.1 for description of band assignments.

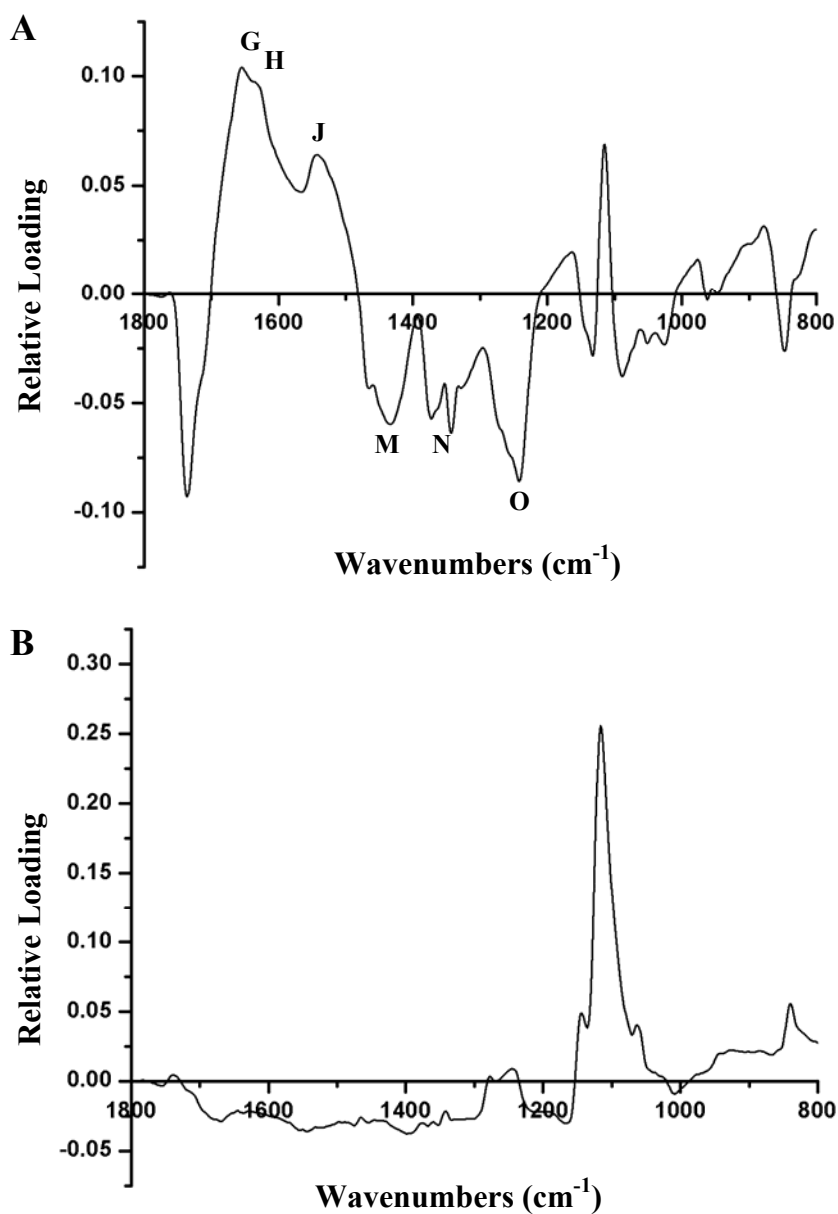
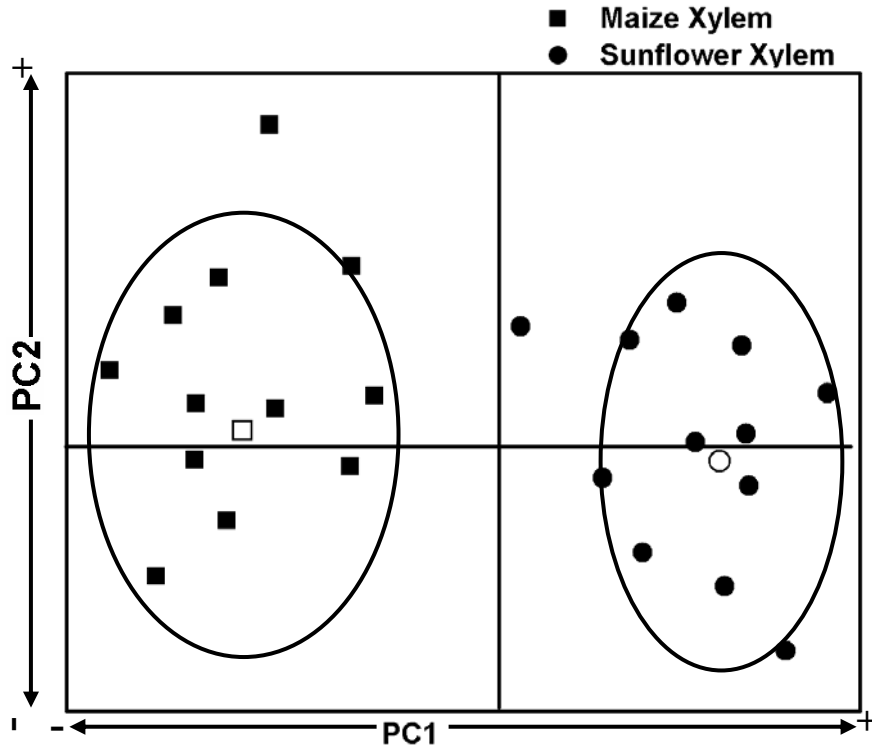


**Figure 36.** Validation plot used to test the robustness of the model set for maize and sunflower xylem. The hollow symbols represent the ( $\square$ ) maize and ( $\circ$ ) sunflower group centers. The ovals represent the 95% tolerance regions. 2 observations from each test set fell outside the 95% tolerance region and were not assigned to a group.



**CHAPTER 4 - MONITORING THE FATE AND EFFECT OF 1H-BENZOTRIAZOLE  
(BT) IN SUNFLOWER AND MAIZE PLANTS USING SR-IMS**

## Introduction

Due to the vast amount of research conducted on the uptake kinetics of BT in sunflowers by Dr. Sigifredo Castro Diaz in the laboratory of Dr. Larry Davis (Castro Diaz, 2001; 2003; Castro *et al.*, 2004a; 2004b; 2003; 2001; 2000), BT was used as the model compound to determine the potential of IR to monitor the fate and effect of organic compounds in plants. Prior to conducting studies using SR-IMS, experiments were performed on conventional FTIR and ATR instruments. The results from this work showed that it was feasible to use IR to observe the presence of the BT within the plant tissue as well as the changes to plant structure.

BT is a corrosion inhibitor commonly found in airplane deicing fluid, antifreeze, and gasoline. BTs have been detected in soil and surface and ground waters near facilities that utilize or produce them (Bausmith and Nuefeld, 1999; USEPA, 1977). BTs are toxic to many aquatic organisms and bacteria and mildly carcinogenic (N.C.I., 1978; USEPA, 1977). They are resistant to ultraviolet radiation and very soluble in water rendering them highly stable and mobile in the environment. At present, there are no known bacterial degradation pathways for BT (Young *et al.*, 2001; Rollinson and Callely, 1986). Sunflowers have shown potential for remediating BT from contaminated waters and soil (Castro *et al.*, 2004a; 2004b; 2003; 2001; 2000). To our knowledge, there has not been a previous report describing the use of maize to remediate BT. Therefore, the fate of BTs within the sunflower and maize plants are unknown. Acid and organic solvent extraction of BTs from treated sunflower plants has been unsuccessful. Studies using isotopically labeled 5-methyl-benzotriazole have shown that a large fraction is unextractable after several days of exposure, with a significant amount remaining in the root (Castro Diaz, 2003). However, previous studies provided evidence that BTs may be

incorporated into the plant structure by lignification (Castro *et al.*, 2001). Due to their aromatic structure, BTs could possibly be biotransformed by the sunflower and mimic the phenylpropanoid subunits that constitute lignin. Lignin has been widely studied by FTIR due to its negative impact on paper pulping and forage digestibility (Akin *et al.*, 1993; Jung and Deetz, 1993; Thomas, 1970). This provides the ability to determine spectral differences in the lignin portion of the plant cell wall sunflowers that are treated with BT. Our working hypothesis is that the peroxidatic system responsible for lignification ultimately incorporates benzotriazole into a polymeric material that is no longer bioavailable. This chapter will discuss how the combination of synchrotron FTIR microspectroscopy and PCA can be used to determine the location where BT is being sequestered within the root tissue, as well as how the structure of the plant root is altered due to exposure to BT.

## **Results and Discussion**

### *Uptake of BT by maize and sunflower plants*

After the two-week growth period, HPLC analysis revealed the disappearance of BT from all the growth solutions containing 10, 20, and 30 mg/L BT as seen in Table 4. A fraction of BT was not absorbed from growth solutions containing 60, and 90 mg/L BT. On average, sunflowers were able to uptake about 48% and 13% of the BT from hydroponic solutions containing 60 and 90 mg/L BT, respectively. Maize plants were slightly more tolerant of the higher concentrations, absorbing 56% and 28% of the BT from the 60 and 90 mg/L BT solutions. No polar UV detectable byproducts that the plants may have produced, as a consequence of the BT treatment, were observed. These results, together with the growth rate and solution uptake data, were similar to that observed in previous growth experiments by

Castro *et al.* (2004a; 2004b; 2003; 2001; 2000). At low concentrations, BT disappeared from the growth solutions and BT was unextractable from sunflower roots (Castro, 2003). This provided evidence that BT was irreversibly bound or chemically incorporated into the roots. Due to these data it was assumed that the BT had remained in the roots of the sunflower plants (this was also assumed for maize plants in this study) (Castro *et al.*, 2003; Dokken *et al.*, 2002). The amount of BT present in the dry roots of maize and sunflower plants can be observed in Table 4. The amount of BT in the dry root was highest in both maize and sunflower plants treated with 30 mg/L BT, resulting in 3.5% and 3.8% of the total root weight, respectively.

#### *Conventional FTIR and ATR spectroscopy of BT in Dried Sunflower Root Tissue*

The FTIR spectrum of BT seen in Figure 37 resembles previously reported spectra by Mohan and Settu (1993). The absorbance bands at 1208, 775, 745, and 739  $\text{cm}^{-1}$  are of particular importance due to their high intensity. These bands represent C-H in-plane and out-of-plane bending for the benzene ring of BT as seen in Table 5. Since these bands are highly intense they should be easily seen in sunflower plants treated with BT. Absence of these peaks may suggest that the sunflower plant could have transformed BT in some manner. This is a definite possibility because the BT could not be extracted from treated dry plant matter as mentioned previously.

Obvious spectral differences between untreated and treated root samples with various concentrations of BT can be observed in Figure 38. The disappearance of the intense peak at 1208  $\text{cm}^{-1}$  is quite noticeable. Spectral subtraction of untreated root sample from the treated root samples did not yield a peak at 1208  $\text{cm}^{-1}$ , further suggesting a change in the BT structure upon absorption by the sunflower plant. However, the appearance of peaks at around 745  $\text{cm}^{-1}$

in the treated samples does represent a part of BT that may have not been modified by the plant. The other interesting point to notice is the concentration dependence in absorption intensity at  $745\text{ cm}^{-1}$  (Figure 38). The absorption intensity increases as the concentration of BT increases. The disappearance of the peak at  $870\text{ cm}^{-1}$ , representing an aromatic C-H wag of lignin, may imply that the plant structure is changed when treated with higher concentrations (60 and 90 mg/L) of BT.

A simple experiment can be conducted in order to determine if the sunflower plant actually biotransforms BT. Dried untreated root samples can be spiked with BT and subsequently be analyzed by FTIR. The results of this procedure can be observed in Figures 39A and 39B. The  $1208\text{ cm}^{-1}$  and  $775\text{ cm}^{-1}$  bands represent C-H in-plane and out-of-plane bending for the aromatic ring in BT both appear in the spiked sample. Also, the lignin peak at  $870\text{ cm}^{-1}$  still can be observed (Figure 39) within the spiked sample as well. Upon spectral subtraction of the untreated root sample and spiked sample, a spectrum that is similar to BT is produced. This provides further evidence that the BT is being transformed by the sunflower plant. Standard FTIR spectroscopic analysis of ground sunflower root material spiked with BT also revealed that BT was easily detected at levels as low as 0.5% of the dry root material (Dokken *et al.*, 2002). This indicated that it is feasible to use synchrotron FTIR microspectroscopy to search for the presence of BT in the sunflower and maize root sections.

Using ATR spectroscopy, fifty-eight spectra were recorded from individual botanical parts of dissected primary and secondary roots grown in 0, 30, 60, and 90 mg/L BT. The most obvious spectral changes were found in the xylem of the secondary root specimens contaminated with 60 mg/L of BT. Four out of five of the 60 mg/L treated samples exhibited a peak at  $749\text{ cm}^{-1}$  (Figure 40), similar to the peak at  $745\text{ cm}^{-1}$  peak found in the KBr pellets of

secondary root spectra from sunflower plants grown in the presence of 60 mg/L BT. Among the dissected primary roots analyzed by ATR spectroscopy, only one specimen displayed the 749  $\text{cm}^{-1}$  peak in a more subtle, but nevertheless distinct form as shown in Figure 41. The results of both conventional IR and ATR spectroscopy show that it is feasible to use SR-IMS to monitor the fate and effect of BT or other organic compounds in plants.

#### *SR-IMS of sunflower root tissue exposed to BT*

The typical spectra of untreated control, 10 mg/L BT treated, and 30 mg/L treated sunflower root sectioned at 400  $\mu\text{m}$  can be seen in Figure 42. The spectrum for each sample is an average of ten spectra taken from arbitrarily selected transect of the root sections. The main changes that can be seen in the spectra of untreated and BT treated root tissue are at 795  $\text{cm}^{-1}$ , 1000-1100  $\text{cm}^{-1}$ , and 1265  $\text{cm}^{-1}$ . The appearance of a peak at 795  $\text{cm}^{-1}$  is especially interesting because it is a characteristic peak of BT representing out-of-plane bending of the C-H groups on the aromatic ring (Mohan and Settu, 1993). This is an indication that the aromatic ring of BT stayed intact upon incorporation into the sunflower plant tissue. It also provides additional evidence that BT may be incorporated into sunflower tissue by lignification because the main components of lignin are aromatic in nature. Of greater significance is the appearance of a commonly observed characteristic lignin peak at 1265  $\text{cm}^{-1}$  peak signifying C=O stretch from the guaiacyl ring (Faix, 1992). The lignin peak appears as a sharp peak at 1265  $\text{cm}^{-1}$  with a shoulder at 1240  $\text{cm}^{-1}$ , indicative of cellulose, in the presence of BT. In the absence of BT, only a broad band at 1240  $\text{cm}^{-1}$  representing cellulose is observed. This may indicate an uncharacteristic distribution of lignin or lignin monomers not commonly seen in the cortex of sunflowers at 400  $\mu\text{m}$  from the root tip. It is known that uncharacteristic lignin formation



commonly occurs in response to mechanical damage induced by pathogen attack (Vance *et al.*, 1980), so it may possible that lignification could be induced by exposure to organic contaminants. An increase in intensity and shape of the carbohydrate fingerprint region at 1200 – 900  $\text{cm}^{-1}$  can also be observed in Figure 42, indicating either an increase in the production of polysaccharides, a change in the type of polysaccharides, or different cross-linking of the polysaccharides or a combination of all these changes.

To obtain a better picture of the distribution of the incorporated BT, we took IR maps of cross sectioned root tips from untreated and BT treated sunflowers using a  $12 \times 12 \mu\text{m}$  aperture. Figures 43A – C show the visible image of the cross sectioned root tips from untreated, 10 mg/L BT treated, and 30 mg/L BT treated sunflower plants, respectively. The blue rectangle in each root cross section denotes the area that was mapped using the Atlus mapping software. Figures 43D – F show the functional groups maps of untreated and BT treated sunflower root tissue. The spatial distribution of BT is scattered in high concentrations throughout the cortex or vascular region and evenly distributed at a lower concentration in the epidermis of 10 mg/L BT treated (Figure 43E) and 30 mg/L BT treated (Figure 43F) root sections. (Blue denotes little or no concentration and red denotes high concentration in the functional group maps. Refer to the intensity ruler under each functional group map.) This patchy distribution of BT in the cortex may be due to the location in which the root was sectioned. These particular sections are from the region that is less than  $400 \mu\text{m}$  from the root tip which contains unorganized vascular tissue. Previous results have shown that incorporated BT was predominantly found in the xylem region in sections taken more than  $800 \mu\text{m}$  from the root tip (Dokken *et al.*, 2004). The appearance of blue color throughout the entire functional group map of the untreated control (Figure 43G) obviously indicates the lack of the BT band at  $745 \text{ cm}^{-1}$ . There are two small red

areas that probably indicate noise or a bad scan. The intensity ruler shows that both areas are of low in intensity (0.3 maximum). A uniform distribution of protein (amide I band at  $1650\text{ cm}^{-1}$ ) is observed throughout the vascular region in the untreated control (Figure 43G). The 10 mg/L BT treated (Figure 43H) and 30 mg/L (Figure 43I) displayed substantially diminished concentration of proteins throughout the vascular region with scattered areas of high concentration. This difference in protein distribution was not initially obvious by visual inspection. However, by using principal components analysis (PCA), we were able to resolve this difference.

To determine the major variability between the untreated control and BT treated sunflower roots, we arbitrarily selected 60 spectra (observations) from the cortex (vascular region) of the function group map data sets of 10 mg/L and 30 mg/L BT treatments and the untreated control for a total of 180 observations. Exploratory PCA resulted in separation of the untreated control from the 10 mg/L BT treated and 30 mg/L BT treated observations using the first 2 PC scores (Figure 44). Also, 178 out of 180 observations were correctly assigned to their treatment group, establishing a model set. To establish a validation set, linear discriminant analysis (LDA) using the Mahalanobis distance metric was performed on 60 observations arbitrarily selected from independent samples (20 samples for each treatment). Using the first 2 PC scores, 54 out of 60 observations were correctly assigned to their treatment group (Figure 45). The first PC (Figure 46A) and second PC (Figure 46B) loadings accounted for 75% and 14% (total 89%) of the spectral variability between the untreated and BT treated samples. This spectral variability of the first PC loading was predominantly attributed to protein, represented by peaks at  $1650$  and  $1553\text{ cm}^{-1}$ , and the characteristic BT peak at  $745\text{ cm}^{-1}$ . There were some minor contributions by peaks in the carbohydrate region,  $1102$  and  $1039\text{ cm}^{-1}$ , and  $1265\text{ cm}^{-1}$ , a

characteristic lignin peak. It may also be noted that the IR peak at  $1039\text{ cm}^{-1}$  may also be indicative of lignin; as it represents aromatic C-H in-plane deformation of the guaiacyl ring. The second PC loading was also dominated by the aforementioned peaks with more emphasis found in the carbohydrate region and the characteristic lignin peak.

PCA showed obvious separation of the untreated and BT treated samples and the robustness of the model set was 90%. The overwhelming presence of the characteristic BT peak at  $749\text{ cm}^{-1}$  in the IR spectra and PC loadings revealed that BT had been incorporated into the plant structure. Moreover, since this peak represents aromatic C-H out of plane bending, it can be concluded the aromatic ring of BT was not broken upon integration into the plant tissue. Treatment with BT appeared to cause damage to proteins and/or altered their production in the plant tissue, and to facilitate carbohydrate production. The  $1265\text{ cm}^{-1}$  lignin peak appeared in the PC loadings and there was sharpening of this peak in the IR spectra of the BT treated samples.

It was critical to further analyze root tissue at distances greater than  $400\text{ }\mu\text{m}$  from the root tip for the presence of BT. Upon further inspection, BT was found in the xylem tissue of roots treated with  $30\text{ mg/L}$  BT approximately  $1\text{ cm}$  from the root tip. Functional group maps showing the spatial distribution of BT in the xylem of root sections from untreated and BT treated plants sectioned at  $1\text{ cm}$  from the root tip are shown in Figure 47. The  $745\text{ cm}^{-1}$  functional group map for untreated xylem tissue (Figure 47C) is predominantly blue, signifying little or no intensity for this particular peak. There are two small spots representing some intensity but it is probably due to noise since the maximum intensity only reaches 0.3 (see intensity ruler). A similar result was seen in the xylem of two other root sections from untreated plants. Figure 47D shows scattered areas of high concentration of BT in the xylem of  $30\text{ mg/L}$

BT treated sunflower. This type of distribution was seen in three out of four root sections from 30 mg/L BT treated sunflowers. Figure 48 shows the spectra for the xylem tissue from sections of the untreated control and 30 mg/L BT treated sunflower plants. The BT peak appears at  $745\text{ cm}^{-1}$  in the xylem tissue of the 30 mg/L BT treated plant. The other significant differences that can be seen in the spectrum of xylem tissue from BT treated roots are related to lignin. The huge increase of the peak at  $1265\text{ cm}^{-1}$ , which represents carbonyl stretching, may be due to an increase in the guaiacyl-syringyl subunits of lignin (Faix, 1992; Hergert, 1971). In fact, it can be observed that the IR bands that represent polysaccharides and cellulose in the untreated root tissue have been overwhelmed by the  $1265\text{ cm}^{-1}$  peak in the BT treated root tissue. Also, significant changes to the carbohydrate fingerprint region ( $1200 - 900\text{ cm}^{-1}$ ) were observed suggesting that treatment of the plant with BT causes damage or hinders production of certain polysaccharides. A shoulder at  $1608\text{ cm}^{-1}$  which represents C=O stretch of the guaiacyl ring commonly found in lignin spectra (Faix, 1992), and an increase in peak intensity at  $821\text{ cm}^{-1}$  combined with a shoulder at  $845\text{ cm}^{-1}$  further suggests an increase in lignin production or a different type of substitution of the subunits in lignin.

The xylem of plant roots is the conduit in which nutrients are transported from the roots into the upper tissues of the plant. It is also the site of abundant lignin production. Lignin is a highly substituted polymer composed of monolignols produced by the phenylpropanoid pathway which is produced as reinforcement for vascular tissues in herbaceous plants and grasses (Waisal *et al.*, 1996). The biosynthesis of lignin takes place by coupling of monolignol subunits through a free radical, nonenzymatic process (Faix, 1992). With this in mind, it is very significant that the most prominent changes in the roots of benzotriazole treated plants are found in the xylem tissue, and it is the area where the intense benzotriazole peak can be found.

This may confirm a previous speculation that benzotriazole is sequestered in the xylem and then incorporated into lignin via the phenylpropanoid pathway rendering benzotriazole no longer bioavailable (Dokken et al., 2002). This scenario is highly possible since other aromatic compounds, such as 2,4-dichlorophenol, have been found to irreversibly bind to lignin residues (Pogany *et al.*, 1990).

#### *SR-IMS of maize root tissue exposed to BT*

To better understand the ability of SR-IMS to monitor changes to plant structure due to exposure to organic contaminants; it is crucial that a different plant be studied. Maize was utilized because it is a common agricultural plant that is often exposed to organic contaminants and serves a model organism for monocots, especially since its genome has been sequenced. A survey of maize root tissue from plants treated with BT using SR-IMS did not yield the same results observed in the sunflower root tissue. There was no evidence of the 745  $\text{cm}^{-1}$  peak (C-H in-plane bending of aromatic ring in BT) in any structural component of the maize root tissue. This suggests that maize metabolizes BT in a different manner than sunflowers. However, the exposure to BT did cause changes to the structure of the maize root tissue.

Exploratory PCA was conducted on spectra extracted from line or area maps of the root cortex sectioned at 400  $\mu\text{m}$  from the root tip of untreated and 90 mg/L BT treated maize plants. Twenty-six spectra from each treatment were sampled for the analysis. The PC score plot depicts in Figure 49 shows separation of the untreated and 90 mg/L BT treated cortex tissue using the first two PCs. The first PC accounted for about 73% of the total spectral variation while the second PC accounted for 16.5% of the variability (total of 89.5%). The first PC loading (Figure 50A) contained peaks representing lignin at 1635  $\text{cm}^{-1}$  and 1513  $\text{cm}^{-1}$ , protein

at  $1549\text{ cm}^{-1}$  (amide II), and polysaccharides at  $1126$  and  $1008\text{ cm}^{-1}$ . This large negative lignin peak at  $1635\text{ cm}^{-1}$  provided evidence that the cortex of the  $90\text{ mg/L}$  BT treated maize plant was more lignified than the untreated control plant. The second PC loading seen in Figure 50B displayed positive IR peaks at  $1653\text{ cm}^{-1}$  representing amide I band of proteins and a carbohydrate band at  $1083\text{ cm}^{-1}$ . The presence of positive IR bands for protein in the first and second PC loadings suggests that BT causes protein damage or alters the production of protein in maize plants. A similar effect was observed earlier in the cortex of sunflower tissue.

Figure 51 shows the PC score plot from exploratory PCA of root epidermal tissue from untreated and  $90\text{ mg/L}$  BT treated maize plants. Twenty spectra from each treatment were arbitrarily extracted from line or area maps. The first two PCs were able to separate the two sample groups with the first PC accounting for almost 80% of the overall spectral variability. The first PC loading shown in Figure 52A is dominated by negative peaks diagnostic for lignin at  $1638\text{ cm}^{-1}$ ,  $1600\text{ cm}^{-1}$ , and  $1515\text{ cm}^{-1}$ . As in the case of the cortex, BT caused increased lignification in the maize epidermis. Spectral features indicative of pectic polysaccharides and arabinogalactan can be seen in the second PC loading (Figure 52B) suggesting a decrease in the production of these polysaccharides in the epidermis. The increased lignification may have caused changes to the cross-linking of the polysaccharides altering the cell wall structure of the epidermis. Further evidence of increased lignification due to treatment with BT can be seen in Figure 53, which displays the functional group area maps showing the spatial distribution and concentration of lignin or lignin components in cross sections of maize roots  $400\text{ }\mu\text{m}$  from the tip. The amount of lignification increases as the concentration of BT the maize plants are exposed to increases. There is very little change in the spatial distribution and concentration of lignin between the untreated (Figure 53A) and  $30\text{ mg/L}$  BT treated (Figure 53B) root tissue. In

both cases, the spatial distribution of lignin was limited to the epidermis, as the epidermis in the roots of untreated control plants possesses lignin. However, once the BT concentration was increased to 60 and 90 mg/L, lignin was found in the cortex tissue and in the epidermis at higher concentrations. It is uncharacteristic for maize to possess lignin in the cortex especially at 400  $\mu\text{m}$  from the root tip.

It is clear that increased and uncharacteristic lignification occurs in both sunflower and maize roots when exposed to BT. However, it is not certain whether the lignification is a means to metabolize BT or a consequence of BT exposure. It may be possible that exposure to certain organic contaminants may activate genes that regulate lignification as a defense mechanism similar to that against a pathogen attack (Vance *et al.*, 1980). Stunted root growth and radial swelling were some common symptoms observed in the plants exposed to higher concentrations of BT. Similar effects have been noted in ectopic lignification mutants of arabidopsis, like *pom1-2* (polarity misplaced) (Hauser *et al.*, 1995; Rogers and Campbell, 2004). In fact, Mouille *et al.* (2003) were able to successfully identify and classify cell wall mutants (including several lignin mutants) of arabidopsis using FTIR microspectroscopy and PCA.

The characteristic BT peak at  $745\text{ cm}^{-1}$  was most often found in the vascular tissue and xylem of sunflower roots. Since lignification commonly occurs in this area we hypothesize that the BT is incorporated into lignin. The IR data shows that a change in the lignin structure occurred in the roots of BT treated sunflowers. This could be a consequence of incorporation of BT into lignin which would change the linkages that are commonly found between the monlignols of lignin. It is also important to note that the presence of the characteristic  $745\text{ cm}^{-1}$

implies that the aromatic ring of BT was not broken. However, at this point there is no evidence indicating the state of the triazole ring or the overall final state of BT in sunflower root tissue.

The absence of a characteristic BT peak in the root tissue of BT treated maize plants suggests that maize metabolizes BT by a method different from sunflower plants. The uptake data in Table 4 did show that maize plants were more tolerant of BT at all concentrations, particularly at 60 and 90 mg/L BT. Ectopic lignification was observed in the cortex of BT treated maize roots. However, the structure of the maize lignin did not seem to be altered meaning that abnormality of the lignification was not in the structure but rather the location. At this point, it can be concluded that maize copes with BT contamination in a manner different from sunflowers, but the final fate and form of BT in maize tissue is still uncertain.



**Table 4.** Uptake of BT by maize and sunflower plants exposed to various concentrations of BT for a 2 week growth period.\*

<b>Plant</b>	<b>BT conc. (mg/L)</b>	<b>% BT disappearance</b>	<b>mg BT/g per dry plant</b>	<b>% BT in dry root</b>
Sunflower	10	100	15.74±1.04	0.9
	20	100	32.70±1.93	2.2
	30	100	47.40±2.40	3.5
	60	48.4±8.24	28.36±3.74	2.7
	90 <sup>†</sup>	13.2±4.71	9.31±4.43	2.2
Maize	30	100	61.56±3.42	3.8
	60	56.7±7.98	52.06±1.34	3.1
	90	29.1±8.17	23.89±4.26	2.9

\*Plants were exposed to the various concentrations of BT for 14 days. Starting volume of the growth solution was 450 mL. Five replicates were used for each treatment. <sup>†</sup>Sunflower plants exposed to 90 mg/L died after 6 days of exposure.

**Table 5.** Assignment of important bands in the FTIR spectrum of pure 1H-benzotriazole. (Mohan and Settu, 1993; Fischer *et al.*, 1996)

<b>Assignment</b>	<b>Frequency range (cm<sup>-1</sup>)</b>	<b>Comments</b>
C – N stretching	≈1384	Triazole ring
C – H in-plane bending	≈1208	Benzene ring
C-C-C trigonal bending	≈1005	Benzene ring
C – H out-of-plane bending	774 – 780	Benzene ring
C – H out-of-plane bending	739 – 745	Benzene ring

**Figure 37.** FTIR spectrum of 1H-benzotriazole (BT) in KBr.

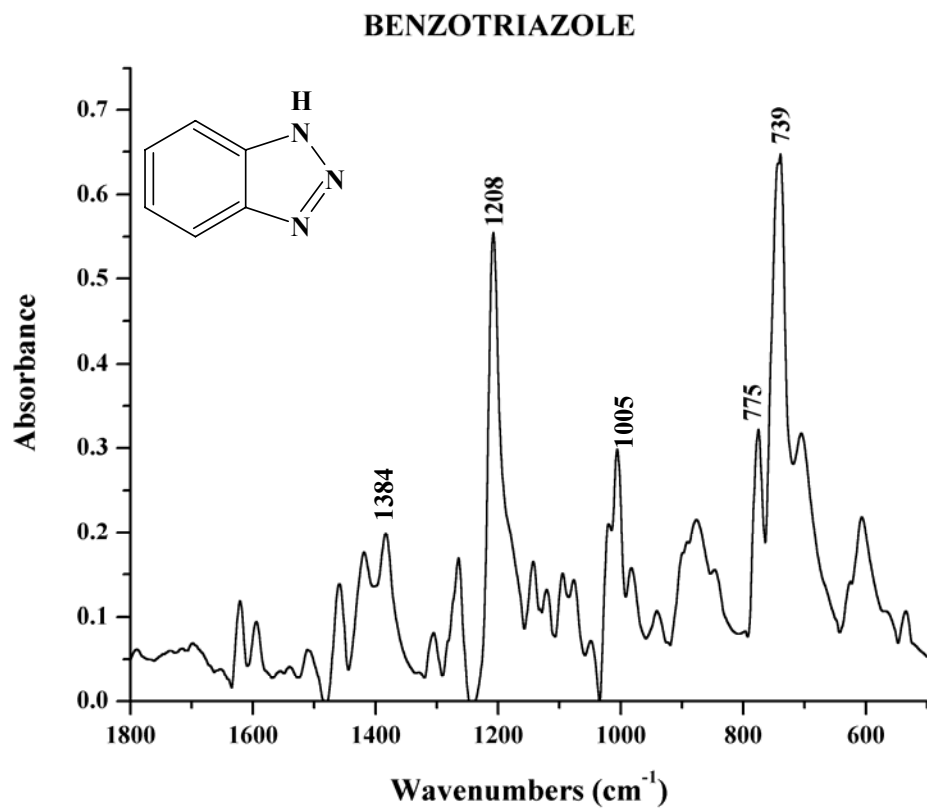


**Figure 38.** FTIR spectra of dried sunflower root samples that were untreated and treated with 30, 60, and 90 mg/L benzotriazole, respectively. A) FTIR spectrum from 1800-600  $\text{cm}^{-1}$ . B) FTIR spectrum from 900-700  $\text{cm}^{-1}$ .

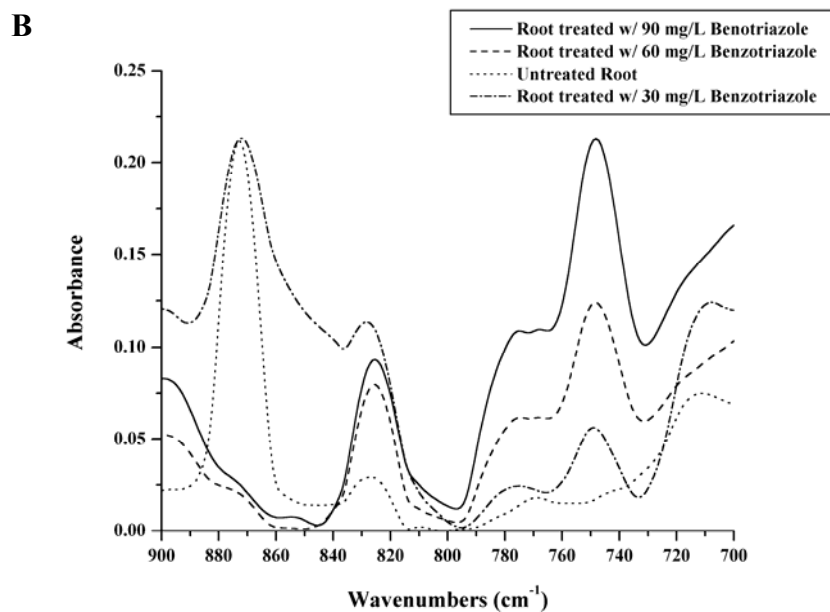
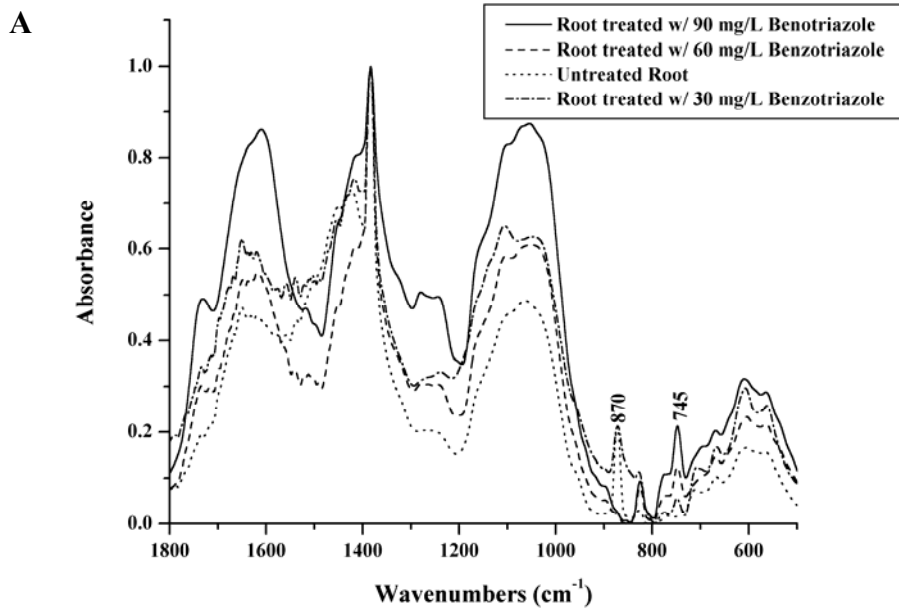


**Figure 39.** FTIR spectra of sunflower root samples that are untreated, untreated spiked with 5% benzotriazole, and treated with 60 mg/L benzotriazole respectively. A) FTIR spectrum from 1800-600  $\text{cm}^{-1}$ . B) FTIR spectrum from 900-700  $\text{cm}^{-1}$  (spectrum of pure benzotriazole included).

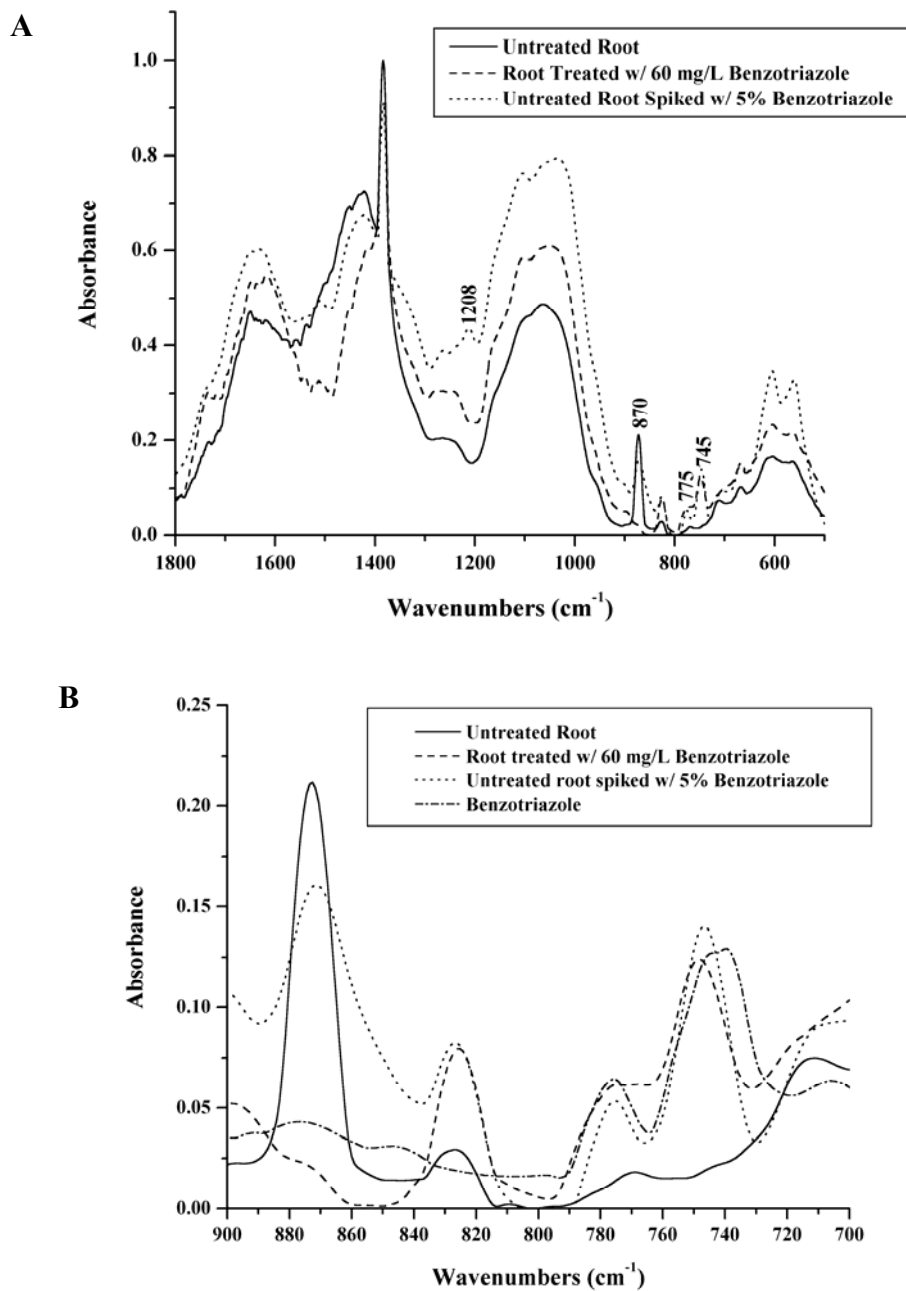


**Figure 40.** ATR spectra of secondary roots taken from sunflower plants untreated (•••) and treated (—) with 60 mg/L BT. An expanded scale of the 900-700  $\text{cm}^{-1}$  region is shown to display the 745  $\text{cm}^{-1}$  peak.

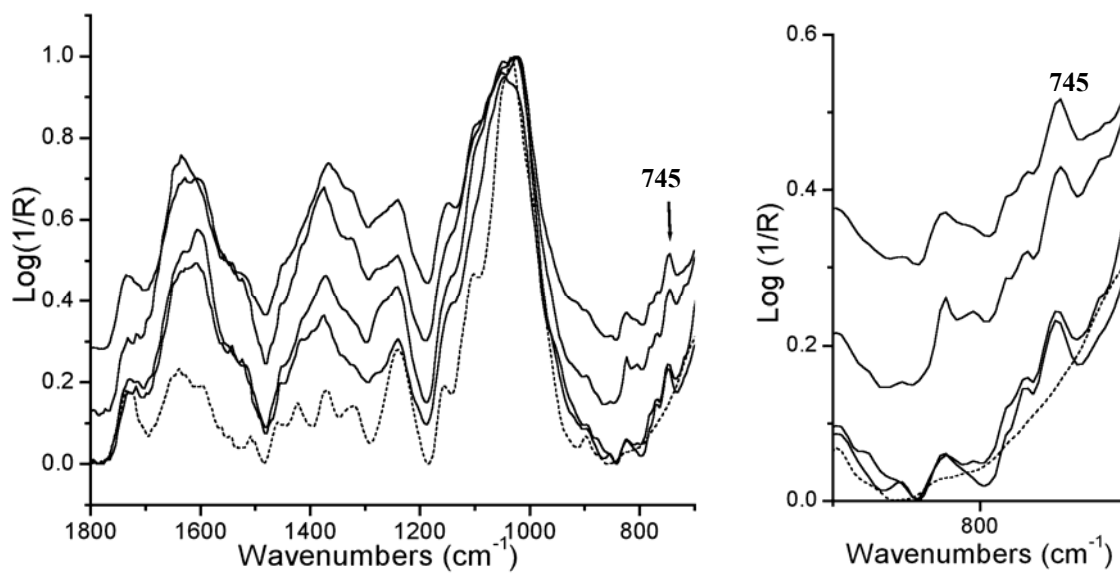


**Figure 41.** ATR spectra of primary root taken from sunflower plants untreated (••••) and treated (—) with 60 mg/L 1H-benzotriazole.

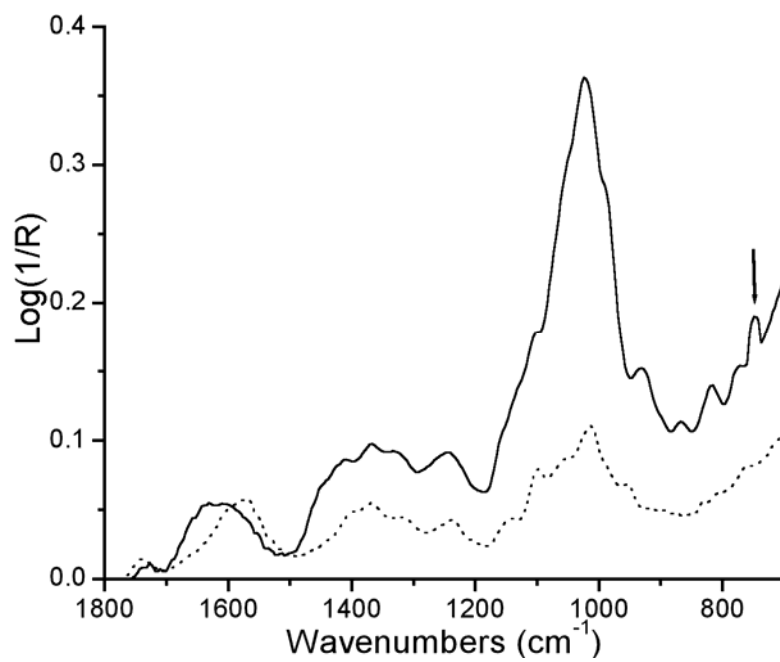


**Figure 42.** FTIR spectra of root cortex sectioned at 400  $\mu\text{m}$  from the roots of untreated control, 10 mg/L BT treated and 30 mg/L treated sunflower plants. Each spectrum is an average of ten spectra taken from arbitrarily locations from their respective IR maps. Changes can be observed in the characteristic aromatic C-H peak of BT at 795  $\text{cm}^{-1}$  (A), carbohydrate region at 1000-1100  $\text{cm}^{-1}$  (C), and a characteristic lignin peak at 1266  $\text{cm}^{-1}$  (L).

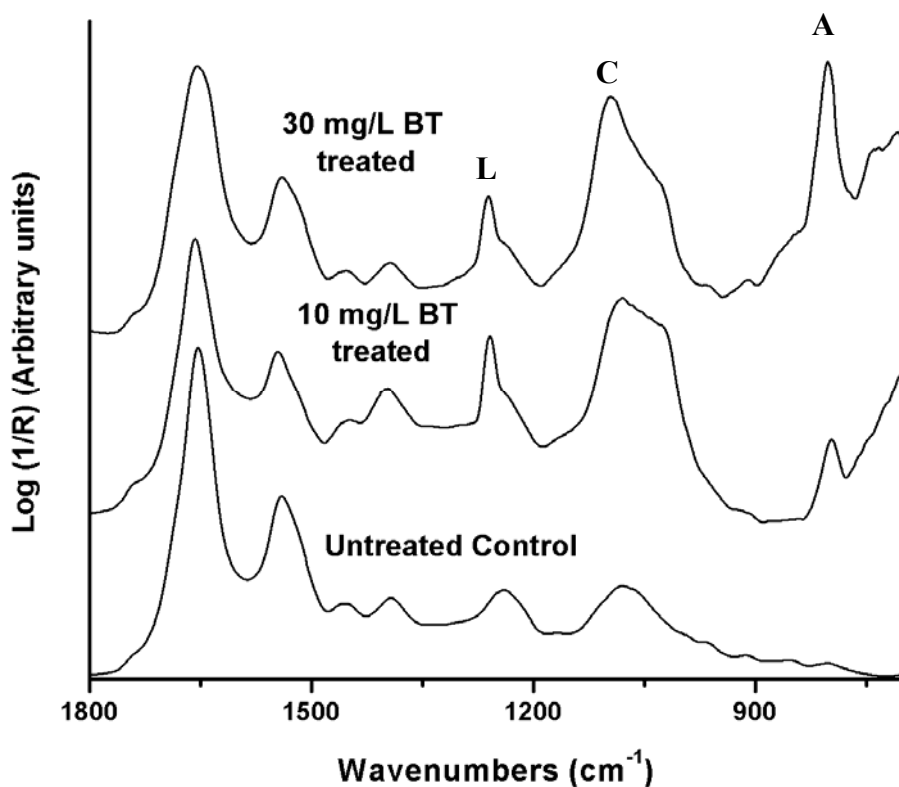




**Figure 43.** Functional group area maps showing the distribution of protein and BT in the root tissue of untreated and BT treated sunflowers sectioned at about 400  $\mu\text{m}$  from the root tip. The intensity ruler is displayed under each functional group map. The blue rectangle on the visible image of each root section denotes the area studied. (A) Visible image of root section from untreated (control) sunflower. Dimensions of the area studied: 240  $\mu\text{m}$  x 70  $\mu\text{m}$ . (B) Visible image of root section from sunflower treated with 10 mg/L BT. Dimensions of the area studied: 210  $\mu\text{m}$  x 40  $\mu\text{m}$ . (C) Visible image of root section from sunflower treated with 30 mg/L BT. Dimensions of the area studied: 230  $\mu\text{m}$  x 40  $\mu\text{m}$ . Area under the peak centered at 1650  $\text{cm}^{-1}$  representing the protein concentration and distribution in untreated root tissue (D), 10 mg/L BT treated root tissue (E), and 30 mg/L BT treated root tissue (F). Area under the peak centered at 749  $\text{cm}^{-1}$  representing the concentration and distribution of BT in untreated root tissue (G), 10 mg/L BT treated root tissue (H), and 30 mg/L BT treated root tissue (I).

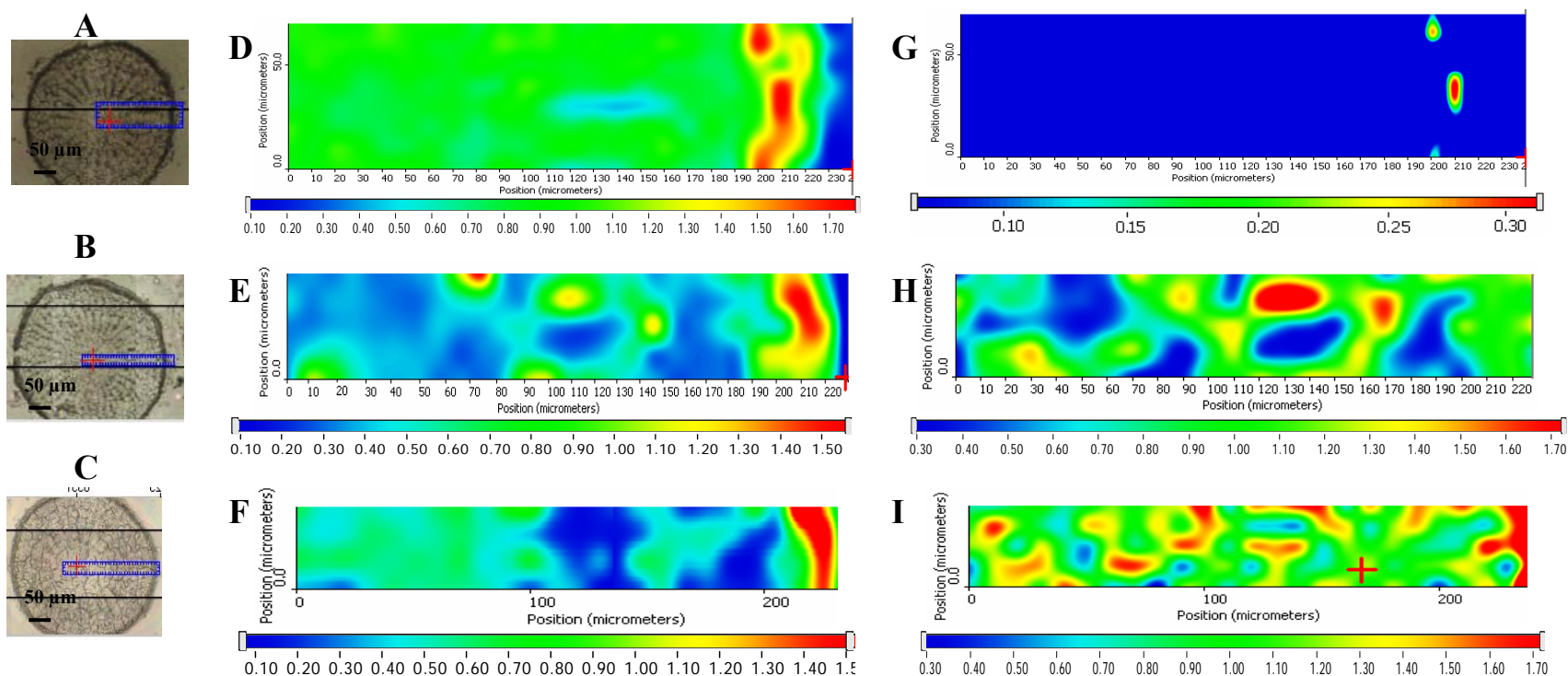


**Figure 44.** PCA shows separation between the vascular (cortex) tissue of untreated control (●) and the BT treated sunflower plants, 10 mg/L BT (▲) and 30 mg/L (■) using the first 2 PC scores.

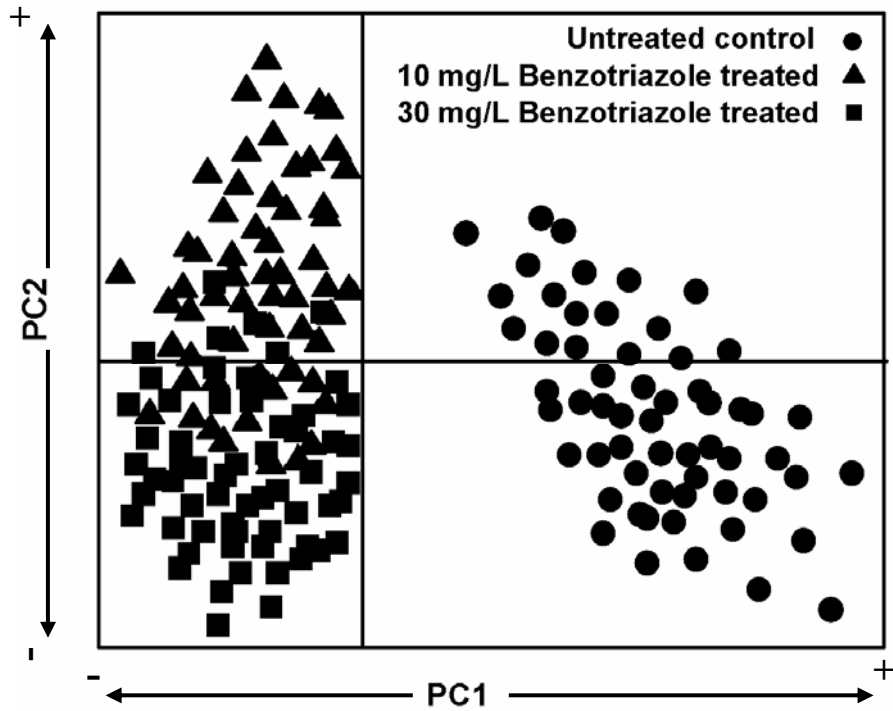


**Figure 45.** LDA using the Mahalanobis distance metric was performed on 60 observations arbitrarily selected from independent sample sets to validate the model set. 54 out of 60 observations were correctly assigned using the first 2 PC scores. Bold symbols represent the group centers for (●) the untreated control, (▲) 10 mg/L BT treated, and (■) and 30 mg/L treated sunflower plants.

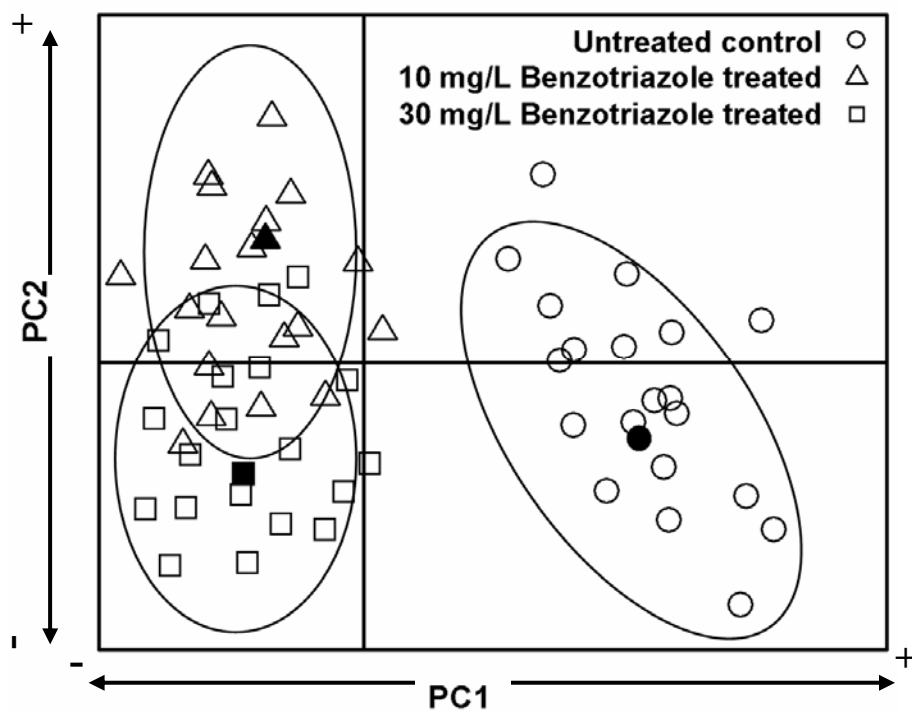


**Figure 46.** The PC loadings derived from the exploratory PCA of vascular (cortex) tissue from untreated control, 10 mg/L BT treated and 30 mg/L treated sunflower plants. The first PC loading (A) shows major variability in the protein region (1650 and 1553  $\text{cm}^{-1}$ ) and the characteristic BT peak at 745  $\text{cm}^{-1}$ . The second PC loading (B) shows major variability in the protein, carbohydrate, and 745  $\text{cm}^{-1}$  regions.

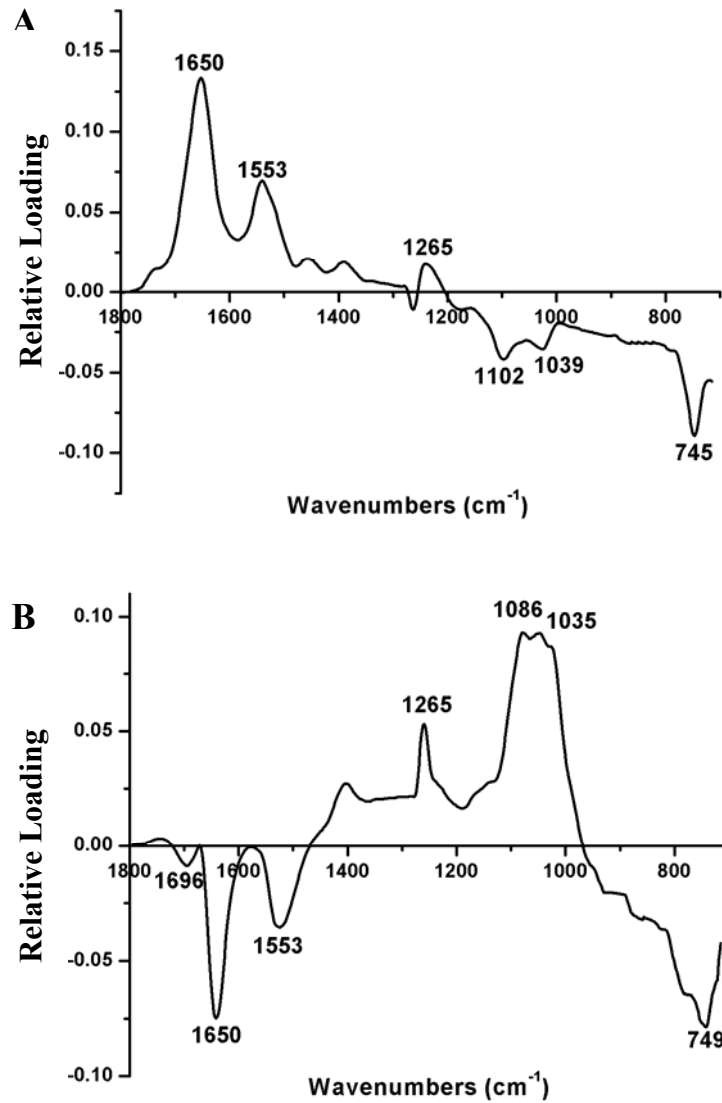


**Figure 47.** Functional group area maps showing the spatial distribution and concentration of BT in the root tissue of untreated and 30 mg/L BT treated sunflowers sectioned at about 1cm from the root tip. The intensity ruler is displayed under each functional group map. The blue rectangle on the visible image of each root section denotes the area studied. (A) Visible image of root section from untreated (control) sunflower. Dimensions of the area studied: 300  $\mu\text{m}$  x 50  $\mu\text{m}$ . (B) Visible image of root section from sunflower treated with 30 mg/L BT. Dimensions of the area studied: 130  $\mu\text{m}$  x 80  $\mu\text{m}$ . Area under the peak centered at 745  $\text{cm}^{-1}$  representing the concentration and distribution of BT in untreated root tissue (C) and 30 mg/L BT treated root tissue (D).

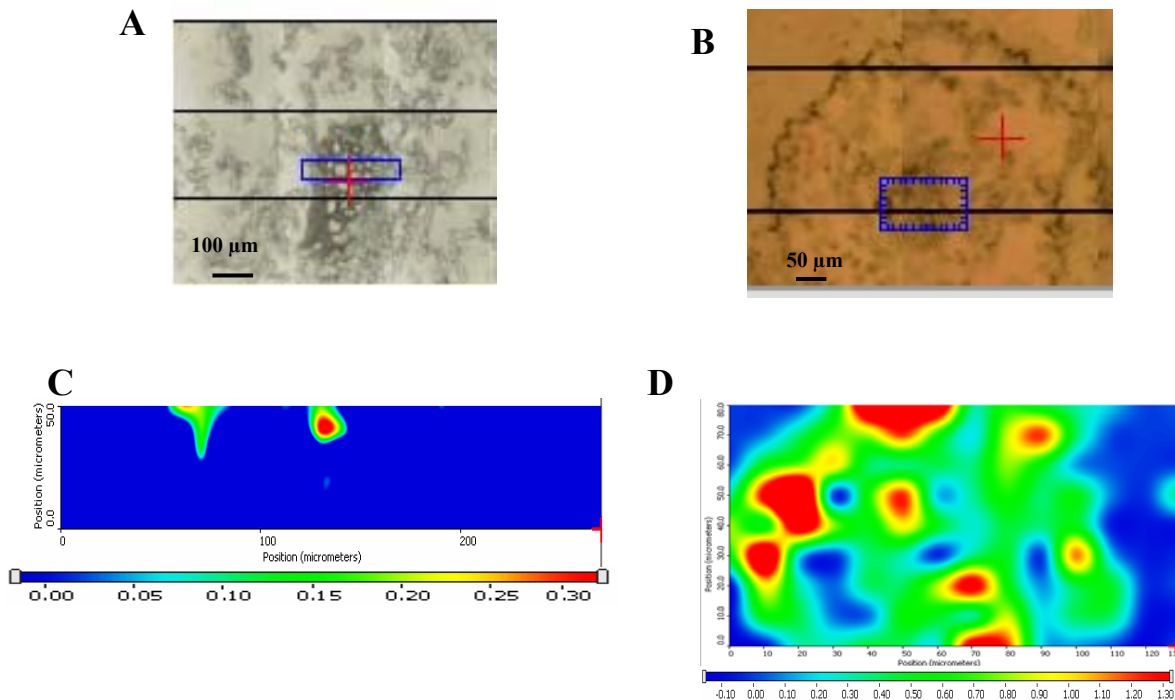


**Figure 48.** IR spectra of root xylem from untreated and 30 mg/L BT treated sunflower plants (listed bottom to top). Each spectrum is an average of xylem ten spectra extracted from spot and area maps using a 12 x 12  $\mu\text{m}$  aperture. Spectra are arbitrarily offset for ease of presentation.

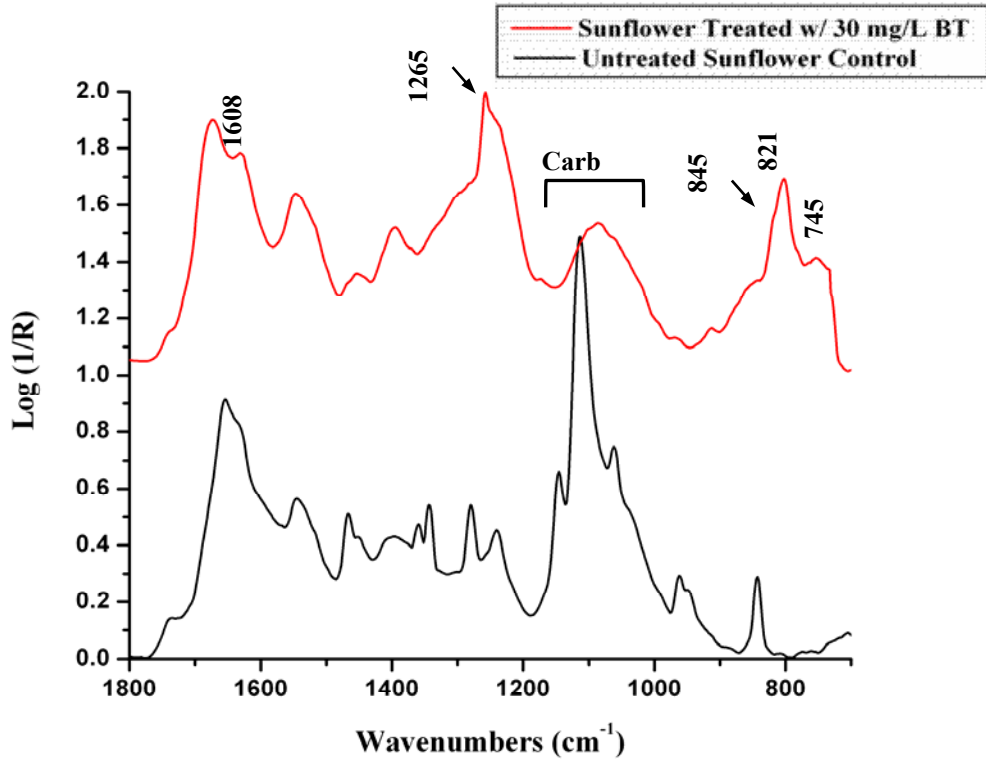


**Figure 49.** Exploratory PCA shows separation between the root vascular (cortex) tissue of untreated control (■) and the 90 mg/L BT treated maize plants (▲) using the first 2 PC scores.

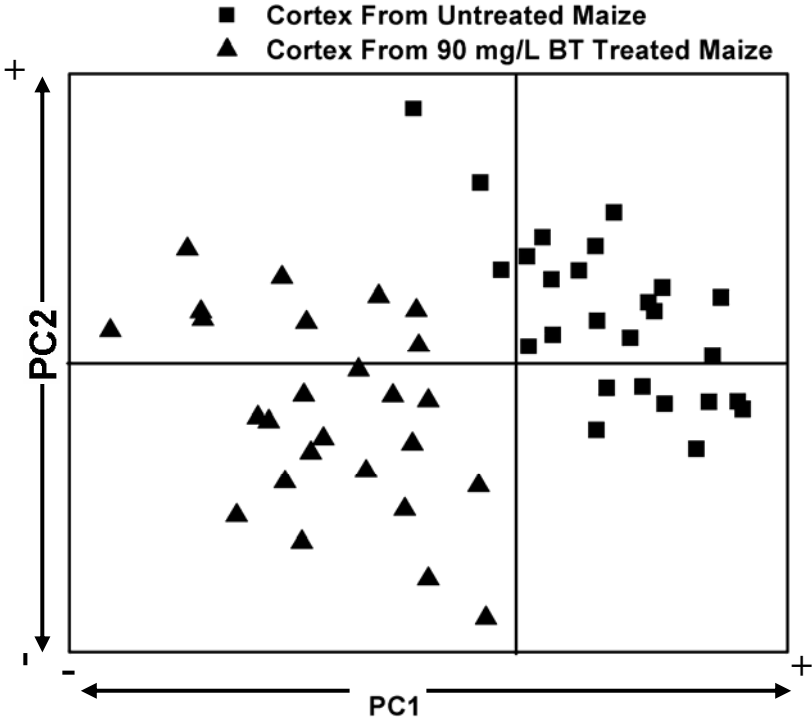


**Figure 50.** The PC loadings derived from the exploratory PCA of vascular (cortex) tissue from untreated control and 90 mg/L BT treated maize plants. The first PC loading (A) displays peaks pertaining to lignin (1635  $\text{cm}^{-1}$  and 1513  $\text{cm}^{-1}$ ), protein (amide II), and the carbohydrate fingerprint region. The second PC loading (B) shows major variability in the protein (amide I band at 1653  $\text{cm}^{-1}$ ) and carbohydrate content.

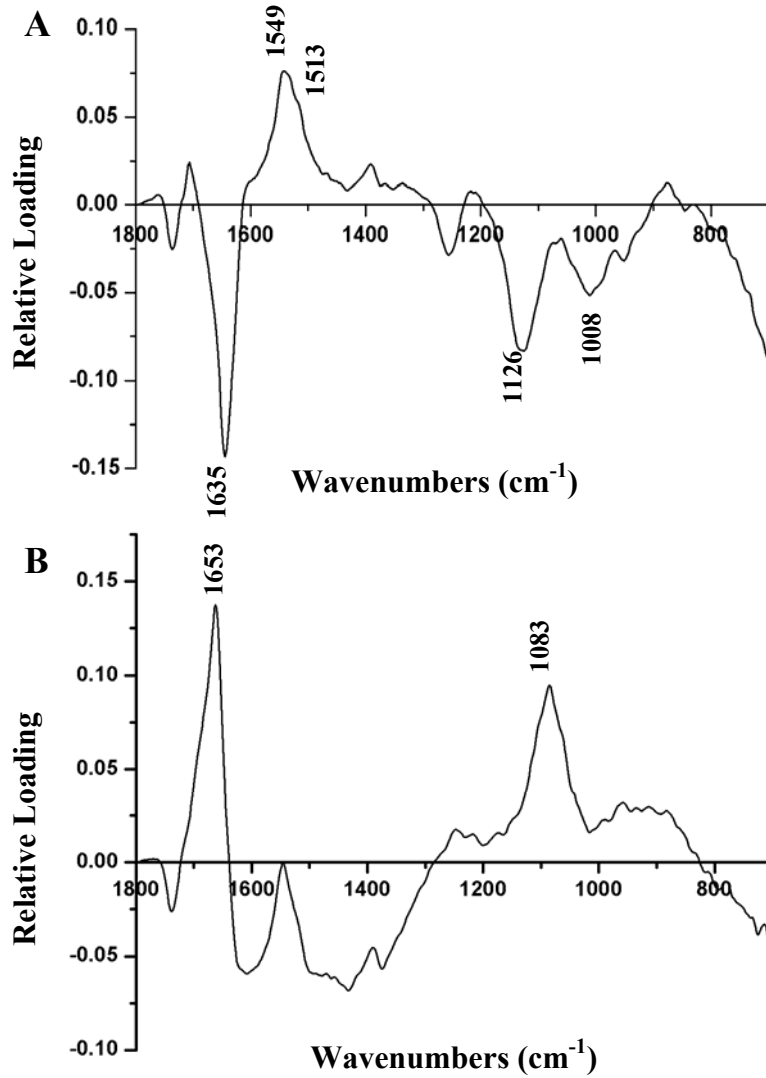




**Figure 51.** Exploratory PCA shows separation between the root epidermal tissue of untreated control (■) and the 90 mg/L BT treated maize plants (▲) using the first 2 PC scores.

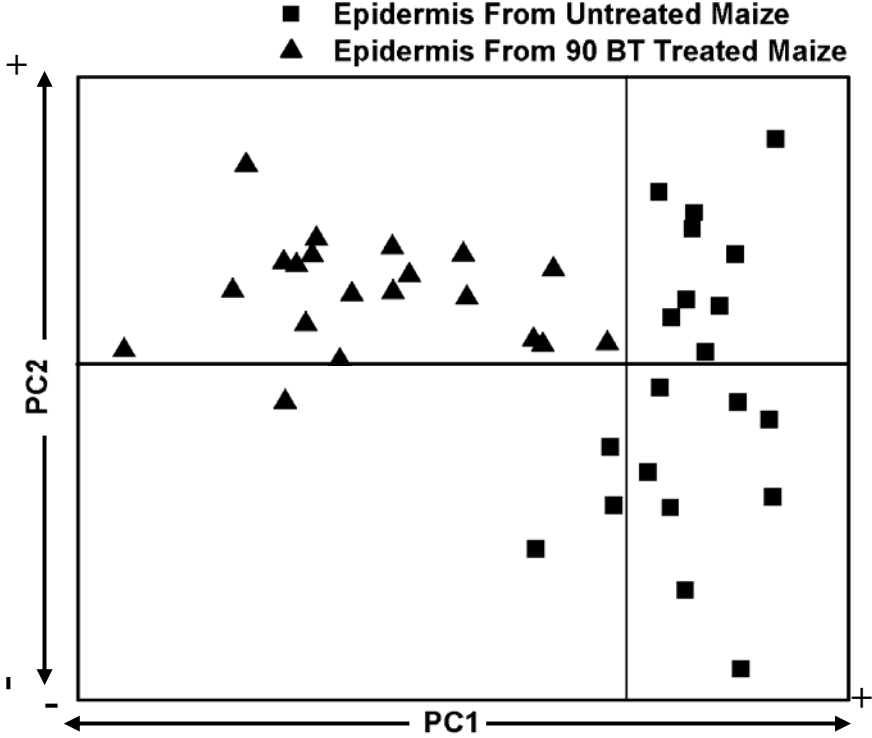


**Figure 52.** The PC loadings derived from the exploratory PCA of epidermal tissue from untreated control and 90 mg/L BT maize plants. The first PC loading (A) displays peaks pertaining to lignin (1638  $\text{cm}^{-1}$ , 1600  $\text{cm}^{-1}$ , and 1515  $\text{cm}^{-1}$ ) and the carbohydrate fingerprint region. The second PC loading (B) is composed of IR peaks in the carbohydrate fingerprint region.

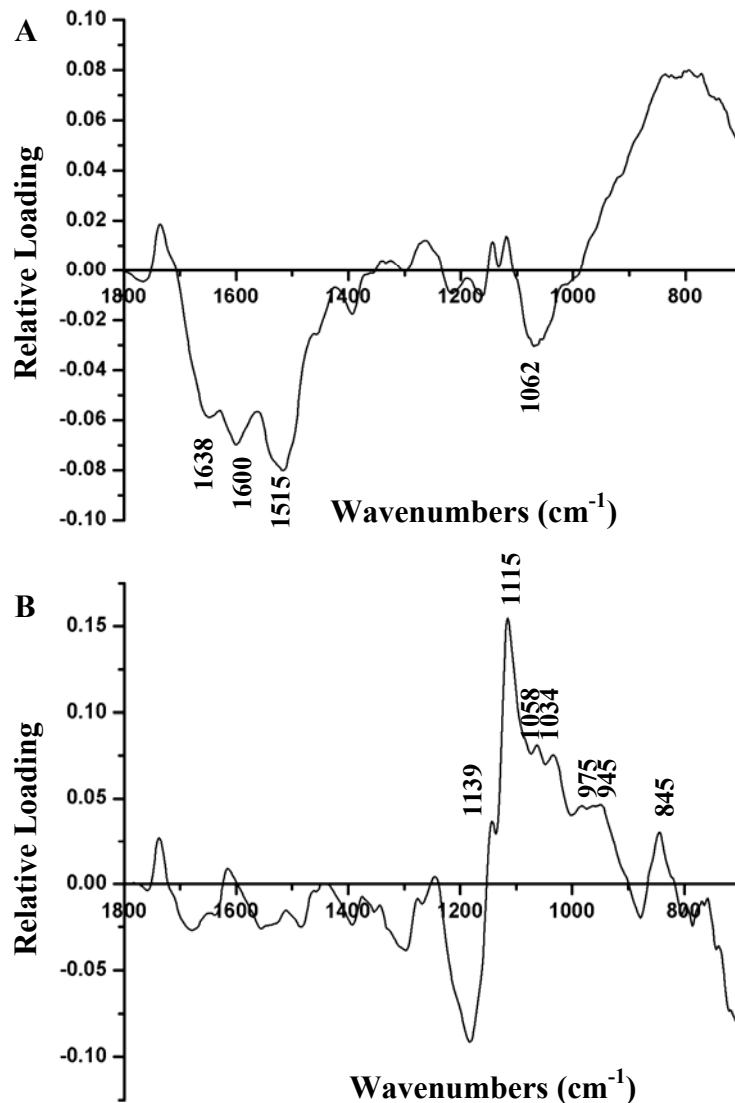
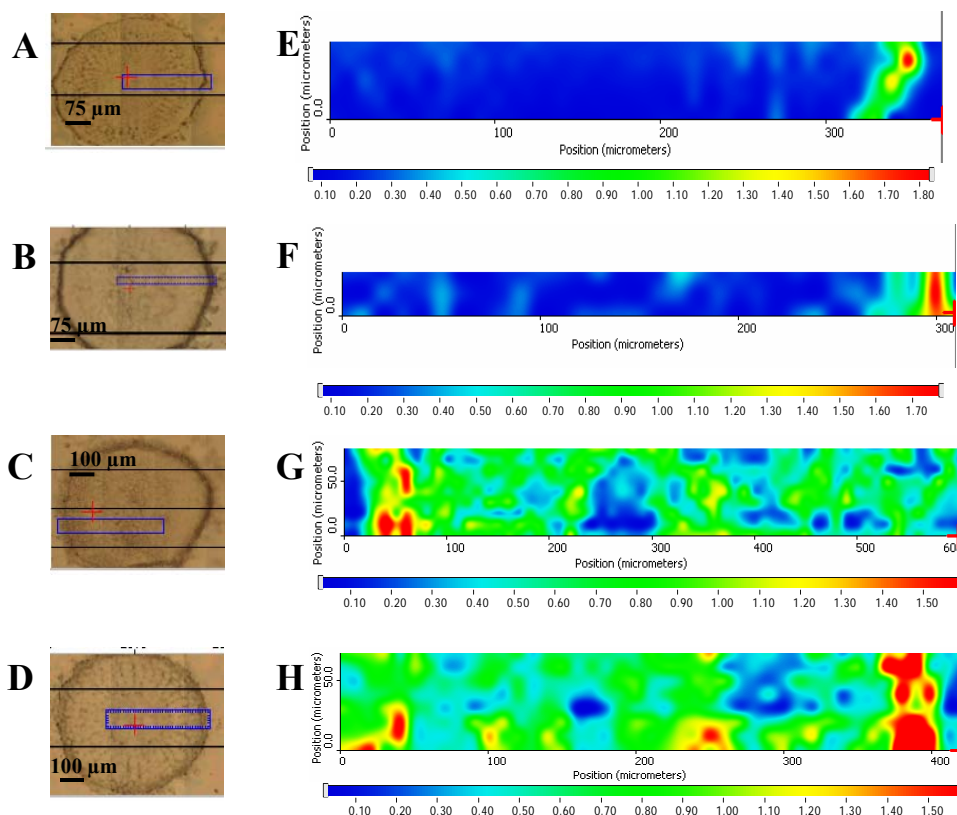


**Figure 53.** Functional group area maps showing the spatial distribution and concentration of lignin components in the root tissue of untreated, 30 mg/L BT, 60 mg/L BT, and 90 mg/L BT treated maize plants sectioned at about 400  $\mu\text{m}$  from the root tip. The intensity ruler is displayed under each functional group map. The blue rectangle on the visible image of each root section denotes the area studied. (A) Visible image of root section from untreated (control) sunflower. Dimensions of the area studied: 370  $\mu\text{m}$  x 40  $\mu\text{m}$ . (B) Visible image of root section from sunflower treated with 30 mg/L BT. Dimensions of the area studied: 300  $\mu\text{m}$  x 20  $\mu\text{m}$ . (C) Visible image of root section from sunflower treated with 60 mg/L BT. Dimensions of the area studied: 600  $\mu\text{m}$  x 80  $\mu\text{m}$ . (D) Visible image of root section from sunflower treated with 90 mg/L BT. Dimensions of the area studied: 420  $\mu\text{m}$  x 70  $\mu\text{m}$ . Area under the peak centered at 845  $\text{cm}^{-1}$  representing the concentration and distribution of lignin in untreated root tissue (E), 30 mg/L BT (F), 60 mg/L BT (G), and 90 mg/L BT (H) treated root tissue.



**CHAPTER 5 - MONITORING THE FATE AND EFFECT OF 2,4-DINITROTOLUENE  
(2,4-DNT) AND 2,6-DINITROTOLUENE (2,6-DNT) IN SUNFLOWER AND MAIZE  
PLANTS USING SR-IMS**

## Introduction

The fate, transport, and phytotoxicity of dinitrotoluenes (DNTs) in plants have not been well characterized. Most studies have focused on the parent compound 2,4,6-trinitrotoluene (TNT) where the phytotransformation pathway has been well characterized (Hannink *et al.*, 2002). Both 2,4-dinitrotoluene (2,4-DNT) and 2,6-dinitrotoluene (2,6-DNT) are common by-products of TNT production at explosive and munitions plants and a common intermediate in the production of polyurethanes. These DNTs most often occur as a mixture of the isomers 2,4-DNT and 2,6-DNT (approximately 78% and 19%, respectively) in waste streams of munitions plants and in the soil of military installations where explosives have been used (Etnier, 1987). These DNTs are known to be neurotoxic, cause a variety of blood cell disorders and reproductive problems, and possibly are carcinogenic (no human data has been reported but DNTs have been found to cause cancer in rats and dogs), resulting in their listing as a priority pollutant by the U.S. Environmental Protection Agency (1990). The 2,6 isomer of DNT is considered to be the more toxic form, but there is little experimental evidence to support this assumption. In a report by Picka and Friedl (2004), DNTs were found to be the most phytotoxic among the nitroaromatics, although, another report suggests the hydroxylamino derivatives of DNTs, produced by the partial reduction of one nitro group, were more phytotoxic than their parent DNT compound (Tadros *et al.*, 2000). In both studies, germination rate, root length and area, and dry weight dramatically decreased especially at high levels of DNT contamination. Both isomers of DNT appeared to be equally phytotoxic. However, it is clear that the current research is somewhat inconclusive on the phytotoxic properties of DNTs. There are only two reports that have discussed the fate of DNTs in plants. Schneider *et al.* (1996) conducted a survey on the fate of eight different plant species exposed

to DNTs in soil from an ammunition plant at 1 mg of DNT/kg of soil. In this study, most of the DNT accumulation took place in the roots and to a much lesser extent in the stems and leaves. Similar results were reported in a review written by Hannink et al. (2002) about the phytoremediation of explosive compounds.

In this chapter, the potential for SR-IMS to determine the fate and effect of DNTs in maize and sunflower roots is reported. Though no study has been conducted using SR-IMS to determine the location of DNTs in plants, an unpublished study by Ghosh and Luthy (2006) showed the use of SR-IMS to characterize the location and association of TNT in soils. This suggests that SR-IMS has the ability to probe the presence of DNTs in an organic medium like plant tissue. The study is conducted under the premise that DNTs may bind to the epidermis or vascular (xylem) tissue since these tissues contain lipids. This reasoning is due to the fact that both 2,4-DNT and 2,6-DNT have a log octanol/water partition coefficient ( $\log K_{OW}$ ) around 2 (refer to Table 2 for physical properties of 2,4 and 2,6-DNT). Compounds that possess a  $\log K_{OW}$  between 1.5 and 3 are moderately hydrophobic and will bind to tissues containing lipids (Burken, 2003). Also, the fate of TNT in plants such as wheat (Sens *et al.*, 1999) and smooth brome grass (Sun *et al.*, 2000) was found predominantly in the cell walls where a major portion was bound to lignin residues. Similar results have been observed in hydroponically grown legumes and alfalfa plants (Davis *et al.*, 2002), where up to 80% of the labeled TNT remained in the root.

## Results and Discussion

### *Uptake of 2,4-DNT and 2,6-DNT by maize and sunflower plants*

Maize and sunflower plants were grown in amber stock jars containing 150 mL of either 0, 5, 10, or 15 mg/L of 2,4-DNT or 2,6-DNT. Growth solutions were replenished after the fourth day. Samples for HPLC analysis were taken on the fourth day and after the completion of the one week growth period. HPLC analysis revealed the disappearance of 2,4-DNT and 2,6-DNT from the hydroponic growth solutions of maize and sunflower as seen in Table 6. Overall, maize plants were more tolerant than sunflower plants to both forms of DNT. Maize plants were able to absorb 100% of the DNT from solutions containing 5 mg/L 2,4-DNT and 5 mg/L 2,6-DNT, and about 91% of the 10 mg/L 2,4-DNT. Sunflowers were only able to completely uptake DNT from the 5 mg/L 2,4-DNT growth solution. The phytotoxic effect of 2,6-DNT can be observed at levels greater than 5 mg/L. At 15 mg/L 2,6-DNT, both plants species died within eight days of exposure while half of the sunflowers exposed to 10 mg/L 2,6-DNT died after eight days of treatment. Lower solution uptake, decreased fresh weight gain and total dry weights were the trends associated with higher concentrations of both DNTs. A decrease in root and shoot lengths was observed in both plants at all the concentrations of DNTs tested. In general, it appears that both isomers of DNT exert a phytotoxic effect at concentrations greater than 5 mg/L. Although this level seems low, it is not an unusual result as other plants have experienced phytotoxic effects from TNT concentrations as low as 1.5 mg/L (Pavlostathis *et al.*, 1998). Burken and coworkers (2000) have indicated that TNT and its degradation products are more toxic in hydroponic solution than in soil.

### *Interpretation of the FTIR spectra of 2,4-DNT and 2,6-DNT*

The FTIR spectra of research grade 2,4-DNT and 2,6-DNT in potassium bromide pellets are depicted in Figure 54 A and B. The IR peaks of importance for the both 2,4-DNT and 2,6-DNT are listed in Table 7 (Stewart *et al.* 1986). The peaks of corresponding to the asymmetric and symmetric stretch of NO<sub>2</sub> at 1530 cm<sup>-1</sup> and 1350 cm<sup>-1</sup> are of particular interest. The appearance of these peaks in the root tissue would suggest that the nitro groups were not reduced to amino groups. However, upon reduction of the nitro groups to amino groups, the peaks representing asymmetric and symmetric stretch of NO<sub>2</sub> would disappear and peaks representing aromatic amines in the regions of 1350 – 1260 cm<sup>-1</sup> (C-N stretching) and 1638 – 1602 cm<sup>-1</sup> (NH<sub>2</sub> scissoring) may appear (Lin-Vien *et al.*, 1991). This will be the basis for determining whether or not the maize and sunflower plants are able to metabolize and/or modify the DNTs.

### *SR-IMS of sunflower roots exposed to 2,4-DNT*

First it is important to note that SR-IMS was not conducted on root tissues from sunflowers treated with 2,6-DNT and 15 mg/L 2,4-DNT. As previously mentioned, the 10 and 15 mg/L 2,6-DNT were lethal to the sunflower plants. The roots from sunflower plants treated with 5 mg/L 2,6-DNT, and 10 and 15 mg/L 2,4-DNT were dark brown and unsuitable for examination using SR-IMS. An example of the SR-IMS spectra taken from a section of a dark brown sunflower root can be seen in Figure 55. The infrared beam is completely saturated by the dark root section so that no discernable peaks can be observed. Even when using the 25 point smooth function provided by OMNIC 6.1, it was still difficult to differentiate between



peaks due to noise and actual plant material. For this portion of the study, only roots from sunflower plants treated with 5 mg/L 2,4-DNT were studied.

The location of peaks associated with  $\text{NO}_2$  symmetric and asymmetric stretching and aromatic amines are fairly close to those commonly found in untreated sunflower tissue. This was especially true in the cortex where visual inspection of untreated and 5 mg/L 2,4-DNT treated maize roots was not conclusive. For this reason, exploratory PCA was employed to uncover the major spectral variability between the cortex of untreated and 2,4-DNT treated sunflower plants. Figure 56 shows a PCA score plot conducted on thirty spectra arbitrarily (15 from each treatment) selected from cortex of untreated and 5 mg/L 2,4-DNT treated sunflower plants. The cortex spectra from the 2,4-DNT treated sunflowers were sampled from three different root sections; one area map and two line maps. The cortex spectra from the untreated sunflower were taken from those used to generate the model set in Chapter 3. Exploratory PCA was able to separate both treatment groups using the first two PC scores. The PC loadings derived from the PCA plot revealed that the first PC loading (Figure 57A) accounted for 90% of the overall spectral variance while the second PC loading (Figure 57B) only accounted for 5.3%. This indicates that even though the spectra from the cortex of untreated and 2,4-DNT treated sunflowers were visually similar they are, in fact, distinguishable. The first PC loading contains IR peaks that indicate the presence of 2,4-DNT and the modified form where one of the nitro groups was reduced to an amine group. These peaks can be seen a  $1346\text{ cm}^{-1}$ , representing  $\text{NO}_2$  symmetric stretch, and  $1628\text{ cm}^{-1}$ , representing  $\text{NH}_2$  scissoring in aromatic amines. A peak at 1461 may indicate the presence of the methyl group on 2,4-DNT, but it may also signify the C-H bend of  $\text{OCH}_3$  found in cellulose or pectic polysaccharides. A band at  $1093\text{ cm}^{-1}$ , in the carbohydrate fingerprint region, suggests damage or changes in the cross-

linking of polysaccharides in the 2,4-DNT treated sunflowers. This IR band is commonly found in the pectic polysaccharide, arabinan (Kacurakova *et al.*, 2000). This suggests that 2,4-DNT may affect the production of this particular polysaccharide. A change or damage in the protein portion of the root of 2,4-DNT treated sunflowers is evidenced by the presence of the amide I and amide II peaks in the second PC loading (Figure 57B).

Spectra from epidermal tissue of roots from 2,4-DNT treated sunflower plants were easy to distinguish from untreated root tissue as depicted in Figure 58. IR peaks associated with both 2,4-DNT and its aromatic amine modified form can be observed. Both IR bands, which are diagnostic for aromatic amines, are present at  $1628\text{ cm}^{-1}$  ( $\text{NH}_2$  scissoring) and  $1258\text{ cm}^{-1}$  (C-N stretch). As in the case with the first PC loading of cortex, only the  $\text{NO}_2$  symmetric stretch of 2,4-DNT was present at  $1346\text{ cm}^{-1}$ . Also, it appeared that the epidermal tissue from the 2,4-DNT treated maize was more lignified evidenced by the large increase in intensity at  $845\text{ cm}^{-1}$  (aromatic C-H bend). Polymers derived from DNT reduction products might have similar features.

The functional groups area maps showing the spatial distribution and concentration of 2,4-DNT and pectic polysaccharides in the root tissue of untreated and 5 mg/L 2,4-DNT treated sunflowers sectioned at about  $400\text{ }\mu\text{m}$  from the root tip are displayed in Figure 59. It is clear that 2,4-DNT is associated with both cortex and epidermal tissue in the DNT treated sunflower with higher concentrations in the epidermis (Figure 59D). Figures 59 E and F show the area under the peak centered at  $1093\text{ cm}^{-1}$  representing the concentration and distribution of pectic polysaccharide in untreated root tissue and 5 mg/L 2,4-DNT treated root tissue, respectively. As expected, the cortex of the 2,4-DNT treated sunflower is predominantly blue and light green

indicating little or no presence of the  $1093\text{ cm}^{-1}$  confirming the results of the PCA conducted earlier on cortex of untreated and 2,4-DNT treated sunflower.

From the above results, it can be concluded that sunflowers are very sensitive to both 2,4-DNT and 2,6-DNT. The SR-IMS and PCA data indicate that 2,4-DNT and its aromatic amine form are both present in cortex and epidermal tissue. However, the presence of both aromatic amine peaks in the epidermis does provide evidence that aromatic amines are primarily associated with epidermal tissue. Modification of 2,4-DNT is also evidenced by the lack of the IR peak for  $\text{NO}_2$  asymmetric stretch in either the PCA or IR spectra of roots from 2,4-DNT treated sunflower. At the DNT concentrations studied, it appears that sunflowers are able to metabolize only a fraction of the 2,4-DNT they absorb. This was confirmed by the presence of peaks for both 2,4-DNT and aromatic amines. This shows that The SR-IMS supports the evidence obtained through wet chemistry methods that plants modify 2,4-DNT to an aromatic monoamine. In order to better understand the fate and effect of DNTs on sunflower plants further studies need to be conducted with concentrations lower than 5 mg/L of DNT.

#### *SR-IMS of maize roots exposed to 2,4-DNT and 2,6-DNT*

Roots from maize plants treated with 15 mg/L 2,4-DNT and 2,6-DNT were not examined in this study. The 15 mg/L 2,6-DNT solutions were lethal to the maize plants and the 15 mg/L 2,4-DNT treatment produced dark brown roots that were unable to be analyzed by SR-IMS (see Figure 55). Maize roots were studied from the 5 and 10 mg/L 2,4-DNT and 2,6-DNT treatments.

Three separate roots sections taken from about  $700\ \mu\text{m}$  from the root tip from maize plants treated with 5 mg/L 2,4-DNT were sampled for the presence of 2,4-DNT in their root

tissue. Forty spectra from untreated and 5 mg/L 2,4-DNT treated maize (20 spectra from each treatment) were randomly selected for exploratory PCA of the epidermal tissue. The epidermal spectra from the untreated maize were taken from those used to generate the model set in Chapter 3. The PCA score plot shown in Figure 60 depicts distinct separation between the epidermal tissue of untreated and 5 mg/L 2,4-DNT treated maize plants using the first two PCs. The first (Figure 61A) and second PC loadings (Figure 61B) derived from the PCA represented 61% and 25.6% (total 86.6%) of the spectral variance, respectively. The first PC loading seen in Figure 61A contains the IR band at  $1627\text{ cm}^{-1}$  indicating the presence of the aromatic amine, derived from 2,4-DNT, in the epidermis. This same peak was also present in the second PC loading (Figure 61B). However, no peaks representing nitro groups were present in either loading. This suggests that the maize was able to metabolize the 5 mg/L 2,4-DNT and reduce the nitro groups to amine groups. These plants appeared healthy and completely absorbed the 2,4-DNT as seen in Table 6. Both PC loadings contained the methyl ester peak at  $1734\text{ cm}^{-1}$  and peaks indicative of pectic polysaccharides. The peaks at  $1143\text{ cm}^{-1}$  and  $1117\text{ cm}^{-1}$  are commonly found in spectra of arabinogalactan and xyloglucan. This could mean that the cross-linking for pectic polysaccharides is altered by 2,4-DNT treatment. Further evidence of this can be found in the second PC loading, which displays spectral features characteristic of pectin at  $1108\text{ cm}^{-1}$ ,  $1054\text{ cm}^{-1}$ , and  $1024\text{ cm}^{-1}$  (Sene *et al.*, 1994; Kacurakova *et al.*, 2000). This indicates that 2,4-DNT causes an increase the production of pectin in epidermal cell walls of maize. Similar results were observed in PCA of native and CesA mutants of potato tubers in which some mutants displayed increased pectin production to compensate for lower cellulose production (Oomen *et al.* 2004). Confirmation of an increase of the pectin content can be seen in Figure 62H showing the functional group area map of the spatial distribution and

concentration of pectin in the root tissue from maize plants treated with 5 mg/L-DNT. When compared to the pectin content in the untreated root tissue (Figure 62G), it is clear that the epidermis of the 2,4-DNT treated maize contains more pectin. This intensity of the pectin peaks for the 2,4-DNT treated plants are about 27% more than the those observed in the untreated maize plants. Figure 62F shows the area under the peak centered at  $1627\text{ cm}^{-1}$  representing concentration and distribution of aromatic amines in the 2,4-DNT treated root tissue. The aromatic amines were highly concentrated in the epidermis of maize with scattered areas of low concentration in the cortex. Aromatic amines were absent from the untreated tissue (Figure 62E).

Figure 63 displays the typical spectra of xylem tissue from untreated and 10 mg/L 2,4-DNT treated maize plants. IR peaks due to symmetric and asymmetric stretching of nitro groups at  $1529$  and  $1348\text{ cm}^{-1}$  were observed in the xylem spectra of 10 mg/L treated maize plants. Interestingly, the DNT treated tissue appears to have more protein due to higher intensities for the amide I and amide II bands and higher lignin content ( $845\text{ cm}^{-1}$ ). Another significant feature is the difference in the carbohydrate fingerprint region at  $1200 - 900\text{ cm}^{-1}$  between the DNT treated and untreated xylem. The pectic polysaccharide content was altered due to 2,4-DNT treatment. The absence of IR bands characteristic of aromatic amines suggests that the maize plants were not able to reduce the nitro groups or the level of aromatic amines were too low to detect by SR-IMS. A significant decrease in intensity at  $1734\text{ cm}^{-1}$  in the 2,4-DNT treated tissue suggests an increase in unesterified pectins. This usually correlates with changes in pectic polysaccharides as seen with tobacco cells adapted to high concentrations of sodium chloride (McCann *et al.*, 1994).

The functional group area maps showing the distribution of 2,4-DNT and esterified pectins in the root tissue of untreated and 10 mg/L 2,4-DNT treated maize plants sectioned about 1 cm from the root tip are depicted in Figure 64. The distribution of nitro groups was highest in the epidermis followed by less deposition in the xylem and endodermis (Figure 64F). Overall, the xylem and epidermis of the untreated maize tissue contained more esterified pectin (Figure 64G) than the root tissue of 10 mg/L 2,4-DNT treated maize plants (Figure 64H).

The above results suggest that maize was able to metabolize 5 mg/L 2,4-DNT, reducing the nitro groups producing aromatic amines, although, the treatment caused significant changes to the pectin and pectic polysaccharides in the maize plant cell wall. Also, maize plants treated with 2,4-DNT exhibited a developmental effect similar to *slr* (stunted lateral root) mutants of maize which possess altered pectin structure (Hochholdinger et al., 2004). At 10 mg/L 2,4-DNT, the nitro groups were present in the root tissue; however IR bands for aromatic amines were not present. This suggests that maize plants probably metabolize 2,4-DNT at concentrations between 5 and 10 mg/L. However, it would be beneficial to study the metabolism of 2,4-DNT in maize plants at concentrations lower than 5 mg/L.

Three separate roots sections taken from about 700  $\mu\text{m}$  from the root tip from maize plants treated with 10 mg/L 2,6-DNT were sampled for the presence of DNT in their root tissue. Forty spectra from untreated and 10 mg/L 2,6-DNT treated maize (20 spectra from each treatment) were randomly selected for exploratory PCA of the cortex tissue. The cortex spectra from the untreated maize were taken from those used to generate the model set in Chapter 3. The PCA score plot shown in Figure 65 shows some separation between the cortex tissue of untreated and 10 mg/L 2,6-DNT treated maize plants using the second and third PCs. The second (Figure 66A) and third PC loadings (Figure 66B) derived from the PCA represented

29% and 10.7% of the spectral variance, respectively. The second PC loading seen in Figure 5.13A contains IR bands that represent protein at  $1655\text{ cm}^{-1}$  and  $1547\text{ cm}^{-1}$  and a characteristic pectin peak at  $1101\text{ cm}^{-1}$ . This peak was also observed in the third PC loading (Figure 66B) along with a characteristic cellulose peak at  $1240\text{ cm}^{-1}$  which suggests an alteration to the cellulose structure. Also present in the third PC loading are a peak diagnostic for aromatic amines at  $1635\text{ cm}^{-1}$  and a nitro peak at  $1528\text{ cm}^{-1}$ . This provides evidence that both 2,6-DNT and its aromatic amine are present, but only at low concentration since the third PC loading contributes only a minor amount to the overall spectral variance. Exploratory PCA did show separation between epidermal tissue of untreated and 10 mg/L 2,6-DNT treated maize plants using the first two PC scores in Figure 67. The first PC loading (Figure 68A) contributed 71% of the spectral variance. The asymmetric and symmetric  $\text{NO}_2$  stretching bands are both observed in the first PC loading. IR bands associated with pectic polysaccharides and cellulose are present in both the first and second PC loadings. No bands associated with aromatic amines were present in either loading. This mimics the results seen for maize treated with 10 mg/L 2,4-DNT. This is confirmed by Figure 69 which displays the functional group area maps showing the spatial distribution of 2,6-DNT in the root tissue of untreated and 10 mg/L 2,6-DNT treated maize plants sectioned between 700 and 800  $\mu\text{m}$  from the root tip. The distribution of 2,6-DNT was confined to the vascular tissue and epidermis with only small amounts seen in the cortex.

A similar pattern of metabolism was seen for both 2,4-DNT and 2,6-DNT in maize root tissue. DNTs and the derivative aromatic amines were predominantly associated with epidermis and xylem. These results confirm the initial hypothesis that DNTs are bound primarily to tissues that contain lignin. Also, both isomers of DNT altered the structure and production of pectin and pectic polysaccharides. It is important to note that aromatic amines were only seen at

the 5 mg/L concentrations for both DNTs in maize and sunflower treated tissue. However, at 10 mg/L DNT, only nitro groups were present in the maize treated tissue. This suggests maize (and probably sunflower) are unable to metabolize effectively at concentrations higher than about 5 mg/L DNT in hydroponic solution. The plant growth results in Table 6 also provide evidence to this fact. A more accurate assessment of how maize metabolizes DNTs may be seen at experiments conducted at lower than 5 mg/L DNT.



**Table 6.** Plant growth and uptake of 2,4-DNT and 2,6-DNT by maize and sunflower plants exposed to various concentrations of DNTs for a 1 week growth period.\*

Plant n=4	DNT concentration (mg/L)	% DNT disappearance	Solution uptake (mL)	Fresh weight gain (g)	Dry weight (g)
Maize	0	-----	127±12	8.85±2.31	1.37±0.31
	5 mg/L 2,4-DNT	100	115±22	7.88±1.89	0.78±0.22
	10 mg/L 2,4-DNT	91.1±8.76	96±23	4.98±1.56	0.52±0.23
	15 mg/L 2,4-DNT	85.6±10.55	77±14	3.20±0.62	0.38±0.18
	5 mg/L 2,6-DNT	100	122±17	7.60±1.21	0.70±0.23
	10 mg/L 2,6-DNT	52.1±3.27	83±22	4.10±0.43	0.48±0.11
	15 mg/L 2,6-DNT <sup>§</sup>	16.5±5.23	49±27	1.03±0.21	0.18±0.08
Sunflower	0	-----	136±21	5.63±1.28	0.82±0.18
	5 mg/L 2,4-DNT	100	124±24	5.31±0.66	0.74±0.12
	10 mg/L 2,4-DNT	84.2±10.45	88±33	3.97±0.41	0.53±0.08
	15 mg/L 2,4-DNT	37.6±8.89	39±27	2.56±0.92	0.31±0.09
	5 mg/L 2,6-DNT	56.4±2.45	107±19	3.24±1.46	0.38±0.12
	10 mg/L 2,6-DNT <sup>†</sup>	23.4±12.33	61±25	1.87±0.62	0.22±0.15
	15 mg/L 2,6-DNT <sup>‡</sup>	7.8±3.29	33±16	0.57±0.34	0.07±0.02

\* Four replicates were used for each treatment. Starting volume for all growth solutions was 150 mL. Solutions were replenished as needed after the fourth day of the growth period. <sup>§</sup>All four maize plants that were exposed to 15 mg/L 2,6-DNT died after 6 days of treatment. <sup>†</sup>Two sunflower plants exposed to 10 mg/L 2,6-DNT died after 6 days of treatment. <sup>‡</sup>All four sunflower plants exposed to 15 mg/L of 2,6-DNT died after 5 days of exposure.

**Table 7.** Assignment of some important bands in the FTIR spectrum of pure 2,4-DNT and 2,6-DNT (Stewart *et al.*, 1986).

Frequency (cm <sup>-1</sup> )		Assignment
2,4-DNT	2,6-DNT	
1608	1614	C-C ring stretch, Ring H-C-C in-plane bending
1530	1531	NO <sub>2</sub> asymmetric stretch
1466	1458	Methyl umbrella
1440		CH <sub>3</sub> , H-C-H asymmetric bending
	1424	CH <sub>3</sub> , H-C-H asymmetric bending
1383	1387	C-C ring stretch
1346	1350	NO <sub>2</sub> symmetric stretch
1266	1297	Unassigned
1209	1204	Ring H-C-C in-plane bending
1153		Ring H-C-C in-plane bending
	1080	CH <sub>3</sub> , H-C-H asymmetric bending
1065		C-H out-of-plane bending of ring
914	893	C-H out-of-plane bending of ring
	841	C-C ring stretch
834	823	CH <sub>3</sub> rocking, C-C ring stretch, H-C-C in-plane bend
788		H-C-C in-plane bend, C-N bend
733	729	H-C-C in-plane bend, C-N-O bend
705	710	C-N-O bend

**Figure 54.** FTIR spectrum of (A) 2,4-dinitrotoluene (2,4-DNT) and (B) 2,6-dinitrotoluene (2,6-DNT) in KBr.

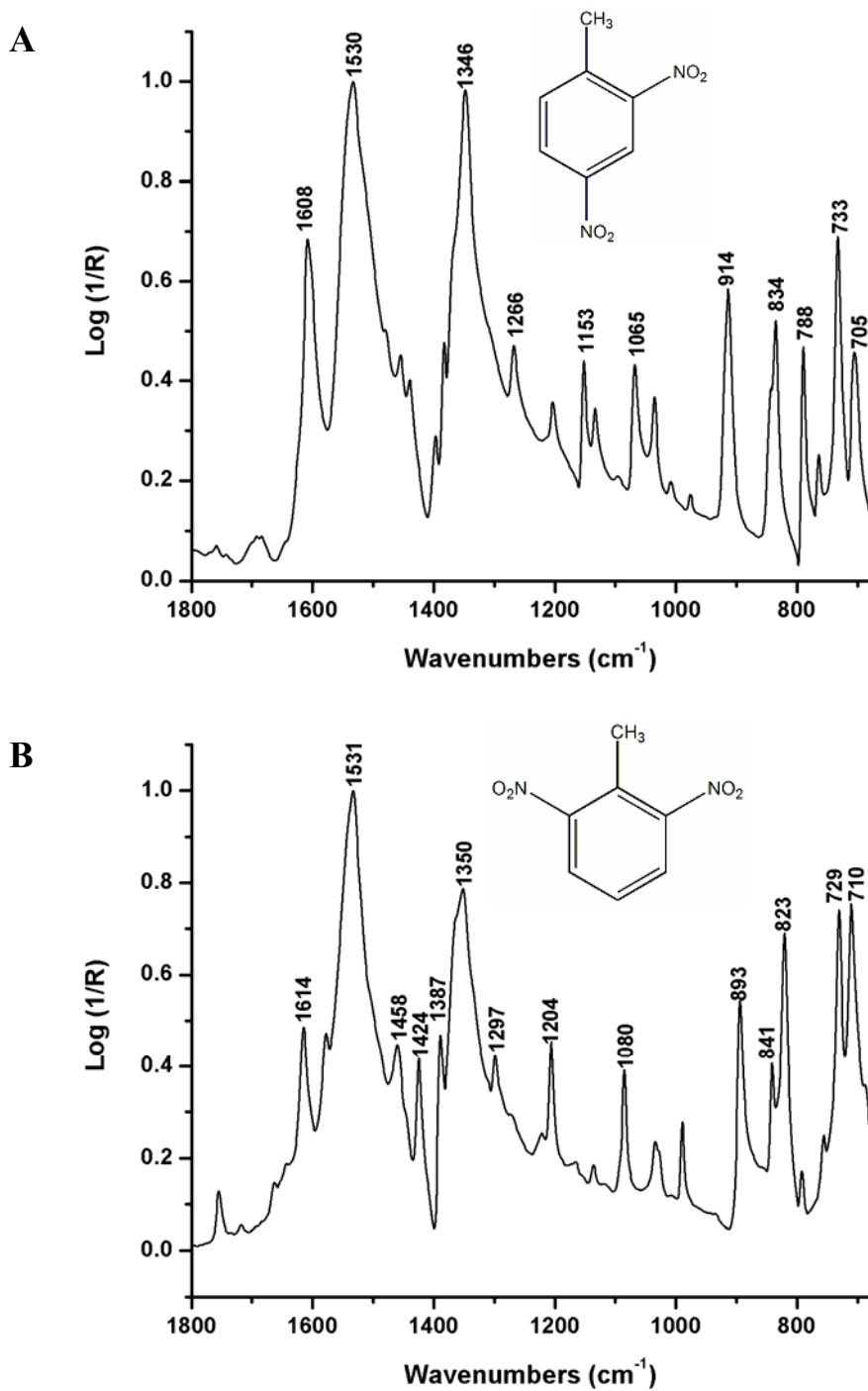


**Figure 55.** An example of the SR-IMS spectra taken from a section of a dark brown sunflower root from 2,6-DNT treated plants. The infrared beam is completely absorbed by the dark root section so that no discernable peaks can be observed.

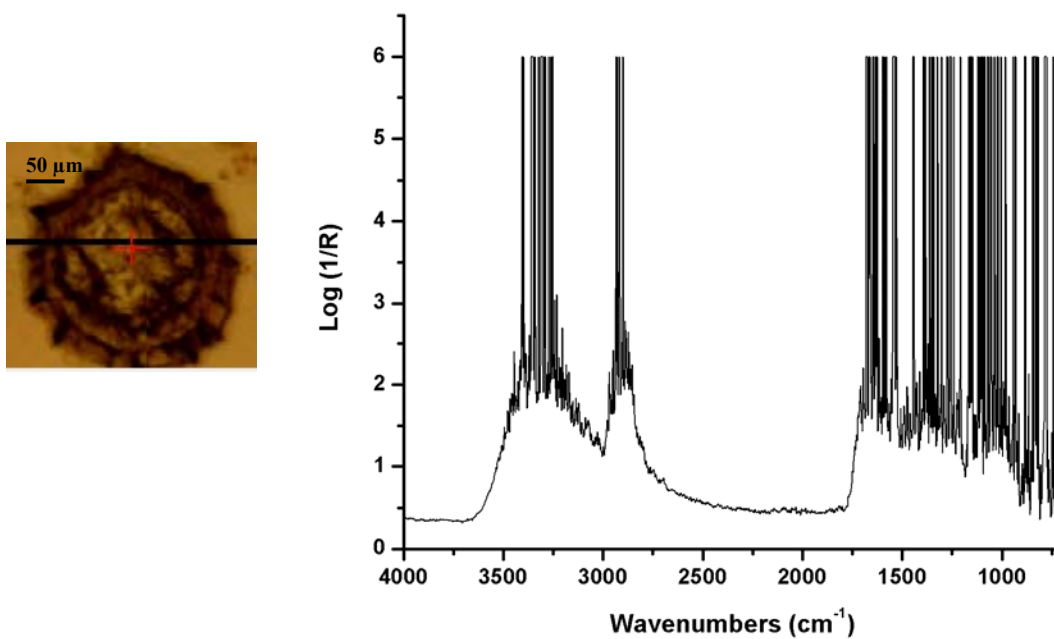


**Figure 56.** Exploratory PCA shows separation between the root vascular (cortex) tissue of untreated control (■) and 5 mg/L 2,4-DNT treated sunflower plants (●) using the first 2 PC scores.

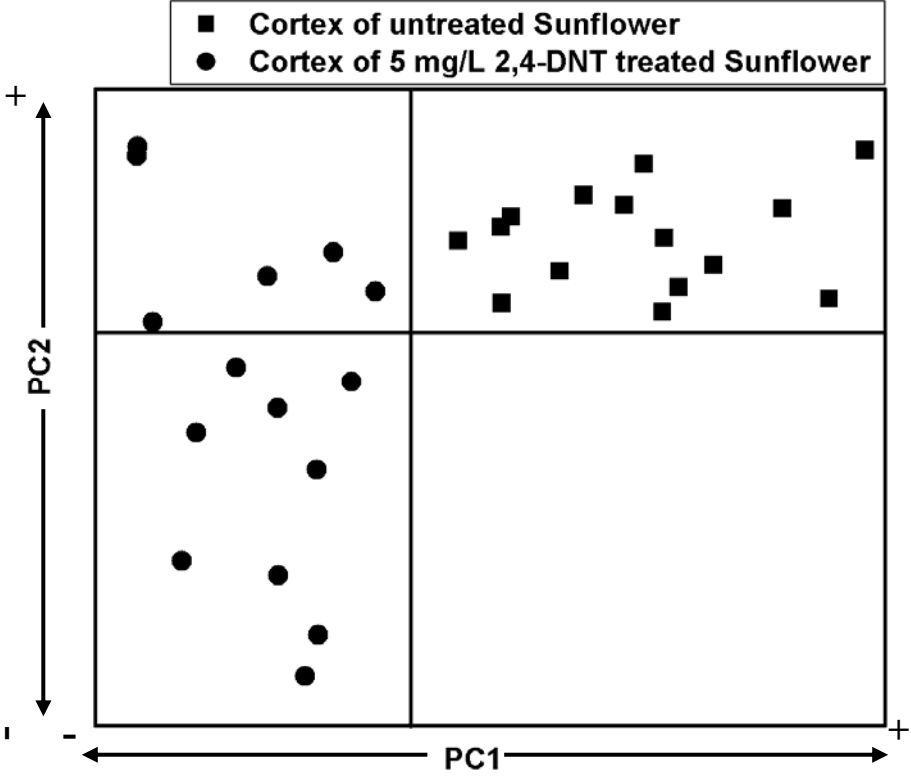


**Figure 57.** The PC loadings derived from the exploratory PCA of vascular (cortex) tissue from untreated control and 5 mg/L 2,4-DNT treated sunflower plants. (A) The first PC loading accounted for almost 90% of the overall spectral variance. (B) The second PC loading accounted for only 5.3% of the spectral variance.

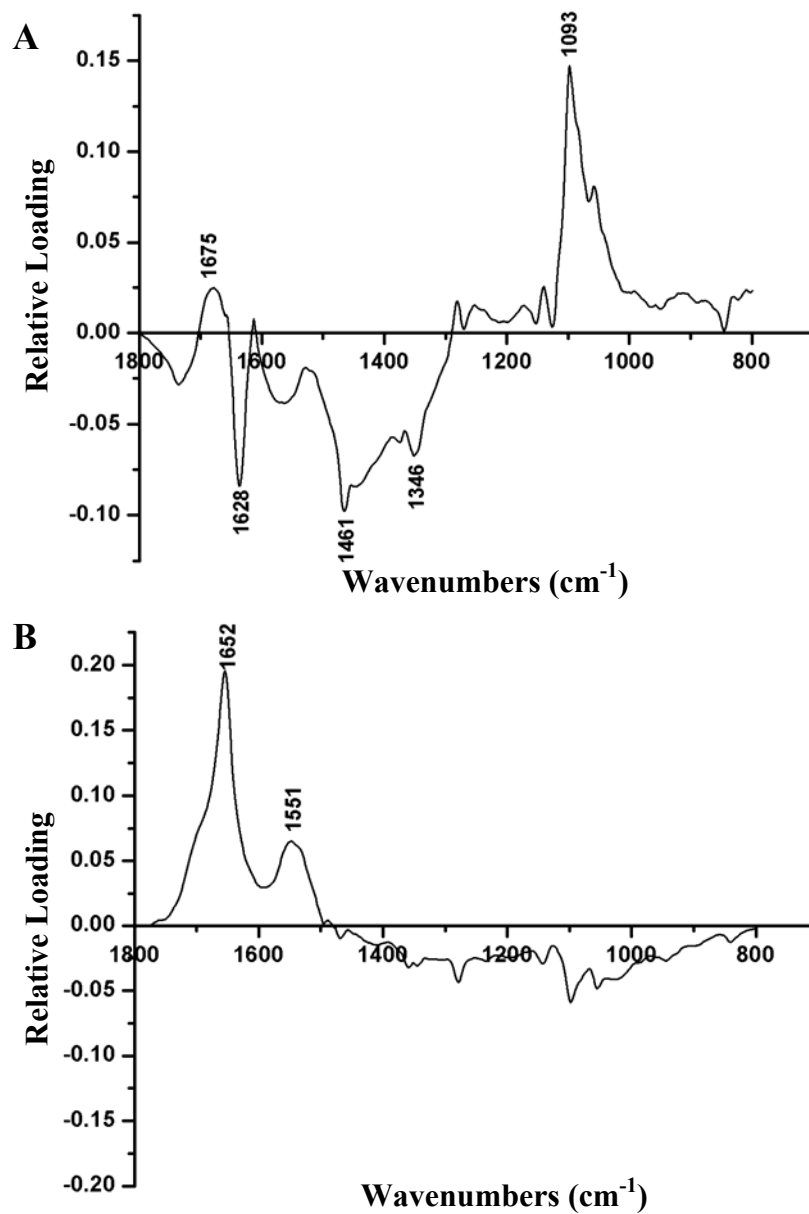


**Figure 58.** Typical spectra of epidermis tissue from untreated and 5 mg/L 2,4-DNT treated sunflower plants (listed bottom to top). Each spectrum is an average of 10 epidermal spectra sampled at 400  $\mu\text{m}$  from the root tip. The spectra were normalized to the OH peak at 3350  $\text{cm}^{-1}$ . Spectra are arbitrarily offset for ease of presentation.

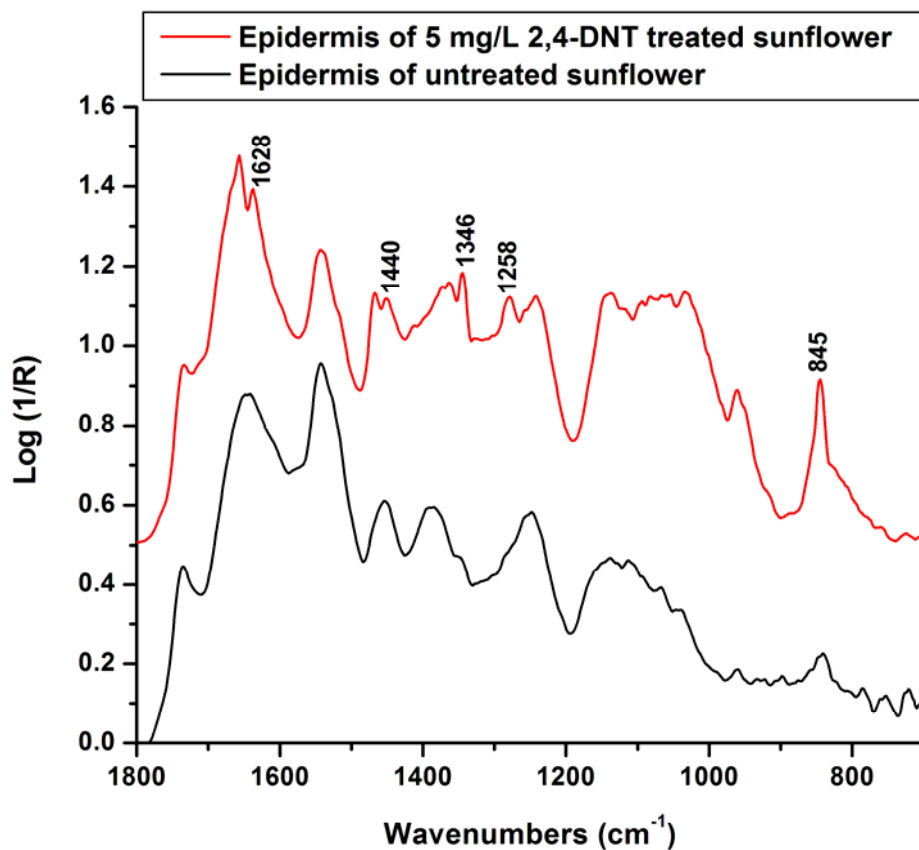


**Figure 59.** Functional group area maps showing the spatial distribution and concentration of 2,4-DNT and pectic polysaccharides in the root tissue of untreated and 5 mg/L 2,4-DNT treated sunflowers sectioned at about 400  $\mu\text{m}$  from the root tip. The intensity ruler is displayed under each functional group map. The red rectangle on the visible image of each root section denotes the area studied. (A) Visible image of root section from untreated (control) sunflower. Dimensions of the area studied: 200  $\mu\text{m}$  x 30  $\mu\text{m}$ . (B) Visible image of root section from sunflower treated with 5 mg/L 2,4-DNT. Dimensions of the area studied: 200  $\mu\text{m}$  x 50  $\mu\text{m}$ . Area under the peak centered at 1346  $\text{cm}^{-1}$  ( $\text{NO}_2$  symmetric stretch) representing the concentration and distribution of 2,4-DNT in untreated root tissue (C) and 5 mg/L 2,4-DNT treated root tissue (D). Area under the peak centered at 1093  $\text{cm}^{-1}$  representing the concentration and distribution of pectic polysaccharide in untreated root tissue (E) and 5 mg/L 2,4-DNT treated root tissue (F).

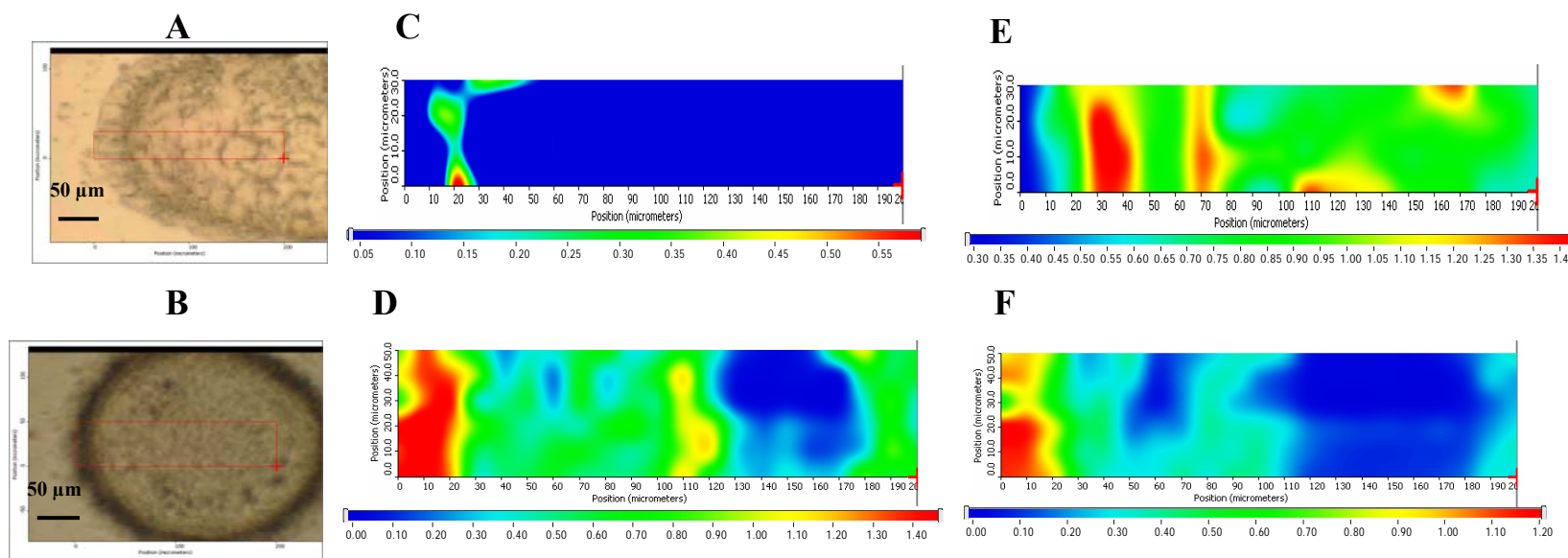




**Figure 60.** Exploratory PCA shows separation between the root epidermis of untreated control (■) and 5 mg/L 2,4-DNT treated maize plants (●) using the first 2 PC scores.

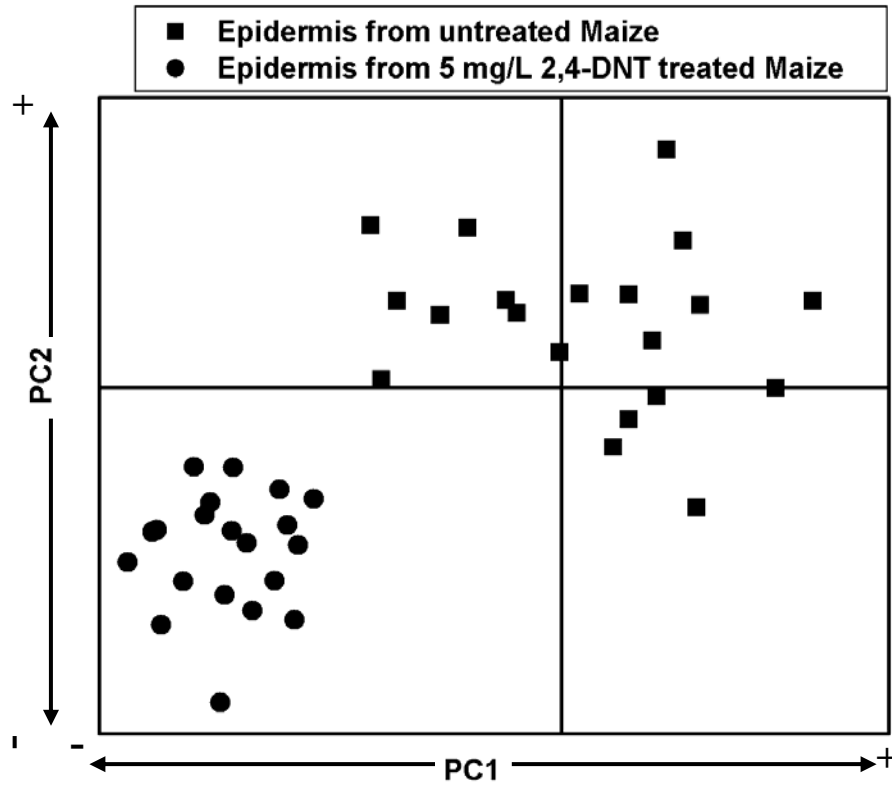


**Figure 61.** The PC loadings derived from the exploratory PCA of epidermal tissue from untreated control and 5 mg/L 2,4-DNT treated maize plants. (A) The first PC loading accounted for almost 62% of the overall spectral variance. (B) The second PC loading accounted for 25.6% of the spectral variance.

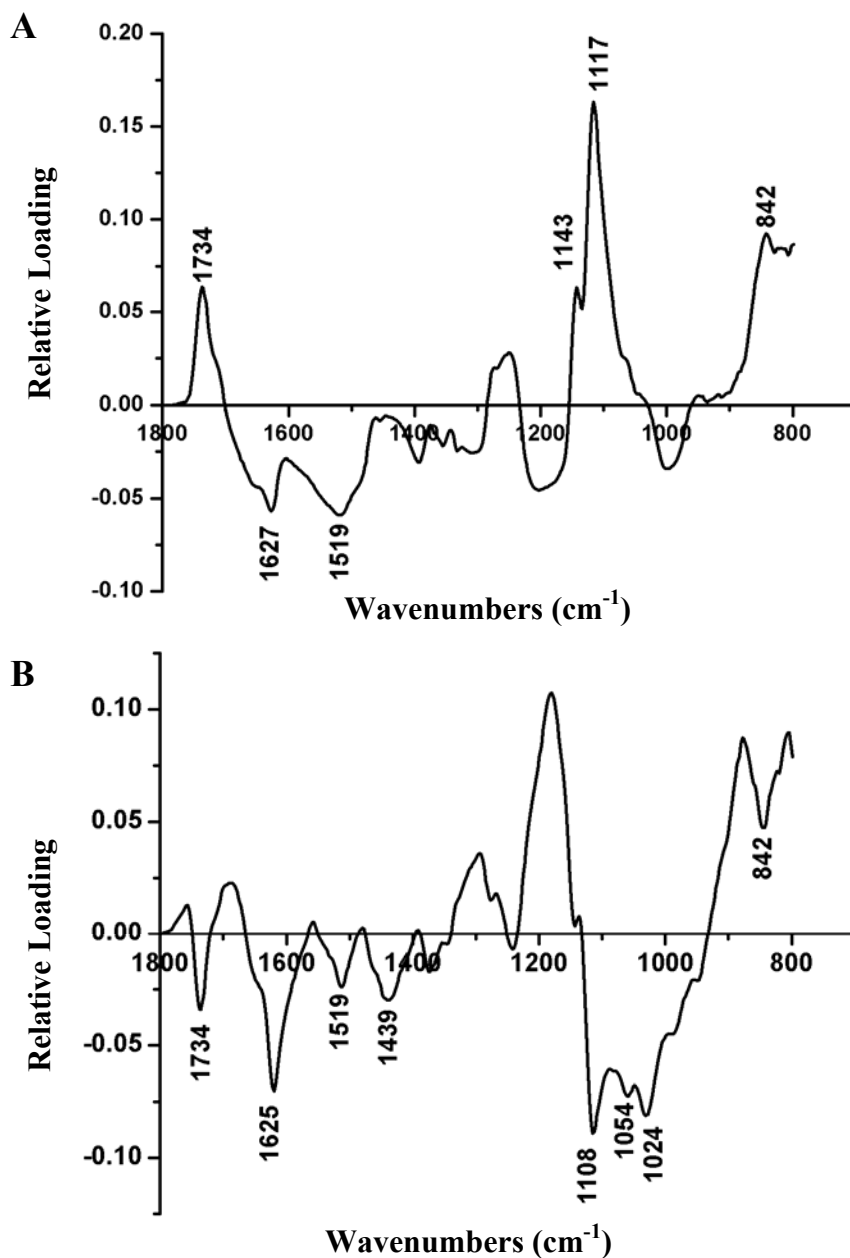


**Figure 62.** Functional group area maps showing the distribution of aromatic amines and pectic polysaccharides in the root tissue of untreated and 5 mg/L 2,4-DNT treated maize plants sectioned between 700 and 800  $\mu\text{m}$  from the root tip. The intensity ruler is displayed under each functional group map. (A) Visible image of root section from untreated (control) maize. (B) The blue rectangle denotes the area studied; dimensions: 380  $\mu\text{m}$  x 45  $\mu\text{m}$ . (C) Visible image of root section from maize treated with 5 mg/L 2,4-DNT. (D) The blue rectangle denotes the area studied; dimensions: 330  $\mu\text{m}$  x 70  $\mu\text{m}$ . Area under the peak centered at 1627  $\text{cm}^{-1}$  representing concentration and distribution of aromatic amines in untreated root tissue (E), 5 mg/L 2,4-DNT treated root tissue (F). Area under the peaks centered at 1100  $\text{cm}^{-1}$ , 1054  $\text{cm}^{-1}$  and 1024  $\text{cm}^{-1}$  representing concentration and distribution of pectin in untreated root tissue (G), 5 mg/L 2,4-DNT treated root tissue (H).

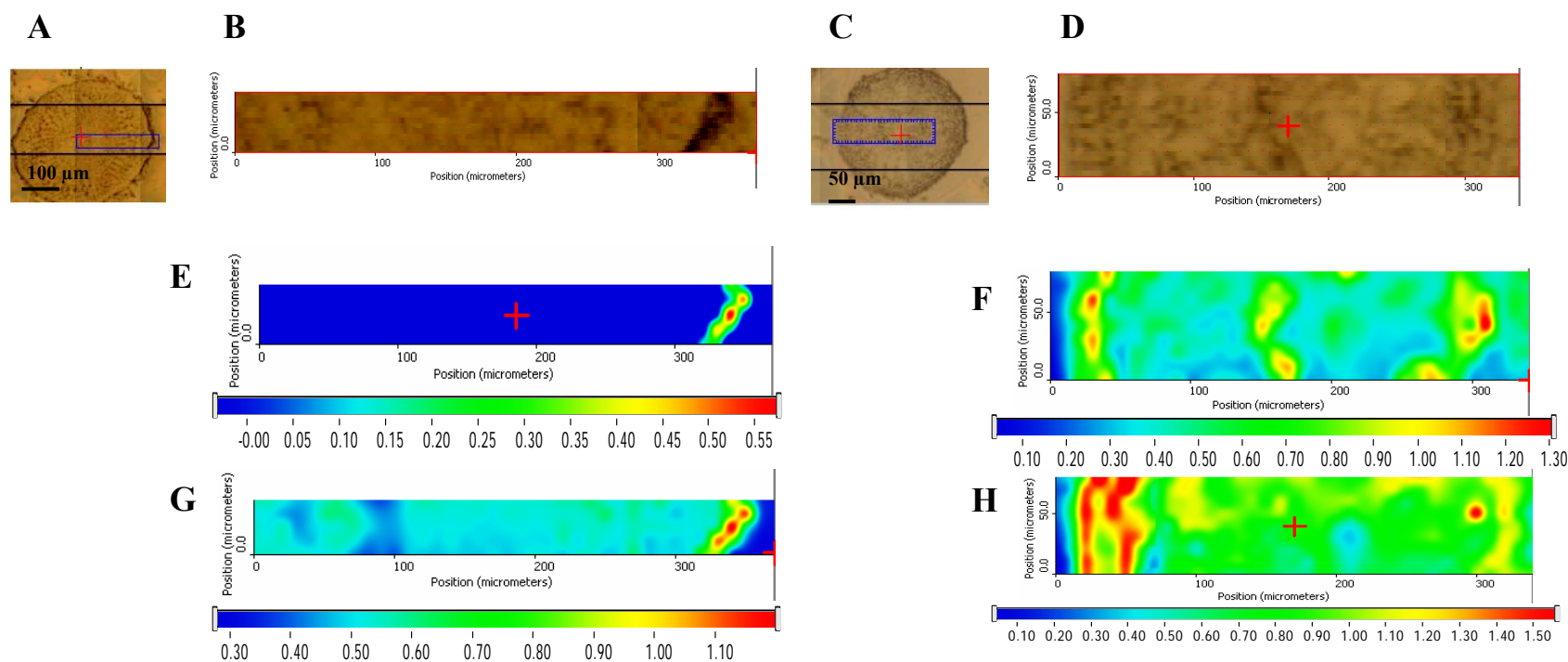


**Figure 63.** Typical spectra of xylem tissue from untreated and 10 mg/L 2,4-DNT treated maize plants (listed bottom to top). Each spectrum is an average of 10 xylem spectra. The spectra were normalized to the OH peak at 3350  $\text{cm}^{-1}$ . Spectra are arbitrarily offset for ease of presentation.

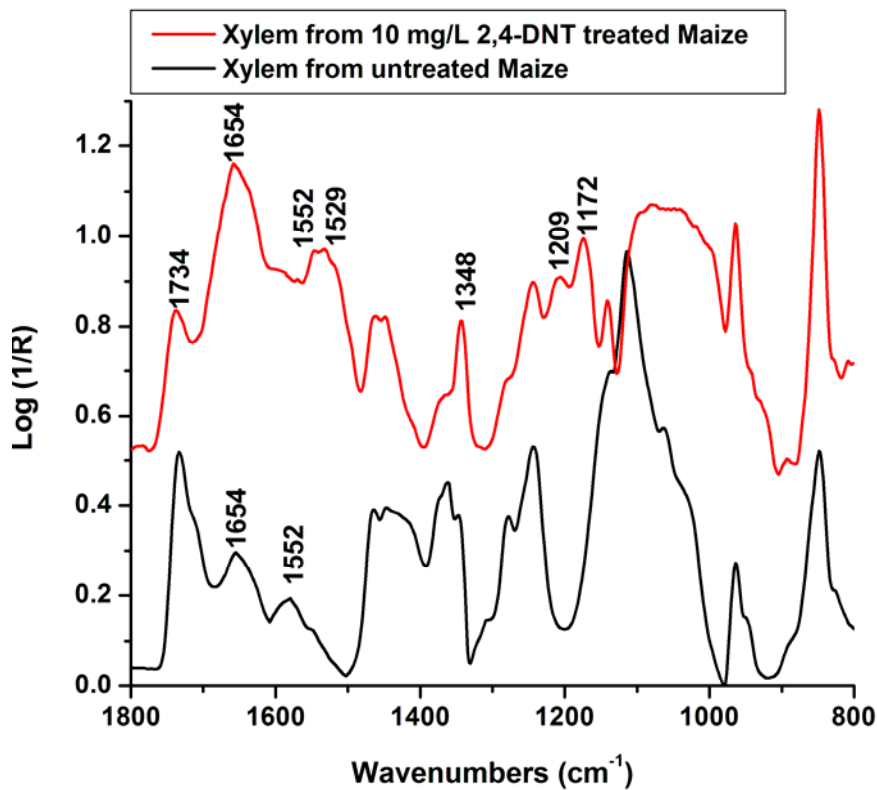


**Figure 64.** Functional group area maps showing the distribution of DNT and proteins in the root tissue of untreated and 10 mg/L 2,4-DNT treated maize plants sectioned about 1 cm from the root tip. The intensity ruler is displayed under each functional group map. (A) Visible image of root section from untreated (control) maize. (B) The blue rectangle denotes the area studied; dimensions: 480  $\mu\text{m}$  x 50  $\mu\text{m}$ . (C) Visible image of root section from maize treated with 10 mg/L 2,4-DNT. (D) The blue rectangle denotes the area studied; dimensions: 300  $\mu\text{m}$  x 80  $\mu\text{m}$ . Area under the peak centered at 1346  $\text{cm}^{-1}$  ( $\text{NO}_2$  symmetric stretch) representing the concentration and distribution of 2,4-DNT in untreated root tissue (E), 10 mg/L 2,4-DNT treated root tissue (F). Area under the peak centered at 1734  $\text{cm}^{-1}$  representing concentration and distribution of esterified pectins (methyl ester) in untreated root tissue (G), 10 mg/L 2,4-DNT treated root tissue (H).

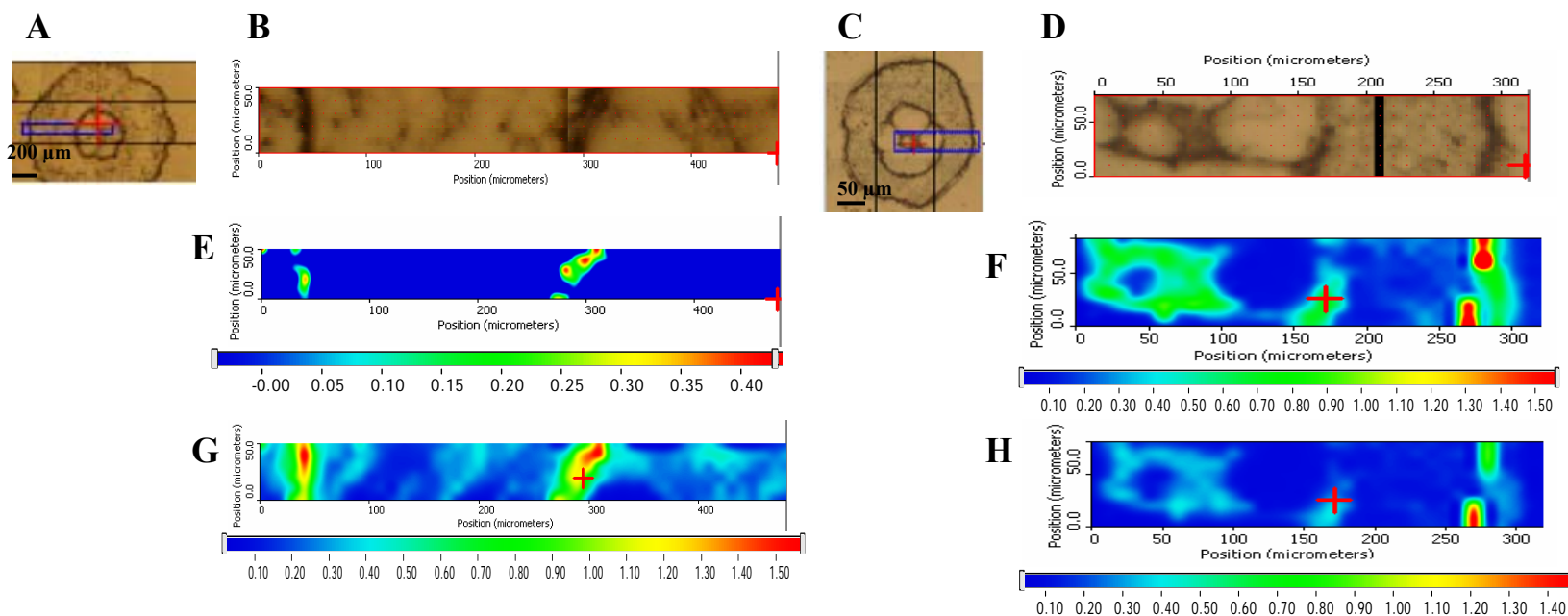


**Figure 65.** Exploratory PCA shows separation between the root vascular (cortex) tissue of untreated control (■) and 10 mg/L 2,6-DNT treated maize plants (●) using the second and third PC scores.

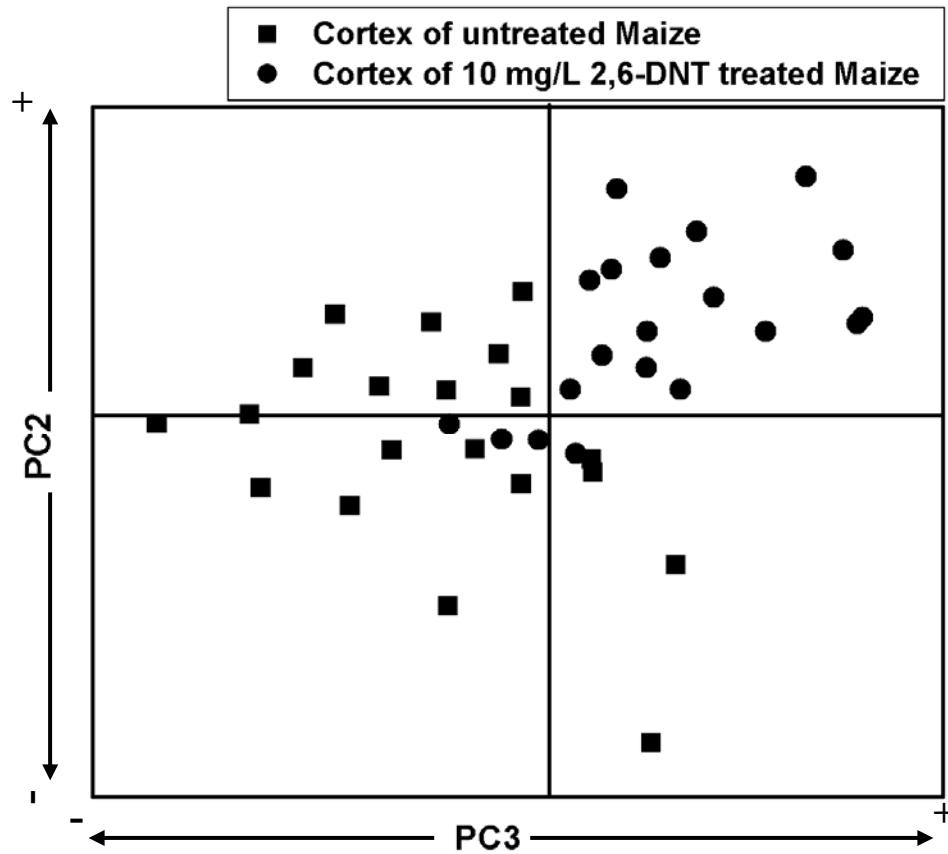


**Figure 66.** The PC loadings derived from the exploratory PCA of vascular (cortex) tissue from untreated control and 10 mg/L 2,6-DNT treated maize sunflower plants. (A) The second PC loading accounted for almost 30% of the overall spectral variance. (B) The third PC loading accounted for only 10.6% of the spectral variance.

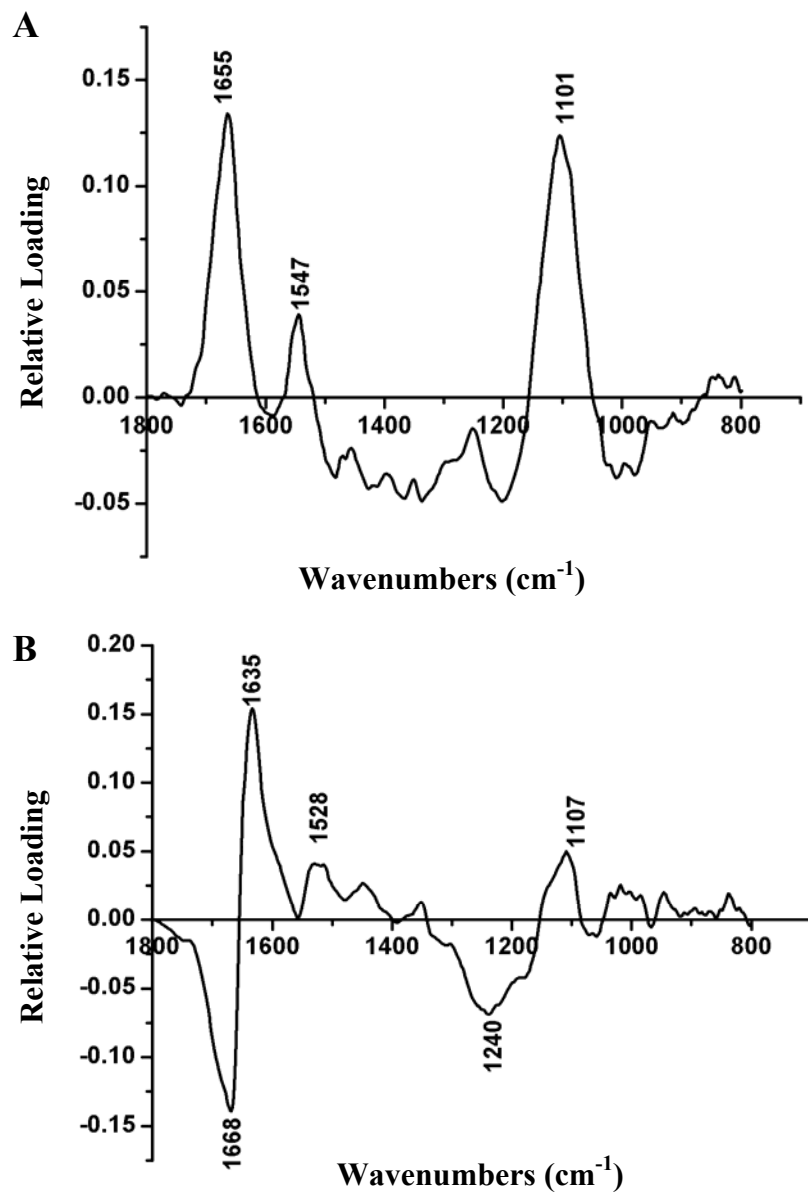






**Figure 68.** The PC loadings derived from the exploratory PCA of epidermal tissue from untreated control and 10 mg/L 2,6-DNT treated maize plants. (A) The first PC loading accounted for almost 71% of the overall spectral variance. (B) The second PC loading accounted for 18% of the spectral variance.

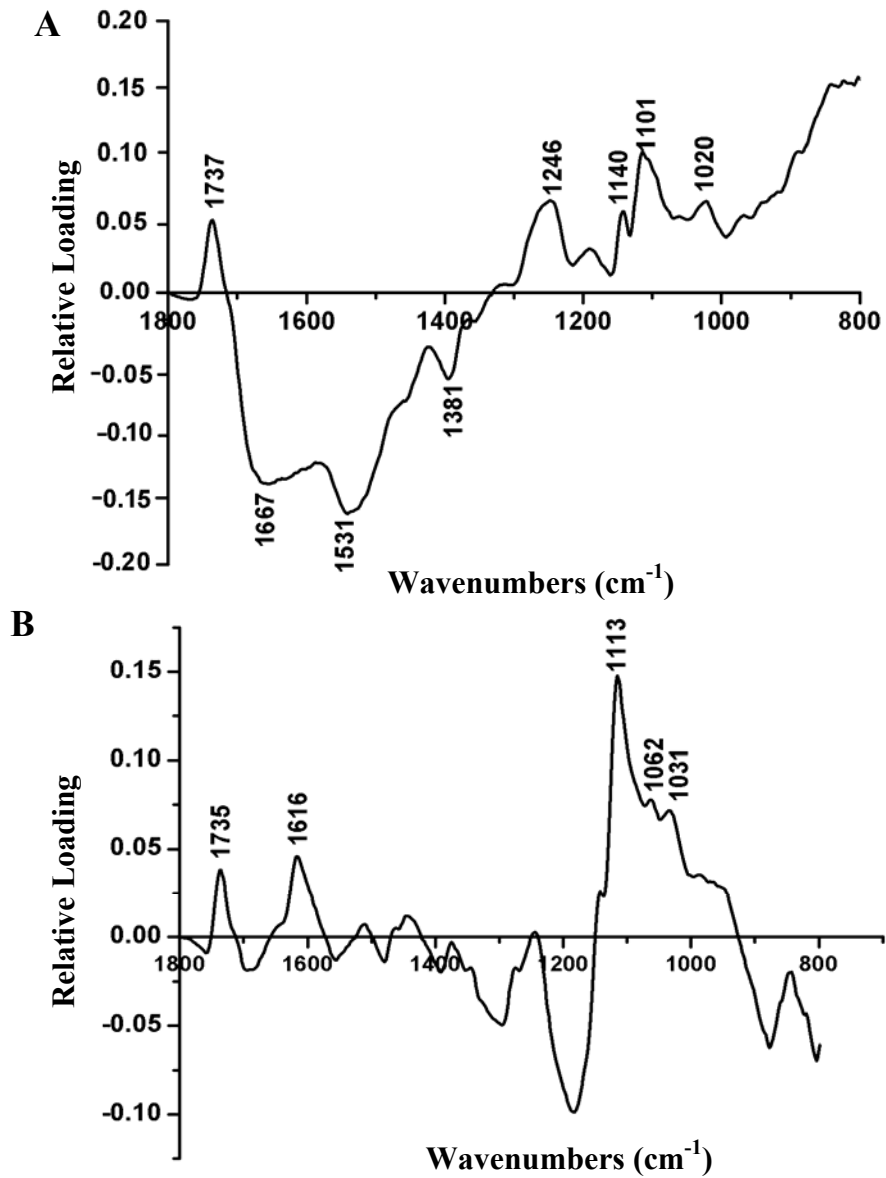
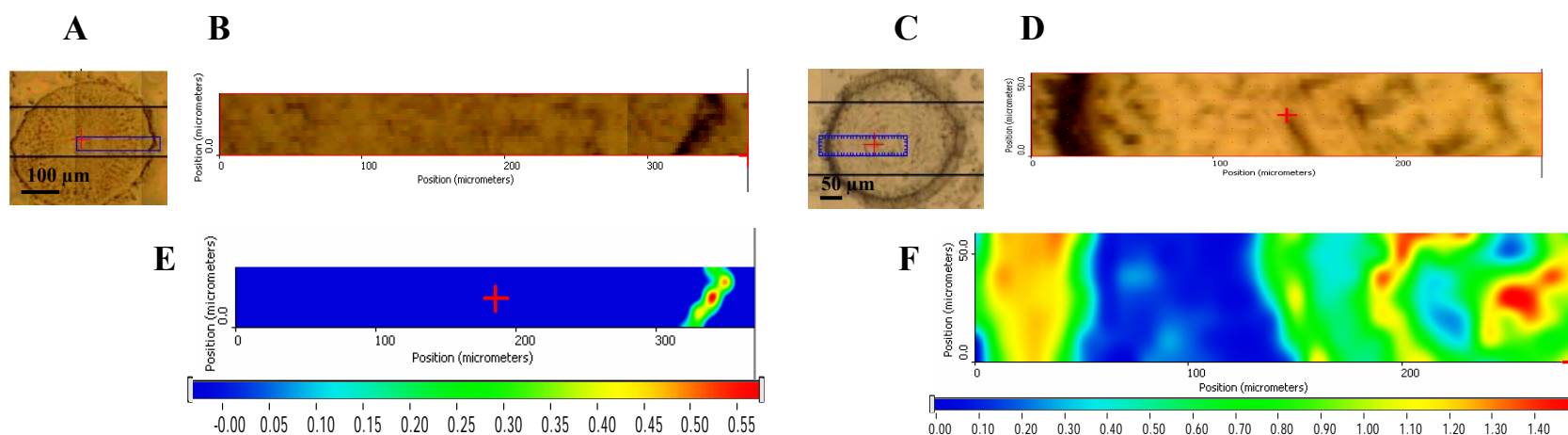


**Figure 69.** Functional group area maps showing the spatial distribution of DNT in the root tissue of untreated and 10 mg/L 2,6-DNT treated maize plants sectioned between 700 and 800  $\mu\text{m}$  from the root tip. The intensity ruler is displayed under each functional group map. (A) Visible image of root section from untreated (control) maize. (B) The blue rectangle denotes the area studied; dimensions: 380  $\mu\text{m}$  x 45  $\mu\text{m}$ . (C) Visible image of root section from maize treated with 10 mg/L 2,6-DNT. (D) The blue rectangle denotes the area studied; dimensions: 280  $\mu\text{m}$  x 60  $\mu\text{m}$ . Area under the peak centered at 1346  $\text{cm}^{-1}$  ( $\text{NO}_2$  symmetric stretch) representing the concentration and distribution of DNT in untreated root tissue (E), 10 mg/L 2,6-DNT treated root tissue (F).



**CHAPTER 6 - MONITORING THE FATE AND EFFECT OF 2,6-DICHLOROPHENOL (2,6-DCP) IN SUNFLOWER AND MAIZE PLANTS USING SR-IMS**

## Introduction

The metabolism of 2,6-dichlorophenol (2,6-DCP) by plants has not been well studied. Most of the focus has been devoted to 2,4-dichlorophenol (2,4-DCP) since it is a common intermediate in the production of the herbicide 2,4-dichlorophenoxyacetic acid. Ensley *et al.* (1997) report that 2,6-DCP is used for the production of pesticides, herbicides, and fungicides, as an intermediate for the production of 2,4,6-trichlorophenol, in wood treatment plants, and in paper pulping. Long term exposure to DCPs (both 2,4 and 2,6-DCP) causes permanent damage to skin, eyes, liver and kidneys as well as being a suspected carcinogen (TOXNET, 2004). However, 2,6-DCP is thought to be the more toxic form of DCP.

There are only limited reports on the phytotoxic properties of 2,6-DCP. A study by Feng *et al.* (1996) reported EC<sub>50</sub> levels based on root elongation to be around 17 mg/l for cabbage grown in solutions containing 2,6-DCP. However, another study reports that *Brassica napus* can tolerate concentrations between 100 – 1000 mg/L of 2,4-DCP (Agostini *et al.*, 2003). There is clearly a lack of knowledge in regards to the phytotoxicity of DCPs in general. There are also no reports regarding the fate of 2,6-DCP in plant tissue, although, there are several papers that have studied the fate of 2,4-DCP in aquatic plants (Tront, 2004; Day, 2004; Ensley *et al.*, 1997; 1994). *Lemna minor* (duckweed) was found to modify 2,4-DCP by glycosidation and subsequently formed intermediate compounds that were either transferred to vacuoles or bound to cell walls through carbohydrates (Day, 2004). Another study using dried roots and shoots from rice indicated preferential absorption to the roots, about 2.75 times higher than shoots (Su and Zhu, 2006). 2,6-DCP is toxic to many bacteria and it is resistant to microbial degradation. This provides a reason for the lack of reports concerning the bioremediation of 2,6-DCP. However, there are works that discuss the use of biofilms such as *Alcaligenes*

*eutrophus* (a gram-negative chemolithotroph) to dehalogenate 2,4-DCP after its reduction to 3,5-dichlorocatechol (Koh *et al.*, 1997).

The above described publications are the extent of the research conducted on the fate and effect of DCPs in plants. Clearly there is a need for further study on DCPs, particularly 2,6-DCP, and its fate, effect, or phytotoxicity in plants. In this chapter, SR-IMS will be employed to determine the fate and effect of 2,6-DCP in the roots of maize and sunflower plants grown in Hoagland's solution initially containing 3, 6, and 10 mg/L for a one week period. IR spectroscopy has been used to follow the degradation of 2,4-dichlorophenol in cell suspensions of *A. eutrophus* (Koh *et al.*, 1997); thus showing the potential of SR-IMS to determine the fate of 2,6-DCP in plant tissue. Although there are no data discussing the fate of 2,6-DCP in plants, it is plausible to suggest that it will bind to tissues containing lipids or lignin, based on its log  $K_{OW}$  of 2.75 (refer to Table 2 for physical properties of 2,6-DCP).

## **Results and Discussion**

### *Loss of 2,6-DCP with maize and sunflower plants*

The plant growth and loss of 2,6-DCP for maize and sunflower plants grown in 150 mL of either 0, 3, 6, or 10 mg/L of 2,6-DCP for one week can be seen in Table 8. The data shows that most or all of the 2,6-DCP disappeared at all the concentrations tested. The reduction in fresh weight gain and dry weights at 6 and 10 mg/L reflects a toxic effect on both plants. A reduction in root and shoot elongation was observed for 2,6-DCP treatments at 6 and 10 mg/L whereas there was little or no effect at 3 mg/L. Also, the roots of both maize and sunflowers turned light brown after the one week of exposure to all concentrations of 2,6-DCP signifying the presence of phenolic compounds binding to the root surface (Agostini *et al.*, 2003). These

data put forward a different reason for the disappearance of 2,6-DCP from the growth solutions other than metabolism by the plants. A vapor pressure of  $4.74 \times 10^{-5}$  atm and Henry's law constant of  $2.7 \text{ atm}\cdot\text{m}^3/\text{mol}$  suggest that volatility may have played a role in the disappearance of 2,6-DCP. In order to determine if volatility causes loss of 2,6-DCP from the growth solutions a simple experiment was conducted. The amber stock jars used for the growth experiments were filled with 150 mL or partially filled with 50 mL of 10 mg/L 2,6-DCP (each case was tested in triplicate) and placed under lighting and conditions as used for the plant growth experiments. A first order decrease was observed resulting in about 30% decrease in concentration per day from the bottle initially containing 150 mL of solution. The loss of 2,6-DCP was faster when the starting solution was 50 mL. This provides evidence that volatility played a major role in the disappearance of 2,6-DCP from the growth solutions. Consequently, the amount of 2,6-DCP disappearance due to plant metabolism cannot be accurately determined.

#### *Interpretation of the FTIR spectrum 2,6-DCP*

The FTIR spectrum of 2,6-DCP in KBr is displayed in Figure 70. The band assignments for the spectrum are shown in Table 9 (Lin-Vien *et al.*, 1991). The most intense peak at  $766 \text{ cm}^{-1}$  represents C-H out-of-plane bending of the phenolic ring. An adjacent peak at  $712 \text{ cm}^{-1}$  corresponds to C-Cl stretch. If dehalogenation is part of the metabolism process, then this peak should become less intense after the loss of one Cl and disappear after the loss of the second Cl. IR bands corresponding to C=C stretch can be seen at  $1576 \text{ cm}^{-1}$ ,  $1465 \text{ cm}^{-1}$ , and  $1447 \text{ cm}^{-1}$ . Changes in intensity or shifts may indicate that the aromatic ring was broken during metabolism. The peak at  $1336 \text{ cm}^{-1}$  is diagnostic for phenolic rings, as it represents in-plane

bending of the O-H functional group. A loss of this peak would suggest a modification to the hydroxyl functionality of the phenolic ring. The IR bands for C-O stretching at  $1174\text{ cm}^{-1}$  and  $1144\text{ cm}^{-1}$  would concomitantly be affected upon loss of the hydroxyl group. The remaining bands correspond to C-H in-plane and out-of-plane bending.

#### *SR-IMS of sunflower roots exposed to 2,6-DCP*

Spectra collected from the cortex of 2,6-DCP treated and untreated sunflower plants sectioned  $400\text{ }\mu\text{m}$  from the root tip were similar upon visual inspection. Therefore, exploratory PCA was performed to determine the spectral variance, if any, that could be observed between them. Thirty spectra were used to perform the PCA. Fifteen spectra from the cortex region were randomly selected from two IR area maps of root tissue from  $3\text{ mg/L}$  2,6-DCP treated sunflower plants. The spectra of cortex from the untreated control were derived from PCA of maize and sunflower tissue in Chapter 3. Figure 71 displays the PCA plot showing separation between the cortex of untreated and  $3\text{ mg/L}$  2,6-DCP treated sunflower plants using the first and third principal component. The first component accounted for almost 91% of the spectral variance represented by its PC loading in Figure 72A. The first PC loading contains IR peaks indicative of amide I and amide II bands for protein. This result provides evidence that 2,6-DCP treatment causes damage to the production of protein in sunflower plants. Even though this difference in protein composition is not quantifiable using the current spectral data, the extremely high spectral variance associated with the first PC loading proves that the protein loss is a direct result of 2,6-DCP exposure. The spectral positions show no overlap with the spectrum of 2,6-DCP indicating that most spectral variance is associated with inhibitory effects of the compound on protein deposition. The second PC loading (Figure 72B) only accounts for

5.85% of the variance but the peaks are indicative of actual IR bands representing root material (usually a loading with low spectral variance contains mostly spectral noise). IR bands at 1257  $\text{cm}^{-1}$ , 1140  $\text{cm}^{-1}$ , and 1105  $\text{cm}^{-1}$  signify changes in the cellulose and polysaccharide structure in the 2,6- DCP treated sunflower plants. The region of 1000 – 817  $\text{cm}^{-1}$  contains peaks diagnostic for phenolic compounds. They are representative of C-H in-plane and out-of-plane bending of the aromatic ring. However, these bands are located at a different location than those observed in 2,6-DCP. This suggests a modification to the ring structure. The presence of a modified phenolic ring is also evidenced by peaks at 1625, 1562, and 1494  $\text{cm}^{-1}$ . However, since this loading contributes a very small amount to the overall spectral variance, it is likely that the modified phenolic ring is present at a very low concentration and the changes to the cellulose and polysaccharide portion are relatively minor.

Figure 73 depicts the functional group area maps showing the spatial distribution and concentration of 2,6-DCP or phenolics and proteins in the root tissue of untreated and 3, 6, and 10 mg/L 2,6-DCP treated sunflowers sectioned at about 400  $\mu\text{m}$  from the root tip. The concentration of phenolics, represented by the area under the peak centered at 817  $\text{cm}^{-1}$ , distributed in the cortex of the 2,6-DCP treated plants decreases as the concentration of 2,6-DCP increases (Figures 73E-H). The reverse trend can be observed for the distribution of phenolics in the epidermis of the 2,6-DCP treated plants. In Figures 73I-L, the concentration distribution of protein decreased as the concentration of 2,6-DCP was increased reflecting protein damage or less protein production.

The above results suggest that 2,6-DCP has been modified as evidenced by the shift of the IR peaks representing phenolic compounds. The fate of the modified form appears to be predominantly associated with the epidermis. However, at lower concentrations, the modified



form was observed in the cortex. The reason for this behavior is uncertain, but one possibility would be that the sunflower plant is able to completely absorb lower concentrations of 2,6-DCP into deeper tissues of the root before the modified phenolic form saturates the root surface. At higher concentrations, the sunflower root tissue is overwhelmed by increased binding of the modified phenolic polymer to the root surface, therefore, hindering absorption into deeper tissues.

#### *SR-IMS of maize roots exposed to 2,6-DCP*

IR functional maps obtained from root tissue of maize plants treated with 3 mg/L 2,6-DCP could not be used for analysis due to problems experienced with the synchrotron beam during their collection. Analysis of the roots of 6 and 10 mg/L 2,6-DCP treated maize plants was successful and will be discussed herein.

Exploratory PCA was performed on cortex tissue from untreated and 6 mg/L treated maize plants. Twenty spectra from each treatment were used to conduct the analysis. Spectra from 2,6-DCP treated tissue were randomly selected from three area IR maps, while spectra for untreated maize were obtained from the exploratory PCA of sunflower and maize cortex presented in Chapter 3. The PCA plot shown in Figure 74 depicts separation of the untreated and 6 mg/L 2,6-DCP treated tissue using the first two PCs. The first two PCs accounted for 89% and 6.2% of the spectral variability, respectively. The first PC loading (Figure 75A) shows IR peaks for protein (1654 and 1537  $\text{cm}^{-1}$ ) and polysaccharides (1072  $\text{cm}^{-1}$ ) indicating damage to the protein component and changes in the cross-linking or production in polysaccharides. Additional evidence of changes to the polysaccharide and cellulose component are observed at 1600, 1246, 1080, 973, and 939  $\text{cm}^{-1}$  in the second PC loading displayed in Figure 75B. Bands

associated with phenolic or aromatic compounds were not seen in either PC loading. However, peaks diagnostic for 2,6-DCP and phenolic compounds were seen in the spectra of epidermis of 10 mg/L 2,6-DCP treated maize plants (Figure 76). These peaks were located at 860, 827, and 799  $\text{cm}^{-1}$ . As in the PCA analysis of cortex of untreated and 2,6-DCP treated sunflower, changes in the polysaccharide (1464  $\text{cm}^{-1}$  and region of 1200 – 900  $\text{cm}^{-1}$ ), cellulose (1248  $\text{cm}^{-1}$ ), and proteins (1647 and 1550  $\text{cm}^{-1}$ ) regions were observed.

Figure 77 displays the functional group area maps showing the spatial distribution and concentration of 2,6-DCP or phenolics and proteins in the root tissue of untreated and 6 and 10 mg/L 2,6-DCP treated maize sectioned at about 700  $\mu\text{m}$  from the root tip. The distribution of 2,6-DCP or phenolics was isolated to the epidermis and endodermis of the maize root tissue (Figures 6.8D-E). The concentration of protein decreased as the concentration of 2,6-DCP exposed to the maize plants increased (Figures 77G-I). This same trend was observed for sunflower root tissue seen in Figures 73I-L.

The addition of 2,6-DCP demonstrated similar adverse effects to the protein, polysaccharide and cellulose portion of the root tissue of sunflower and maize plants. In both cases, the 2,6-DCP and/or its phenolic modified intermediate was primarily associated with tissues containing lignin and large amounts of lipids, such as the epidermis and endodermis, as was previously hypothesized based on the  $\log K_{\text{OW}}$  of 2,6-DCP. However, phenolics were detected in the cortex of 2,6-DCP treated sunflowers. The above results also propose that both maize and sunflower modify or change 2,6-DCP into a phenolic intermediate. But the mechanism in which sunflowers and maize metabolize 2,6-DCP still requires additional study. The identity of the root bound modified form of 2,6-DCP is unknown and the glycosylated

forms of DCP have not been characterized using IR spectroscopy. These must be determined in order to further ascertain the fate and transport of 2,6-DCP in sunflower and maize plants.

**Table 8.** Plant growth and uptake of 2,6-DCP by maize and sunflower plants exposed to various concentrations of 2,6-DCP for a 1 week growth period. \*

Plant n=3	DCP concentration (mg/L)	% DCP disappearance	Solution uptake (mL)	Fresh weight gain (g)	Dry weight (g)
Maize	0	-----	75±6	8.41±1.27	1.21±0.32
	3 mg/L 2,6-DCP	100	61±12	7.42±0.96	0.91±0.19
	6 mg/L 2,6-DCP	95.6±13.44	53±9	4.09±1.18	0.7±0.29
	10 mg/L 2,6-DCP	98.2±12.62	45±21	1.60±0.69	0.65±0.15
Sunflower	0	-----	109±11	5.48±0.81	0.97±0.18
	3 mg/L 2,6-DCP	100	93±8	5.94±1.36	1.10±0.30
	6 mg/L 2,6-DCP	80±5.38	61±7	4.45±1.27	0.86±0.25
	10 mg/L 2,6-DCP	77±10.23	52±11	3.66±1.03	0.51±0.19

\*Three replicates were used for each treatment. Starting volume for all growth solutions was 150 mL. Solutions were not renewed over the one week growth period.

**Table 9. Assignment of some important bands in the FTIR spectrum of pure 2,6-DCP (Lin-Vien et al., 1991).**

<b>Frequency (cm<sup>-1</sup>)</b>	<b>Assignment</b>
1576	C=C stretch
1465	C=C stretch
1447	C=C stretch
1336	in-plane O-H bend
1241	out-of-plane C-C-O stretch
1174	C-O stretch
1144	C-O stretch
1095	C-H in-plane bending of ring
1065	C-H in-plane bending of ring
799	C-H out-of-plane bending of ring
766	C-H out-of-plane bending of ring
712	C-Cl stretch

**Figure 70.** FTIR spectrum of 2,6-dichlorophenol (2,6-DCP) in KBr.

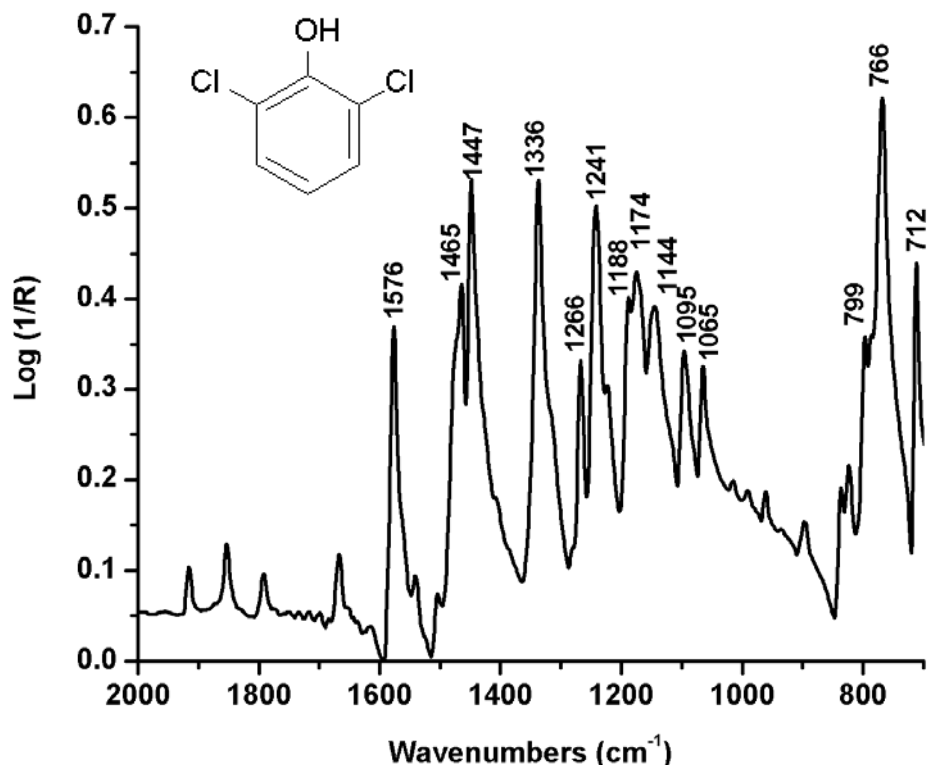


**Figure 71.** Exploratory PCA shows separation between the root vascular (cortex) tissue of untreated control (■) and 3 mg/L 2,6-DCP treated sunflower plants (●) using the first and third PC scores.

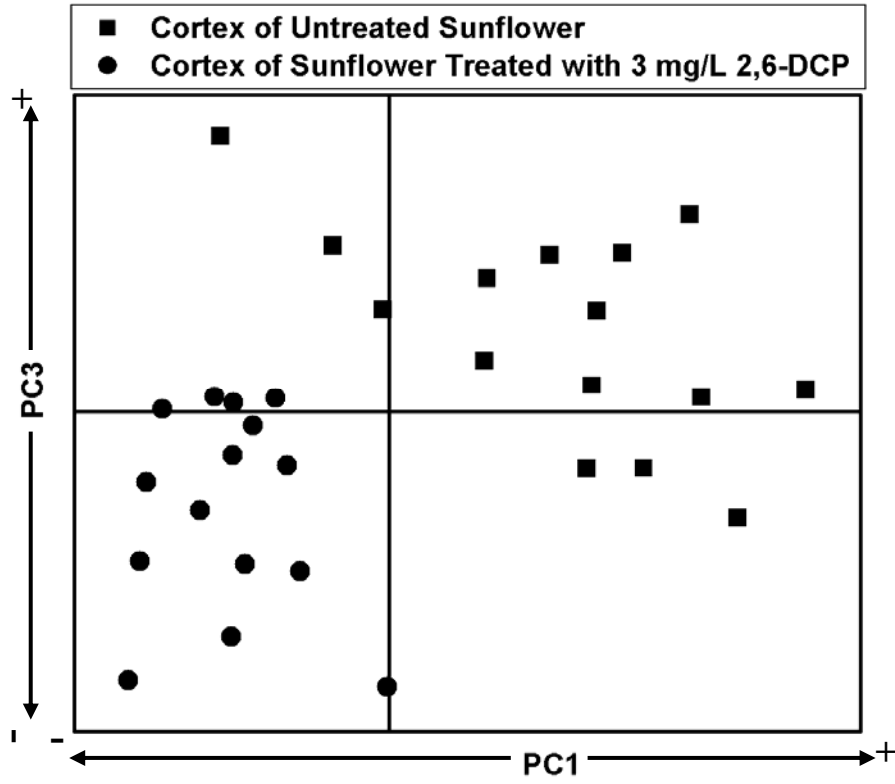


**Figure 72.** The PC loadings derived from the exploratory PCA of vascular (cortex) tissue from untreated control and 3 mg/L 2,6-DCP treated sunflower plants. (A) The first PC loading accounted for almost 92% of the overall spectral variance. (B) The third PC loading accounted for only 5.85% of the spectral variance.

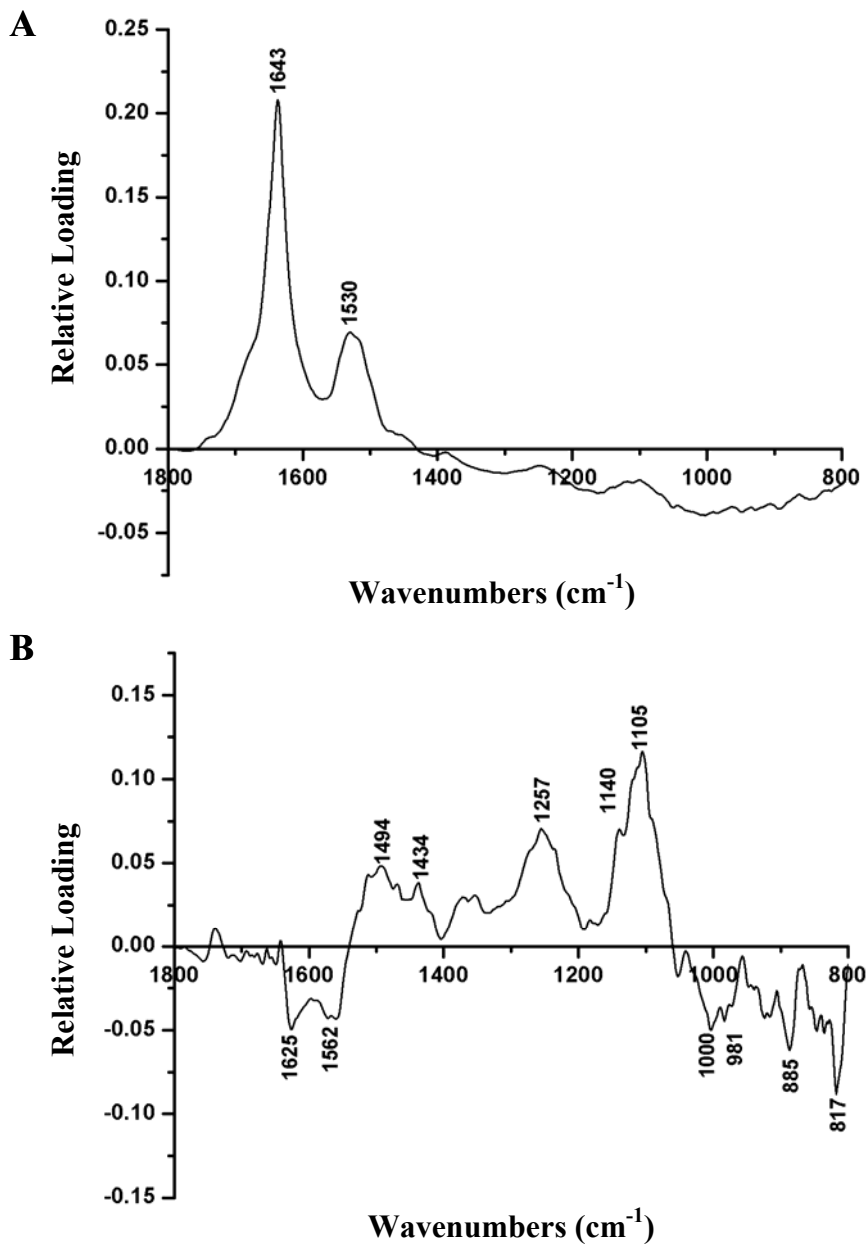




**Figure 73.** Functional group area maps showing the spatial distribution and concentration of 2,6-DCP or phenolics and proteins in the root tissue of untreated and 3, 6, and 10 mg/L 2,6-DCP treated sunflowers sectioned at about 400  $\mu\text{m}$  from the root tip. The intensity ruler is displayed under each functional group map. The blue rectangle on the visible image of each root section denotes the area studied. (A) Visible image of root section from untreated (control) sunflower. Dimensions of the area studied: 200  $\mu\text{m}$  x 30  $\mu\text{m}$ . (B) Visible image of root section from sunflower treated with 3 mg/L 2,6-DCP. Dimensions of the area studied: 210  $\mu\text{m}$  x 30  $\mu\text{m}$ . (C) Visible image of root section from sunflower treated with 6 mg/L 2,6-DCP. Dimensions of the area studied: 200  $\mu\text{m}$  x 20  $\mu\text{m}$ . (D) Visible image of root section from sunflower treated with 10 mg/L 2,6-DCP. Dimensions of the area studied: 220  $\mu\text{m}$  x 20  $\mu\text{m}$ . Area under the peak centered at 817  $\text{cm}^{-1}$  representing the concentration and distribution of 2,6-DCP or phenolics in untreated root tissue (E) and 3 mg/L 2,6-DCP (F), 6 mg/L 2,6-DCP (G), and 10 mg/L 2,6-DCP (H) treated root tissue. Area under the peak centered at 1643  $\text{cm}^{-1}$  representing the concentration and distribution of protein in untreated root tissue (I), 3 mg/L 2,6-DCP (J), 6 mg/L 2,6-DCP (K), and 10 mg/L 2,6-DCP (L) treated root tissue.

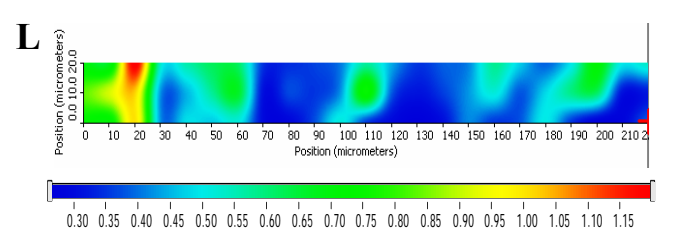
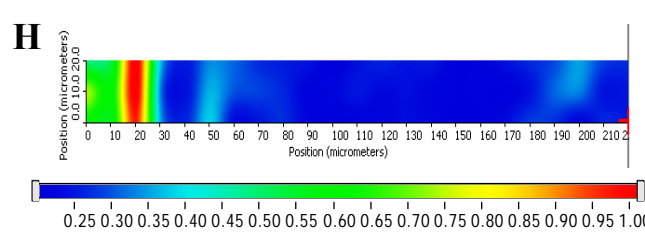
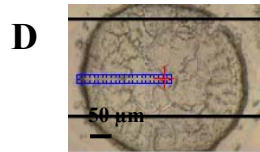
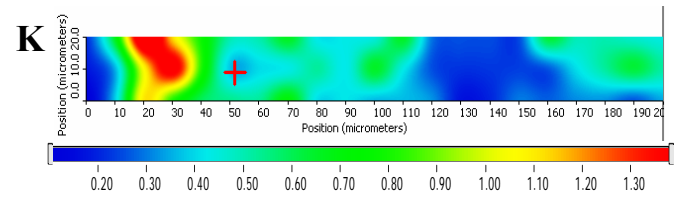
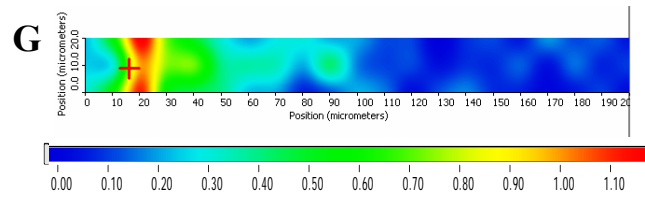
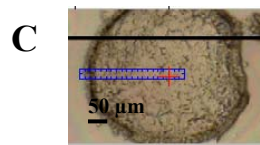
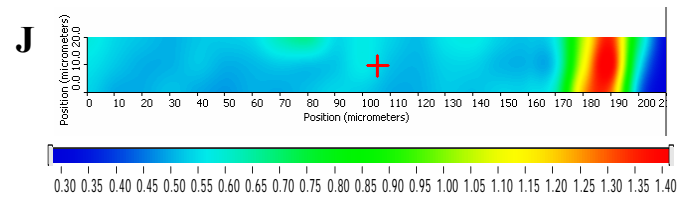
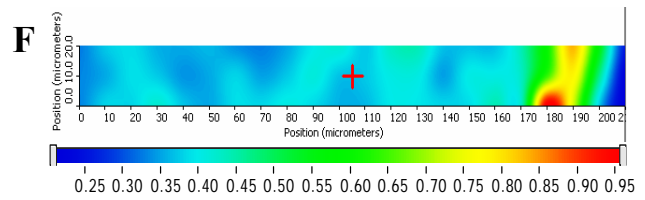
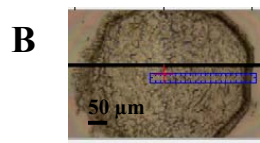
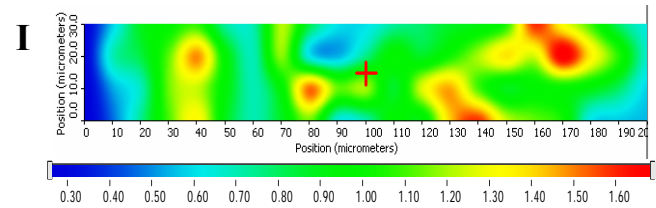
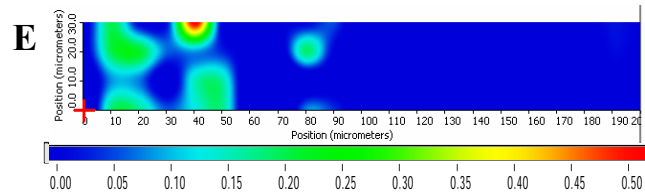
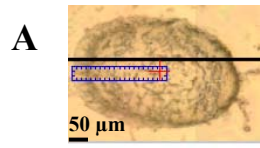


**Figure 74.** Exploratory PCA shows separation between the root vascular (cortex) tissue of untreated control (■) and 6 mg/L 2,6-DCP treated maize plants (●) using the first two PC scores.

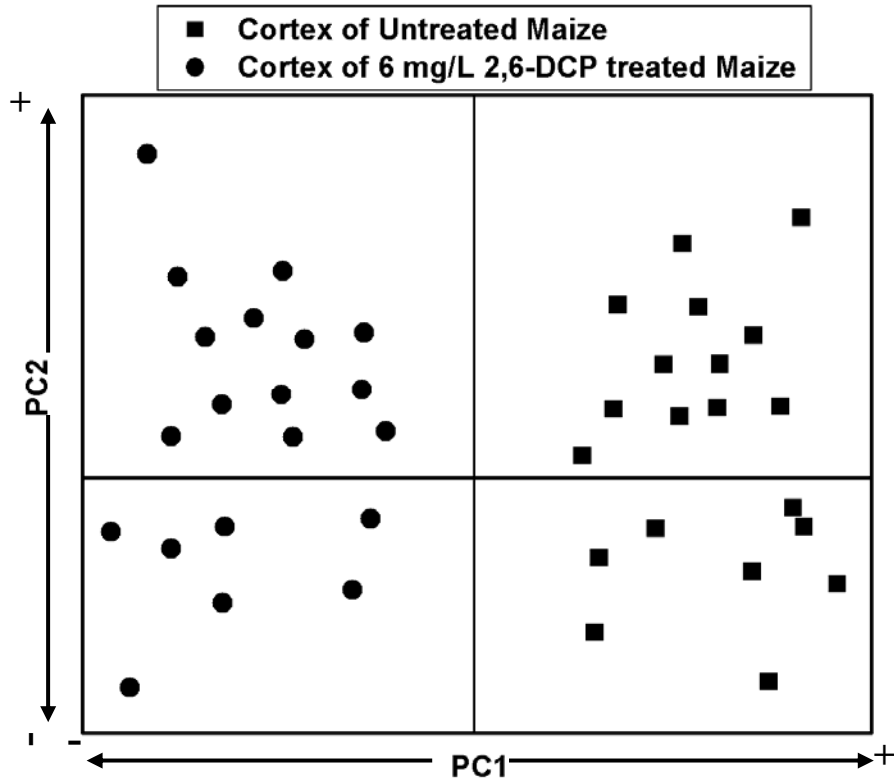


**Figure 75.** The PC loadings derived from the exploratory PCA of vascular (cortex) tissue from untreated control and 6 mg/L 2,6-DCP treated maize plants. (A) The first PC loading accounted for almost 89% of the overall spectral variance. (B) The second PC loading accounted for only 6.2% of the spectral variance.

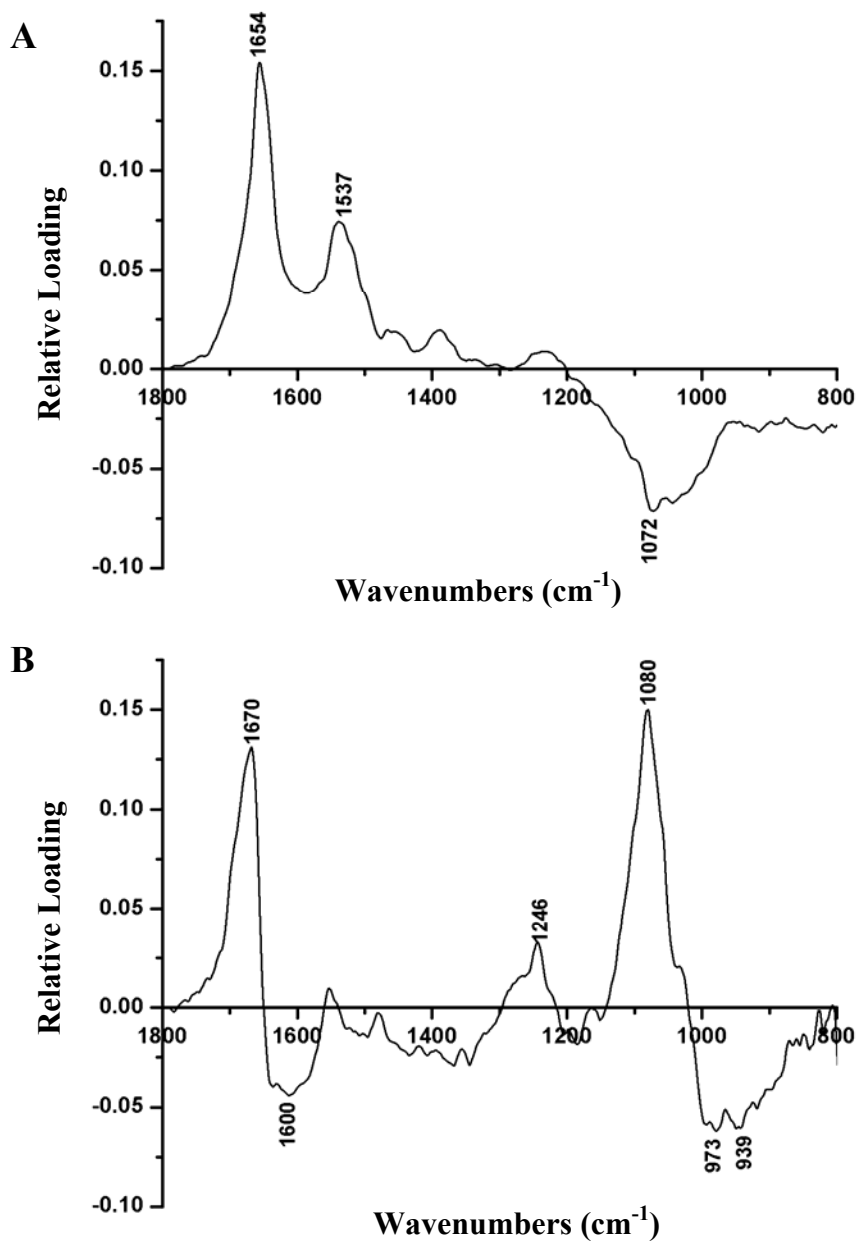


**Figure 76.** Typical spectra of epidermis tissue from untreated and 10 mg/L 2,6-DCP treated maize plants (listed bottom to top). Each spectrum is an average of 10 epidermal spectra sampled at 700  $\mu\text{m}$  from the root tip. The spectra were normalized to the carbohydrate fingerprint region at 1200 – 900  $\text{cm}^{-1}$ . Spectra are arbitrarily offset for ease of presentation.

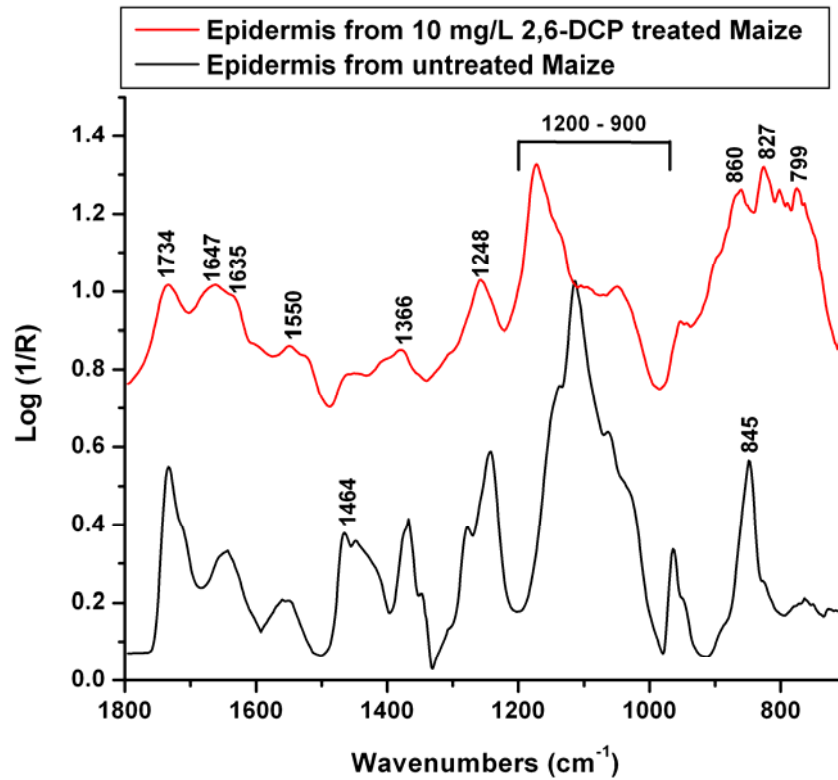
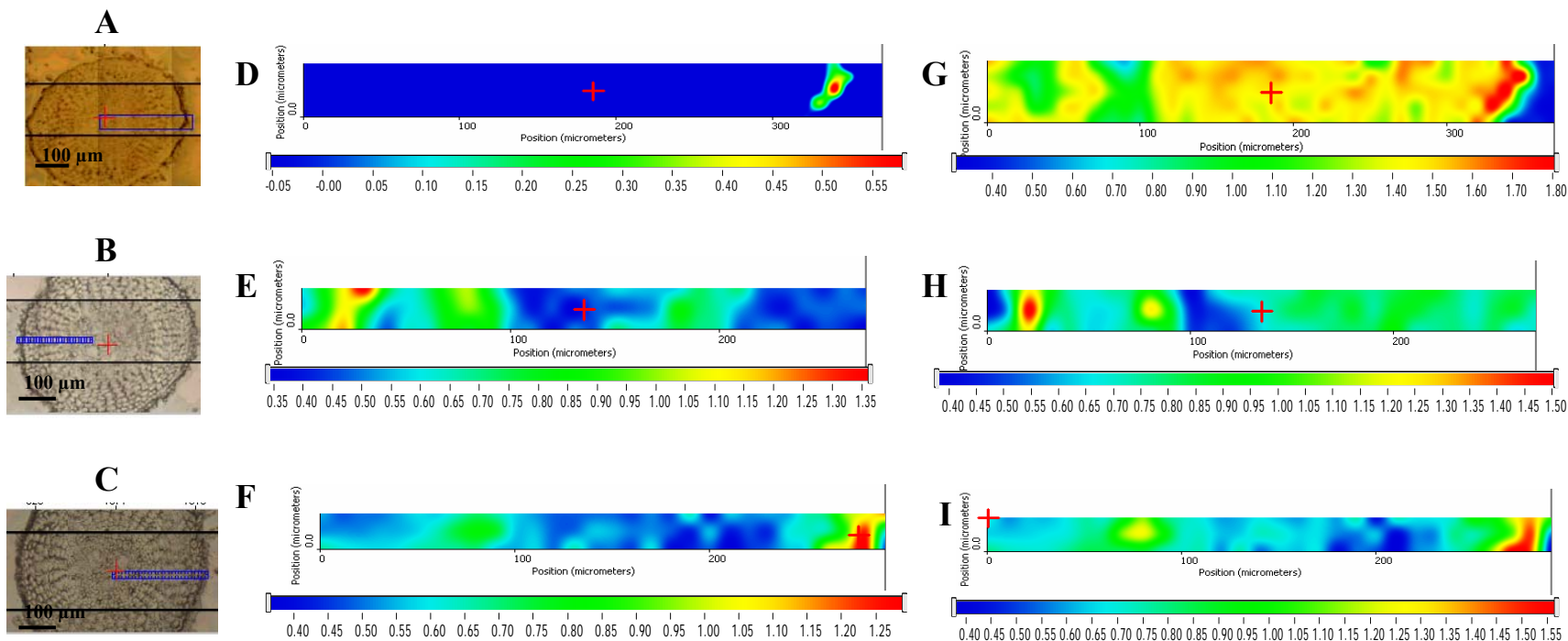


**Figure 77.** Functional group area maps showing the spatial distribution and concentration of 2,6-DCP or phenolics and proteins in the root tissue of untreated and 6 and 10 mg/L 2,6-DCP treated maize sectioned at about 700  $\mu\text{m}$  from the root tip. The intensity ruler is displayed under each functional group map. The blue rectangle on the visible image of each root section denotes the area studied. (A) Visible image of root section from untreated (control) maize. Dimensions of the area studied: 370  $\mu\text{m}$  x 40  $\mu\text{m}$ . (B) Visible image of root section from maize treated with 6 mg/L 2,6-DCP. Dimensions of the area studied: 270  $\mu\text{m}$  x 20  $\mu\text{m}$ . (C) Visible image of root section from maize treated with 10 mg/L 2,6-DCP. Dimensions of the area studied: 290  $\mu\text{m}$  x 20  $\mu\text{m}$ . Area under the peak centered at 799  $\text{cm}^{-1}$  representing the concentration and distribution of 2,6-DCP or phenolics in untreated root tissue (D) and 6 mg/L 2,6-DCP (E), 10 mg/L 2,6-DCP (F) treated root tissue. Area under the peak centered at 1643  $\text{cm}^{-1}$  representing the concentration and distribution of protein in untreated root tissue (G) and 6 mg/L 2,6-DCP (H) and 10 mg/L 2,6-DCP (I) treated root tissue.



## **CHAPTER 7 - FUTURE RESEARCH**

The potential of SR-IMS to study the microstructure in plant root tissue and to monitor the fate and effect of organic contaminants in plants was demonstrated herein. The limits and capabilities of this technique revealed the need for additional research. The study of plant structure using SR-IMS must be extended to the aerial parts of the plants including stems, leaves, and flowers. To this point there are only a handful of publications that have described the use of SR-IMS to study these types of tissues (Dokken *et al.* 2005a). Since this study only focused on roots it would be important to probe other tissues in order to provide an accurate assessment of the ultimate fate of a particular organic compound in plant. It would also be crucial to study the effects of organic contaminants in live plants. There is potential for this type of research as two reports have demonstrated the use of IMS to study live tissue using a hydration cell or root microcosms constructed of zinc selenide IR transmissive windows (Raab and Martin, 2001; Chen *et al.*, 1997). In this manner, it would be possible to study the effects of organic contaminants in real time. Sampling was an issue, as in some cases PCA was unable to differentiate between the cortex of sunflower and maize. It would also be beneficial to obtain additional independent samples in order to construct a more robust model set. With this in mind, it would also be important to study other plants in order to build a library of characteristic IR features in a variety of plant tissues. The examination of additional organic compounds possessing different chemical and physical properties would ensure a better understanding of the effect of a particular class of compounds on plant development. The results could then be compared to different developmental plant mutants to provide more insight on the plant response to a specific class of organic compounds. A further extension of this study would be to use SR-IMS to study plant tissues from actual contaminated soil. In the long term, SR-IMS may be developed as a tool to assess the ability of certain plants to remediate a particular class of compounds.



## **CHAPTER 8 - REFERENCES**

- Agostini, E., M.S. Coniglio, S.R. Milrad, H.A. Tigier, A.M. Giulietti, 2003. Phytoremediation of 2,4-dichlorophenol by *Brassica napus* hairy root cultures. *Biotechnology and Applied Biochemistry*, **37**, 139-144.
- Akin, D.E., D.S. Himmelsbach, R.T. Carl, W.W. Hanna, F.E. Barton, 1993. Mid-Infrared microspectroscopy to assess lignin in plant tissues related to digestibility. *Agronomy Journal*, **85**, pp. 171-175.
- Aspinall, G.O., 1980. Chemistry of cell wall polysaccharides, In: *The Biochemistry of Plants, Volume 3 Carbohydrates: Structure and Function*. J. Preiss (Ed.), Academic Press, New York, pp. 473-500.
- Barile, F.A., 2004. *Clinical Toxicology: Principles and Mechanisms*. CRC Press LLC, Boca Raton, Florida.
- Bausmith, D. and R. Neufeld, 1999. Soil biodegradation of propylene glycol based aircraft deicing fluids. *Water Environment Research*, **71**, pp. 459-464.
- Briggs, G.G., R.H. Bromilow, A.A. Evans, 1982. Relationship between lipophilicity and root uptake and translocation of non-ionised chemicals by barley. *Pesticide Science*, **13**, pp. 495-504.
- Briggs, G. G., 1981. Theoretical and Experimental Relationships Between Soil Adsorption, Octanol-Water Partition Coefficients, Water Solubilities, Bioconcentration Factors, and the Parachor. *Journal of Agricultural and Food Chemistry*. **29**, pp. 1050-1059.
- Brooks, R.R., 1998. *Plants that Hyperaccumulate Heavy Metals*. CAB International, New York City, New York.
- Brown, K., 1995. The Green Clean: The emerging field of phytoremediation takes root. *Bioscience*, **45**, p. 579.
- Budevskas, B.O., Sum, S.T., Jones, T.J., 2003. Application of multivariate curve resolution for analysis of FT-IR microspectroscopic images of *in situ* plant tissue. *Applied Spectroscopy*. **57**, pp. 124-131.
- Burken, J.G., 2003. Uptake and metabolism of organic compounds: Green-Liver Model, In *Phytoremediation: Transformation and Control of Contaminants*. S.C. McCutcheon and J.L. Schnoor (Eds.), John Wiley & Sons, Inc., New York, pp. 59-84.
- Burken, J.G., J.V. Shanks, P.L. Thompson, 2000. Phytoremediation and plant metabolism of explosives and nitroaromatic compounds. In: *Biodegradation of Nitroaromatic Compounds and Explosives*. J.C. Spains, J.B. Hughes, H. Knackmuss (Eds.), CRC Press, Boca Raton, FA, pp. 239-276.

- Cadet, F., C. Robert, B. Offman, 1997. Simultaneous determination of sugars by multivariate analysis applied to mid-infrared spectra of biological samples. *Applied Spectroscopy*, **51**, pp. 369-375.
- Carpita, N.C., 1996. Structure and biogenesis of the cell walls of grasses. *Annual Review of Plant Physiology and Plant Molecular Biology*, **47**, pp. 445-476.
- Carpita, N.C. and M.C. McCann, 2002. The functions of cell wall polysaccharides in composition and architecture revealed through mutations. *Plant and Soil*, **247**, pp. 71-80.
- Carpita, N.C., M. Defernez, K. Findlay, B. Wells, D.A. Shoue, G. Catchpole, R.H. Wilson, M.C. McCann, 2001. Cell wall architecture of the elongating maize coleoptile. *Plant Physiology*, **127**, pp. 551-565.
- Carr, G.L. 1999. High resolution microspectroscopy and sub-nanosecond time-resolved spectroscopy with the synchrotron infrared source. *Vibrational Spectroscopy*, **19**, pp. 53-60.
- Castro Diaz, S. 2003. Experimental study on phytotransformation of benzotriazoles in hydroponic culture of sunflowers. Ph.D. Dissertation, Kansas State University, Manhattan, KS.
- Castro Diaz, S. 2001. Use of vegetation for environmental management of aircraft deicing fluids. Masters Thesis, Department of Chemical Engineering, Kansas State University, Manhattan, KS, USA.
- Castro, S., L.C. Davis, L.E. Erickson, 2004a. Natural, cost-effective, and sustainable alternatives for treatment of aircraft deicing fluid waste. *Environmental Progress*, **24**, pp. 26-33.
- Castro, S., L.C. Davis, L.E. Erickson, 2004b. Temperature and pH effects on plant uptake of benzotriazoles by sunflowers in hydroponic culture. *International Journal of Phytoremediation*, **6**, pp. 209-225.
- Castro, S., L.C. Davis, L.E. Erickson, 2003. Phytotransformation of Benzotriazoles. *International Journal of Phytoremediation*, **5**, pp. 245-265.
- Castro, S., L.C. Davis, L.E. Erickson, 2001. Plant enhanced remediation of glycol-based aircraft deicing fluids. *Practice Periodical of Hazardous, Toxic, and Radioactive Waste Management*, **5**, pp. 141-152.
- Castro S., L. C. Davis, L. E. Erickson, 2000. Phytoremediation of aircraft deicer and antifreeze formulations. Proceedings of the 2000 Conference on Hazardous Waste Research, Denver, CO, pp. 141-152.
- Chen, D., 1993. *Plant uptake and soil adsorption of RDX*. M.S. Thesis. University of Illinois, Urbana-Champaign, Illinois, USA.

- Chen, L., N.C. Carpita, W.-D. Reiter, R.H. Wilson, C. Jeffries, M.C. McCann, 1998. A rapid method to screen for cell-wall mutants using discriminant analysis of Fourier transform infrared spectra. *Plant Journal*, **16**, pp. 385-392.
- Chen, L., R.H. Wilson, M.C. McCann, 1997. Infra-red microspectroscopy of hydrated biological systems: design and construction of a new cell with atmospheric control for the study of plant cell walls. *Journal of Microscopy*, **188**, pp. 62-71.
- Coates, J. 2000, Interpretation of infrared spectra, a practical approach. In: *Encyclopedia of Analytical Chemistry*. R.A. Meyers (Ed.), John Wiley and Sons Ltd., Chichester, pp 1-23.
- Cunningham, S.D., T.A. Anderson, A.P. Schwab, F.C. Hsu, 1996. Phytoremediation of soils contaminated with organic pollutants. In: *Advances in Agronomy*. D.L. Sparks (Ed.), Academic Press, Inc., San Diego, CA, **56**, pp. 56-114.
- Davis, L.C., S. Castro-Diaz, Q. Zhang, L.E. Erickson, 2002. Benefits of vegetation for soils with organic contaminants. *Critical Reviews in Plant Sciences*, **21**, pp. 457-491.
- Davis, L.C., D. Luper, J. Hu, and L.E. Erickson, 1999. Transport of trichloroethylene through living plant tissues. In: *Proceedings of the 1999 Conference on Hazardous Waste Research*. L.E. Erickson and M.M. Rankin (Eds.), Kansas State University, Manhattan, Kansas, pp. 203-209.
- Day, J.A., and F.M. Saunders, 2004. Glycosidation of Chlorophenols by *Lemna minor*. *Environmental Toxicology and Chemistry*, **23**, pp. 102-109.
- Deferenez, M. and E.K. Kemsley, 1997. The use and misuse of chemometrics for treating classification problems. *Trends in Analytical Chemistry*, **16**, pp. 216-221.
- Dokken, K.M., L.C. Davis, N.S. Marinkovic, 2005a. Use of infrared spectroscopy in plant growth and development. *Applied Spectroscopy Reviews*, **40**, pp. 301-326.
- Dokken, K.M, Davis, L.C., Marinkovic, N.S., 2005b. Synchrotron radiation, infrared microspectroscopy (SR-IMS) as a tool to study the fate and transport of organic contaminants in plants. *Spectroscopy*, **20**, pp. 14-20.
- Dokken, K.M., Davis, L.C., Erickson, L.E., Castro-Diaz, S., Marinkovic, N.S., 2005c. Synchrotron Fourier transform infrared microspectroscopy: A new tool to monitor the fate of organic contaminants in plants. *Microchemical Journal*, **81**, pp. 86-91.
- Dokken, K.M., L. C. Davis, L. E. Erickson, N. Marinkovic, 2004. Synchrotron Fourier transform infrared microspectroscopy as a tool to monitor the fate of organic contaminants in plants. In: *Proceedings of the 33rd Annual Biochemical Engineering Symposium*. P.J. Reilly (Ed.), University of Nebraska, Omaha, Nebraska, pp. 47-54.

- Dokken, K.M., L. C. Davis, L. E. Erickson, S. Castro, 2002. Fourier transform infrared spectroscopy as a tool to monitor changes in plant structure in response to soil contaminants. In: *Proceedings of the 2002 Conference on Application of Waste Remediation Technologies to Agricultural Contamination of Water Resources*. L.E. Erickson (Ed.), Kansas City, Kansas, pp. 250-256.
- Dumas, P. and L. Miller, 2003. Biological and biomedical applications of synchrotron infrared microspectroscopy. *Journal of Biological Physics*, **29**, pp. 201-218.
- Duncan, W.D., and G.P. Williams, 1983. Infra-red synchrotron radiation from electron storage rings. *Applied Optics*, **22**, pp. 2914-2923.
- Ensley, B.D., 2000. Rational use of phytoremediation. In *Phytoremediation of Toxic Metals: using plants to clean-up the environment*. I. Raskin and B.D. Ensley (Eds.), John Wiley & Sons, Inc., New York, pp. 3-12.
- Ensley, H.E., J.T. Barber, M.A. Polito, A.I. Oliver, 1994. Toxicity and Metabolism of 2,4-Dichlorophenol by the Aquatic Angiosperm *Lemna gibba*. *Environmental Toxicology and Chemistry*, **13**, pp. 325-331.
- Ensley, H.E., H.A. Sharma, J.T. Barber, M.A. Polito, 1997. Metabolism of Chlorinated Phenols by *Lemna gibba*, Duckweed. In *Phytoremediation of Soil and Water Contaminants*. E.L. Kruger, T.A. Anderson, T.A., J.R. Coats (Eds.), American Chemical Society, Washington, DC, pp. 238-253.
- Etnier, E.L., 1987. Water quality criteria for 2,4-dinitrotoluene and 2,6-dinitrotoluene. Final Report. In: *2,4-Dinitrotoluene*. ADA188713. Fort Derick, MD: U.S. Army Medical Bioengineering Research and Development Laboratory.
- Faix, O., 1992. Fourier transform infrared spectroscopy, In *Methods in Lignin Chemistry*. S.Y. Lin and C.W. Dence (Eds.), Springer-Verlag, Berlin, Germany, pp.83-109.
- Feng, L., L. Wang, Y. Zhao, B. Song, 1996. Effects of substituted anilines and phenols on root elongation of cabbage seeds. *Chemosphere*, **32**, pp. 1575-1583.
- Fischer, G., X. Cao, R.L. Purchase, 1996. FT-IR spectrum of the 2H-tautomer of benzotriazole in a supersonic jet. *Chemical Physics Letters*, **262**, pp. 689-698.
- Fringliei, U.P., 1992. In situ infrared internal reflection membrane spectroscopy, in *Internal Reflection Spectroscopy*. F.M. Mirabella, Jr. (Eds.), Marcel Dekker, New York, pp. 225-324.
- Gardea-Torresdey, G.L., J.R. Peralta-Videa, G. de la Rosa, J.G. Parsons, 2005. Phytoremediation of heavy metals and study of the metal coordination by X-ray absorption spectroscopy. *Coordination Chemistry Reviews*, **249**, pp. 1797-1810.

- Ghosh, U. and R.G. Luthy, 2006, Identification of location and nature of organic matter and contaminants on sediments. <http://www.als.lbl.gov/als/compendium/AbstractManager/uploads/00089.pdf>. Unpublished data.
- Gibeaut, D.M. and N.C. Carpita, 1991. Tracing cell wall biogenesis in intact cells and plants: selective turnover and alteration of soluble and cell wall polysaccharides in grasses. *Plant Physiology*, **97**, pp. 551-561.
- Hannink, N.K., S.J. Rosser, N.C. Bruce, 2002. Phytoremediation of explosives. *Critical Reviews in Plant Sciences*, **21**, pp. 511-538.
- Hart, D.S., L.C. Davis, L.E. Erickson, T.M. Callender, 2004. Sorption and partitioning parameters of benzotriazole compounds. *Microchemical Journal*, **77**, pp. 9-17.
- Hashimoto, A., K. Nakanishi, Y. Motonaga, T. Kameoka, 2001. Sugar metabolic analysis of suspensions of plant cells using an FT-IR/ATR method. *Biotechnology Progress*, **17**, pp. 560-564.
- Hashimoto, A. and T. Kameoka, 2000. Mid-infrared spectroscopic determination of sugar contents in plant-cell culture media using an ATR method. *Applied Spectroscopy*, **54**, pp. 1005-1011.
- Hauser, M.-T., A. Morikami, P.N. Benfey, 1995. Conditional root expansion mutants of *Arabidopsis*. *Development*, **121**, pp. 1237-1252.
- Heberle, J. and C. Zscherp, 1996. ATR/FT-IR difference spectroscopy of biological matter with microsecond time resolution. *Applied Spectroscopy*, **50**, pp. 588-596.
- Hergert, H.L., 1971. Infrared spectra, in *Lignins: Occurrence, Formation, Structure, and Reactions*. K.V. Sarkanen and C.H. Ludwig (Eds.), John Wiley and Sons, New York, pp.267-297.
- Hochholdinger, F., K. Woll, M. Sauer, D. Dembinsky, 2004. Genetic dissection of root formation in maize (*Zea mays*) reveals root-type specific developmental programmes. *Annals of Botany*, **93**, pp. 359-368.
- Hose, E., D.T. Clarkson, E. Steudle, L. Schreiber, W. Hartung, 2001. The exodermis: a variable apoplastic barrier. *Journal of Experimental Botany*, **52**, pp. 2245-2264.
- Jackson, M. and H.H. Mantsch, 1996. *Infrared spectroscopy of biomolecules*. H.H. Mantsch (Ed.). Wiley-Liss Inc., Toronto, Canada, pp. 311-319.
- Jarvis, M.C. and M.C. McCann, 2000. Macromolecular biophysics of the plant cell wall: Concepts and methodology. *Plant Physiology and Biochemistry*, **38**, pp. 1-13

- Jung, H.J.G., D.A. Deetz, 1993. Cell wall lignification and degradability. In: *Forage cell wall structure and Digestibility*. H.G. Jung, D.R. Buxton, J. Ralph (Eds), ASA-CSSA-SSSA, Madison, WI, pp. 315-346.
- Kacurakova, M., P. Capek, V. Sasinkova, N. Wellner, A. Ebringerova, 2000. FT-IR study of plant cell wall model compounds: pectic polysaccharides and hemicelluloses. *Carbohydrate Polymers*, **43**, pp. 195-203.
- Kemsley, E.K., 1998. *Discriminant Analysis and Class Modelling of Spectroscopic Data*. John Wiley and Sons, Chichester, UK.
- Koh, S., M.V. Mccullar, D.D. Focht, 1997. Biodegradation of 2,4-dichlorophenol through a distal meta-fission pathway, *Applied and Environmental Microbiology*, **63**, pp. 2054-2057.
- Komossa, D., C. Langerbartels, H. Sandermann, Jr., 1995. Metabolic processes for organic chemicals in plants. In: *Plant Contamination: Modeling and Simulation of Organic Chemical Processes*. S.Trapp and J.C. McFarlane (Eds.), CRC Press, Boca Raton, FA, pp. 69-103.
- Korte, F., G. Kvesitadze, D. Ugrekhelizde, M. Gordeziani, G. Khatisashvili, O. Buadze, G. Zaalishvili, F. Coulston, 2000. Organic toxicants and plants. *Ecotoxicology and Environmental Safety*, **47**, pp. 1-26.
- Larson, S.L., 1997. Fate of explosive contaminants in plants. *Annals of the New York Academy of Science*. **829**, pp. 195-201.
- Larson, S.L., R.P. Jones, L. Esacalon, D. Parker, 1999. Calssification of explosives transformation products in plant tissue. *Environmental Toxicology Chemistry*. **18**, pp. 1270-1276.
- Lasat, M.M., A.J.M. Baker, L.V. Kochian, 1996. Physiological characterization of root Zn<sup>2+</sup> absorption and translocation to shoots in Zn hyperaccumulator and nonaccumulator species of *Thlaspi*. *Plant Physiology*, **112**, pp. 1715-1722.
- Lin-Vien, D., N.B. Colthup, W.G. Fateley, J.G. Grasselli, 1991. *The Handbook of infrared and raman characteristic frequencies of organic molecules*. Academic Press, Inc., San Diego, California.
- Marsh, D., 1999. Quantitation of secondary structure in ATR infrared spectroscopy, *Biophysical Journal*. **77**, pp. 2630-2637.
- Marinkovic, N.S. and M.R. Chance, 2005. Synchrotron infrared microspectroscopy, In *Encyclopedia of Molecular Cell Biology and Molecular Medicine, Vol. 10*. R.A. Meyers (Ed.), VCH-Wiley, New York, pp. 1-29.

- Mascarenhas, M., J. Dighton, G.A. Arbuckle, 2000. Characterization of plant carbohydrates and changes in leaf carbohydrate chemistry due to chemical and enzymatic degradation measured by microscopic ATR FT-IR spectroscopy. *Applied Spectroscopy*, **54**, pp. 681-686.
- McCann, M.C., M. Bush, D. Milioni, P. Sado, N.J. Stacey, G. Catchpole, M. Deferenez, N.C. Carpita, H. Hofte, P. Ulvskov, R.H. Wilson, K. Roberts, 2001. Approaches to understanding the functional architecture of the plant cell wall. *Phytochemistry*, **57**, pp. 811-821.
- McCann, M.C., L. Chen, K. Roberts, E. K. Kemsley, C. Sene, N.C. Carpita, N.J. Stacey, R.H. Wilson, 1997. Infrared microspectroscopy: Sampling heterogeneity in plant cell wall composition and architecture. *Physiologia Plantarum*, **100**, pp. 729-738.
- McCann, M.C., K. Roberts, R.H. Wilson, M.J. Gidley, D.M. Gibeaut, J.-B. Kim, N.C. Carpita, 1995. Old and new ways to probe plant cell-wall architecture. *Canadian Journal of Botany*, **73**, pp. S103-S113.
- McCann, M.C., J. Shi, K. Roberts, N.C. Carpita, 1994. Changes in pectin structure and localization during the growth of unadapted and NaCl-adapted tobacco cells. *Plant Journal*, **5**, pp. 773-785.
- McCann, M.C., M. Hammouri, R. Wilson, P. Belton, K. Roberts, 1992. Fourier transform infrared microspectroscopy is a new way to look at plant cell walls. *Plant Physiology*, **100**, pp. 1940-1947.
- McCutcheon, S.C., and J.L. Schnoor, 2003. Overview of Phytotransformation and Control of Wastes, In *Phytoremediation: Transformation and Control of Contaminants*. S.C. McCutcheon and J.L. Schnoor (Eds.), John Wiley & Sons, Inc., New York, pp. 3-58.
- McCutcheon, S.C., V.F. Medina, S.L. Larson, 2003. Overview of Phytotransformation and Control of Wastes, In *Phytoremediation: Transformation and Control of Contaminants*. S.C. McCutcheon and J.L. Schnoor (Eds.), John Wiley & Sons, Inc., New York, pp.429-480.
- Mohan, S., K., K. Settu, 1993. Vibrational spectra and analysis of 1,2,3-benzotriazole. *Indian Journal of Pure and Applied Physics*, **31**, pp. 850-854.
- Morrison, III, W.H., D.S. Himmelsbach, D.E. Akin, J.D. Evans, 2003. Chemical and spectroscopic analysis of lignin in isolated flax fibers. *Journal of Agricultural and Food Chemistry*, **51**, pp. 2565-2568.
- Mouille, G., S. Robin, M. Lecomte, S. Pagant, H. Hofte, 2003. Classification and identification of Arabidopsis cell wall mutants using Fourier-transform infrared (FT-IR) microspectroscopy. *The Plant Journal*, **35**, pp. 393-404.



- National Cancer Institute, 1978. Bioassay of benzotriazole for possible carcinogenicity. National Cancer Institute, Bethesda, MD, DHEW Pub No. NIH 78-1338.
- Olson, P.E. and J.S. Fletcher, 2000. Ecological recovery of vegetation at a former industrial sludge basin and its implication in phytoremediation. *Environmental Science and Pollution Research*, **7**, pp. 195-204.
- Olson, P.E., J.S. Fletcher, P.R. Philip, 2001. Natural attenuation/phytoremediation in the vadose zone of a former industrial sludge basin. *Environmental Science and Pollution Research*, **8**, pp. 243-249.
- Oomen, R.J.F.J., E.N. Tzitzikas, E.J. Bakx, I. Straatman-Engelen, M.S. Bush, M.C. McCann, H.A. Schols, R.G.F. Visser, J.-P. Vincken, 2004. Modulation of the cellulose content of tuber cell walls by antisense expression of different potato (*Solanum tuberosum* L.) *Cesa* clones. *Phytochemistry*. **65**, pp. 535-546.
- Pavlostathis, S.G., K.K. Comstock, M.E. Jacobson, F.M. Saunders, 1998. Transformation of 2,4,6-trinitrotoluene by the aquatic plant *Myriophyllum spicatum*, *Environmental Toxicology and Chemistry*, **17**, pp. 2266-2273.
- Picka, K. and Z. Friedl, 2004. Phytotoxicity of some toluene nitroderivatives and products of their reduction. *Fresenius Environmental Bulletin*, **13**, pp. 789-794.
- Prasad, M.N.V. and H.M. Freitas, 2003. Metal hyperaccumulation in plants-Biodiversity prospecting for phytoremediation technology. *Electronic Journal of Biotechnology*, **6**, pp. 285-321.
- Pogany, E., K.-H. Pawlitzki, P. R. Wallnöfer, 1990. Formation, distribution and bioavailability of cell wall bound residues of 4-chloroaniline and 2,4-dichlorophenol. *Chemosphere*, **21**, pp. 349-358.
- Raab, T.K. and M.C. Martin, 2001, Visualizing rhizosphere chemistry of legumes with mid-infrared synchrotron radiation. *Planta*, **213**, pp. 881-887.
- Raab, T.K. and J.P. Vogel, 2004. Ecological and agricultural applications of synchrotron microscopy. *Infrared Physics and Technology*, **24**, pp. 393-402.
- Reiter, G., M. Siam, D. Falkenhagen, W. Gollneritsch, D. Baurecht, U.P. Fringeli, 2002. Interaction of a bacterial endotoxin with different surfaces by in situ Fourier infrared transform infrared attenuated total reflection spectroscopy. *Langmuir*, **18**, pp. 5761-5771.
- Rogers, L.A. and M.M. Campbell, 2004. The genetic control of lignin deposition during plant growth and development. *New Phytologist*, **164**, pp. 17-30.

- Rollinson, G. and A. G. Calley, 1986. No evidence for the biodegradation of benzotriazole by elective culture or continuous enrichment. *Biotechnology Letters*, **8**, pp. 303- 304.
- Schneider, K., J. Oltmanns, T. Radenberg, T. Schneider, D. PaulyMundegar. 1996. Uptake of nitroaromatic compounds in plants – implications for risk assessment of ammunition sites. *Environmental Science and Pollution Research*, **3**, pp.135-138.
- Séné, C.F.B., M.C. McCann, R.H. Wilson, R. Grinter, 1994 Fourier-transform Raman and Fourier-transform infrared spectroscopy: An investigation of five higher plant cell walls and their components. *Plant Physiology*, **106**, pp.1623-1631.
- Sens, C., P. Scheidemann, D. Werner, 1999. The distribution of <sup>14</sup>C-TNT in different biochemical compartments of the monocotyledonous *Triticum aestivum*. *Environmental Pollution*, **104**, pp. 113-119.
- Shone, M.G.T. and A.V. Wood, 1974. A comparison of the uptake and translocation of some organic herbicides and a systemic fungicide by barley. I. Absorption in relation to physiochemical properties. *Journal of Experimental Botany*, **25**, pp. 390-400.
- Smiths Detection, 2004. Application Brief AB-056, Visual microscopic analysis with a diamond ATR infrared objective, [www.smithsdetection.com](http://www.smithsdetection.com), pp. 1-2.
- Stewart, J.J.P., S.R. Bosco, W.R. Carper, 1986. Vibrational spectra of 2,4,6-TNT and its isotopically substituted analogues. *Spectrochimica Acta Part A: Molecular Spectroscopy*, **42**, pp. 13-21.
- Su, Y.-H. Y.-G. Zhu, 2006. Bioconcentration of atrazine and cholorphenols into roots and shoots of rice seedlings. *Environmental Pollution*, **139**, pp.32-39.
- Sun, W.-H., G.L. Horst, R.A. Drijber, T.E. Elthon, 2000. Fate of 2,4,6-trinitrotoluene in axenic sand culture systems containing smooth brome grass. *Environmental Toxicology and Chemistry*, **19**, pp. 2038-2046.
- Sung, K., M.Y. Corapcioglu, M.C. Drew, C.L. Munster, 2001. Plant contamination by organic pollutants in phytoremediation. *Journal of Environmental Quality*, **30**, pp. 2081-2090.
- Sutherland, G.B.B.M., 1952. Infrared analysis of amino acids, polypeptides and proteins. *Biochimica Biophysica Acta*, **6**, pp. 291-318.
- Tadros, M.G., A. Crawford, A. Mateo-Sullivan, C. Zhang, J.B. Hughes, 2000. Toxic effects of hydroxyamino intermediates from microbial transformation of trinitrotoluene and dinitrotoluenes on *Selenastrum capricornutum*. *Bulletin of Environmental Contamination and Toxicology*, **64**, pp. 579-585.

- Thomas, B.B., 1970. Pulp properties. In: *Handbook of Pulp and Paper Technology*. K.W. Britt (Ed), Van Nostrand Reinhold Co., New York, pp. 225-238.
- TOXNET, Toxicology Data Network, United States National Library of Medicine, <http://toxnet.nlm.nih.gov>, August 6, 2004.
- Tront, J., 2004. Plant Activity and Organic Contaminant Processing by Aquatic Plants. Doctoral Thesis. School of Civil and Environmental Engineering, Georgia Institute of Technology, Atlanta, GA, USA.
- United States Environmental Protection Agency, 1977. Investigation of selected potential environmental contaminants: benzotriazoles. USEPA 560/2-77-001.
- United States Environmental Protection Agency, 1990. Integrated Risk Information System: 2,4-/2,6-dinitrotoluene mixture.
- United States Environmental Protection Agency, Basic Query Results for Superfund sites on the National Priorities List <http://www.epa.gov/superfund/sites/query/basic.htm>, October 12, 2005.
- University of Arkansas at Little Rock, Department of Biology, Root Anatomy – Biology 2402 Image Database, <http://www.ualr.edu/botany/rootanatomy.html>, February 13, 2006.
- Vance, C.P., T.K. Kirk, R.T., Sherwood, 1980. Lignification as a mechanism of disease resistance. *Annual Reviews of Phytopathology*, **18**, pp. 259-288.
- Vicre, M., C. Santaella, S. Blanchet, A. Gateau, A. Driouich, 2005. Root border-like cells of Arabidopsis. Microscopical characterization and the role in the interaction with rhizobacteria. *Plant Physiology*, **138**, pp. 998-1008.
- Waisal, Y., A. Eshel, U. Kafkafi, Eds. 1996, *Plant Roots: The Hidden Half*, Marcel Dekker, New York.
- Wetzel, D.L., P. Srivarin, J.R. Finney, 2003, Revealing protein infrared spectral detail in a heterogeneous matrix dominated by starch. *Vibrational Spectroscopy*, **31**, pp. 109-114.
- Wetzel, D.L. and S.M. LeVine, 2001. Biological applications of infrared microspectroscopy, In: *Infrared and Raman Spectroscopy of Biological Materials*. H-U. Gremlich and B. Yan (Eds.), Marcel Dekker, New York, pp.101-142.
- Wetzel, D.L., A.J. Eilert, L.N. Pietrzak, S.S. Miller, J.A. Sweat, 1998. Ultraspatially resolved synchrotron infrared microspectroscopy of a plant tissue *in situ*. *Cellular and Molecular Biology*, **44**, pp. 145-167.

- Williams, D.H. and I. Fleming, 1980. Infrared Spectroscopy, In: *Spectroscopic Methods in Organic Chemistry*. McGraw Hill, New York, pp. 35-73.
- Young, K., L.E. Erickson, L.C. Davis, S. Castro-Diaz, 2001. Microbial degradation of 5-methyl benzotriazole, In: *Proceedings of the 31<sup>st</sup> Annual Biochemical Engineering Symposium*, L.E. Erickson (Ed.), Kansas State University, Manhattan, KS, pp. 29-34.
- Yu, P. 2005. Application of Cluster Analysis (CLA) in feed chemical imaging to accurately reveal structural-chemical features of feed and plants within cellular dimension. *Journal of Agricultural and Food Chemistry*, **53**, pp. 2872-2880.
- Yu, P. 2004. Applications of advanced synchrotron radiation-based Fourier transform infrared (SR-FTIR) microspectroscopy to animal nutrition and feed science: a novel approach. *British Journal of Nutrition*, **92**, pp. 869-885.
- Yu, P., C.R. Christensen, D.A. Christensen, J.J. McKinnon, 2005. Ultrastructural-chemical makeup of yellow-seeded (*Brassica rapa*) and brown-seeded (*Brassica napus*) canola within cellular dimensions, explored with synchrotron reflection FTIR microspectroscopy. *Canadian Journal of Plant Science*, **85**, pp. 533-541.
- Yu, P., D.A. Christensen, C.R. Christensen, M.D. Drew, B.G. Rossnagel, J.J. McKinnon, 2004a. Use of synchrotron FTIR microspectroscopy to identify chemical differences in barley endosperm tissue in relation to rumen degradation characteristics. *Canadian Journal of Animal Science*, **84**, pp. 523-527.
- Yu, P., J.J. McKinnon, C.R. Christensen, D.A. Christensen, 2004b. Using synchrotron-based FTIR microspectroscopy to reveal chemical features of feather protein secondary structure: Comparison with other feed protein sources. *Journal of Agricultural and Food Chemistry*, **52**, pp. 7353-7361.
- Yu, P., J.J. McKinnon, C.R. Christensen, D.A. Christensen, 2004c. Imaging molecular chemistry of Pioneer corn. *Journal of Agricultural and Food Chemistry*, **52**, pp. 7345-7352.
- Yu, P., J.J. McKinnon, C.R. Christensen, D.A. Christensen, 2004d. Using synchrotron transmission FTIR microspectroscopy as rapid, direct, and nondestructive analytical technique to reveal molecular microstructural-chemical features within tissue in grain barley. *Journal of Agricultural and Food Chemistry*, **52**, pp. 1484-1494.
- Yu, P., J.J. McKinnon, C.R. Christensen, D.A. Christensen, N.S. Marinkovic, L.M. Miller, 2003. Chemical imaging of microstructures of plant tissues within cellular dimension using synchrotron infrared microspectroscopy. *Journal of Agricultural and Food Chemistry*, **51**, pp. 6062-6067.

Zeier, J. and L. Schreiber, 1999. Fourier transform infrared-spectroscopic characterization of isolated endodermal cell walls from plant roots: chemical nature in relation to anatomical development. *Planta*, **209**, pp. 537-542.

Zeier, J. and L. Schreiber, 1997. Chemical composition of hypodermal and endodermal cell walls and xylem vessels isolated from *Clivia miniata*. *Plant Physiology*, 113, pp. 1223-1231.

Zumdahl, S.S., 1997, *Chemistry: Fourth Edition*, Houghton Mifflin Company, Boston, Massachusetts, pp. 288-289.